PHASE TRANSITIONS IN LINEAR POLYMERS:

FUNDAMENTAL MECHANISMS AND BIOTECHNOLOGICAL & BIOMEDICAL APPLICATIONS

Pauline Julika Kolbeck

München, 22. November 2023

PHASE TRANSITIONS IN LINEAR POLYMERS:

FUNDAMENTAL MECHANISMS AND BIOTECHNOLOGICAL & BIOMEDICAL APPLICATIONS

PAULINE JULIKA KOLBECK

München
22.11.2023

PHASENÜBERGÄNGE IN LINEAREN POLYMEREN:

GRUNDLEGENDE MECHANISMEN SOWIE BIOTECHNOLOGISCHE & BIOMEDIZINISCHE ANWEDUNGEN

PAULINE JULIKA KOLBECK

Dissertation
durchgeführt an der Fakultät für Physik
der Ludwig-Maximilians-Universität
München

vorgelegt von
Pauline Julika Kolbeck
aus München

München, 22.11.2023

Erstgutachter: Prof. Dr. Jan Lipfert
Zweitgutachter: Prof. Dr. Thorben Cordes

Tag der Abgabe: 22.11.2023

Tag der mündlichen Prüfung: 20.02.2024

"You are young yet, my friend," replied my host, "but the time will arrive when you will learn to judge for yourself of what is going on in the world. Believe nothing you hear, and only one half that you see."

Edgar Allan Poe, The System of Doctor Tarr and Professor Fether (1845)

ACKNOWLEDGEMENTS

I would like to express my gratitude to all the people who have been significant in supporting this work and my PhD in general.

First of all, I would like to thank my parents, Christine and Helmut, as well as my sister Lea and my brother Benjamin for everything.

Thank you, Jan, for all the support, advice, and independence you have given me over the years. I could explore and learn new concepts while maintaining my own research interests and ideas – thank you for making this possible.

I would like to thank Aidin Lak and Hermann Gaub for scientific and non-scientific support, and for being great role models and mentors to me. Thank you, Tarik, for legal support. And Arthur, I can't thank you enough for all throughout my PhD. Last but not least, I'd like to thank my collaborators, current and former group members, and all other people who supported and inspired me – each of them knows what I'm grateful for:

Achim Löf
Adina Hausch
Aksana Svirydava
Angelika Kardinal
Anna Baptist
Annalena Salditt
Anna Salvetti
Annika Tölke
Ann-Kathrin Wagner
Aron Venczel
Barbara Müller
Carleen Kluger
Carola Lampe
Caroline Körösy
Cees Dekker
Cendrine Moskalenko
Chris Sikeler
Christian Gebhardt
Constantin Schöler
Damla Tetiker
Dave van den Heuvel
Diana Pippig
Dihia Benaoudia
Elleke van Harten
Ellis Durner
Enrico Carlon
Enrico Skoruppa
Fabien Montel
Felix Müller
Franzi Kriegel
Gerd Gemmecker
Gerhard Blab
Gloria Müller
Grega Posnjak
Hemani Chhabra
Irina Martynenko
Jérôme Mathé
Joachim Rädler
Jochen Müller
Juliette Authier
Katy Erlich
Kelly Brouwer
Klaus Beckord
Laura Filion
Laura Krumm
Lea Wassermann
Leo Schendel
Linda Brützel
Linh Nguyen
Louis de Gaste
Lukas Milles
Magnus Bauer
Margherita Gallano
Marjolein de Jager
Martin Benoit
Marvin Freitag
Max Urban
Melanie Burkhard
Michael Hafner
Michi Scheckenbach
Midas Segers
Mihir Dass
Miloš Tišma
Moritz Weck
Nick Hundt
Nina Beier
Patrick Kudella
Paulo Onuchic
Philipp Nickels
Philipp Walker
Relinde van Dijk-Moes
Res Jöhr
Sabine Hohenester
Samuel Stubhan
Sebastian Konrad
Sha Li
Simone Ezendam
Stefanie Pritzl
Steffen Sedlak
Steven Boeynaems
Steven De Feyter
Susanne Hennig
Susi Kempter
Sylvia Kreuzer
Thomas Zettel
Thorben Cordes
Tim Liedl
Tine Brouns
Tobi Forster
Tom Nikolaus
Willem Vanderlinden
Wolfgang Ott
Yi-Yun Lin
Zeger Debyser
and any others
I may have overlooked.

Thank you.

PUBLICATIONS

RESEARCH CONTRIBUTIONS WHICH ARE PART OF THIS THESIS

[1] P. J. Kolbeck, D. Benaoudia, L. Chazot-Franguiadakis, G. Delecourt, J. Mathé, S. Li, R. Bonnet, P. Martin, J. Lipfert, A. Salvetti, et al. "Thermally Switchable Nanogate Based on Polymer Phase Transition." In: *Nano Letters* 23.11 (2023), pp. 4862–4869. ISSN: 1530-6984. DOI: 10.1021/acs.nanolett.3c00438.

[2] P. J. Kolbeck, M. Dass, I. V. Martynenko, R. J. A. van Dijk-Moes, K. J. H. Brouwer, A. van Blaaderen, W. Vanderlinden, T. Liedl, and J. Lipfert. "DNA Origami Fiducial for Accurate 3D Atomic Force Microscopy Imaging." In: *Nano Letters* 23.4 (2023). PMID: 36745573, pp. 1236–1243. DOI: 10.1021/acs.nanolett.2c04299.

[3] P. J. Kolbeck, M. de Jager, M. Gallano, T. Brouns, S. F. Konrad, F. Christ, Z. Debyser, S. De Feyter, L. Fillion, W. Vanderlinden, et al. "HIV integrase compacts viral DNA into biphasic condensates." In preparation.

OTHER RESEARCH CONTRIBUTIONS

[1] W. Vanderlinden, T. Brouns, P. U. Walker, P. J. Kolbeck, L. F. Milles, W. Ott, P. C. Nickels, Z. Debyser, and J. Lipfert. "The free energy landscape of retroviral integration." In: *Nature Communications* 10.1 (2019), p. 4738. ISSN: 2041-1723. DOI: 10.1038/s41467-019-12649-w.

[2] W. Vanderlinden, P. J. Kolbeck, W. Frederickx, S. F. Konrad, T. Nicolaus, C. Lampe, A. S. Urban, C. Moucheron, and J. Lipfert. "Ru(TAP)32+ uses multivalent binding to accelerate and constrain photo-adduct formation on DNA." In: *Chemical Communications* 55.60 (2019), pp. 8764–8767. ISSN: 1359-7345. DOI: 10.1039/C9CC02838B.

[3] W. Vanderlinden, P. J. Kolbeck, F. Kriegel, P. U. Walker, and J. Lipfert. "A benchmark data set for the mechanical properties of double-stranded DNA and RNA under torsional constraint." In: *Data in Brief* 30 (2020), p. 105404. ISSN: 2352-3409. DOI: https://doi.org/10.1016/j.dib.2020.105404.

[4] P. J. Kolbeck, W. Vanderlinden, G. Gemmecker, C. Gebhardt, M. Lehmann, A. Lak, T. Nicolaus, T. Cordes, and J. Lipfert. "Molecular structure, DNA binding mode, photophysical properties and recommendations for use of SYBR Gold." In: *Nucleic Acids Research* 49.9 (2021), pp. 5143–5158. ISSN: 0305-1048. DOI: 10.1093/nar/gkab265.

[5] W. Vanderlinden, E. Skoruppa, P. J. Kolbeck, E. Carlon, and J. Lipfert. "DNA fluctuations reveal the size and dynamics of topological domains." In: *PNAS Nexus* 1.5 (2022). ISSN: 2752-6542. DOI: 10.1093/pnasnexus/pgac268.

[6] Y.-Y. Lin, T. Brouns, P. J. Kolbeck, W. Vanderlinden, and J. Lipfert. "High-yield ligation-free assembly of DNA constructs with nucleosome positioning sequence repeats for single-molecule manipulation assays." In: *Journal of Biological Chemistry* 299.7 (2023). ISSN: 0021-9258. DOI: 10.1016/j.jbc.2023.104874.

[7] A. Lak, Y. Wang, P. J. Kolbeck, C. Pauer, M. S. Chowdhury, M. Cassani, F. Ludwig, T. Viereck, F. Selbach, P. Tinnefeld, et al. "Cooperative dynamics of DNA grafted magnetic nanoparticles optimize magnetic biosensing and coupling to DNA origami." In: *bioRxiv* (2023), p. 2023.04.11.536349. DOI: 10.1101/2023.04.11.536349.

[8] P. J. Kolbeck, M. Tišma, B. T. Analikwu, W. Vanderlinden, C. Dekker, and J. Lipfert. "Supercoiling-dependent DNA binding." In: *Nucleic Acids Research* In.press (2023).

[9] P. J. Kolbeck, W. Vanderlinden, H. Chhabra, A. Aksimentiev, and J. Lipfert. "Exploring the limits of AFM-based nano-mechanical property mapping using DNA origami." In preparation.

[10] P. J. Kolbeck, W. Vanderlinden, E. Skoruppa, M. Segers, J. Boltersdorf, M. Gallano, E. Carlon, and J. Lipfert. "A critical point for DNA at low forces." In preparation.

[11] W. Vanderlinden, P. J. Kolbeck, D. Tetiker, and J. Lipfert. "Quantifying DNA length distributions by high throughput AFM analysis." In preparation.

[12] D. Tetiker, E. Skoruppa, P. J. Kolbeck, W. Vanderlinden, and J. Lipfert. "Decimating the DNA persistence length." In preparation.

[13] L. Chazot-Franguiadakis, J. Eid, G. Delecourt, P. J. Kolbeck, S. Brugère, B. Molcrette, M. Socol, M. Mougel, A. Salvetti, V. Démery, et al. "Soft jamming of viral particles in nanopores." Submitted.

[14] J. Mathé, S. Li, P. J. Kolbeck, F. Montel, D. Benaoudia, P. Guégan, V. Bennevault, C. Huin, and J.-C. Lacroix. "Filtration of biomolecules using nanoporous membranes functionalized by eletrografted polymers mimicking the nuclear pore." In: *European patent, EP2022057121W* (2022). European patent, EP2022057121W.

ZUSAMMENFASSUNG

Phasenübergänge sind allgegenwärtig und werden in der Physik schon seit langer Zeit untersucht. Seit einigen Jahren finden Phasenübergänge auch in biologischen Systemen große Beachtung und sind zunehmend als wichtiges regulatorisches Prinzip etabliert. In dieser Arbeit stelle ich drei Forschungsprojekte vor, die sich mit Phasenübergängen in linearen Polymeren befassen und zeige, wie wir sie im biologischen Kontext verstehen und anwenden können. Außerdem stelle ich neu etablierte Methoden für quantitative Messungen und Anwendungen auf der Nanoskala vor.

Im ersten Teil beschreibe ich ein neues selektives und schaltbares Nanoporensystem für Biomakromoleküle. Durch Ausnutzung des Einflusses verschiedener Polymerbeschichtungen im Inneren künstlicher Nanoporen auf den Transport von Biomolekülen konnte ich eine thermisch schaltbaren Nanopore schaffen. Das System basiert auf einem Phasenübergang der in die Nanopore selektiv angebundenen Polymere, der über die Temperatur einstellbar ist. Der resultierende Thermoschalter eröffnet neue Perspektiven für die Kontrolle des Transports und der Filtration von Makromolekülen und insbesondere von Viruspartikeln.

Im zweiten Teil stelle ich eine neue Methode zur Charakterisierung von Rasterkraftmikroskopie (AFM)-Spitzen und zur Bildrekonstruktion auf Grundlage einer DNA-Origami-Referenzstruktur vor. Diese Methode ermöglicht es, AFM-Spitzen im Detail zu charakterisieren und diese Informationen dann zu nutzen, um präzise 3D-AFM-Bilder und genaue Größenschätzungen von Biomolekülen und ihren Komplexen sowie anderen Arten von (nicht-)biologischen Nanostrukturen zu erhalten.

Im dritten Teil untersuche ich die Wechselwirkung des Proteins HIV ontegrase (IN) mit DNA. Mit Hilfe von Rasterkraftmikroskopie (AFM)-Bildgebung, AFM-basiertem Elastizitätsmapping und Einzelmolekülmessungen mit der magnetischen Pinzette (MT) zeige ich, dass IN neben der viralen Integrationskatalyse eine weitere, bisher unbekannte Rolle spielen kann, nämlich bei der Kompaktierung der vialen DNA. Ich zeige auf, dass die Kompaktierung in zwei verschiedenen Konzentrationsregimen stattfindet und zur Bildung von zweiphasigen Kondensaten führt, die einen harten Kern haben, der von einer weicheren äußeren Schicht umgeben ist und durch zwei thermodynamisch und mechanisch verschiedene Arten von Wechselwirkungskräften zusammengehalten wird.

Die hier vorgestellten Ergebnisse unterstreichen die Bedeutung von Phasenübergängen in linearen Polymeren und eröffnen neue Anwendungsmöglichkeiten in der Biotechnologie, der Biomedizin und anderen angrenzenden Forschungsbereichen.

ABSTRACT

Phase transition are ubiquitous and have long been studied in physics. In recent years, phase transitions in biological systems have attracted growing interest and are more and more established as an important regulatory principle. In this thesis, I will present three research projects investigating phase transitions in linear polymers, how we can understand them in a biological context, and demonstrate their use for biotechnological and biomedical applications. In addition, I will introduce and apply newly established methods that are essential for quantitative measurements at the nanoscale.

The first part focuses on a newly developed selective and switchable nanopore system for biomacromolecules. By exploiting the influence of different polymer graftings inside artificial nanopores on the translocation of biomolecules, I will demonstrate the creation of a thermally switchable nanogate. The system is based on a polymer phase transition of the polymers grafted in the nanopore which is tunable via temperature. This thermoswitch opens up new perspectives for controlling transport and filtration of macromolecules and, particularly, viral particles.

In the second part, I will present a novel method for atomic force microscopy (AFM) tip characterization and image reconstruction based on a DNA origami reference structure. The method allows to characterize AFM tips in detail and then use this information to obtain precise 3D AFM images and accurate size estimates of biomolecules as well as other types of (non-)biological nanostructures. This versatile and easy-to-use system greatly improves current AFM imaging and has broad applications in improving imaging results for samples ranging from biological macromolecules and their complexes to synthetic nanoparticles.

Finally, in the third part, I will analyze and characterize the interaction of the protein HIV integrase (IN) with DNA. Using AFM imaging, AFM-based elasticity mapping, and single-molecule magnetic tweezers measurements, I show that IN can play an additional, previously unknown role beyond viral integration catalysis, namely in DNA compaction. Intriguingly, compaction occurs in two distinct concentration regimes and results in the formation of biphasic condensates with a rigid core and a softer outer layer which are held together by two mechanically and thermodynamically distinct types of interaction forces.

The results of the following work highlight the importance of phase transitions in linear polymers and pave the way for new applications of these systems and techniques in nanotechnology, biomedicine, and beyond.

CONTENTS

LIST OF FIGURES

ABBREVIATIONS

1D	one-dimensional
2D	two-dimensional
3D	three-dimensional
AFM	atomic force microscope
AIDS	acquired immunodeficiency syndrome
cDNA	copy DNA
DNA	deoxyribonucleic acid
dsDNA	double-stranded DNA
FJC	freely-jointed chain
HIV	human immunodeficiency virus 1
IN	HIV integrase
LCST	lower critical solution temperature
MT	magnetic tweezers
NMR	nuclear magnetic resonance
NPC	nuclear pore complex
PCR	polymerase chain reaction
PIC	pre-integration complex
RNA	ribonucleic acid
SAXS	small-angle X-ray scattering
ssDNA	single-stranded DNA
TEM	transmission electron microscope
vDNA	viral DNA
WLC	worm-like chain
ZMW	zero-mode waveguide

1 PREFACE

1.1 PHASE TRANSITIONS AND CRITICAL PHENOMENA

1.1.1 *States of matter*

The German physicist and emeritus of my former chair (Lehrstuhl of Professor Hermann Gaub at the LMU Munich) Klaus Stierstadt begins his 1979 article "Phase Transitions in Physics and Biology" in the Journal *Physics Bulletin* as follows:

The original and more extensive version of this article first appeared in 1978 in German, see Ref. [1].

> The origin of phase transitions is one of the oldest problems of physics. Since the beginning of natural philosophy people have investigated why there are four different 'elements' in nature – fire, water, earth and air – and under which conditions these forms of matter transform into one another. We now know a much larger number of different 'elements', states of aggregation, structures or – to use an all embracing word – phases of matter [2].

These states of matter often correspond to three fundamental forms of matter: solid, liquid, and gas, with a prominent example being the three phases of water. Ice, liquid water, and water vapor each represent a phase of water as a collection of macroscopic numbers of water molecules. In recent years, the field of materials science has undergone significant expansion. In addition to evaporation, melting, and solidification processes, the importance of magnetic transitions, critical phenomena, and superconductivity cannot be overstated. These developments have made the physics of phase transitions a crucial area at the crossroads of several fields [3, 4].

1.1.2 *Historical developments in the field of phase transitions*

1.1.2.1 *Superfluidity in liquid helium*

A particularly remarkable phase transition is that in liquid helium. Liquid helium is a physical state it reaches at very low temperatures (at standard atmospheric pressure). In 1908, Heike Kamerlingh-Onnes, pioneer of cryogenics, first succeeded in liquefying a small amount of helium for the first time – an achievement for which he was awarded the Nobel prize in Physics in 1913 [5–7]. Only much later, in the 1940s, the Soviet physicist Lev Davidovich Landau [8] first theoretically described the phase transition in liquid helium. In 1962, he received the Nobel Prize in Physics for developing a mathematical theory of superfluidity

that explains the properties of liquid helium (also called helium II) at temperatures below 2.17 K (-270.98 °C, also called the lambda temperature) [9]. Landau's work is particularly noteworthy because he was the first to apply quantum theory to the motion of superfluid helium. He focused on the quantized states of motion of the entire liquid, unlike other scientists who had previously studied the states of individual atoms. He began by studying the state of the liquid at absolute zero, or its ground state, and described its excited states in terms of the motion of fictive particles called quasiparticles. With this, Landau could provide a quantitative theory of the flow properties of Helium II assuming two components: the "superfluid" component, which he identified as the part of the liquid that remained in its ground state, and a "normal" component corresponding to the quasiparticles [8, 10]. In addition, he integrated experimental results with his calculations and derived the mechanical properties of the quasiparticles. These results aided in the calculation of fluid properties and were later verified by research on the scattering of neutrons in liquid helium. Landau's research was of great importance for subsequent work, because it helped to better understand the properties of liquids as well as those of solid materials and rarefied gases. His theories on liquid helium serve as a remarkable and pivotal achievement in modern physics [9].

1.1.2.2 *A universal theory for continuous phase transitions*

Twenty years after Landau received the Nobel Prize in Physics, another great scientist was honored for his work on phase transitions: in 1982, the American physicist Kenneth Wilson was awarded the Nobel Prize in Physics "for his theory for critical phenomena in connection with phase transitions" [11]. He was the first to develop a general procedure for constructing improved theories concerning the transformations of matter in a continuous way – also called continuous or second-order phase transitions (which will be discussed in more detail in the next section). These transitions occur at characteristic temperatures (or pressures). However, unlike first-order transitions, they appear throughout the volume of a material once that temperature (called the critical point) is reached. The complete loss of ferromagnetic properties of certain metals when heated to their Curie points (about 750 °C for iron) is an example of such a transition [11–14].

In general, Wilson was a pioneer in the development of mathematical theory for physical systems near the critical point. The concept of phases of matter has long been known, as well as the fact that very different systems, such as liquids and magnetic materials, behave in much the same way, but a successful general theory of how phase transitions occur had long been missing. Because phase transitions involve fluctuations on many different length scales, they have been difficult to describe at a fundamental level. For example, when liquid water is cooled to the freezing point, tiny pieces of ice just a few molecules in size form

and then disappear alongside millimeter- and centimeter-sized pieces. Therefore, in this type of system, it is not possible to only work within a certain length scale –which would make calculations much easier – because fluctuations at all length scales are important. Wilson tackled this problem by using an existing framework called renormalization group theory, which allowed him to fit the physics at all relevant length scales into a manageable calculation. A fundamental result of this technique is that he showed that the nature of a phase transition is defined by just two parameters: the dimensionality of the system (one-dimensional (1D), two-dimensional (2D), or three-dimensional (3D)) and the dimensionality of a key quantity called the order parameter. This explains why very different physical systems undergo phase transitions in the same way [11–15].

1.1.2.3 *Topological phases of matter*

The last Nobel Prize in the field of phase transitions to be highlighted in this chapter was awarded in 2016 jointly to the British physicists David J. Thouless and F. Duncan M. Haldane, as well as the Scottish-American physicist J. Michael Kosterlitz "for theoretical discoveries of topological phase transitions and topological phases of matter" [16]. Already in 1972, Kosterlitz and Thouless identified a novel phase transition in 2D systems where topological defects play a key role [17, 18]. The theory they developed was subsequently very important in understanding the quantum theory of 1D systems at very low temperatures, as applied to certain types of magnets and to superconducting and superfluid films. In the early 1980s, Thouless and Haldane then worked out theoretical methods to characterize phases of matter that cannot be identified by their pattern of symmetry breaking. Based on these topological concepts, they were then able to explain, for example, the very precise quantization of the Hall conductance in 2D electron gases, as well as a theory for spin chains that incorporates topological effects [16, 19–21].

1.1.3 *Theoretical aspects and nomenclature of phase transitions and critical phenomena*

As discussed in the previous section, phase transitions are a central aspect of physics and are ubiquitous in various systems. The following section will focus on the theoretical aspects and nomenclature of phase transitions. Very fundamentally, a state of matter is called a phase when it is in thermodynamic equilibrium such that its properties are macroscopically homogeneous. This includes the well-known example of solid, liquid, and gas phases, as well as less common examples such as plasma – a state of matter consisting of a particle mixture of ions, free electrons, and neutral atoms or molecules that can be generated from the gaseous state by further energy input – or Bose-Einstein (BE) condensates – an extreme state of matter of a system of indistinguishable

particles in which the predominant part of the particles are in the same quantum mechanical state [4, 22–31]. A phase is characterised by a thermodynamic function, usually the free energy F of the system, which is determined by the partition function Z of the system:

$$Z = \exp\left(\frac{-F}{k_B T}\right) \tag{1}$$

with $k_B T$ the thermal energy of the system, consisting of the Boltzmann constant k_B and the absolute temperature T. A thermodynamic function then represents quantities or properties of a thermodynamic system. So it is a function of macroscopic parameters such as temperature or pressure. The phase of a macroscopic substance is then determined by the values of these parameters.

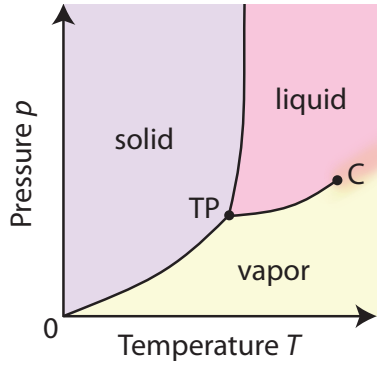

Figure 1: A typical phase diagram. The values of the control parameters (here the temperature T and the pressure p) determine the phase. 'C' is the critical point and 'TP' is the triple point.

Visually, different phases of a substance and their transitions can be represented in a phase diagram (Figure 1). Specific features such as phase boundaries (separating different phases), critical points (point 'C' in Figure 1), triple points (point 'TP' in Figure 1; where three phase boundaries meet) can then be identified in the phase diagram. At a phase boundary, a significant change in the properties of a system at the macroscopic level, so a change of a system parameter, e.g. pressure or temperature, driven by the same microscopic forces between its constituents, can result in a drastic modification of the macroscopic properties of the system, also called a phase change. For example, a solid phase changes to a liquid phase when the melting temperature is exceeded. This is then called a phase transition. The phase boundaries can disappear at a so-called critical point ('C') because the two phases are no longer distinguishable and the material exhibits anomalous behaviour. This universality of physical properties near critical points is a particularly intriguing property. Also coexistence of more than two phases is possible, for e.g. three phases this is then called a triple point ('TP') of the system [2, 31–35].

Phases can be characterized by a variety of physical parameters, one of the most important being the order parameter. This parameter measures how the microscopic elements that make up the macroscopic phase are ordered or in a similar state, i.e. the degree of (a)symmetry. It is non-zero in the ordered phase (low-symmetry state) and vanishes in the disordered phase (high-symmetry phase). Thus the order parameter is related to the breaking of a symmetry of the system being studied. In magnetic materials, for instance, the magnetization is the characteristic order parameter, and the alignment of the microscopic electronic spins gives rise to the macroscopic magnetism. The symmetry that is spontaneously broken is associated with the rotation of the spins. In solids, atoms or molecules occupy lattice positions, so here, the spatial periodicity of the molecules/atoms is the order parameter [3, 31, 32].

Phase transitions can be classified into first order phase transitions and second order phase transitions depending on the degree of singularity (non-analyticity) in functions representing their physical quantities: a phase transition is of first order (or discontinuous) if the first-order derivative of the free energy shows a discontinuity, which is reflected as discontinuity (jump), a cusp or a divergence in the function. In contrast, if the second (or higher order) derivative of the free energy show a discontinuity or a divergence, the transition is of second order (or also called continuous) [31, 32]. Often, continuous phase transitions are synonymous with critical phenomena, i.e., anomalous phenomena that occur around the critical point ('C' in Figure 1) at which two or more phases are no longer distinguishable. An intrinsic characteristic of critical phenomena is that fluctuations of all length scales occur simultaneously, leading to non-analytic behavior of physical variables. Due to the presence of these singularities, standard theoretical perturbative approaches are not applicable anymore [32, 34].

1.1.4 *Biological phase transitions*

Recently, phase transitions in living systems have become a very active field of research [28, 29, 33, 36–41]. They occur, for example, on a large scale in flocks of birds and in general animal population dynamics, but also on a small scale, for example in the complex organization in the cytoplasm of a cell, compartmentalization of biological systems, or in the collective migration of cell tissues during the development of organisms. From a physical point of view, phase transitions are of central interest because of the universal behaviour that occurs during a phase transition, i.e. certain properties of the system become largely independent of the microscopic details of the system. A key difference between physical and biological phase transitions is that in physical phase transitions, a group of inanimate particles move from one well-defined state of organisation to another whereas biological phase transitions are often much more complex and often out of equilibrium. In a complex biological system,

it is also more difficult to quantify an ordered state than in a physical system, further complicating the study of phase transitions in such systems. Overall, the complex non-equilibrium nature of biological systems has led to novel universal behaviors that were previously unobserved and have received increased attention in recent years [2, 33, 38].

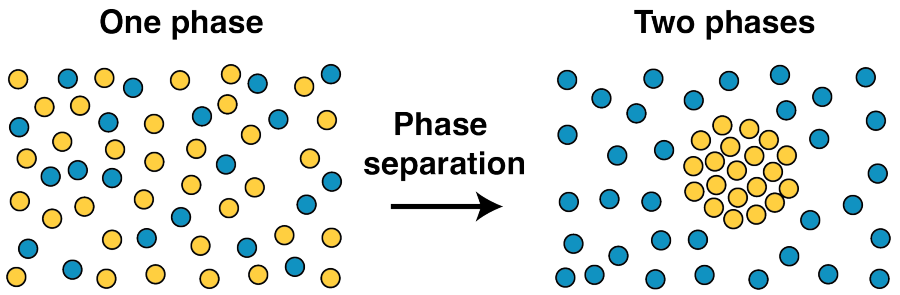

Figure 2: Very simple representation of two phases, mixed (left) and phase separated (right). A practical example would be a hydrophobic substance in a hydrophilic environment, such as oil in water.

Phase separation is a key regulatory mechanism in biology which plays an essential role in a variety of cellular processes – especially in confined systems – including signaling complexes as well as the formation of membraneless organelles and various other supramolecular assemblies. Membraneless organelles – supramolecular assemblies of proteins and nucleic acid molecules – can be formed, for example, by protein phase separation. The molecular properties, formation, regulation and function of these supramolecular assemblies have been elucidated by recent discoveries. To create a non-membrane-bound compartment, the compartment has to be isolated from the liquid cytoplasm, which can be accomplished by liquid-liquid phase separation, or demixing (Figure 2). This comprises several advantages for the cell, for example, that the components can be rapidly concentrated (or depleted) at a certain position in the cell, making phase separation a very powerful mechanism to organize cellular compartments, assemblies, and processes. It is now well established that cells use phase transitions (among other mechanisms), and in particular liquid-liquid phase separation, as a way to concentrate certain molecules and facilitate the formation of membraneless organelles. However, it is still challenging to study phase separation *in vivo*, especially under physiological conditions. Also, since it remains difficult to specifically perturb phase separation properties without affecting other functions of the protein, many functional consequences of phase separation *in vivo* remain to be elucidated. Understanding the physical concepts and fundamental molecular principles involved in the separation of phases in biological systems by combining techniques from cell biology, biophysics, physical chemistry, structural biology, and bioinformatics thus opens the door to important discoveries in the field of phase separation in living systems, including therapeutic interventions for e.g. protein aggregation diseases by targeting intracellular phase behavior [28, 36, 41, 42].

1.2 SCIENTIFIC SCOPE OF THIS THESIS

In this thesis, I will present a series of projects, which underline the relevance of classical concepts from the physics of polymer phase transitions for understanding complex biological systems as well as the structure of their components. To thoroughly understand polymeric phase transitions at the molecular level, precise and accurate measurements are required. Therefore, this thesis is a combination of newly established methods that significantly improve existing measurement techniques and application of these methods for an in-depth study of different phase transitions in linear polymers and how they can be used to improve existing methods and develop new approaches in biotechnology and biomedicine. I anticipate that the results presented in this work will increase our knowledge and understanding of phase transitions in linear polymers and the role they play in diagnostics and diseases.

Following this short preface, in Chapter 2, I will introduce important background concepts about polymers, deoxyribonucleic acid (DNA), and the human immunodeficiency virus 1 (HIV). In Chapter 3, I will explain the experimental techniques used to acquire the data presented in this thesis. The focus of Chapter 4 will be on a newly developed nanopore system that can be used to control the transport of bio-macromolecules and virus particles. By exploiting the grafting of different polymer types inside artificial nanopores, I show how to create a selective, temperature-controlled nanopore for macromolecular transport. In Chapter 5, I will introduce an atomic force microscope (AFM) fiducial structure for accurate AFM imaging in 3D. I will present a newly designed DNA origami structure for AFM tip characterization via blind tip reconstruction and AFM image reconstruction based on the obtained tip shape. Chapter 6 represents the heart of this thesis. It focuses on HIV integrase (IN) and its role in compacting viral DNA (vDNA) into biphasic condensates. I use a variety of techniques to obtain accurate and high-resolution measurements to study the interaction of the viral protein IN with DNA: Using AFM imaging, AFM-based elasticity mapping, and magnetic tweezers (MT), I will show how IN locally alters DNA structure by bending and bridging and globally compacts kilobase DNA into supramolecular IN-DNA-condensates. Through the combination of these powerful and highly complementary techniques, the work presented in this chapter contributes to the understanding of the mechanisms of HIV replication at the molecular level. Finally, in Chapter 7, I will summarize my findings and provide an outlook for possible future work.

2

BACKGROUND

2.1 POLYMERS

According to its translation from the ancient Greek, a polymer (composed of $\pi o \lambda \upsilon$ 'many' and $\mu \epsilon \rho o \varsigma$ 'part') is a chemical substance consisting of several (identical) subunits. The French physicist and Nobel Prize winner Pierre-Gilles de Gennes[1] was one of the global pioneers of soft matter research, which is the overarching field of research in polymer physics. He also dedicated his Nobel lecture from December 9, 1991 to this concept, from which the following lines are taken:

> What do we mean by soft matter? Americans prefer to call it "complex fluids". This is a rather ugly name, which tends to discourage the young students [44].

Despite the term complex fluids being "rather ugly" (at least to the ears of a Frenchman), de Gennes continued to elaborate in his lecture that it actually fits very well because it embodies two main concepts of soft matter physics, namely complexity and flexibility: Soft matter is a complex field that has evolved over many years and now ranges from polymers, surfactants, droplets, liquid crystals, colloidal grains, and binary mixtures, to biological systems such as micelles and liquid membranes [45, 46]. Flexible polymer chains can change from a liquid to a solid network structure, such as rubber, by forming bridges between the chains (e.g. by the oxygen from the air). This shows a characteristic feature of soft matter: a relatively mild chemical action results in a drastic change of the mechanical properties [44, 47].

Due to their distinctive properties, their high tunability, their convenience in manufacture, and their robustness, polymers have developed into indispensable materials in many areas of research as well as industry. Some well-known examples of synthetic polymers are nylon, teflon, polyvinyl chloride (PVC), and polyethylene terephthalate (PET). Famous biopolymers are for example polynucleotides (like nucleic acids), polypeptides (like proteins), as well as collagen, actin, fibrin, and polysaccharides. Thereby, biopolymers not only play an important role in living organisms, but are also used in many other areas, e.g. in food industry or pharmaceutical and biomedical technology. Biological polymers are

1 The Nobel Prize in Physics 1991 was awarded to Pierre-Gilles de Gennes "for discovering that methods developed for studying order phenomena in simple systems can be generalized to more complex forms of matter, in particular to liquid crystals and polymers" – another significant Nobel Prize in the history of phase transitions in physics [43].

often referred to as macromolecules because they are built up of thousands of covalently bonded atoms. The term macromolecule goes back to the German chemist and Nobel laureate Hermann Staudinger, who suggested as early as the 1920s that polymers are formed by covalent bonds linking smaller molecules [48, 49]. There are many structurally different forms of biopolymers, linear macromolecules, branched macromolecules, and wide- or close-meshed cross-linked polymers. In the context of this thesis' work, I will focus on linear polymers.

2.1.1 *Scaling concepts in polymer physics and polymer models*

Many essential concepts of polymer physics[2] can be explained in simple terms and follow universal scaling laws [47]. One of the simplest idealizations of a flexible linear polymer chain is to replace it with a chain of rigid segments whose orientations are completely uncorrelated with each other. In other words, the polymer chain is considered to consist of N segments of length b. These segments are assumed to be completely rigid and inextensible. The total polymer length (also called contour length L_C) is then given by $L_C = N \cdot b$. The segments are connected by perfectly flexible hinges or joints. It is also assumed that the segments do not interact and can even pass through each other, that means, there is no self-avoidance [51]. A visual description of the freely-jointed chain (FJC) model is that of a random walk, i.e. a walker taking each step in a random direction, irrespective of its previous step [52]. All steps have equal length, namely the segment length b, and any direction of a step has equal probability. If $\vec{b}_i$ is a vector that specifies step i, the total displacement of the walker after n steps (Figure 3), $\vec{S}$, can be written as

The analogy between a thread-like polymer and a random walk was first described 1934 by the Swiss Chemist Werner Kuhn in Ref. [52] (in German).

$$\vec{S} = \sum_{i=1}^{n} \vec{b}_i \tag{2}$$

The average value of $\vec{S}$, $\langle S \rangle$, over all possible walks with n steps is, of course, zero. However, the root mean square end-to-end distance $S_0 = \sqrt{\langle S^2 \rangle}$ is not zero:

$$S_0 = \sqrt{\langle S^2 \rangle} = \sqrt{\left\langle \left(\sum_{i=1}^{n} b_i \right)^2 \right\rangle} = \sqrt{\sum_{i=1}^{n} \langle b_i^2 \rangle} = \sqrt{\underbrace{b^2 + b^2 + ... + b^2}_{n \text{ times}}} =$$
$$= \sqrt{nb^2} = \sqrt{n} b \tag{3}$$

The root mean square end-to-end distance gives a measure of the average distance that the walker makes after n steps. The spatial extent of a

2 The derivations in this and the following section are strongly based on my notes from the course "Biophysics of Macromolecules" by Prof. Jan Lipfert and Prof. Ralf Jungmann from 2017 – a course I can only highly recommend – and supplemented with calculations from the book "Physical biology of the cell" by Rob Phillips [50].

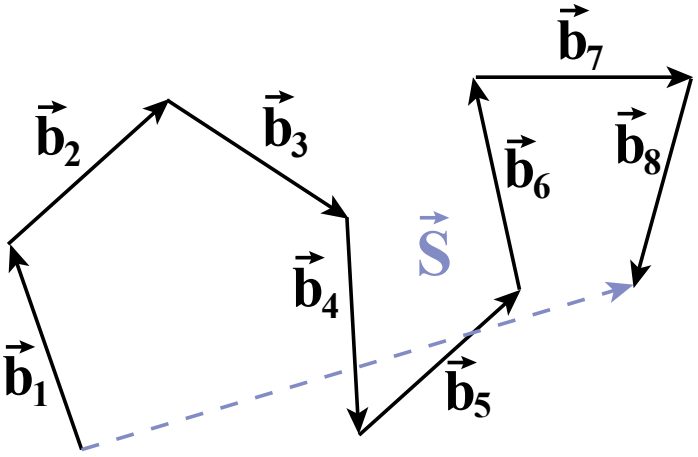

Figure 3: Vector representation of a random walk. Nine steps ($\vec{b}_1$ to $\vec{b}_8$) of the trajectory are shown as solid line arrows; the total displacement, $\vec{S}$, is shown by a dashed line arrow.

polymer chain can also be characterised by the radius of gyration R_g. This is a measure of the distribution of the chain around the mean position of the centre of mass of the chain. The two quantities are closely linked by

$$R_g^2 = \frac{1}{2N^2}\sum_{i,j}(\vec{b_i} - \vec{b_j})^2 = \frac{S_0^2}{\sqrt{6}} = b \cdot \sqrt{\frac{N}{6}} \tag{4}$$

The FJC model offers a relatively simplistic description, but only an approximate one, depending on the type of polymer. For macromolecules like double-stranded DNA (dsDNA) a much better description is given by a more elaborate semi-flexible polymer model, namely the worm-like chain (WLC) model, also called Kratky-Porod model in its discrete form, named after the Austrian physicists Otto Kratky and Günther Porod [53]. The basis for this model is the polymer's bending resistance that can be described in the form of a bending energy E_{bend} that penalizes deformations:

$$E_{bend} = -\kappa_b \sum_{s=1}^{N-1} \vec{t}(s) \cdot \vec{t}(s+1) = -\kappa_b \sum_{s=1}^{N-1} \cos(\theta(s)) \tag{5}$$

with κ_b the bending modulus, $\vec{t}(s)$ the unit tangent vector in s, which describes the local bending at position s of the polymer, and θ the bend angle. The partition function Z can then be factorized into a product of single junction contributions $Z = Z_1^N$, since the energy only couples neighboring vectors. Each single junction contribution can be expressed as:

$$Z_1 = \int_0^{\pi} \sin(\theta)\, \exp\left(\frac{\kappa_b \cdot \cos(\theta(s))}{k_B T}\right) d\theta = \frac{2\, \sinh\left(\frac{\kappa_b}{k_B T}\right)}{\frac{\kappa_b}{k_B T}} \tag{6}$$

From this, the correlation function of the orientation $\langle\cos(\theta)\rangle$ can then be written as

$$\langle\cos(\theta(s))\rangle = \frac{\partial \ln(Z_1)}{\partial(\frac{\kappa_b}{k_B T})} = \frac{1}{\tanh(\frac{\kappa_b}{k_B T})} - \frac{\kappa_b}{k_B T} \tag{7}$$

Expanding this equation to the lowest non-vanishing order, gives

$$\langle\cos(\theta(s))\rangle \approx 1 - \frac{k_B T}{\kappa_b} \tag{8}$$

In the following step, the tangent vector $\vec{t}(s)$ is decomposed in its parallel and orthogonal components:

$$\vec{t}(s+1) = \vec{t}(s)\cos(\theta(s)) + \vec{t}(s)^{ortho}\sin(\theta(s)) \tag{9}$$

From this, it follows that

$$\langle\vec{t}(s)\cdot\vec{t}(s+i)\rangle = (\langle\cos(\theta)\rangle)^i \tag{10}$$

The combination of the Equations 8 and 10 then results in

$$\langle\vec{t}(s)\cdot\vec{t}(s+i)\rangle \approx \exp\left(-\frac{i\cdot k_B T}{\kappa_b}\right) \equiv \exp\left(-\frac{i\cdot b}{L_P}\right) \tag{11}$$

with $L_P \equiv \frac{b\cdot\kappa_b}{k_B T}$ the bending persistence length of DNA. The persistence length is a measure of the rigidity or stiffness of a polymer and is defined as the length, over which the directional correlation of the segments in the polymer chain has decreased to 1/e (∼37%).

In addition to the discrete form of the WLC model, there is also a continuous form [51, 54]. Here, the position in the polymer is continuous and uniform through space, described by the coordinate along the polymer s. $\vec{t}(s)$ is again defined as the tangent vector in s with unit length to describe the local bending at position s in the polymer. The end-to-end vector $\vec{S}$ for a polymer of length L_C can then be written as

$$\vec{S} = \int_0^{L_C} \vec{t}(s)ds \tag{12}$$

The mean square end-to-end distance $\langle S^2\rangle$ can then be calculated as

$$\begin{aligned}\langle S^2\rangle = \langle\vec{S}\cdot\vec{S}\rangle &= \langle\int_0^{L_C}\vec{t}(s)ds\cdot\int_0^{L_C}\vec{t}(s')ds'\rangle = \\ &= \int_0^{L_C}ds\int_0^{L_C}ds'\langle\vec{t}(s)\cdot\vec{t}(s')\rangle = \int_0^{L_C}ds\int_0^{L_C}ds' e^{-\frac{|s-s'|}{L_P}} = \\ &= 2\cdot L_P\cdot L_C\cdot(1-\frac{L_P}{L_C}(1-e^{-\frac{L_C}{L_P}}))\end{aligned} \tag{13}$$

2.1.2 *Excluded volume effects*

There is an important difference between the trajectories of a random walk and the conformations of a polymer chain. Two segments of a polymer cannot spatially coincide. All interactions between monomers, between monomers and solvent and within the solvent have been ignored up to this point. In reality, however, a monomer cannot occupy the same volume of space as another monomer. This restriction is called excluded volume effect and has been introduced by Werner Kuhn in 1934 and shortly thereafter applied to polymer molecules by the American chemist Paul Flory. The concept refers to the idea that one part of a long-chain molecule cannot occupy a space already occupied by another part of the same molecule. In good solvents, the monomers prefer to come into contact with the solvent rather than with other monomers. This causes the inside of the chain to move outward to surround the monomers with solvent, so having the solvent around enlarges the volume occupied by the polymer. This results in a decrease in entropy due to positions becoming inaccessible to monomers as they are either already occupied by another monomer or by the solvent [51, 55].

By combining these two contributions to the free energy of the polymer, Flory could show that the polymer adopts a configuration of intermediate size. The radius of gyration then varies as a function of N as

$$R_g \propto N^{\frac{3}{5}} \tag{14}$$

with $\nu = \frac{3}{5}$ the Flory exponent in 3D space. Thus, the importance of these volume effects depends on the length of the polymer, and for a long polymer chain, the impact is not negligible.

2.2 THE DNA MOLECULE

Unless stated otherwise, the information in this section is mainly based on Ref. [50] and [56], two very good books about cellular biophysics and beyond.

DNA is the molecule that carries the genetic information for development and functioning of an organism and has therefore very high relevance. But, as discussed in the previous section, DNA can also be considered a biological polymer because of its repeating subunits. Along with proteins, nucleic acids are probably the best known biological polymers. Structurally, DNA can be described as a heteropolymeric biomolecule (Figure 4) because it consists of four different types of residues, called nucleotides. These nucleotides are composed of three entities: a nucleobase, a sugar (monosaccharide deoxyribose) and a phosphate group. The "alphabet" of the genetic code consists of the different nucleobases: A (adenine), T (thymine), C (cytosine), and G (guanine).

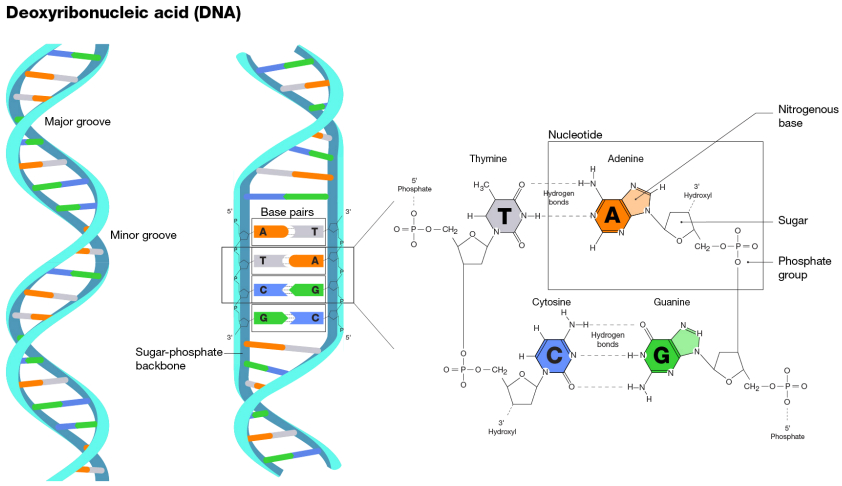

Figure 4: The double-helical structure of DNA. The DNA molecule consists of two strands that are twisted around each other like a wound ladder. Each strand has a backbone consisting of alternating sugars (deoxyribose) and phosphate groups. Attached to each sugar group is a nitrogenous base, also called nucleobase. Together a sugar group, a phosphate group, and a nucleobase form a nucleotide, which can be seen as the building blocks of DNA. The four nucleobases are T (thymine), A (adenine), C (cytosine), and G (guanine), which pair via complementary base pairing with one partner only: A forms two hydrogen bonds only with T, and G forms three hydrogen bonds only with C. Taken from Ref. [57]. Courtesy: National Human Genome Research Institute.

Nucleotides are assembled covalently into a strand of DNA (single-stranded DNA (ssDNA)) by linking the phosphate group of one nucleotide to the 3'-carbon of the deoxyribose ring of another nucleotide (Figure 4), called DNA backbone. Due to the asymmetric phosphodiester bond between two adjacent deoxyribose rings, it is possible to

assign a direction to a ssDNA molecule. One end of the ssDNA molecule terminates with a hydroxyl group at the 3'-carbon (the 3'-end), while the opposite end terminates with a phosphate group at the 5'-carbon (the 5'-end). Enzymes are sensitive to this directionality and normally process DNA from the 5'-end to the 3'-end.

Two strands of ssDNA can then form a DNA double helix, in which the bases establish stable hydrogen bonds with their respective partners, A with T and G with C. The double helical structure of DNA was discovered in 1953 by the American biologist James Watson and the English physicist (and later also molecular biologist) Francis Crick building on the x-ray diffraction data of the British chemists Rosalind Franklin and Raymond Gosling [58–61]. There are two hydrogen bonds between A and T, versus three that form between G and C. This consistent way to join the nucleobases is called complementary base pairing, or Watson-Crick base pairing and allows for straight forward replication of the nucleotide sequence during DNA replication. The aromatic rings of the nucleotides are arranged almost perpendicular to the length of the DNA strand, so that the π orbitals of the aromatic ring of one base overlap with the π orbitals of the aromatic ring of the adjoining base. As a result, the aromatic rings align. This effect is called base pair stacking, and greatly stabilizes the double helix (even more than the hydrogen bonds between complementary nucleobases).

The DNA structure shown in Figure 4 is referred to as B-(form) DNA, which is considered the canonical and most common form of DNA, and the form which the DNA double helix adopts in aqueous, neutral to basic solutions. It is a right-handed helix with a helical period close to 10.5 – 10.75 base pairs per turn, which corresponds to ∼3.5 nm. Its external diameter is ∼2.0 nm and the vertical distance between two adjacent base pairs is 0.34 nm [62–64]. B-DNA exhibits a larger groove, called the major groove, and a smaller one, called the minor groove. The two grooves are opposite each other, and run both continuously along the DNA molecule (Figure 4). For the sake of completeness, it should be mentioned that there are also other forms of dsDNA that are not dealt with here, as they are not relevant in the context of this work. These forms usually occur under extreme conditions of salt or pH or under higher forces and/or torques [51].

For biological meaning, the four-letter genetic code is divided into sections, the most important of which are genes, parts of DNA that contain information about the sequence of amino acids in proteins. The relationship between a DNA sequence and a protein sequence, was described by the British physicist and (co-)discoverer of the DNA double helix Francis Crick as the "two great polymer languages" of cells. The finding that the sequence of nucleic acid subunits in the DNA of the cell is directly responsible for determining the amino acid sequence of the proteins of the same cell was an enormous success of molecular

biology [65]. This relationship is also the basis for the central dogma of molecular biology, first expressed by Crick in 1958:

> The Central Dogma. This states that once "information" has passed into protein it cannot get out again. In more detail, the transfer of information from nucleic acid to nucleic acid, or from nucleic acid to protein may be possible, but transfer from protein to protein, or from protein to nucleic acid is impossible. Information means here the precise determination of sequence, either of bases in the nucleic acid or of amino acid residues in the protein [66].

The central dogma of molecular biology, which describes the universal flow of genetic information in cells can accordingly be summarised in simple words as 'DNA makes ribonucleic acid (RNA), and RNA makes protein'. Or more precisely, genetic DNA carries the necessary information for the synthesis of cell proteins, but is not directly responsible for protein production, but RNA is instead used as a middleman. So to express a certain protein, the relevant nucleotide sequence of the cellular DNA is transcribed into RNA, which is then translated into a amino acid sequence, which then forms a protein [67].

Nevertheless, over the years, other mechanisms of information transmission beyond the central dogma have been discovered in various biological systems, one example being retroviruses, like HIV (see Section 2.3 for more details on this group of viruses). In contrast to most organisms who store their genetic information in form of DNA, retroviruses use RNA to store their genetic information. In order for the retrovirus to insert their genetic material into the DNA genome of the host, the RNA must first be reverse transcribed into DNA. This process is called reverse-transcription because the flow of genetic information from RNA to DNA is opposite to the direction of transcription in the central dogma [67, 68].

2.2.1 *Physical and chemical properties of DNA*

For the storage of genetic information, the molecular structure of DNA is an important aspect. But also the physical and chemical properties of DNA are of major relevance. The genome, for instance, needs to be physically stored while still being accessible for genomic processes. The biological properties of DNA are therefore highly influenced by the specific elastic properties of the molecule, which are modified by local interactions.

2.2.1.1 *Mechanical properties of DNA*

In the early 1990s, newly developed techniques made it possible to perform the first quantitative studies of individual DNA molecules to

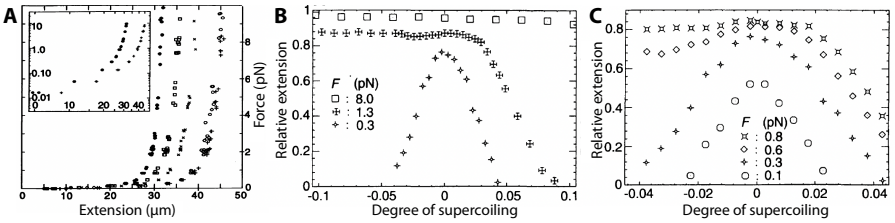

Figure 5: Single DNA molecules under force and torque. A) Force-extension behaviour of dsDNA in a buffered solution with 5 mM Na_2HPO_4 with various concentrations of ethidium bromide (a DNA stain; increasing concentration from 0.03 µg/mL to 2 µg/mL from left to right). As can be seen from the shift in the asymptotic value of the contour length of DNA, the dye-DNA interaction does not significantly alter the intrinsic elastic properties of DNA, the molecules simply become longer. Figure taken from Ref. [69]. B) Relative DNA elongation as a function of degree of supercoiling at different forces: $f = 8$ pN, 1.3 pN, and 0.3 pN. C) Same as in panel B for $f = 0.8$ pN, 0.6 pN, and 0.3 pN, and 0.1 pN. For small forces, the DNA behaviour is symmetrical, while for larger forces there is a transition to an extended state – first for negative supercoilings (> 0.45 pN) and subsequently for positive supercoilings (> 3 pN). Figure taken from Ref. [72].

examine their mechanical properties [69–72]. In 1992, Steven Smith from the group of the Peruvian-American biophysicist Carlos Bustamante at the University of Oregon conducted single-molecule measurements to study of the relationship between stretch and elongation on single DNA molecules [69] (Figure 5A). As experimental setup, they used single lambda phage DNA (λ-DNA) molecules that they chemically attached by one end to a glass surface and by the other end to a magnetic bead. These tethered beads were then subjected to various combinations of magnetic and hydrodynamic forces applied in perpendicular directions using movable magnets and variable currents [69, 70].

Further single-molecule experiments by Smith *et al.* in 1996 examined the elastic response of single dsDNA and ssDNA molecules to forces of tens of pN. They found that after the DNA molecule was fully stretched, a further increase in force resulted in a sharp transition to an overstretched DNA conformation, in which the average distance between adjacent base pairs was 1.6 times greater than in normal B-DNA [71]. In the same year, Terence Strick from the group of Vincent Croquette at the ENS in Paris performed the first experiments to study the elastic behavior of individual over- and underwound DNA molecules [72] (Figure 5B,C).

These first single-molecule DNA force-extension measurements in the early 1990s made it compelling to try to unravel the molecular mechanisms responsible for the elastic response of the DNA molecule over a wide range of forces and extensions, and to test the theories of polymer elasticity As introduced in the previous section (Section 2.1.1), it is a

characteristic of polymers that in solution, under physiological ionic conditions and at physiological temperatures, the polymer chain adopts many different conformations, which can be described in statistical terms by different models. First, the simple FJC was used to fit the experimental data and to interpret the measurements [70]. The model was found to fit the data reasonably well on the grand scheme, but the fit showed systematic deviations, especially at intermediate forces (Figure 6).

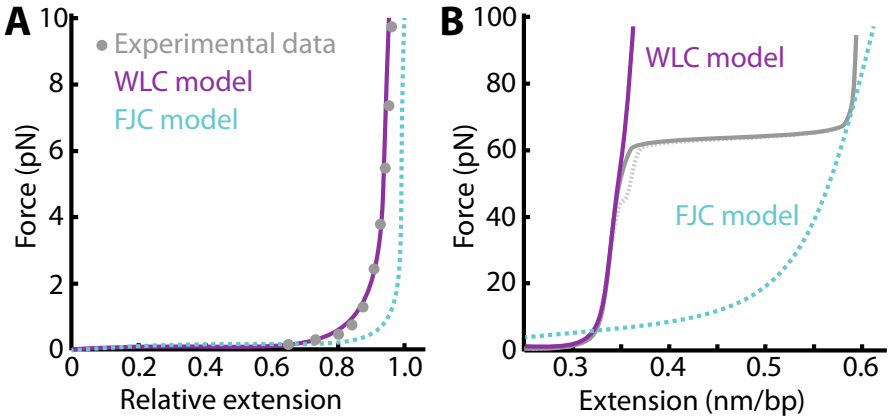

Figure 6: Force-extension relation of dsDNA in experiment and theory. A) Experimental and theoretical dependence of DNA elongation on stretching force at relatively low force ($f < 10$ pN). The experimental data are from Smith *et al.* [69]. The FJC model (turquoise dashed line) describes the data quantitatively, but does not as well as the WLC model (solid violet line). B) Force-extension data for dsDNA for forces up to 100 pN. Experimental data are shown as a solid black line (relaxation data depicted as a dotted line). A force-induced melting transition from dsDNA to ssDNA occurs near the L_C of dsDNA. The WLC model (solid violet line) describes the dsDNA well, whereas the FJC model (turquoise dashed line) describes only the ssDNA behavior approximately.

One reason for this deviation is that dsDNA has a non-zero bending stiffness, it behaves like a semi-flexible polymer. Thus, there is a preferential alignment between two consecutive monomers that imparts stiffness to the polymer chain. The more sophisticated WLC model achieves a better approximation to real nucleic acid molecules (Figure 6) [54, 73, 74]. In particular, fitting models to these single-molecule force-extension experiments provided a new way to determine stiffness measures of the polymer, representing the average angular correlation length between the monomers. The two important length scales characterizing the stiffness of a polymer are the Kuhn length and persistence length. In the FJC model, the Kuhn length l_{Kuhn} is simply the segment length b, since each segment can randomly orient in any direction regardless of the directions of the other segments. For models in which the molecule behaves semi-flexibly (such as dsDNA), the Kuhn length l_{Kuhn} is then

The Kuhn length is named after the Swiss chemist Hans Kuhn, who was in the group of Werner Kuhn (the two are, however, unrelated).

defined as twice the persistence length L_P [55, 75]. Using the WLC model, the persistence length could be accurately determined for varying environmental conditions (sequence, salt, temperature etc.), e.g. close to 50 nm for physiological conditions, which was a big breakthrough in the field of global DNA conformations in the 1990s [51, 70].

2.2.1.2 *Optical properties of DNA*

DNA quantification is an important pre-analytical step that is often performed by exploiting the optical properties of DNA. The two most commonly used methods are UV-Vis and fluorescence spectroscopy. Measures the absorbance of a sample using UV-Vis spectroscopy has the advantage of being fast and easy to perform. The four nucleobases of DNA, A, T, C and G, have an absorption maximum at a wavelength of 260 nm. In order to distinguish unbound nucleotides from ssDNA or ssDNA via spectral photometry, an effect called hypochromism plays an important role: The absorption of dsDNA is up to 25% less than the absorption of ssDNA and up to 40% less than the absorption of individual nucleotides. This means that a single strand of DNA absorbs less than the combined sum of its nucleotides, and dsDNA absorbs less than both strands of ssDNA.

On the other hand, fluorescence techniques for DNA quantification offer the advantage of higher accuracy and greater sensitivity to low concentrations. But – since DNA molecules emit almost no absorbed radiation – these techniques require additional steps such as special treatment of the samples with fluorescent substances [54, 76, 77].

2.2.1.3 *Polyelectrolyte properties of DNA*

At neutral pH, every phosphate in the backbone is de-protonated and thus negatively charged. As a result, each base pair of the DNA carries two elementary negative charges. Hence, the DNA molecule has an extremely high linear charge density in aqueous solution. These negative charges attract small cations from the solution, which then form a positively charged *cloud* around the DNA chain. Due to the electrostatic interaction between the charged DNA molecule and the *cloud* of counter ions, several important properties of DNA are strongly dependent on the salt concentration [51, 54, 78].

A detailed discussion of interactions between DNA and ions can be found in Ref. [78], which is also the main reference of this chapter.

The first complete and quantitative theoretical description of the complex ionic atmosphere associated with nucleic acids and proteins was already derived in the early 20th century independently by the French physicist Louis Gouy (1910) and the British physicist David Chapman (1913), equating the chemical potential and the force acting on small adjacent volumes in an ionic solution between two plates at a different voltage [79, 80]. This so-called Poisson-Boltzmann theory, named after the French physicist and mathematician Siméon Poisson and the Austrian physicist Ludwig Boltzmann, describes the interaction of mobile

ions with fixed charges in solution [78, 81]. The charged molecule is surrounded by a solvent, which is approximated as a continuum with a dielectric constant $\epsilon(\vec{r})$ and mobile ions of charge z_i interacting with a fixed charge density ρ^{fix} and the mean potential of all ions, which is determined by their Boltzmann factor. With the index i, all ion types present with their respective charge in the solution are enumerated. For example if there are magnesium and sodium ions in solution, for i = Mg^{2+} $z_i = +2$ and for i = Na^+ $z_i = +1$. By derivation of a mean-field approximation, the resulting differential equation for the electrostatic potential $\Phi(\vec{r})$ is then called Poisson-Boltzmann equation:

$$\vec{\nabla}(\epsilon(\vec{r})\vec{\nabla}\Phi(\vec{r})) = -4\pi\rho^{fix}(\vec{r}) - \lambda(\vec{r}) \cdot 4\pi \sum_i c_i^{\infty} z_i e \cdot \exp\left(\frac{-z_i e\Phi(\vec{r})}{k_B T}\right) \tag{15}$$

with e the elementary charge, k_B the Boltzmann constant, and T the absolute temperature. The term $\lambda(\vec{r})$ is a measure of accessibility, which deems the areas in space accessible ($\lambda = 1$) or inaccessible ($\lambda = 0$; i.e. inside the polyelectrolyte) to ions. The term c_i^{∞} is the bulk concentration of ion species i, i.e. the concentration far from the charged macromolecule [78, 81].

For small electric potentials, the non-linear Poisson-Boltzmann equation (Equation 15) can be linearized for simplification and to make it more computationally accessible, and then yields the Debye-Hückel approximation [82] developed in 1923 by the Dutch physicist and theoretical chemist Peter Debye together with his habilitand and assistant, the German physicist and chemist Erich Hückel. They introduced the important concept of screening of the electrostatic interactions between two charges in the presence of all other ions in the solution, thus all ions can be treated as a continuum [84]. By means of this approximation, the characteristic length scale, for which the electrostatic interactions are screened can be derived, among others. This length is called Debye length λ_D and is defined as:

Peter Debye received the Nobel Prize in Chemistry 1936 "for his contributions to the study of molecular structure" [83].

$$\lambda_D = \sqrt{\frac{\epsilon \cdot k_B T}{2\sum_i (z_i e)^2 c_i^{\infty}}} \tag{16}$$

with $\epsilon = \epsilon_0 \epsilon_r$ the permittivity of the solvent.

The Debye length can be interpreted as the radius of the ion atmosphere. It varies – depending on the ionic conditions – from about ∼0.3 nm in strong ionic solutions (e.g. ∼1 M NaCl) to ∼1 µm in distilled water.

Due to the complex properties of the ionic atmosphere, it is very difficult visualize and investigate it experimentally. For this reason, the characterization of the ion atmosphere is often based on theoretical models and descriptions [78]. In the early 1970s, the American physicist Gerald Manning first calculated that DNA and other polyelectrolytes

with sufficiently high charge density cause condensation of cations on the polyelectrolyte surface until their effective charge falls below a critical value. According to these simple electrostatic calculations, this condensed or bound layer is expected to neutralise ∼60 – 70% of the charge of the DNA backbone. According to this so-called Manning or counterion condensation theory, the free and condensed counterions exchange between the two concentric regions, since the condensed counterions are not chemically bound to the polyelectrolyte. This leads to the formation of a continuous radial counterion distribution around the polyelectrolyte. The theory agrees with a number of experiments, but it also has its limitations: for example, it does not take into account the properties and interactions of the ions, the solvent molecules and the hydration of the polyelectrolyte at the atomic level [78, 85–88].

2.2.2 *DNA nanotechnology and DNA origami*

DNA as the repository of the genetic information of all life has already been addressed earlier in this Chapter. However, a lot has happened in the last 70 years – since the discovery of the complementary double helix structure for nucleic acids in 1953 [61] – and other fields of DNA research have emerged, in which DNA plays more than just the role of storing genetic material. DNA molecules can also serve purposes outside the cell, for example for the production of nano-functional materials by exploiting the properties of DNA as a programmable polymeric biomolecule. The unique ability for precise molecular recognition and sequence configurability, combined with its rigidity, good biocompatibility and biodegradability, make DNA a powerful tool for use in the fabrication of multifunctional nanomaterials [89]. The field of bionanotechnology has its roots in the physical sciences. In his talk "Plenty of Room at the Bottom", the famous American physicist Richard P. Feynman portrays the newly emerging field to the American Physical Society in Pasadena on December 1959 as follows [90]:

> I would like to describe a field, in which little has been done, but in which an enormous amount can be done in principle. This field is not quite the same as the others in that it will not tell us much of fundamental physics (in the sense of, “What are the strange particles?”) but it is more like solid-state physics in the sense that it might tell us much of great interest about the strange phenomena that occur in complex situations. Furthermore, a point that is most important is that it would have an enormous number of technical applications.

In this famous lecture aimed to explore the towering possibilities of miniaturization, he gives the example of creating a "nanobot" – a robotic vessel on the order of nanometers that could navigate through a patient’s

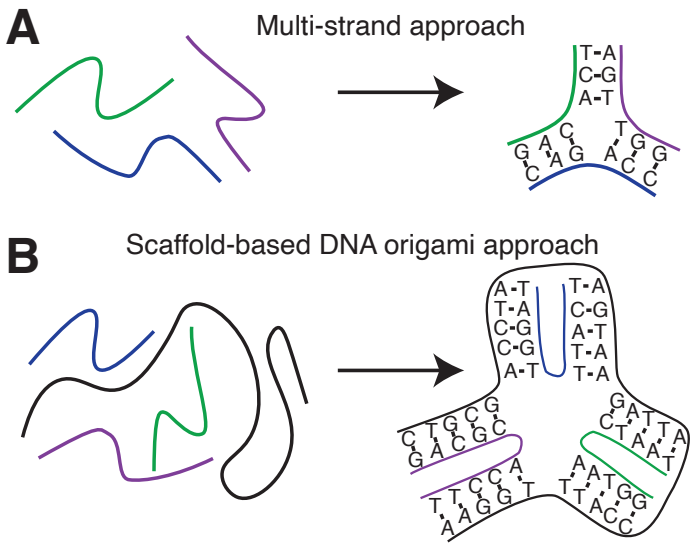

Figure 7: Schematic representation of the two main approaches to construct DNA-based architectures. a) Multi-stranded approach: oligonucleotides are designed to self-assemble and form a well-defined branched DNA motif, also called a tile. The hierarchical assembly of such motifs into larger (finite or infinite) structures is achieved by holding the sticky DNA ends – meaning that one DNA strand is longer than the other (usually by at least a few nucleotides), so that the longer strand has bases that remain unpaired – together. b) Scaffold-based assembly: a long single-stranded scaffold is folded into a desired finite shape using hundreds of shorter staple strands.

bloodstream and thus be used, for example, to repair cells or defend against pathogens [51, 90].

In 1982, the American biochemist and crystallographer Nadrian C. Seeman proposed using DNA as a construction material for the assembly of geometrically defined objects with nanoscale features [91, 92]. His starting idea was to construct a 3D lattice from DNA in order to orient target molecules, which would simplify their crystallographic study by eliminating the difficult process of obtaining pure crystals. This revolutionary idea laid the foundation for a new field of research now known as "structural DNA nanotechnology" [93]. Exploiting the self-recognition properties of DNA, rigid branched DNA motifs were designed based on complementary Watson-Crick base pairing between segments of a given oligonucleotide set. The resulting superstructures – often referred to as DNA tiles – serve as building blocks for further assembly into discrete finite objects or infinite periodic lattices by sticky-end cohesion [92–95].

Despite its proven viability, this multi-stranded approach (Figure 7a) has two major disadvantages: Firstly, the production of sizable structures requires precise stoichiometric control and thorough purification of individual oligonucleotides and/or tiles, leading to error-prone and time-consuming synthesis processes. And secondly, the complexity of

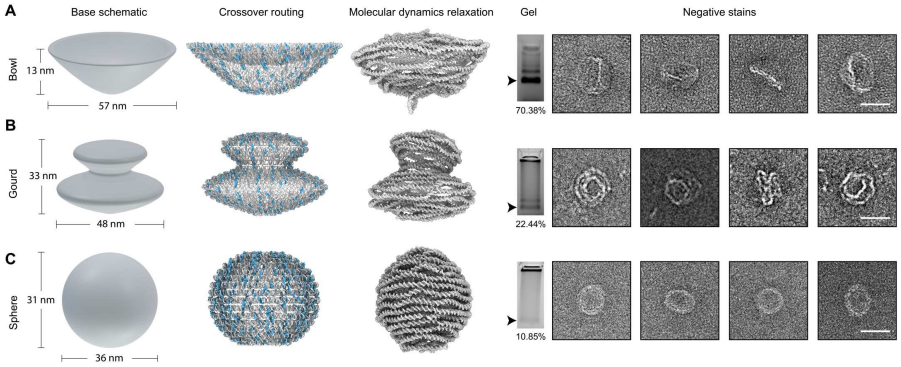

Figure 8: Three differently shaped 3D DNA origami structures: (A) bowl, (B) gourd, (C) sphere. From left to right: Basic schematic, crossover routing, molecular dynamics relaxation, gel electrophoresis, negative stain transmission electron microscope (TEM). All scale bars are 40 nm. Figure taken from Ref. [97].

the structures that can be generated with this approach is restricted to simple geometric shapes and the repetition of basic building units. To overcome these limitations, the American computer scientist Paul Rothemund introduced in 2006 the scaffold-based strategy (Figure 7b) [96]. This approach greatly simplified and accelerated the design and construction of nanometer-sized DNA objects since the self-assembly of a DNA structure is reduced to a straightforward process, in which a long single-stranded DNA, called the scaffold, is folded into basically any desired shape with the help of a multitude of short helper strands. Hence this technique has been given the name DNA origami, in reference to the Japanese art of folding paper.

In Rothemund's study, he used a single-stranded 7000 base pair-long circular M13mp18 genome as a scaffold strand, which was then folded with the help of over 200 short ssDNA staple strands into an array of helices through an arrangement of periodic crossovers. With this approach, he was able to build DNA structures of ∼100 nm in diameter and various shapes with nanoscale spatial resolution (Figure 8). Once synthesized and mixed, the staple and scaffold strands self-assemble in a single step and in a few hours – which is much faster than in the multi-stranded approach where assembly usually took ∼20 h. This superior performance of the scaffold-based DNA origami approach is mainly due to the entropic advantage of using a single long scaffold strand for folding. Because of their small length, staple strands prefer binding to the scaffold than to each other. Additionally, staple strands can (usually) be designed so that their sequences do not match. And lastly, the initial correct arrangement of the scaffold promotes the correct binding of the remaining stable strands, which consequently not only leads to a time advantage but also a decreased misfolding rate [98]. These hallmarks make DNA origami an attractive, robust, and powerful tool in structural DNA nanotechnology when designing 2D or 3D objects.

Today, there are countless possible applications for DNA origami structures, for example in nanofabrication, nanophotonics and nanoelectronics, catalysis, computation, molecular machines, bioimaging, drug delivery, and biophysics – not only as pure DNA materials, but also as hybrid DNA materials in combination with other materials [89, 99–101].

2.2.3 *DNA topology*

If not indicated otherwise, the content of this section is largely based on Ref. [51].

In their paper "The cyclic helix and cyclic coil forms of polyoma viral DNA" published 1963, the American biochemists Roger Weil and Jerome Vinograd describe their finding that the DNA of polyomaviruses is present in a closed-circular form and that this form is typical of bacterial DNA and the DNA of the cytoplasm of eukaryotic cells of animals [102, 103]. When they discovered that the axis of DNA can be coiled, they revealed a fundamental tertiary structural feature of dsDNA, called DNA supercoiling. This higher-order DNA structure involves both the interwinding of two complementary strands around each other and around a common helical axis. There is positively or negatively supercoiled DNA, which refers to a DNA molecule whose double helix has undergone an additional twist in the same direction as the original helix or in the opposite direction. For a dsDNA molecule to be supercoilable, it must be topologically constrained, meaning that both DNA ends are fixed. This is for example the case in (covalently) closed-circular DNA. By definition, closed-circular DNA is a circular dsDNA molecule with no nicks or breaks in either strand. The supercoiled DNA molecule minimizes its elastic energy by forming superhelical structures, also known as DNA supercoils (Figure 9).

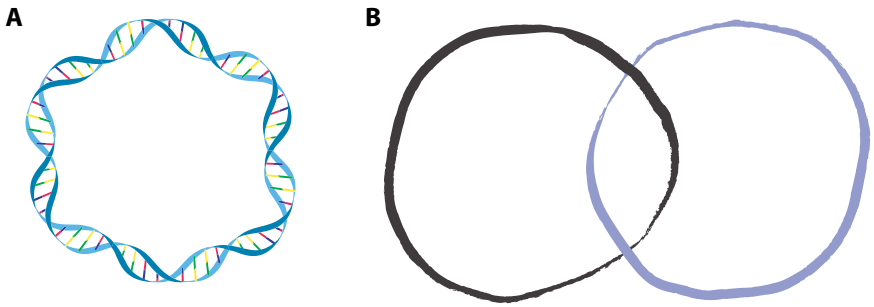

Figure 9: Topological aspects of closed-circular molecules. A) A closed-circular DNA molecule, meaning that both DNA strands are covalently closed. This type of DNA molecule is also called a plasmid. B) Two closed circles that have been linked together once, so the linking number $Lk = 1$.

Closed-circular molecules are characterised by the fact that their topological state cannot be changed by a conformational change that does not involve breaking of at least one DNA strand; only by a geometrical deformation, such as flexure or elongation, can they change their topological state. Polymeric topology generally refers to the properties of crosslinking or entanglement that are invariant under uniform geometric deformation. The unique properties of closed-circular DNA are due to this topological constraint. If one of the strands is broken (or cut), the supercoiled DNA molecule is transformed into an open-circular DNA

molecule, while if both strands are firmly broken, a linear DNA molecule is obtained [51, 54, 74, 102–104].

The number of times that one strand is linked with the other is described by a fundamental property of DNA supercoiling: the linking number Lk [105]. A relaxed, closed-circular DNA molecule has a linking number Lk_0, which can be calculated as the number of base pairs in the molecule N divided by the number of base pairs per helix turn γ:

$$Lk_0 = \frac{N}{\gamma} \tag{17}$$

It needs to be stressed that Lk_0 is not a topological invariant, as it can be changed for example by adding salt.

The introduction of supercoils into a DNA molecule will increase or decrease the number of helical turns enclosed (called DNA over- or undercoiling, respectively) and as a result change the global linking number Lk [106].

$$Lk = Lk_0 + \Delta Lk \tag{18}$$

Often, it is more convenient to express the level of supercoiling in form of a density that is effectively independent of the size of the molecule. To this end, ΔLk is normalized by Lk_0 to a supercoiling density σ:

$$\sigma = \frac{\Delta Lk}{Lk_0} \tag{19}$$

Figure 10 displays exemplary DNA molecules at different σ obtained from Monte Carlo simulations.

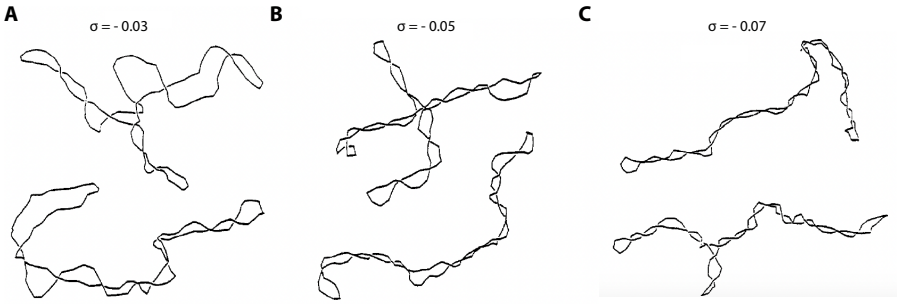

Figure 10: Computer simulated supercoiled DNA structures at different values of superhelical density σ. Data from Klenin *et al.* (Ref. [107]). Figure taken from Ref. [54].

The linking number Lk is related to two geometrical properties of the DNA molecule, namely the twist Tw and the writhe Wr. The twist Tw is a measure of rotation of the strands about the helical axis whereas the writhe Wr is a measure of the path of the helical axis in space [54, 74, 108, 109]. The three properties are related by White's theorem. The

theorem was named after the American physicist James White, who first formulated it in 1969 [109]:

$$Lk = Tw + Wr \tag{20}$$

While Lk is a topological property, Lk_0, Wr, and Tw are geometric properties, which can change their value when the molecule is deformed or e.g. by the addition of salt to the surrounding environment.

2.3 THE HUMAN RETROVIRUS HIV

There is a human striving for simplification and consistency, which seems to be widespread not only in the natural sciences. Sir Francis Bacon described this observation of the human nature already in aphorism XLVI from the first book of the Novum Organum in the 17th century:

> The human understanding when it has once adopted an opinion (either as being the received opinion or as being agreeable to itself) draws all things else to support and agree with it. And though there be a greater number and weight of instances to be found on the other side, yet these it either neglects and despises, or else by some distinction sets aside and rejects; in order that by this great and pernicious predetermination the authority of its former conclusions may remain inviolate [110].

Also biological classification, also called taxonomy, aspires to simplify and organize the enormous diversity of life. Throughout the history of biology, scientists have divided the diversity of living things into discrete groups called kingdoms, which has long been the highest rank of living organisms. One of the pioneers of this method of classification was Carl von Linné, also known by his Latin publishing name Linneaus, an 18th century Swedish naturalist. He distinguished for the first time between the kingdom of animals (Animalia) and that of plants (Plantae) [111, 112]. Over the centuries, further kingdoms have been added or removed, but until today, there is no consensus about which classification scheme to apply to the overall hierarchy of life among the world's taxonomists. The different classification systems were largely based on the comparison of phenotypic characteristics and were often historically influenced. They are therefore now considered as tending to be problematic and outdated, especially with regard to micro- and nano-organisms, but are nevertheless still widely used [113].

Today's classifications attempt to be less phylogenetic and yet not neglect historical and evolutionary aspects. They therefore often represent a consensus view that takes into account taxonomic decisions and practical compromises between different expert opinions. One well-established classification system introduced 2015 by Ruggiero *et al.* proposes seven kingdoms: the prokaryotic kingdoms Archaea (Archaebacteria) and Bacteria (Eubacteria), and the eukaryotic kingdoms Protozoa (single-celled eukaryotes), Chromista (single-celled and multicellular eukaryotic species that share similar features in their photosynthetic organelles), Fungi, Plantae, and Animalia [112].

Viruses are not part of this or any other biological classification system and in general the tree of life because they are seen as non-living entities that only hijack living cells in order to propagate. Nevertheless, viruses are tightly linked to life as they interact with almost every species. They

have therefore also undoubtedly played an essential role in evolution [114]. Interactions between different kingdoms shape population dynamics, evolutionary trajectories, and influence ecosystem functioning. Conversely, populations and communities are in turn shaped by forces acting from the top down. The widespread distribution of viruses in different systems – viruses are found in almost every ecosystem on earth – is a now well-established fact, and has led viral ecologists to quantify the impacts triggered by viral activity at diverse scales [115].

Viruses are infectious organic structures that spread outside cells by transmission. However, by their nature, viruses can only replicate in the living cells of an organism, also known as the host. They consist mostly of nucleic acids and proteins, which enable them to enter a cell and infect other life forms across all kingdoms [115–117]. With their nucleic acids, viruses possess the "code" for their reproduction and propagation, but they have neither independent replication nor their own metabolism and are therefore reliant on the metabolism of a host cell. Consequently, viruses are not considered living organisms, or as the American virologist Thomas Rivers writes in his article "The nature of viruses" already in 1932:

> Viruses are usually characterized by three negative properties, namely, invisibility by ordinary microscopic methods, failure to be retained by filters impervious to well-known bacteria, and inability to propagate themselves in the absence of susceptible cells [116].

Viruses are everywhere and on an almost unimaginable scale. The world we live in would be inconceivable without viruses, all our ecosystems rely on viruses. It is estimated that there are about 10^{31} of individual virus particles living in the oceans alone at any given time – that is 10 billion times the estimated number of stars in the known universe [118].

2.3.1 *The 'family' context of HIV*

Viruses can also be classified. The virus classification that has gained widespread acceptance is the Baltimore classification. It is named after its creator, the American biologist and Nobel laureate David Baltimore, and is based on the production mechanism of a specific type of RNA, namely messenger-RNA or short mRNA. For successful replication, viruses must produce mRNAs from their genomes, which in turn can produce necessary proteins. However, there are different mechanisms for this, which vary from virus family to virus family. For example, viral genomes can be single-stranded (ss) or double-stranded (ds), RNA or DNA, and may or may not use a reverse transcriptase. In addition, ssRNA viruses can be either sense (+) or antisense (-) [118, 119].

A large multimember virus family is the retrovirus family. Viruses of this family insert a DNA copy of their RNA genome into the DNA of

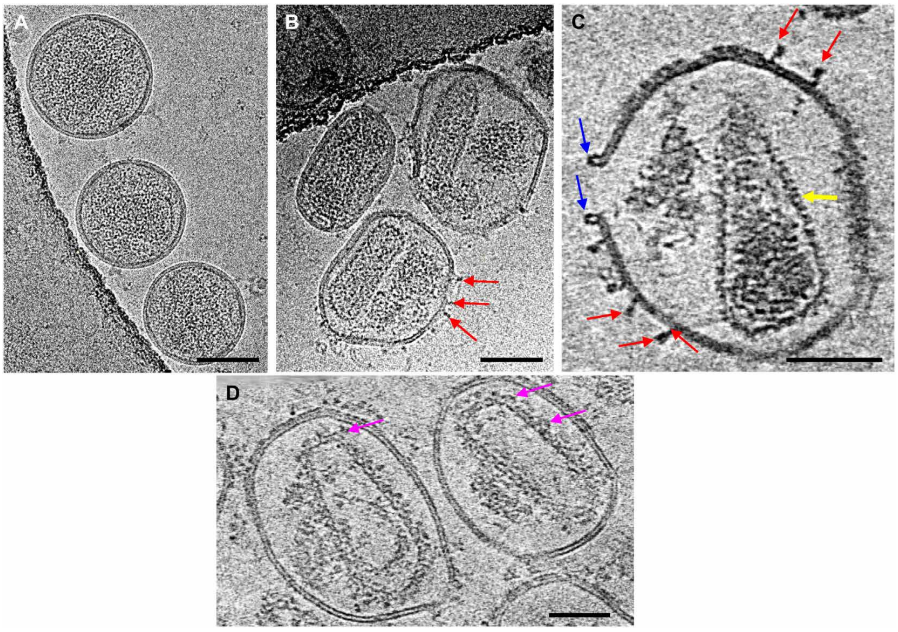

Figure 11: CryoEM of mature HIV virus-like particles (VLPs). For biosafety purposes, noninfectious VLPs were used. Pore-forming protein (PFO) was injected into small holes in the viral membrane while otherwise maintaining membrane integrity and the ability to contain the capsid. (A) CryoEM projection images of envelope HIV mature VLPs without PFO treatment. (B) Same as in panel A but with PFO treatment. (C) Tomographic slices of PFO-treated envelope HIV mature VLPs in the absence of IP6 (cellular metabolite inositol hexakisphosphate, a small molecule shown to modulate capsid assembly and stability) and CypA-DsRed (tetrameric fusion protein of host factor cyclophilin A, efficient capsid label for live-cell imaging assays) (D). Same as in panel C but here in the presence of IP6 and CypA-DsRed. Scale bars are 100 nm in panels A and B, and 50 nm in panel C and D. Figure taken from Ref. [120].

the host cell, thus altering the genome of the infected cell. To this family – or more precisely to its genus of lentivirus (slow retrovirues) – the globally known virus HIV (Figure 11) is also grouped. Following the Baltimore classification system, HIV is a class VI virus, meaning it has a positive sense, single-stranded RNA genome, but replicates through a DNA intermediate. The RNA is reverse-transcribed to DNA, which is then integrated into the host genome for subsequent transcription and translation [117, 119]. Retroviruses are very dangerous, unpredictable, and difficult to control. They insert themselves (randomly) into the genome, which can lead, for example, to the activation of genes that would otherwise remain inactive. In addition, retroviruses evolve very

HIV is classified into two main types: HIV-1 and HIV-2. HIV-1 was first discovered and is distributed worldwide, whereas HIV-2 is less pathogenic and occurs mainly in West Africa. HIV-1 and HIV-2 infections have differences in the mechanism of retroviral pathogenesis. For simplicity, when HIV is used in the following, it refers to HIV-1.

rapidly and are more susceptible to mutation than most other viruses, making them a difficult target for drugs or vaccines.

2.3.2 *A brief (and incomplete) history of HIV*

The reason why the retrovirus HIV is so well known today is because it can lead to the disease acquired immunodeficiency syndrome (AIDS), which to this day is one of the greatest health and development challenges in the world. The history of the domestic HIV/AIDS epidemic begins in 1981: On June 5, 1981, the U.S. Center for Disease Control (CDC) published an article in its Morbidity and Mortality Weekly Report (MMWR) entitled "Pneumocystis pneumonia – Los Angeles" [121]. In it, five cases of a rare lung infection, Pneumocystis carinii pneumonia (PCP), were reported in young, previously healthy men in Los Angeles. In addition, it was noticed that all of the men also had other unusual infections, suggesting that their immune systems were severely compromised. By the time the report was published, two of them had already died, the others died shortly thereafter. This issue of MMWR marked the first official reporting of what would later become known as the AIDS epidemic. AIDS is a chronic, potentially life-threatening condition caused by infection with the retrovirus HIV. By damaging the human immune system, it interferes with the body's ability to fight infection and disease. Since the 1980s, more than 80 million people have been infected with HIV and over 40 million people have died from AIDS-related illnesses. Today, about 38 million people worldwide are living with HIV, of which more than 50% live in Eastern, Central, and Southern Africa with limited access to therapeutic agents [122].

After HIV was first isolated in 1983 [123], much work was subsequently done on the virus itself, its interaction with the human host and its underlying pathogenesis, as well as on developing approaches to study, treat, and prevent HIV infection [124, 125]. Today, HIV is one of the best-studied retroviruses with great importance in biology and medicine. Nevertheless, despite it being a worldwide priority of biomedical research, to this point, there is no vaccine for HIV and no effective cure for AIDS. Antiretroviral therapy (ART), which involves taking a combination of different HIV medicines every day, can reproducibly reduce viremia to levels below the detection limit of routine clinical tests and delay immune degradation. However, this is not sufficient to eradicate viral reservoirs or provoke a powerful enough immune response against the virus [126]. Also, ART is extremely expensive, possibly requiring a lifetime of treatment, which constitutes a key barrier to universal access to HIV/AIDS services in countries in the Global South. Therefore, until today, the HIV/AIDS epidemic needs to be taken very serious. Through extensive research efforts over the past decades and promising developments in virology and immunology, as well as biology, chemistry, and biophysics, a reasonably good understanding of retroviral integra-

A good overview of the key milestones that have been achieved since the isolation of HIV can be found in Ref. [124].

tion has been gained. However, many questions regarding structural conformations and molecular mechanisms of retroviral integration are still unresolved.

2.3.3 *The retroviral replication cycle*

From a biological perspective, retroviruses differ from other viruses in that they have two characteristic steps in the viral replication cycle: The first unique step is reverse transcription, in which the viral RNA genome is transcribed into dsDNA form. The second is retroviral integration, in which the vDNA copy is inserted into the DNA of the host cell [127]. Both are part of the so called retroviral replication cycle depicted in Figure 12. This stable integration of genetic material into a host genome

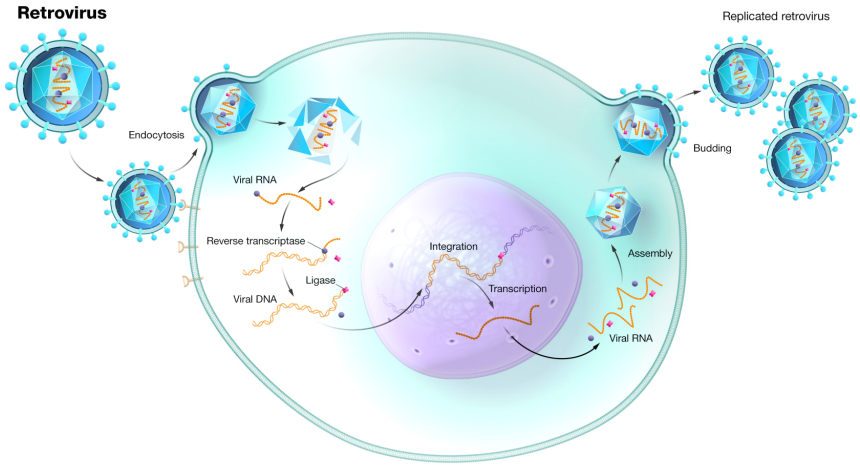

Figure 12: Main steps in the retroviral replication cycle. Inside the viral capsid, the retrovirus transports its RNA genome and important proteins to the host cell. After binding and fusing with the host cell membrane, the retrovirus enters the cell. Next, reverse transcriptase converts the retroviral RNA genome into dsDNA. This vDNA – together with cellular and viral proteins – then forms the pre-integration complex (PIC) and is translocated to the nucleus, where integration into the host genome takes place. Successful integration allows viral genes to be transcribed and translated, enabling the assembly of new viral particles. These can then leave the cell and infect other host cells. Figure taken from Ref. [128]. Courtesy: National Human Genome Research Institute.

is an obligatory step in replication for all retroviruses and is a prerequisite for efficient expression of retroviral genes by the transcriptional machinery of the host and therefore for productive virus replication [129, 130]. Retroviruses carry two copies of plus-sense genomic RNA, in which their genetic information is encoded [129]. Reverse transcription of the retroviral RNA genome results in the formation of a linear dsDNA that

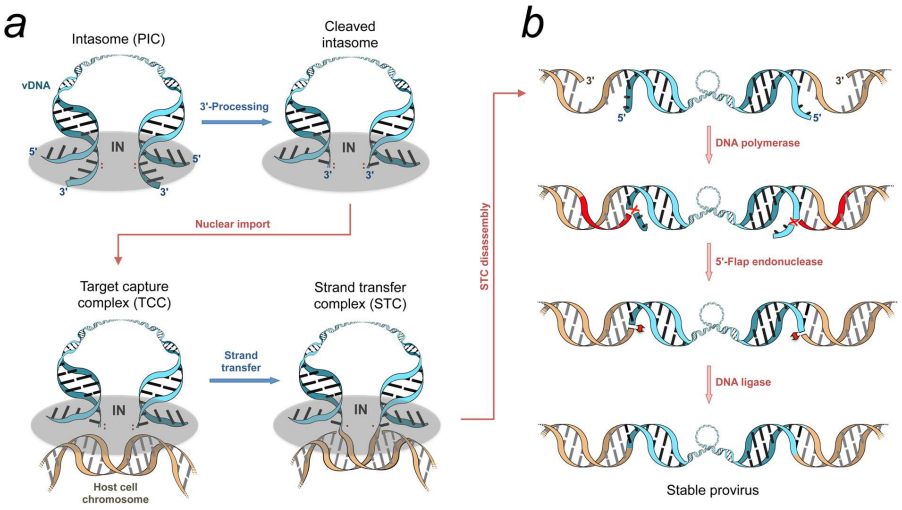

Figure 13: Retroviral integration pathway. a) Starting from the PIC, the intasome composed of an IN multimer (grey oval) and vDNA (cyan), the first two nucleotides are removed (or cleaved) from each 3'-end of the blunt-ended linear vDNA, resulting in the cleaved intermediate. Then, after nuclear import, the target capture complex (TCC) is formed that engages with the host DNA. The processed 3'-ends are then inserted into the host cell genome, resulting in the strand transfer complex (STC). Reactions catalyzed by IN are indicated with blue arrows. b) After intasome disassembly, the strand gaps are filled catalyzed by DNA polymerase. Then, the dinucleotide overhang at the 5'-ends of the vDNA are repaired by endonuclease and the single-strand breaks are glued together by DNA ligase, all three enzymes being part of the host cell enzyme machinery and marked by red arrows. Figure taken from Ref. [125].

carries a copy of the long terminal repeat (LTR) sequence (a pair of identical sequences of DNA) at both ends [125]. This process is catalyzed by the protein reverse transcriptase in the cytoplasm soon after viral entry into the host cell [127, 131]. After reverse transcription, the vDNA stably associates with several cellular and viral proteins, most notably IN, and forms the PIC, a high molecular weight nucleoprotein complex. The PIC is subsequently transported to the nucleus for integration of the vDNA into the cellular chromosome [125].

The integration of a DNA copy containing the viral genome into the host cell chromosome is the defining step of the retroviral replication cycle and a necessary prerequisite for productive infection. Integration is mediated by the viral-encoded protein IN, which is imported into the cell during infection together with the viral RNA, the reverse transcriptase, and other proteins as part of the viral core [127]. The major steps of the retroviral integration process are also depicted in Figure 13.

Within the framework of the retroviral integration pathway, four complexes are formed subsequently, beginning with the PIC and ending with the creation of a stable provirus (Figure 13a). The 3'-processing

and strand transfer are catalyzed by IN, which is attached on the vDNA ends referred to as the intasome or stable synaptic complex at the active site of the PIC [132]. During 3'-processing, IN removes two nucleotides, allowing the intasome to bind to the host DNA, resulting in a complex called the target capture complex (TCC). Performing a nucleophilic substitution, the host DNA strands are cut and both 3'-vDNA ends are joined to opposing strands of host DNA resulting in the so called strand transfer complex (STC). Following the strand transfer reaction, the STC is disassembled by host cell enzymes (Figure 13b). The resulting stable proviral DNA is flanked by a short duplicate of the target DNA sequence originating from integration into the major groove of the target DNA [125].

In this context, the catalytic activities of IN play an important role in DNA cutting and joining steps of retroviral integration, also called 3'-processing and strand transfer. During 3'-processing, IN removes a dinucleotide from each 3'-end of the blunt-ended linear vDNA and thus frees the two 3'-ends. During DNA strand transfer these processed 3'-ends target a pair of phosphodiester bonds on opposite strands of the host DNA across the major groove, while the unprocessed vDNA 5'-ends stay disjointed. In the resulting integration intermediate, the 3'-ends of the vDNA are covalently bound to the target DNA. To complete the integration reaction, the single-strand discontinuities and the two-nucleotide overhang at the 5'-ends of the vDNA are repaired by cellular enzymes. Integration occurs specifically at the endpoints of vDNA, but can occur at many sites in the host genome [125, 127, 133, 134].

Once integrated, proviral DNA is replicated along with cellular DNA during cell division cycles, just like any cellular gene. The transcription and translation of these viral genes enables the formation of new viral RNA and viral proteins that can then translocate to the cell surface to assemble into new viruses [125, 127]. Together with its variability, this is one of the main reasons that successful treatment of HIV infection is so difficult.

2.3.4 *The protein IN and how it interacts with DNA*

Replication-capable retroviruses carry three canonical enzymes that play a major role in retroviral integration: protease, reverse transcriptase, and IN [127, 135, 136]. In this section, I would like to take a closer look at IN, the central protein of retroviral integration. IN is released during proteolytic maturation within the virus particle, also called virion [136, 137]. Approximately 100 – 200 copies of IN are assumed to be present in a mature HIV particle [138, 139]. The precise time and cellular location of the release of vDNA from the HIV capsid is still controversial. It has long been assumed that release already occurs in the cytoplasm, shortly after entry into the cell (as also shown, for example, in Figure 12). However, recent results suggest that release might actually only

occur in the nucleus, near the integration site [140–142]. After reverse transcription, the vDNA is flanked on both sides by LTR sequences. IN acts on these two ends to carry out two enzymatic reactions (Figure 13) and IN hydrolyzes the vDNA within the 3'-processing reaction to release the 3'-hydroxyl groups. Subsequently, during the strand transfer reaction, IN uses the processed 3'-hydroxyl groups to cut both strands of chromosomal DNA and at the same time to link the 3'-ends of the vDNA molecule to the target [125, 127, 136].

2.3.4.1 *IN domain structure*

The protein IN functions as a multimer [143, 144]. While an IN tetramer ("dimer of dimers") is responsible for catalyzing strand transfer activity, the oligomerization state of the enzyme catalyzing 3'-processing is still under debate [132]. A tetrameric structure as during strand transfer is one plausible option [130].

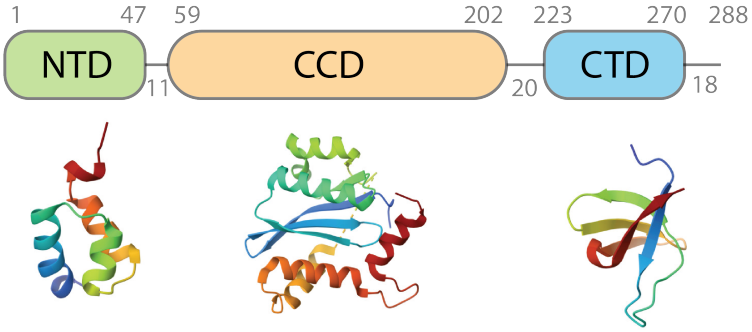

Figure 14: IN domain organization and structures. The N-terminal domain (NTD), core catalytic domain (CCD), and C-terminal domain (CTD) together form the HIV protein IN. Top: Domain sequence shown in boxes aligned to the N-termini of the NTD. The positions of the domain boundaries and the lengths of the interdomain linkers and C-terminal tail region are specified. Bottom: From left to right, the X-ray crystal structure of the IN CCD (protein database (pdb) code 1ITG) [135], the nuclear magnetic resonance (NMR) structure of the IN NTD (pdb code 1WJC), NMR structure of the IN CTD (pdb code 1IHV) [129] are shown.

The protein IN consists of 288 amino acid residues (Figure 14). It has three conserved structural domains connected by flexible linkers: the amino-terminal (N-terminal) domain (NTD), the core catalytic domain (CCD), and the carboxy-terminal (C-terminal) domain (CTD). The structures of these individual IN domains were determined in the 1990s [136]. A high-resolution structure of full-length IN has not been reported so far, largely due to the intrinsic flexibility of IN interdomain linkers [145]. But, there are structures of isolated IN domains and 2-domain constructs that have been elucidated [129]. During 3'-processing and strand transfer, the NTD and the CTD interact with DNA in important

ways and play a crucial structural role within the intasome assembly, whereas the CCD harbors the active site of the enzyme [129, 130, 136, 146, 147]. To perform its catalytic role in retroviral integration, IN assembles at the ends of the vDNA to form the robust intasome-nucleoprotein complex, which appears to remain largely unmodulated along the retroviral integration pathway [148].

2.3.4.2 *Role of IN beyond integration*

Multiple IN point mutants have been reported that exhibit enzymatic activity but do not support viral replication [149]. In addition, IN copy numbers in viral particles are more than 10-fold higher than required for catalysis. These findings suggest that IN has additional functions outside the integration process. For example, it has been shown *in vitro* that IN can bind reverse transcriptase and stimulate reverse transcription [150], suggesting that IN might also play a role in reverse transcription. The capsid of a mature HIV particle contains the genomic RNA, the viral nucleocapsid, and the reverse transcriptase and IN proteins. Recent crosslinking immunoprecipitation experiments have shown that IN is able to interact directly with viral genomic RNA [149, 151]. These findings indicate that IN may play a role in the organization of RNA within mature infectious particles, which would not be inconsistent with the suggested co-factor function observed in reverse transcription [136]. Overall, it is becoming increasingly clear that IN is an essential HIV protein with a variety of functions, some of which have yet to be discovered.

3

EXPERIMENTAL METHODS

Biological macromolecules like DNA or proteins are usually smaller than 100 nm (at least on one of their three spatial axes). This makes it challenging to study these objects experimentally because, for example, classical light microscopy is diffraction-limited and therefore has reduced applicability to such small systems.

The theoretical description of this limitation was formulated by the German physicist Ernst Karl Abbé in 1873. He stated that the distance d that may lie between two objects in the microscope so that they can just be observed separately cannot be infinitely small but is limited by the wavelength λ of the light observing it, the refractive index n, and the aperture angle of the objective α:

$$d = \frac{\lambda}{2n \cdot sin(\alpha)} \tag{21}$$

This so-called Abbé formula describes the achievable resolution in classical light microscopy limited by diffraction. So the resolution of an imaging instrument is ultimately determined not by the manufacturing quality of the instrument, but by the wavelength of the light used for observation and the aperture of the optics. For a standard optical microscope, d can be approximated by $\lambda/2$, so for for the spectral range visible to the human eye of about 400 – 800 nm , d $\geq$ 200 nm. Therefore, it is not possible to visualize biological macromolecules with conventional optical microscopy.

The Abbé limit ended the improvement of the resolution of far-field light microscopy and for a long time, it was considered a fundamental and immutable rule of nature that limited the power range of optical microscopy and the ability to observe structures at the nanometer scale. Over the years, however, various exciting approaches in the fields of biophysics and biochemistry have been developed that now make it possible to circumvent the Abbé limit and study nanometer-sized biomolecules.

One possible approach is near-field microscopy, which works close to the sample, as opposed to far-field approaches that detect optical signals at greater working distances. Near-field microscopy methods detect evanescent signals that decay quickly but contain additional information about the sample [152]. Scanning microscopy, for example, uses forces between a small probe and the surface – rather than light as classical optical microscopy does – to visualize nanoscopic structures, and is therefore not limited in resolution by the Abbé limit (but is limited by other parameters, such as the size of the probe scanning the sample).

Another approach that has generated much excitement in the far-field imaging community is stimulated emission depletion (STED) microscopy, pioneered by the German physicists Stefan Hell from the Max-Planck-Institute for Biophysical Chemistry in Göttingen in the 1990s [153]. This technique belongs to super-resolution microscopy applications. By using two different laser beams, one to stimulate fluorescent molecules to glow, another to cancels out all fluorescence except for that in a nanometer-sized volume, it became possible to switch the fluorescence between adjacent markers on and off. Scanning over the sample with nanometer-sized steps then yields an image with a resolution better than the Abbé limit [152–155]. Together with the American physicists Eric Betzig and William Moerner, two further groundbreakers in super-resolution microscopy, Hell was awarded the Nobel Prize in Chemistry 2014 "for the development of super-resolved fluorescence microscopy" [156]. In 2006, Eric Betzig and William Moerner independently developed a super-resolution fluorescence microscopy technique, in which the fluorescence of individual molecules can be switched switched on and off. Then, when multiple images of the same area are taken, only a few molecules are allowed to glow each time, and by superimposing these images, a merged image is formed that is resolved at the nanoscale [156–159].

Today, there are many biophysical and biochemical methods that allow to investigate biomolecules on the single-molecule level. Since all techniques have their advantages and disadvantages, in this work, I rely on a combination of several highly complementary biophysical and biochemical approaches to study the behaviour of linear polymers in high-resolution.

3.1 ATOMIC FORCE MICROSCOPY

One of the greatest advances in material science was the invention of the scanning tunneling microscope (STM) by the Swiss Physicist Heinrich Rohrer and the German physicist Gerd Binnig at the IBM Research Laboratory in Zurich in 1981. The STM functions by sensing the current between a metal tip located in sub-nanometer distance above a conducting surface when an external voltage is applied. However, this limits the STM to use with well conducting materials. To overcome this shortcoming of the STM when imaging poorly conducting materials such as biomolecules, Gerd Binnig, together with the American engineer Calvin Quate and the Swiss physicist Christoph Gerber, developed the AFM (Figure 15), yet another high-resolution scanning probe microscope just five years later. The AFM has a resolution of fractions of

The design of the STM was highly deservedly awarded the Nobel Prize in Physics 1986 [160].

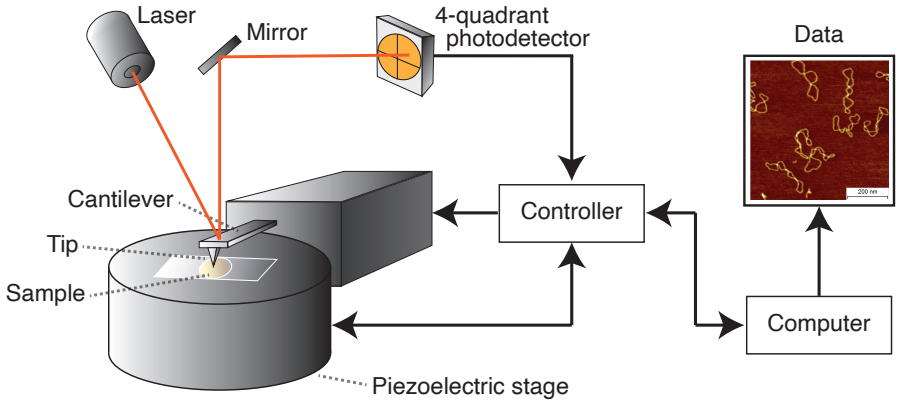

Figure 15: Schematic representation of an AFM with the cantilever tip system, the tip motion unit, the feedback loop, and the image processing and display system. The AFM cantilever has a small, sharp tip that, when close enough to the sample, experiences forces at the sample surface. These forces result in bending of the entire cantilever, which in turn causes a deflection of the laser beam positioned on the cantilever. This deflection is monitored by a 4-quadrant photodetector, and the optical signal is converted to an electrical signal. The controller uses this data to send a feedback system to the piezo actuators that change the relative position of the sample to the cantilever. In addition, the controller transmits the data to create an elevation image of the scanned surface.

a nanometer, which is more than 1000 times higher than the classical diffraction-limited light microscope. The development of the AFM was a turning point in the field and has vastly improved our ability to gain a deeper understanding of the nanoworld. Today it has become an indispensable element of biophysics and nanotechnology [161, 162].

Scanning probe microscopy includes a variety of microscopic methods, all of which rely on strongly distance-dependent interactions between the probe and the sample and are characterized by two operating elements: a sharp probe (tip) and a feedback mechanism. The use of a sharp

tip with a radius of curvature on the order of a few nanometers is a critical component of the AFM because its size limits the resolution of the microscope. The feedback loop describes a specific function that regulates the scanning process by maintaining the interaction parameters constant when scanning the surface of the sample [163].

More specifically, in AFM imaging, the sample surface is scanned with the tip mounted at the end of a flexible cantilever arm. When the tip comes into proximity of the sample surface, forces between the tip and the surface cause a deflection of the cantilever. These interaction forces can be van der Waals forces, electrostatic forces, and/or dipole-dipole interaction forces. The reflection of a laser beam focused at the back side of the cantilever is used to amplify and measure the movement of the cantilever. The reflected beam is directed to an array of photodiodes that provides a voltage depending on the position of the laser beam. This information is used as a feedback parameter to adjust the distance between the tip and the sample and as an output parameter to create a height image of the scanned surface. For imaging, the tip is scanned over the sample (or possibly the sample is moved under the tip in some setups). To move the tip and the sample accurately, piezoelectric materials with subnanometer precision are used. At each imaging position, the cantilever's deflection is read out, and from combining the information of all pixels a topographic map of the sample is constructed [163, 164]. There are different AFM imaging modes. In the following, I will discuss the most commonly used ones with a focus on the methods used in the scope of this thesis.

3.1.1 *Amplitude-modulation AFM*

Amplitude-modulation AFM, also called tapping mode AFM, describes an AFM imaging mode, in which the cantilever is excited by a piezo shaker above but very close to the sample surface, thus oscillating the tip (Figure 16A). The µm-sized cantilever, at the end of which the nm-sized tip is located, is mechanically excited at a fixed frequency, which is very close to but just below the resonant frequency of the cantilever. The free value of the oscillation (free amplitude) is adjusted to the Z-range of the sample. As the tip interacts with the surface, the amplitude of the oscillation decreases from its free value. In amplitude modulation AFM, the experimentally observable parameters are the amplitude of the oscillation and the phase shift between the external excitation and the motion of the tip. The amplitude is taken as a feedback parameter to depict the topography of the surface. The force exerted by the tip on the sample surface depends on several factors, such as the free amplitude, the radius of the tip, the value of the amplitude chosen for the feedback, and the imaging mode [163].

Other dynamic force modes are the frequency modulation mode or the phase modulation mode. They use the frequency or the phase as

feedback parameters, respectively. Amplitude modulation mode is the most commonly used AFM imaging mode since it provides several key advantages. The interaction with the surface is relatively gentle, compared to other imaging modes, because the cantilever swings at (almost) resonance and interacts with the sample only moderately as the tip scans the surface. This way, the sharpness of the tip is preserved. The amplitude modulation imaging mode also minimizes torsional forces between the tip and the sample. These two features of amplitude modulation AFM are particularly important for soft materials such as biopolymers, DNA origami structures, or nanoparticles, because there is less destruction to the sample, compared to other AFM imaging modes.

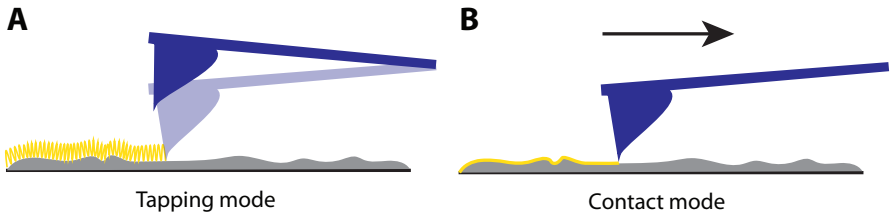

Figure 16: AFM imaging modes. A) Tapping mode. B) Contact mode. AFM imaging in contact mode can damage or distort soft biological samples. Tapping Mode avoids this problem by oscillating the tip oscillate over the sample, and making only short intermittent contacts.

The alternative imaging approach to dynamic force mode is static force mode (Figure 16B). Here, the tip is brought into mechanical contact with the sample. Therefore, this imaging technique is also called contact mode. During the scan, a feedback loop maintains the force constant by adjusting the Z-height with the piezo actuators. This change in Z-height is the topographic signal. Remarkably, in contact mode, it is even possible to distinguish between surfaces made of different materials, since, due to the different interactions with the tip a different Z-height is measured [163, 164].

3.1.2 *AFM in liquid*

Operating the AFM under liquid conditions requires modification of some parts; for example, the sample holder must be large enough to accommodate the sample and the buffer, in which it is immersed, and the mirror guiding the laser beam needs to be adjusted because of the bending of the laser beam at the liquid surface. Another important point is that in solution, charged objects are shielded by counterions. Therefore, electrostatic interactions are of central importance when imaging in liquids (in contrast to imaging in air, where capillary forces between tip and surface are most important). This means that the resolution, which is strongly linked to the distance between tip and

sample, depends on the positioning and screening of the charges in the solution. Thus, high-resolution imaging in liquids is only achievable if there is contact between the tip and the sample. This in turn leads to shear and lateral forces. In order to avoid modifying, damaging or dragging soft samples along the surface, cantilevers with a lower spring constant (i.e. softer cantilevers) are required for imaging in liquids than for imaging in air.

Also, for AFM measurements in liquid, different imaging modes can be selected. Here, in static mode the damages to the sample are less significant as compared to imaging in dry because the setpoint forces are typically much lower. In liquid, the most appropriate imaging mode depends on the characteristic features of the sample and how it is prepared. Contact or dynamic modes, for example, are more suitable for imaging crystalline molecular assemblies. The disadvantage of high lateral or normal force is outweighed here by the advantage of a high image acquisition speed. In contrast, for imaging single macromolecules, such as DNA molecules, which are more weakly bound to the surface, lateral and normal forces are the more relevant factors, and therefore the so-called jumping mode, an imaging mode that minimizes lateral and normal forces, is considered superior to other imaging modes [163–165].

Control and minimization of tip-sample interaction forces are essential for high-resolution AFM imaging. Especially when imaging soft biological materials in liquid, the tensile force of the cantilever prevents the detection of mechanical contact between tip and sample, leading to damaging interactions with the sample. Jumping mode AFM, also

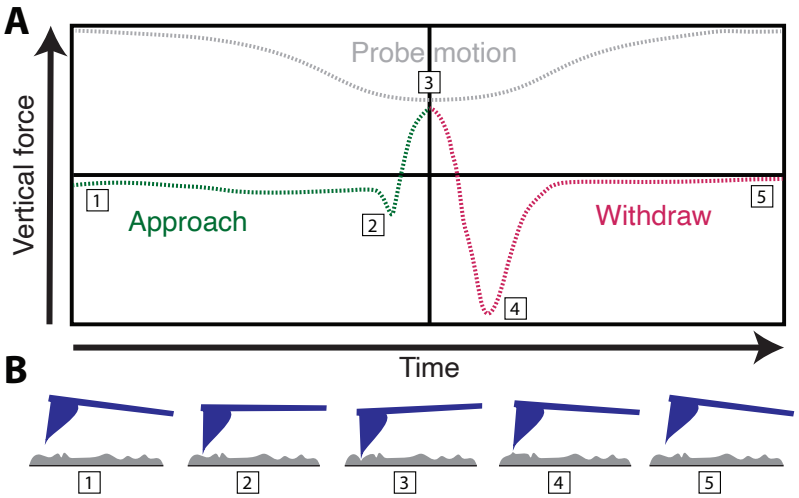

Figure 17: AFM peak force tapping mode. In this AFM mode, the probe periodically taps the sample and the pN-level. Using the deflection of the cantilever, the interaction force can be measured directly. A feedback loop keeps the peak force to its setpoint (peak force). A) Vertical force as a function of time. B) Cantilever movement over one tap.

referred to as peak force tapping mode AFM, enables the detection of tip-sample contact with high accuracy, minimizing the sensing forces (∼100 pN) and sample damages during the approach cycles by combining peculiarities of dynamic mode AFM and contact mode AFM (Figure 17). The movement of the cantilever towards the sample and away from it is off-resonance, meaning that the cantilever operates at a frequency much lower than its resonance frequency. When the tip interacts with the sample, the deflection of the cantilever is a measure of the interaction force. The topography of the sample can be determined by recording a force-distance curve in every pixel on the sampled surface. Jumping mode AFM operates as a sequence of force-distance curves at each pixel on the sample with a feedback time in between. First, the tip is in contact with the surface while the feedback loop keeps the deflection of the cantilever at the set point value (peak force). Next, the feedback system is switched off and the tip is moved vertically away from the surface. At the maximum displacement from the surface the tip is moved to the next measurement point on the sample. Then, the same procedure is repeated until all points of the sampled surface are mapped. From the force-distance curves multiple nanomechanical properties of the sample can be concurrently quantified. Due to the quasi-static process of the cantilever, the interaction force between the tip and the sample in each pixel can be precisely measured and controlled in real time, and operation is simplified even without the tuning process of the cantilever [165–167].

Another off-resonance mode next to peak-force tapping mode is the force-volume mapping mode, also called AFM-based elasticity mapping. In this mode, once the set point (trigger force) is reached, the piezo changes its motion to move the tip away from the specimen. At that point, however, forces higher than the set point (overshoot) are exerted on the sample. Unlike peak force tapping, force-volume mapping records an approach curve and also a retract curve of the cantilever to the sample. For force-distance spectroscopy, the spring constant of the cantilever has to be determined precisely for every cantilever used. The the spring constant of the cantilever specified by the manufacturer is only an approximate value based on the dimensions of the cantilever and, in some cases, the value may deviate by more than 20% from the stated value.

3.1.3 *AFM sample deposition*

Surface preparation is an essential step for reproducible and reliable AFM imaging. To ensure a contamination-free surface for high-resolution imaging and to minimize stress and wear on the tip, a surface as clean and smooth as possible is desirable. To this end, freshly cleaved muscovite mica is used as the standard substrate for AFM imaging. Muscovite mica is a mineral that is easily cleaved in a plane and has an

atomically flat surface (due to the hexagonal sheet-like arrangement of its atoms), which gives the remaining mica a very regular surface after cleavage. In addition, it is compatible with most biological materials. DNA and other biological and non-biological nanostructures can be immobilized to the surface via electrostatic interactions: To do so, the freshly cleaved mica surface (negatively charged) is either saturated with divalent, positively charged ions such as magnesium; alternatively, an additional positively charged layer is added between the mica and the structures, for example Poly-L-lysine (PLL) or aminopropylsilatrane (APS). The negatively charged DNA structures can then adsorb from the solution to the modified surface.

3.2 MAGNETIC TWEEZERS

In addition to its application in different imaging modes (see Section 3.1), the AFM can also be used as a tool for force spectroscopy. AFM force spectroscopy describes a series of point measurements, in which the cantilever approaches the sample, "pokes" into it, and then retracts. Thus, it does not scan the sample like in AFM imaging. During the measurement, the deflection of the cantilever as a function of piezo motion is measured. This can then be converted to a measurement of the force as a function of the distance from the tip to the sample (assuming the spring constant is very well calibrated), providing mechanical information about the sample.

Over the last 30 years, single-molecule force spectroscopy has evolved as an indispensable tool for studying forces and motions associated with biomolecules. Besides AFM, optical tweezers and MT are the most important tools for single-molecule force spectroscopy [170]. In optical tweezers, an optical trap is created by focusing a laser on a diffraction-limited point. As a consequence, dielectric particles near the focus experience a 3D restoring force directed toward the focus [168]. Optical tweezers have become a very popular single-molecule force spectroscopy technique since they enable to exert forces up to 100 pN on particles ranging in size from nm to µm while simultaneously measuring the 3D displacement of the observed particle with sub-nm resolution and sub-ms time accuracy. A major drawback of optical tweezers is the difficulty associated with using light to generate force: Since the stiffness of the trap depends on the gradient of the optical field, optical interference that affects intensity will impact performance. In addition, the system is subject to heating by the high-intensity laser, which can influence the measurement. Another disadvantage of optical tweezers is the lack of selectivity and exclusivity, so impurities in the sample can significantly distort the signal [170].

The American physicist Arthur Ashkin was awarded the Nobel prize in Physics in 2018 for developing the optical tweezers [168, 169].

MT (Figure 18) provide many advantages over other force spectroscopy techniques. Unlike optical tweezers, MT do not suffer from the sample heating and photodamage problems. In addition, magnetic manipulation is highly selective for the magnetic beads used as probes and is generally not as sensitive to sample and microscope chamber preparation as AFM force spectroscopy and optical tweezers. In addition, since a magnetic field is used to apply force, MT offer the ability to perform highly parallel single-molecule measurements, significantly easier and more straightforward than with other single-molecule force spectroscopy techniques. Additionally, MT are compatible with aqueous environments to mimic the conditions inside the living cell, and they are inexpensive and straightforward to implement [170]. With these outstanding properties, MT have evolved in recent years into a uniquely powerful tool for precise measurements at the single-molecule level in real time under external forces and torques with not only nanometer spatial resolution, but also

millisecond temporal resolution. This enables quantitative determination of mechanical parameters, conformational transitions, dynamics and interactions of biological processes involving nucleic acids and proteins at the molecular level [171–174].

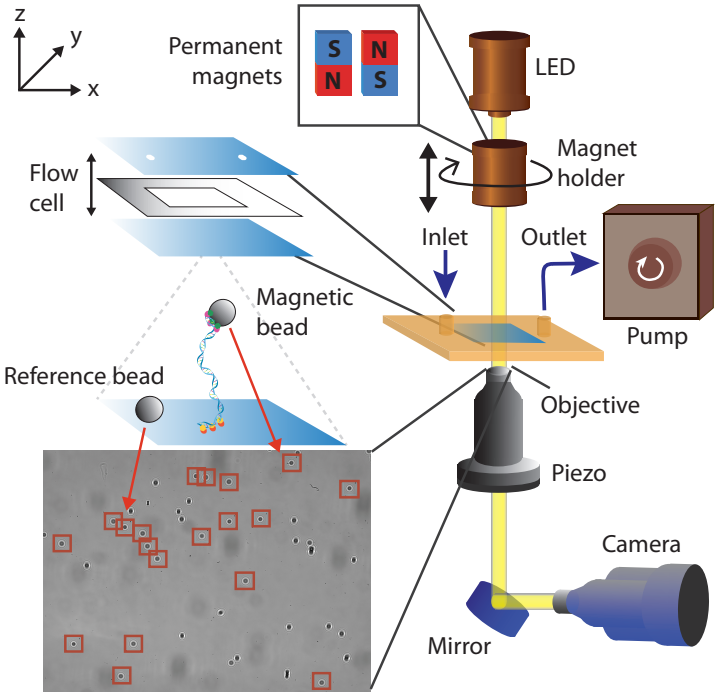

Figure 18: Schematic representation of a MT setup [172–174]. The measurement chamber is formed by a so-called flow cell, which is built from two glass slides (light blue on the left), which are separated by a layer of parafilm (light gray). The flow cell is placed in a flow cell holder (orange) and mounted on a stage to provide direct contact to the objective (with an oil film in between). The objective is mounted on a piezoelectric stage (dark grey) to control the focal plane. A light-emitting diode (LED; brown) illuminates the sample through the magnet assembly. The light beam (yellow) is then deflected by a mirror into a camera (dark blue) connected to a computer to track the beads. The magnet holder, whose Z-position and rotation about the vertical axis are controlled by motors, is placed on top of the flow cell. For fluid exchange the flow cell is connected to a pump (brown on the right).

The first experiments with MT have already been introduced in the previous chapter (Section 2.2.1.1): In 1996, Terence Strick first measured the elasticity of a single supercoiled DNA molecule by tethering a DNA between a glass surface and a paramagnetic bead to apply external forces and torques on the molecule [72]. The individual components of the setup have much involved since then [175–178], but the basic principle stayed the same: To tether the DNA between a flow cell surface and magnetic beads, the DNA molecule is constructed such that on the one end, multiple nucleotides are equipped with a digoxigenin (DIG)

label. The flow cell surface is then coated with Anti-DIG-antibody to attach the DNA to it. On the other DNA end, the same mechanism is used, only with biotin labels on the DNA and streptavidin coating around the magnetic beads. Using a pair of small permanent magnets placed above the flow cell, magnetic fields and thus magnetic forces can be applied on the beads. This, in turn, allows stretching the molecules of interest. The configuration allows to apply precisely calibrated forces between $\lesssim$0.05 pN and $\sim$100 pN [171]. Since the extremities of the DNA molecule are torsionally constrained, it is also possible to exert torques and thus to twist the DNA molecule. To determine the x, y, and z positions of the micrometer-sized magnetic beads in real time, an inverted microscope and monochromatic illumination are used to track the diffraction pattern of each individual bead using video microscopy [72, 172, 173].

Due to Brownian motion, the magnetic bead fluctuates around its equilibrium position at a constant force. These fluctuations depend on the applied force and the flexibility of the bound DNA. Since the fluctuations $\langle \delta x^2 \rangle$ are correlated with the stiffness k_x by the equipartition theorem, this relationship can be used to calculate the stretching force acting on the molecule if the position of the bead and its fluctuations transverse to the stretching direction are known:

The equipartition theorem relates the temperature of a system to its average energies.

$$\frac{F}{l} = k_x = \frac{k_B T}{\langle \delta x^2 \rangle} \tag{22}$$

with T is the temperature, k_B the Boltzmann constant, and l the extension of the DNA molecule, which can be determined by the displacement of the magnetic bead [179]. The drawback of this approach is that due to the finite acquisition frequency of the charge coupled device (CCD) camera, artifacts occur in the variance measurements due to camera blurring and aliasing. Te Velthuis *et al.* have proposed an approach for deconvolution of camera effects that allows reliable power calibration of MT experiments, overcoming the above limitations: they iteratively correct the measured power spectrum and fit the integral of the spectrum until the fitting error is below a set value to determine the underlying correct variance from the measured (incorrect) variance [179, 180].

3.3 ZERO MODE WAVEGUIDE AND APPLICATIONS IN SOLID STATE NANOPORES

Another single-molecule characterization tool are zero-mode waveguide (ZMW)s. These optical nanostructures that were first discovered in the 1990s and have since been used in a variety of applications, including nanopore technology. ZMWs were first proposed by the American scientists Eric Betzig and Jay Trautman in 1992 [181–183], and later developed by the Czech physicist Lukas Novotny and coworkers in 1997 [184, 185]. Originally, they were designed for use in fluorescence microscopy, where they allowed for the detection of single molecules. The name "zero mode" refers to the fact that the optical field is confined to a region smaller than the diffraction limit, resulting in a mode volume that is effectively zero. The aim of these small optical devices is to overcome limitations such as inability to control spatial molecular distributions, limited concentration ranges, and intrinsic phenomena such as photobleaching to allow studying low-affinity ($k_d \approx$ µM – mM) biomolecular interactions. A ZMW is a small aperture, typically a few hundred nanometers in diameter, made of a thin metal (often gold or aluminium) film or dielectric material. The waveguide acts as a light trap, confining the excitation light within a small volume near the aperture. This allows for highly localized sensing or excitation of molecules or particles within the volume and isolation of single molecules for optical and electrochemical analysis [186, 187].

The same Eric Betzig who 10 years later co-developed super-resolution microscopy [156, 157].

ZMWs can be combined with optical probes such as single-molecule fluorescence, fluorescence correlation spectroscopy, and single-molecule resonance energy transfer. This allows to analyze large numbers of single-molecule reactions or simultaneous binding events in a distributed manner. With this, ZMWs have found numerous applications in biological and chemical sensing. They are widely used in single-molecule fluorescence spectroscopy and imaging, where they allow for the detection and manipulation of individual molecules with high sensitivity and specificity. They have also been used for example in surface-enhanced Raman spectroscopy (SERS), where they enable the detection of trace amounts of analytes with high selectivity [188–190].

In recent years, ZMWs have been integrated with nanopore technology, resulting in a powerful tool for DNA sequencing and other bioanalytical applications (Figure 19). A nanopore is a tiny hole on a substrate, typically a few tens of nanometers in diameter, through which biomolecules can pass. When pressure or an electric field are applied across the pore, the biomolecules are pulled through one at a time, allowing for their identification and characterization. By integrating a ZMW with the nanopore, it is possible to excite and detect the fluorescent signals from individual nucleotides as they pass through the pore. Since nanopores in metal films do not permit the propagation of light at a wavelength (significantly) larger than the diameter of the hole whereas molecules

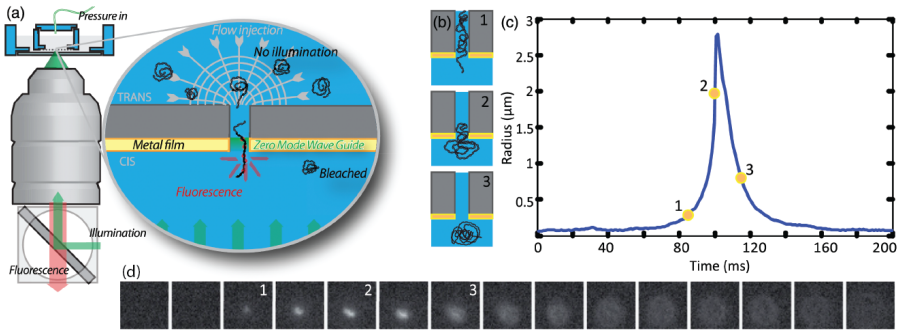

Figure 19: ZMW for nanopores. (a) Schematic representation of the setup used for nanopore translocation with ZMW detection. The one side of the semipermeable membrane contains fluorescently labeled DNA molecules. When applying a pressure, the molecules are pushed through the pore. As they cross the evanescent field at the end of the pore, they are illuminated. After having left the pore, they are unfocused and bleached. (b) Schematic depiction of the DNA exit through the nanopore. (c) Thresholded radius of the DNA fluorescent spot over time. (d) Snapshots of a single DNA exit at a frame rate of 100 fps. Figure taken from Ref. [191]

.

can still pass the pore, such nanopores can create ZMWs for single-molecule detection. Direct measurements of flow-induced injection of DNA through nanopores at the level of a single molecule and a single pore can be made using a modified ZMW method. This enables highly accurate, high-throughput DNA sequencing with single-base resolution, a technique known as ZMW nanopore sequencing [191–193]. In addition to DNA sequencing, ZMW nanopore technology has potential applications in single-molecule analysis, proteomics, and drug discovery. Overall, the integration of ZMWs with nanopore technology represents a promising avenue for advancing our understanding of biological systems and developing new diagnostic and therapeutic tools [186, 187].

3.4 DNA DESIGN AND CLONING

DNA cloning and assembly methods are important tools in molecular biology research to design and assemble large customized DNA constructs. In brief, molecular cloning is a set of experimental techniques that can be used to insert recombinant DNA into a vector (a carrier for a *foreign* nucleic sequence into the host cell) to stimulate replication of the recombinant DNA by a host organism. Thus, generally two DNA sequences (from two different organisms) play an important role: one that is the source of the DNA to be cloned and the other that serves as a living host for replication of the recombinant DNA (e.g., *E. coli*). Molecular cloning is performed in two steps: First, the DNA to be cloned is obtained from a specific organism and processed. The recombinant DNA is then incorporated into a host organism, which is induced to take up and replicate the recombinant DNA. Subsequently, this host cell is exponentially replicated to produce a large number of bacteria, each containing copies of the recombinant molecule (clones) [56, 194]. A broad range of cloning techniques has been developed to clone DNA

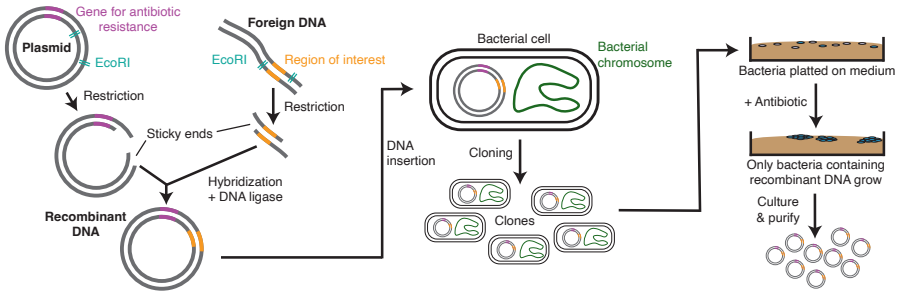

Figure 20: Molecular cloning. A foreign DNA is introduced into a plasmid. Here, an EcoRI restriction site is used. After insertion of the recombinant DNA, competent bacterial cells are used to incorporate the vector DNA, which is afterwards extracted and purified.

fragments of interest. Here, I will focus on commonly applied techniques, which were also used to generate DNA constructs in the scope of this thesis.

In 1993, Kary Mullis, together with Michael Smith, deservedly received the Nobel Prize in Chemistry for developing the PCR method.

As a prerequisite for cloning, the sequence of choice is first amplified using polymerase chain reaction (PCR). PCR is a biochemical method that allows rapid and inexpensive amplification of DNA *in vitro*. Developed in 1983 by the American biochemist Kary Mullis, it has revolutionized the field of modern molecular biology. PCR uses thermal cycling and the ability of the enzyme DNA polymerase to synthesize a new DNA strand complementary to the template strand, which allows the amplification of a single copy (or a few copies) of a DNA fragment over several orders of magnitude, generating a large number of copies of a given DNA sequence [56, 195, 196]. Subsequently, the linear PCR product needs to be circularized it into a plasmid. In the so-called blunt end ligation, the methylated PCR template is cut, the blunt ends are phosphorylated

and then ligated (e.g. using the enzyme T4 DNA ligase) to get a circular plasmid of the desired length and sequence (Figure 20, left part) [67, 197, 198].

After assembly, the second cloning step, the transformation, is carried out. To this end, competent *E. coli* cells (here, competence refers to the ability of the cell to take up foreign (extracellular) DNA) are added to the DNA and processed (by a series of incubation steps at different temperatures) to induce the intake the recombinant DNA. To amplify the amount of those *E. coli* cells that have incorporated the recombinant DNA, the transformed cells are spread on an LB (luria broth, a nutrient-rich growth medium) agar plate containing an antibiotic corresponding the antibiotic resistance gene encoded in the recombinant DNA and incubated at 37 °C for several hours. Subsequently, the vector DNA can be extracted out of the *E. coli* cells and purified from other cellular components for further applications (Figure 20, right part) [67].

Besides blunt-end cloning, there are other methods that use an exonuclease (a nuclease that cleaves one nucleic acid monomer per reaction cycle from the end of the substrate DNA molecule) to create homologous single-stranded regions on the vector and DNA fragment(s) that subsequently attach to each other's (sticky) ends. In the Gibson assembly method, a 5'-to-3' exonuclease activity generates single-stranded 3'-overhangs. This has the advantage of facilitating the assembly of fragments that share homology at the ends. A polymerase then fills the gaps in the individual annealed fragments, and a DNA ligase seals the incisions in the hybrid DNA. This cloning technology is a sequence-independent one-step reaction and is commonly used to efficiently assemble large DNAs by *in vitro* recombination [198].

To clone multiple DNA fragments of interest, conventional methods usually require multiple cloning steps. In each step, a single DNA fragment is transferred from a donor plasmid or PCR product to a recipient vector. Golden Gate cloning was developed to facilitate and accelerate this process by allowing up to nine DNA fragments to be incorporated into a recipient plasmid at once. Cloning is performed by pipetting all plasmid donors, the recipient vector, a type IIS restriction enzyme, and ligase into a single tube and incubating the mixture at the appropriate temperature. It is essential to use carefully designed donor and recipient plasmids for this otherwise very simple cloning procedure [198].

4

MACROMOLECULAR GATING USING A THERMALLY SWITCHABLE NANOPORE BASED ON A POLYMER PHASE TRANSITION

4.1 NANOPOROUS SYSTEMS IN NATURE AND TECHNOLOGY

The formation of compartments is a key component of complex and evolved systems in nature. One example is the storage of genetic information in the nucleus of eukaryotes. The cell nucleus is separated from the cytoplasm by a double membrane called nuclear envelope, thus ensuring the protection of the genetic material inside the nucleus from external influences such as, for example, viruses. Nevertheless, communication between the nucleus and the rest of the cell must still be possible. Therefore, connecting pathways between the nucleus and the cytoplasm are embedded in the nuclear envelope. Each of these pathways is formed by a compound called nuclear pore complex (NPC) (Figure 21), a highly selective passageway for selective and directional transport of a broad spectrum of cargo molecules [199–203]. The specifications of the transport machinery of NPC are also special in the light of evolution; for example, transitional forms of this sophisticated transport system have not yet been found in modern organisms to show how it evolved [205, 206].

Because of its unique characteristics, the NPC represents an intriguing and therefore widely studied pore system. With extreme accuracy and selectivity, each NPC can translocate up to 500 macromolecules per second – even simultaneously in both directions. To do so, its internal channel is filled with unstructured proteins that form a dynamic network responsible for pore selectivity. Nevertheless, despite the broad research interest in medicine, biology, nanotechnology, and biophysics, the exact modalities of how the NPC coordinates bidirectional transport of macromolecules to avoid congestion/jamming and collisions are still not fully understood [56, 206–208].

In many other cellular processes, the entrapment of (bio)polymers in pores or channels of nanometric size has found application, e.g., extranuclear transport of messenger RNA, secretion of proteins through through lipid membranes, or the injection of the genetic material of certain viruses into a host cell. In general, biological nanopores enable the transport of ions and macromolecules between various cellular compartments. Furthermore, nanopores also play an important role in (man-made) technological processes. For example, selective nanomembranes can be used to recover oil in porous media by high pressure injection of polymer solutions. Other applications of artificial nanopores

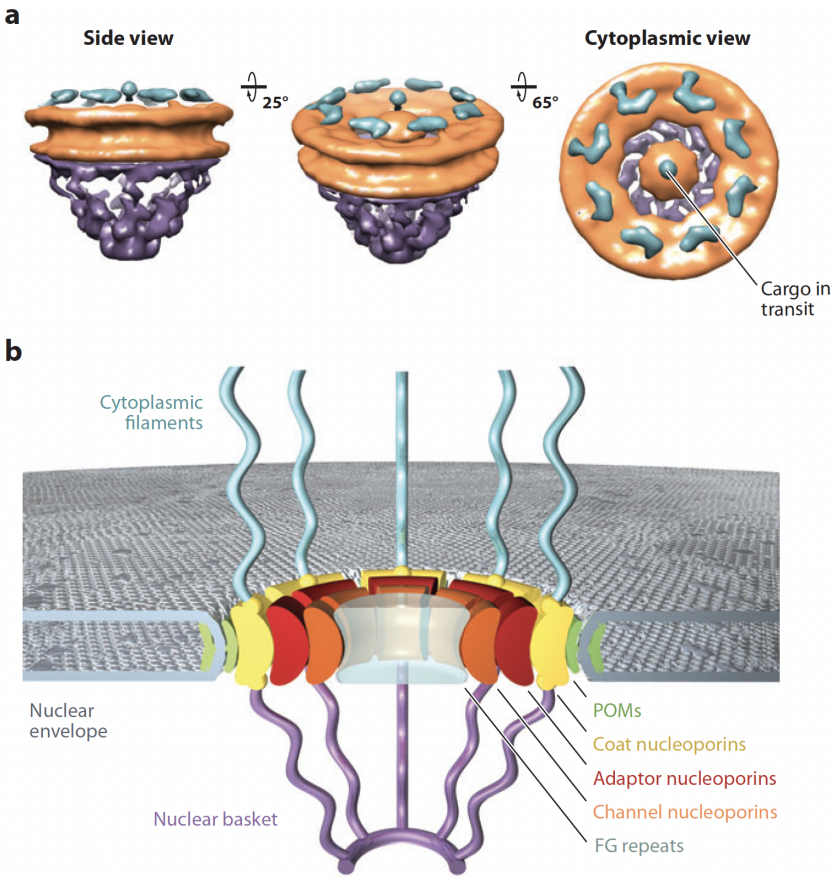

Figure 21: Schematic depiction of the NPC. The pore is anchored to the nuclear envelope by a membrane layer. Natively unfolded phenylalanine-glycine (FG) repeats of a series of nucleoporins form the transport barrier in the central channel. Theses FG repeats, also called FG nups, form a barrier that excludes non-interacting molecules while allowing selective transport of other molecules. Figure taken from Ref. [204].

involve steric exclusion chromatography and capillary electrophoresis, or ultrafast DNA or protein sequencing [209–214].

4.2 LCST POLYMERS: A PHASE TRANSITION BASED ON TEMPERATURE

The mechanics and functioning of the NPC can also be considered as a model system for selective and directed transport on the nanoscale. In this work, I will use the NPC as an inspiration and example system for a tunable nanopore for the selective transport of DNA and viruses. In order to mimic the selectivity of the NPC, I will graft artificial long hydrophobic polymers inside nanoporous membranes, slightly similar to the FG repeats in the NPC (Figure 21). These polymers are simpler than FG repeats, straightforward to produce, and can be varied in structure and polymer length to achieve customized polymer coating inside the

nanopore. In addition, a selection of polymers used in this work exhibits an lower critical solution temperature (LCST). This means that the polymer changes its conformational state when the temperature exceeds a certain value.

In bulk, below the LCST, these polymers are completely soluble. In contrast, above the LCST they accumulate and precipitate (Figure 22). The transition temperature of the LCST polymer is routinely determined by measuring the turbidity of a polymer solution as a function of temperature [215].

- T < LCST (Figure 22a): The system is completely miscible at all ratios. This means that the polymers behave in solution as in good solvent and are free to elongate. In a confined environment (e.g., inside a nanopore), the polymer strands swell and form a network that can even bind together. This leads to a decrease in the effective diameter of the pore, reducing or blocking the passage through the pore (closed pore).
- T > LCST (Figure 22b): Partial mixing of the liquid occurs, implying that the polymer collapses in bulk as it attempts to minimize its contact area with the surrounding solvent. When the polymer is grafted inside a nanopore, the polymer strands are folded, which in turn increases the effective diameter of the nanopore (open pore).

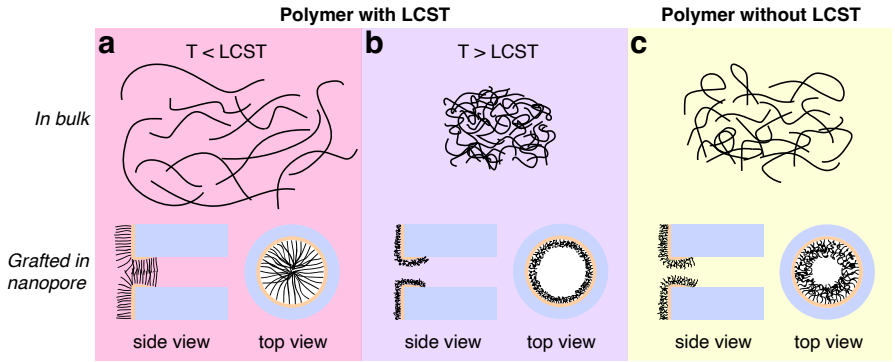

Figure 22: Possible conformations of a polymer possessing an LCST in dependence of the environment and the surrounding temperature. a) For LCST-polymers, at T < LCST and in bulk, the polymers are in good solvent and thus elongated. In a confined environment (grafted inside a nanopore), the effect is even more pronounced and the swelled polymer strand interact with each other, resulting in a closed pore. b) For T > LCST in bulk, the polymer is collapsed. In a confined environment, the polymer strands are collapsed at the pore wall and the pore is open. c) For a polymer without LCST, the polymer is in intermediate solvent (θ-solvent) independent of the surrounding temperature. The diameter of the pore is still reduced by the grafting so the pore is semi-open.

This conformational transition is best explained from an energy vs. entropy perspective: it is very costly to condense polymers in a small area. At T < LCST, the polymers fill most of the area because it is favorable for them to interact with each other since they are in a poor solvent. At T > LCST, the interaction effects gain the upper hand and the polymers are in a collapsed state since the energy gained by the collapse is greater than the entropy loss (as there are fewer degrees of freedom in the collapsed state). In addition, polymers with a similar structure but without an LCST were designed as a negative control (Figure 22c). When these polymers are grafted inside a nanopore, the pore is always half-open independent of the surrounding temperature, because the polymer strands behave as in an intermediate solvent (θ-solvent). The effective diameter of the pore is reduced by grafting, but the pore is never completely closed.

In the following publication, I will use the LCST effect just described for a polymer phase transition by grafting custom-designed LCST polymers inside nanopores. This allows to switch the nanopore between an open and a closed state by changing the temperature of the surrounding medium by a few °C. Therefore, these thermally switchable nanopores represent an important step towards customizable and highly selective nanopores. Here, I will present a newly developed switchable nanopore grafted with various hydrophobic polymers that responds to temperature, to control macromolecular transport. Using electro-chemical grafting of synthetic polymers with an LCST, I will demonstrate that the grafted nanopores exhibit a sharp transition between a closed state at low temperatures and an open state at high temperatures. Mimicking the gating properties of biological pores is of great interest for the fabrication of semipermeable nano-membranes that can be used for the control of transport and filtration of macromolecules and, in particular, viral particles.

4.3 POLYMER PHASE TRANSITION FOR THERMALLY SWITCHABLE NANOGATE

Thermally switchable nanogate based on polymer phase transition

By

Pauline J. Kolbeck[1,2,3,+], Dihia Benaoudia[4,5,+], Léa Chazot-Franguiadakis[1], Gwendoline Delecourt[5], Jérôme Mathé[6], Sha Li[6], Jan Lipfert[2,3], Anna Salvetti[7], Mordjane Boukhet[8], Véronique Bennevault[5,9], Jean-Christophe Lacroix[4], Philippe Guégan[5], Fabien Montel[1]

[1] Univ Lyon, ENS de Lyon, CNRS, Laboratoire de Physique, F-69342 Lyon, France
[2] Department of Physics and Center for NanoScience, LMU Munich, 80799 Munich, Germany
[3] Department of Physics and Debye Institute for Nanomaterials Science, Utrecht University, Princetonplein 1, 3584 CC Utrecht, The Netherlands
[4] Université Paris Cité, ITODYS, CNRS, F-75006 Paris, France
[5] Institut Parisien de Chimie Moléculaire, Equipe Chimie des Polymères, UMR CNRS 8232, Sorbonne Université, Paris 75252, France
[6] Université Paris-Saclay, Univ Evry, CNRS, LAMBE, Evry-Courcouronnes, France
[7] Centre International de Recherche en Infectiologie, INSERM U111, UMR CNRS 5308, Université Claude Bernard Lyon 1, Lyon 69007, France
[8] Center for Molecular Bioengineering (B CUBE), Technical University of Dresden, Dresden, Germany
[9] University of Evry, Evry 91000, France
[+] Both authors contributed equally to this work
[*] Corresponding author

published in

ACS Nano Letters (2023), Vol. 23, No. 11, 4862-4869

My contribution to this publication was performing ZMW measurements, analyzing the resulting data, and co-writing the manuscript with input from all authors.

4.3.1 *Abstract*

Mimicking and extending the gating properties of biological pores is of paramount interest for the fabrication of membranes that could be used in filtration or drug processing. Here, we build a selective and switchable nanopore for macromolecular cargo transport. Our approach exploits polymer graftings within artificial nanopores to control the translocation of biomolecules. To measure transport at the scale of individual biomolecules, we use fluorescence microscopy with a ZMW set up. We show that grafting polymers that exhibit a lower critical solution temperature creates a toggle switch between an open and closed state of the nanopore depending on the temperature. We demonstrate tight control over the transport of DNA and viral capsids with a sharp transition (∼1 °C) and present a simple physical model that predicts key features of this transition. Our approach provides the potential for controllable and responsive nanopores in a range of applications.

4.3.2 *Introduction*

The design of bio-inspired nanopores brings the ability to manipulate and control ionic and molecular transport inside a confined environment and provides insight into ionic and molecular transport processes of biological channels [217–221]. Synthetic nanopores have many advantages over biological ones, such as their stability, tunable dimensions (size and shape), and the possibility to integrate into nanofluidic systems [222, 223]. By functionalizing the surface of the nanopore, their physical and chemical properties (e.g., hydrophobicity, selectivity, surface charges, and specific molecular recognition) and thus the ionic and molecular transport properties can be modified [218, 224–230] and modeled using simulations [231–233].

Poly(ethylene glycol) polymers graftings (PEG) have been employed previously to create a steric repulsive barrier that fills the interior of the nanopore [191, 219, 234, 235]. The PEG grafting collapses by adding proteins in solution that bind to the network and induces a transition between poor and good solvent conditions. Poly(N-isopropylacrylamide) (PNIPAM) can also be used to coat the interior of the pore. PNIPAM is known for its hydrophobic-hydrophilic phase transition at physiological temperatures [217, 221, 236]. It has been previously shown that PNIPAM can be used to reproduce receptor-mediated transport in grafted nanopores [217, 236]. More precisely when grafted onto the pore surface and onto the transported molecule, it enables selective diffusive transport in an artificial system.

Nevertheless, none of these approaches has led to an efficient, reversible and stable toggle switch that allows the transport of DNA and viral capsids through artificial membranes to be controlled in a temperature-modulated manner. In addition, transport in some of the previous studies was diffusive and molecular transport measurements were limited by aborted-diffusion events observed with electrical detection or accumulation effects due to adhesion on the membrane observed for simple fluorescence measurements.

To overcome these limitations, we built a thermally switchable nanopore as a gateway for the transport and filtration of DNA and viral capsids by electrografting temperature responsive polymers on the nanopore membrane. We have used artificial polymers, poly(2-alkyl-2-oxazoline)s, as a new type of grafting inside the nanopore. Specifically, we used two types of poly(2-alkyl-

2-oxazoline)s: hydrophilic poly(2-methyl-2-oxazoline) (PMeOx) and poly(2-*n*-propyl-2-oxazoline) (P*n*PrOx), which becomes hydrophobic at high temperature. For both polymers, we varied the molecular mass. The thickness of the grafted layer depends on both the type of polymer grafted and environmental conditions. PMeOx is in good solvent at all temperatures around room temperature (20 °C) and can be considered an ideal coil. In contrast, P*n*PrOx exhibits an LCST. Below the LCST this polymer is fully soluble in aqueous solution whereas at temperatures higher than the LCST it aggregates and precipitates. This temperature dependence in a range compatible with biomolecules allows us to create a switch between an open and a closed state of the nanopore depending on the temperature inside the nanopore and thus create a switch for macromolecular transport inside through the nanopore. We demonstrate how the transport of biomolecules and viral capsids through artificial nanopores can be controlled by the type of grafted polymer inside the pore and switched on and off by an external stimulus.

Here, we used an optical approach, based on ZMW for nanopores [191], to follow the transport of individual macromolecules in real time and at the scale of the single nanopore. To this end, the macromolecules were fluorescently labeled and driven through the nanopore by applying a pressure difference between the two sides of the membrane (Figure 23). A gold layer was vapor deposited onto the membrane, onto which poly(2-alkyl-2-oxazoline)s with different degrees of polymerization (X_n) were then electro-grafted, which either may or may not exhibit an LCST (see Materials and Methods Section 4.3.9 and Supplementary Information Section 4.3.10.1, Section 4.3.10.2, and Section 4.3.10.9 for characterizations).

4.3.3 *Results*

4.3.3.1 *Polymer grafting inside nanopore creates a thermo-responsive switch for DNA translocation*

With our ZMW for nanopores approach, we were able to directly observe individual DNA translocation events through polymer-grafted nanopores. We recorded and examined the translocation frequency for dsDNA molecules (lambda phage DNA) as a function of temperature for different polymer graftings inside the nanopore. The heating system we used controlled the temperature of the entire membrane (see Materials and Methods Section 4.3.9). The measurements were conducted for the P*n*PrOx and PMeOx graftings and for a membrane without polymer grafting as a negative control (Figure 24A, Supplementary Information Section 4.3.10.10).

In the case of P*n*PrOx, we observed that the translocation frequency was strongly affected by temperature. A sharp drop in translocation frequency was observed when lowering the temperature in a narrow range around the LCST. In contrast, for PMeOx grafted membranes, the translocation frequency remained unchanged with changes in temperature (Figure 24A). This behavior is consistent with the fact that P*n*PrOx possesses an LCST, such that a change in temperature in a range including the LCST switches the conformation of the polymers in the grafted layer between an extended and a collapsed phase. We interpret the changes in translocation frequency as a polymer toggle switch between an open (collapsed polymer) and a closed (extended polymer) state

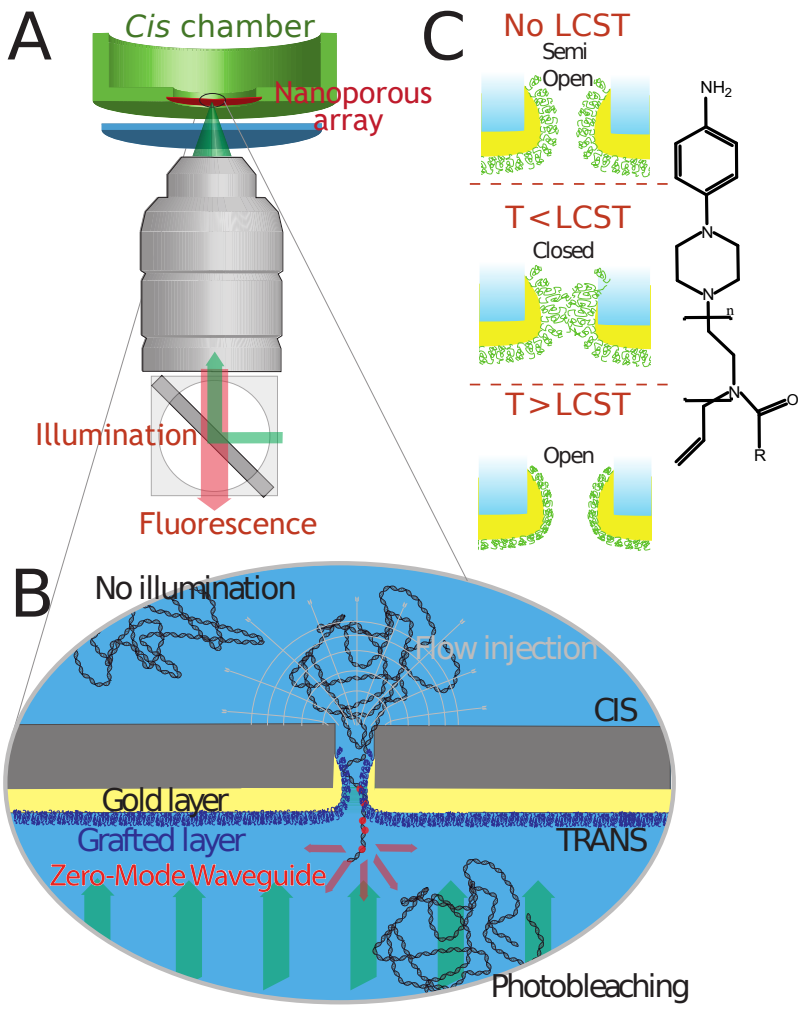

Figure 23: ZMW setup for nanopore with grafted polymer. A, B) Schematic of the ZMW for nanopores setup. It uses a nanoporous array coated with a gold layer for near-field enhancement. When illuminated with a laser, the fluorescent molecules in the *cis* chamber do not receive any light because of metal whereas downstream molecules are unfocused and bleached by the laser. Only the fluorescent molecules in the pore in the vicinity of the metal film are exposed to an enhancement of the electromagnetic field, which leads to reinforcement of the fluorescence. This methodology enables the detection of single molecules translocation events with a high parallelization. In the case of nanoporous arrays functionalized with grafted polymers, the translocation of the transported molecule can be modulated by closing and opening the grafted channels. An exemplary video recording of the translocation events can be found in Supplementary Information Section 4.3.10.12. C) Left: Schematic of how grafted polymers modulate the pore diameter. Polymers that do not exhibit an LCST limit the channel size but cannot completely close the pore. Pores grafted with polymers with an LCST can be triggered by changing the temperature to switch from an open state at high temperature to a closed state at low temperature. Right: Poly(2-alkyl-2-oxazoline)s structure. The -R group corresponds to -CH_3 for PMeOx and for -CH_2-CH_2-CH_3 for P*n*PrOx.

of the nanopore in response to the temperature of the surrounding medium (Figure 23).

To get quantitative results for the mean steepness of the transition m (in $°C^{-1}$) and the mean transition temperature θ (in °C), we fitted the temperature-frequency curves for the PnPrOx grafting (Figure 24B, Supplementary Information Section 4.3.10.10) by an error function $f(T)/f_{max} = 1/2 \cdot (erf(m \cdot (T - \theta)) + 1)$. The error bars were calculated as the standard errors. The steepness of the error function m is found to range between (0.58 ± 0.03) $°C^{-1}$ for $X_n = 33$ and (0.66 ± 0.05) $°C^{-1}$ for $X_n = 59$ (the complete set of values is shown in Table 1). This shows that the transition between the open state of the nanopore and the closed state is extremely sharp. A change of the surrounding temperature of less than 1 °C is already enough to evoke a conformational change of the polymer grafting and with this, a change in the openness of the pore from a completely closed pore (no translocation events) to an open pore. The second fitting parameter is the midpoint position θ that gives the transition temperature. We find that this temperature is reduced at higher molar masses of the grafting and ranges from (29.4 ± 0.1) °C for $X_n = 33$ to (24.9 ± 0.1) °C for $X_n = 538$ (Table 1, Figure 24B "PnPrOx grafted"). While the grafting and geometry of the pore make a direct comparison to measurements in free aqueous solution challenging, the measured values are close (26 °C for the PnPrOx $X_n = 33$ and 23 °C for PnPrOx $X_n = 59$, measured using optical turbidity). For the PMeOx grafting and the membrane without polymer grafting, the translocation frequency was found to be temperature-independent (Figure 24A).

X_n	33	59	210	538
m (1/°C)	0.58 ± 0.03	0.66 ± 0.05	0.61 ± 0.05	0.52 ± 0.03
θ (°C)	29.4 ± 0.1	28.4 ± 0.2	25.8 ± 0.1	24.9 ± 0.1

Table 1: Transition temperature θ and steepness m for different degrees of polymerization of PnPrOx grafting.

Interestingly, we find that the transition temperature θ systematically decreases with increasing chain length for PnPrOx (Figure 24C). A decrease in LCST with increasing chain length or degree of polymerization has been observed for several polymers [237–240]. We find that the transition temperatures for our grafted polymers are overall similar to values determined by Hoogenboom *et al.* [237]. For ungrafted PnPrOx in aqueous solution while showing a less steep dependence on chain length (Figure 24C "PnPrOx bulk"). This difference in scaling behavior might be due to the effect of grafting the polymer onto gold support, which has been shown to lead to an altered chain length dependence for PNIPAM previously [239].

In another series of experiments (Supplementary Information Section 4.3.10.4), we cooled the system down until the translocation frequency reached zero. These results demonstrate the reversibility of the system and show that, at low temperature, the pore reaches a state that efficiently blocks DNA molecules.

Having established thermal gating by heating the entire device, we were also able to demonstrate an even simpler and more elegant alternative heating method: local heating using a fluorescence lamp (Supplementary Information Section 4.3.10.3). We found that adsorption of heat from the light source by

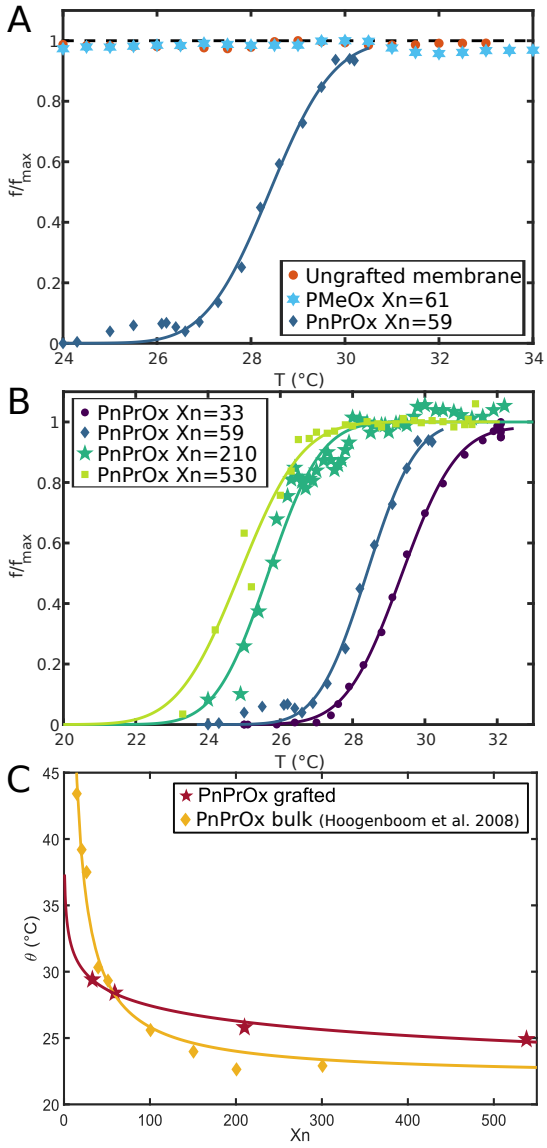

Figure 24: Normalized translocation frequency as a function of temperature for differently grafted pores. A) Comparison of the frequency of translocation of λ-DNA as a function of temperature for PMeOx (X_n = 61), PnPrOx (X_n = 59), and ungrafted membrane. Pore diameter (42 ± 0.5) nm. Applied pressure: 80 mbar. The blue solid line represents the fitting by the error function. The dashed black line represents the constant f/f$_{max}$ = 1. Unaveraged curves are shown in Supplementary Information Section 4.3.10.8. B) Comparison of the frequency of translocation of λ-DNA as a function of temperature for different number-average degree of polymerization of PnPrOx (X_n = 33, X_n = 59, X_n = 210, X_n = 538). Pore diameter (42 ± 0.5) nm. Applied pressure: 80 mbar. Solid lines represent the fitting by error function. Unaveraged curves are shown in Supplementary Information Section 4.3.10.8. C) Transition temperature θ for different polymerization degrees X_n. Red stars correspond to the PnPrOx graftings used in this study. Yellow diamonds correspond to a study from Hoogenboom *et al.* [237]. Solid lines represent model fitting with a power law $\theta = a \cdot X_n^b + \theta_\infty$. The exponent b is equal to -0.3 for our data and -0.9 for *et al.* [237].

Polymer	PMeOx	PMeOx	PMeOx	PMeOx	P*n*PrOx	P*n*PrOx	P*n*PrOx
X_n	61	83	178	387	33	59	538
L_c (nm)	26	36	76	166	14	25	230
P_c (mbar)	135±3	150±4	223±4	327±7	96±4	104±2	185±4
R_p (nm)	2.5±0.5	3.0±0.6	4.6±0.6	6.1±0.7	0.8±0.5	1.2±0.6	3.9±0.6

Table 2: Critical pressure and grafted polymer thickness extracted from our experimental data. For the track-etched pores used here, the radius was measured by electron microscopy, (R_{pore} = (21 ± 0.25) nm), and Auger *et al.* found the critical pressure to be P_c= (82 ± 4) mbar in the absence of grafting polymers [191]. For P*n*PrOx graftings, the experiments were carried out at T (31 °C) > LCST. The contour length, L_c (i.e., maximum length of the molecule), is the number of monomers multiplied by their size (MeOx and P*n*PrOx monomers are about 428 pm).

the membrane can indeed be used to locally control the transition between coil and globule and modulate transport through the pore.

4.3.3.2 *A simple polymer model can account for the gating experiments*

To provide a deeper understanding of the polymer phase transition inside the nanopore, we compared the temperature gating observed in our experiments to a simple theoretical model. Our theoretical description of the gating phenomenon is based on the work of Halperin on grafted polymer chain collapse in poor solvent and the suction model [241, 242] (see Supplementary Information Section 4.3.10.5 for more details). Briefly, the configuration of the grafted chains is modeled by a mean field theory. We assume that the free energy F of the chains is composed of two main contributions: F_{el}, which accounts for the configurational entropy and F_{mix}, which accounts for the interaction of the monomer units with the solvent and with the other monomer units. The total free energy can then be expressed as a function of the number of monomer units per chain N, the coil radius R, as well as ν and ω, the second and third virial coefficients, which quantify respectively the 2-monomer and 3-monomer interactions, respectively. The coil radius was then determined by the numerical minimization of the polymer chain free energy for each temperature. From this value, R_{eff} the effective radius of the pore and the critical pressure of translocation P_c are determined. Using the suction model, f the frequency of translocation as a function of temperature was finally calculated as:

$$f = k \cdot \left(\frac{R_{eff}}{R_{pore}}\right)^4 \cdot \frac{P}{P_c^0} \exp\left(-\frac{P_c^0}{P}\left(\frac{R_{pore}}{R_{eff}}\right)^4\right) \tag{23}$$

with R_{pore} the radius of the pore without polymer grafting and P_c^0 the critical pressure without polymer grafting (i.e for $R_{eff} = R_{pore}$).

The model predicts that the translocation frequency as a function of temperature exhibits a sharp transition between no translocation at low temperature and full transmission at high temperature (Figure 25A and see Supplementary Information Section 4.3.10.5 for details about the choice of parameters). The sharpness of the transition is dominated by the influence of the third virial

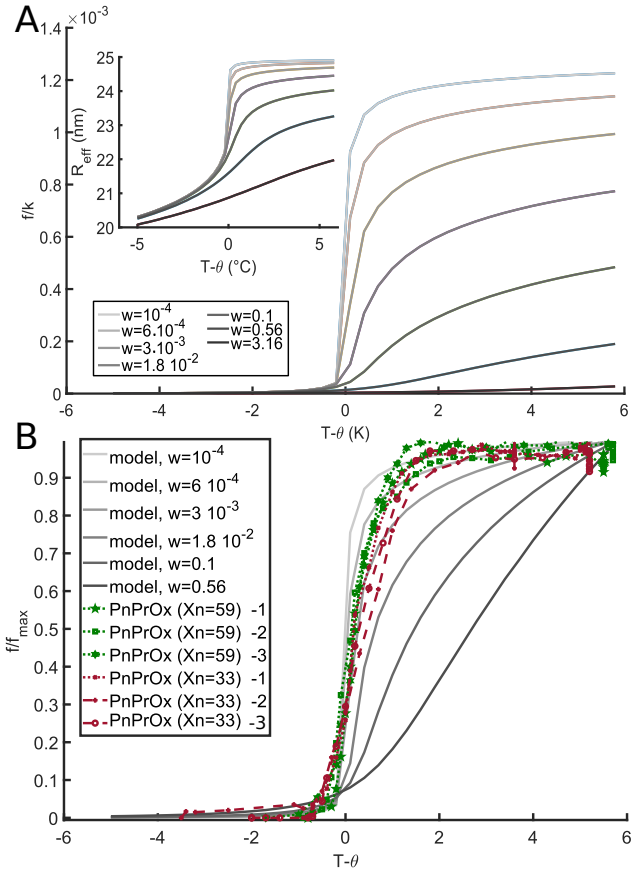

Figure 25: Theoretical modeling of the gating phenomenon. A) (main) Modeling of the frequency of translocation normalized by the suction model prefactor k. This prefactor corresponds to the frequency of translocation for $P = P_c$. (inset) Modeling of the effective radius of the grafted nanopore, R_{eff}, as a function of temperature difference T - θ with θ the critical temperature. Different values of the third virial coefficient ω are represented by different colors. B) Comparison be-tween the coarse-grained model and individual translocation experiments (numbers 1 to 3) for different PnPrOx graftings (X_n = 33 and X_n = 59) normalized by the maximum frequency f_{max}.

coefficient ω may be varied by chemical modification of the polymer (change of side groups etc.). For ω values, used here as a fitting parameter, between 10^{-3} to 10^{-4} comparable to values from the literature, this model reproduces well the transition observed experimentally for individual measurements with grafted polymers of different molar masses (Figure 25B).

This result shows that the key features of the temperature induced gating can be readily recovered by a simple physical model including the collapse of the polymer inside the pore and the relation between the effective diameter of the pore and the energy barrier of transport.

4.3.3.3 *Flow-driven DNA translocation experiments provide a tool to characterize grafted polymer layers inside nanopores*

To examine the correlation between translocation frequency and the spatial extension of the polymer layer grafted inside the nanopore, we performed single-molecule ZMW experiments and measured the translocation frequency of DNA molecules through the membrane as a function of the applied pressure. Since the critical pressure of translocation depends strongly on pore radius $P_c \approx R_{pore}^{-4}$ (see Supplementary Information Section 4.3.10.6), a small change in the pore radius is expected to result in a large difference in the critical pressure.

We recorded the frequency of translocation of DNA molecules for different graftings (PMeOx and P*n*PrOx) and degree of polymerization as a function of pressure (Figure 26A-B). Notably, the grafted polymers remained stable over a 6-month period (Supplementary Information Section 4.3.10.11) For the DNA translocation experiments using membranes with a PMeOx grafting, the experiments were performed at room temperature (20 °C) as the surrounding temperature had no influence on the translocation frequency for this grafting (Figure 24). For the experiments using membranes with a P*n*PrOx grafting of various polymerization degrees ($X_n = 33$, $X_n = 59$, $X_n = 210$, $X_n = 538$), we heated the system to a temperature higher than 30 °C. Heating the system made the grafted polymers collapse and as a result, partially opened the pore (Figure 24). As a control experiment, we performed the same measurements with membranes with P*n*PrOx graftings at room temperature (20 °C). In the same pressure range, we recorded no translocation events confirming the assumption that the pores were indeed closed at 20 °C.

All the pressure-frequency curves were fitted with the suction model [241] and the results were then compared to the findings originating from membranes without a polymer grafting [191]. For the track-etched pores used here, the radius measured by electron microscopy (see Supplementary Information Section 4.3.10.9), $R_{pore} = 21 \pm 0.25$ nm, Auger *et al.* found the critical pressure to be $P_c^0 = 82 \pm 4$ mbar in the absence of grafting polymers. We used these values to calculate the thickness of the grafted polymer layer. As shown in Section 4.3.10.6, the effective thickness of the polymer layer (R_p) can indeed be expressed as:

$$R_p = R_{pore}\left(1 - \left(\frac{P_c^0}{P_c}\right)^{1/4}\right) \tag{24}$$

where P_c is the critical pressure through the pore grafted with polymers. This relation was checked with mPEG graftings by measuring the critical pressure P_c for different molecular masses of the grafted polymer (see Section 4.3.10.6).

The systematic variation in critical pressures with polymer type and length (Table 2) shows that the translocation of DNA through nanopores is strongly influenced by the grafting inside the pore. The observed trends are consistent with the additional polymer layer controlling the translocation by reducing the diameter of the nanopore. As a result, the DNA molecules to be transported must be spatially confined even further, and consequently, the critical pressure increases with increasing thickness of the polymer grafting.

For both PMeOx and P*n*PrOx, the increase of grafted polymer thickness Rp with polymerization degree X_n are well-described by power law fits of the

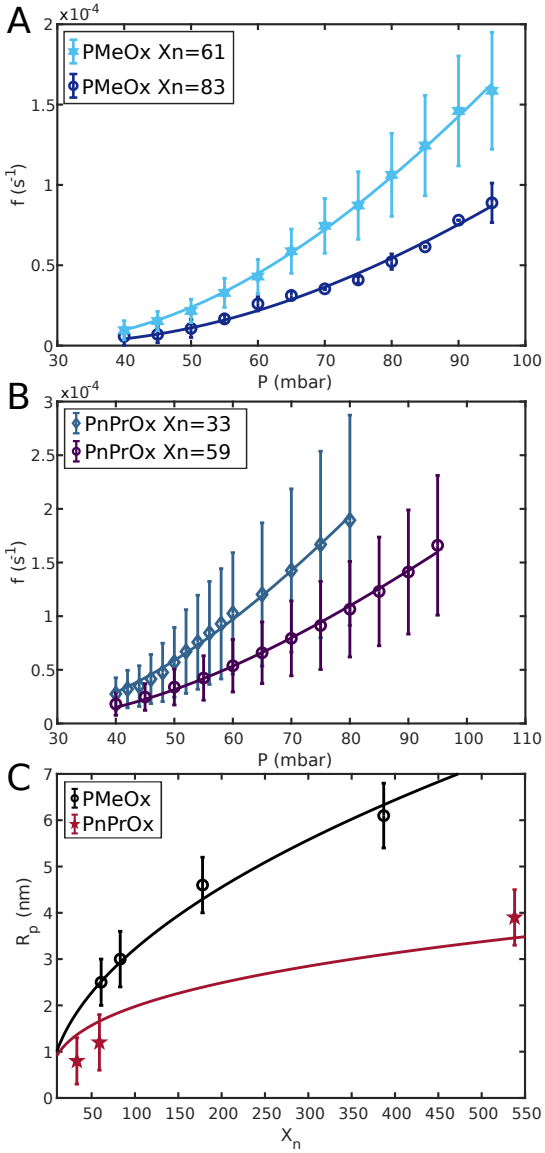

Figure 26: Averaged translocation frequency as a function of the applied pressure for different graftings. Frequency of translocation of λ-DNA was measured for membranes grafted with A) PMeOx: $X_n = 61$ in light blue and $X_n = 83$ in dark blue and B) P*n*PrOx: $X_n = 33$ in blue and $X_n = 59$ in purple at high temperature (T = 30 °C). Pore diameter (42 ± 0.5) nm. The solid lines correspond to the suction model, which provides the critical pressure P_c as well as the constant k. The different polymers grafting inside the pore lead to a change in translocation frequency implying a different state of openness of the nanopore that can be related to an effective radius of the pore. Each experiment was repeated at least 3 times. Error bars are standard errors. Unaveraged curves are shown in Supplementary Information Section 4.3.10.8. C) Evolution of the grafted polymer thickness R_p as a function of polymerization degree X_n for various graftings. Black circles represent PMeOx graftings and red stars represent P*n*PrOx graftings. Solid lines correspond to a fit with a simple scaling law: $R_p = a \cdot X_n^{\nu}$ with $\nu = 0.5$ for PMeOx and $\nu = 0.33$ for P*n*PrOx. We found a(PMeOx)=0.32 nm and a(P*n*PrOx) = 0.43 nm.

form $R_p = aX_n^{\nu}$ (Figure 26C). For PMeOx, we have used the scaling exponent $\nu = 0.5$, as expected for the end-to-end distance of an ideal polymer chain. The fitted Kuhn length $a = 0.32$ nm for PMeOx is in the same order of the theoretical monomer length obtained from its chemical structure (0.428 nm). These findings suggest that grafted PMeOx behaves like a flexible polymer chain in good solvent, similar to PMeOx in free solution. In contrast, while the grafted polymer thickness for P*n*PrOx above the critical temperature (Figure 26C) also increases with increasing chain length, the observed values are much smaller. In this case, we have used the scaling exponent $\nu = 0.33$, as expected for the end-to-end distance of a collapsed polymer in bad solvent. The fitted apparent monomer length $a = 0.43$ nm, which is as expected larger than PMeOx. These results support not only the idea that the P*n*PrOx polymers exhibit a reversible coil-globule transition inside the pore when heated above the LCST, but also that our nanopore methodology can be used as a precise tool to determine grafted polymer thickness in nanoporous membranes.

4.3.3.4 *Thermo-switchable nanopores control the translocation of viral particles*

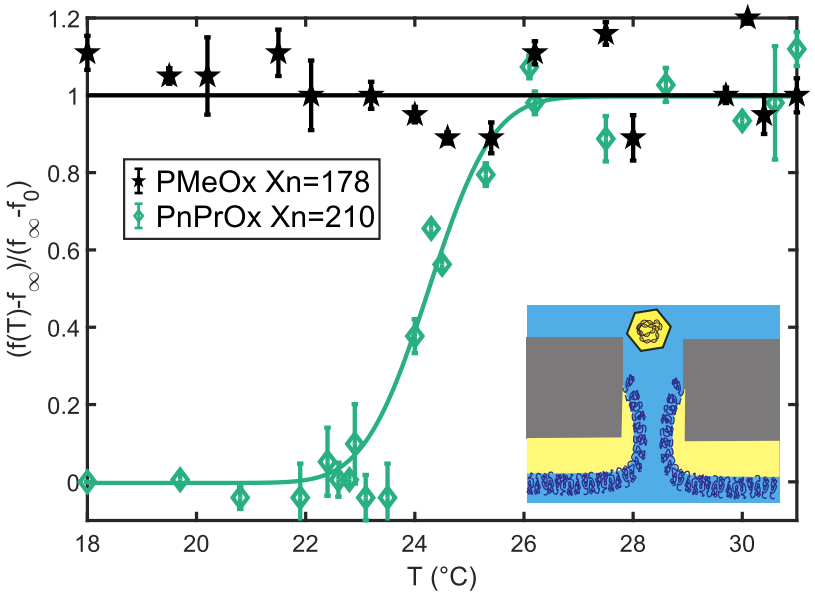

Figure 27: Controlled translocation of viral particles. Normalized frequency of translocation of AAV viral particles as a function of the temperature for two different graftings: black stars are PMeOx and green diamonds are P*n*PrOx. Pore diameter (220 ± 1.8) nm. Applied pressure: 4 mbar. The green solid line is the result of fitting by an error function. Black solid line is the constant $(f(T) - f_\infty)/(f_\infty - f_0) = 1$. N > 2 for each experiment. Errors bars are standard errors. Insert: Scheme of an AAV virus at the entry of a grafted nanopore.

As an application of the gating behavior observed for DNA molecules, we extended our approach to gating viral capsids derived from Adeno-Associated Virus (AAV) as a model system. We translocated viral particles (with a diameter of 25 ± 3 nm [243]) through grafted membranes (PMeOx and P*n*PrOx) and measured the translocation frequency as a function of the

temperature. In this case, the pore diameter was chosen to be 200 nm in order to avoid self-interaction between viral capsids. The switching phenomenon observed for DNA molecules was also observed for AAV for P*n*PrOx grafting, but not for PMeOx grafting (Figure 27 and Supplementary Information Section 4.3.10.9). Remarkably, the critical temperature measured for viral particles (T_{crit} = 25.5 °C for P*n*PrOx X_n = 210) was very close to the one observed for DNA molecules (T_{crit} = 25.8 °C for P*n*PrOx X_n = 210). This result strengthens the idea that the grafted polymers of P*n*PrOx undergo a global reorganization during the coil-globule transition and that the toggle switch phenomenon observed is not limited to one type of transported biomolecule but has far-reaching relevance for a wide range of biological and non-biological systems.

4.3.4 *Conclusion*

In this study, we report a thermally switchable and reversible gate for the transport and filtration of macromolecules and viral particles. The properties of this nanogate are controlled by a network of electro-grafted polymers. We systematically characterize the effects of the chemical composition and molar mass of the grafted macromolecules on the opening of the pore. In addition, we show that the transport properties of the membrane can be controlled by changes in temperature induced by light illumination via heating up the membrane.

The temperature switch between the extended and the collapsed state observed in this work for P*n*PrOx polymers occurs in a well-defined and sharp temperature range (∼1 °C). Because of the limitation of our temperature measurement and averaging effects (see Supplementary Information Section 4.3.10.8) we think that the steepness of this effective transition is in fact higher and may depend on grafted polymer molar mass. The difference of transport properties between the two types of polymers at low temperature may be interpreted, beyond a simple coil-globule transition, as a difference of cohesivity of the network induced by the different chemical nature of the monomer units. A detailed investigation with polymers composed of a mixture of these two monomers might enable to probe these effects in the future.

Future works may use this approach to investigate other viral capsids tolerance and plasticity and benefit from the proposed model to engineer the shape of critical transition. Overall, we believe that nanopores grafted with thermo-switchable polymers have the potential to enable smart filters, act as sensors, and provide a new dimension of control over translocation, with possible applications in drinking water treatment, pharmaceutical production, and more.

4.3.5 *Author Contributions*

F.M, P.G, J-C.L, J.M, and S.L conceived the project. D.B, R.B, P.M and G.D performed polymer synthesis, characterization, and electro-grafting on nanoporous membranes. A.S produced the AAV capsids. P.J.K, L.C-F, G.D, and M.B performed nanopore experiments. P.J.K, L.C-F, M.B, and F.M performed data analysis. F.M performed theoretical modeling. F.M, P.G, V.B, J-C.L, J.M., and J.L supervised the work. P.J.K, L.C-F, and F.M wrote the manuscript. All authors contributed to the ideas and reviewed the manuscript.

4.3.6 *Funding*

This work was supported by the Centre National de la Recherche Scientifique under: the 80 Prime project "NanoViro", and the ANR "Golden Gates".

4.3.7 *Notes*

The authors declare no competing financial interest.

4.3.8 *Acknowledgements*

The authors would like to thank Jens Uwe-Sommer, Holger Merlitz, Cendrine Moskalenko, Martin Castelnovo, Saskia Brugère, Kassandra Gérard, Thomas Auger, Jean-Marc Di Meglio, Loic Auvray, Arthur Ermatov, Willem Vanderlinden and Hermann Gaub for helpful comments and discussions.

4.3.9 *Materials and Methods*

4.3.9.1 *Experimental setup*

Our experimental setup combines optical detection and pressure control to induce the transport of polymers through a porous membrane as previously described by Auger *et al.* [191, 192] (Figure 23). Briefly, the experimental setup is based on an inverted fluorescence microscope (Axiovert 200) with a filter box – including several pairs of excitation and emission filters and an associated dichroic mirror – connected to an electron-multiplying charge-coupled device camera (EMCCD camera, Andor, iXon 897). When imaging directly, it shows a maximum resolution of 512 × 512 pixels in 32 bits and a maximum frame rate of 60 Hz. A water objective (ZEISS C-Apochromat) with 63x magnification, 1.2 numerical aperture, and 0.28 mm operating distance for a 0.17 mm glass slide is mounted on the microscope. We use a laser (Cobolt blues 50, Cobolt AB), which emits at 473 nm wavelength, as excitation source. The beam is expanded by a telescope and parallelized inside the optical path. The membrane is illuminated from the *trans* side. The setup has a second light source, a fluorescent lamp (Uvico, Optoelectronics GmbH), directly connected to the microscope via an optical fiber. The two possible excitation wavelengths are 488 nm and 568 nm. The lamp is used to get a better overview of the sample and to light the sample with or without heating, depending on the selected excitation wavelength.

The centerpiece of the setup is composed of two chambers separated by a porous membrane: the upper chamber (called the *cis* chamber) consists of a screw cap (Nanion) made of a glass bottom with a small hole, on which a piece of membrane is glued. This chamber is linked to a pressure control system (MFCS, Fluigent) that allows the application of pressures up to 1 bar with a precision better than 0.1 mbar. Sealing is accomplished by a Teflon gasket inside the cap. The lower chamber also called *trans* chamber, is made of a Teflon ring, on which a 0.17 mm thick glass strip is attached. In addition, the setup has a smaller Teflon ring fitted around the screw cap to maintain it vertically in the *trans* chamber. The translocated polymer – labeled with a fluorescent dye – is introduced into the *cis* chamber, and by applying a pressure difference between the two chambers, the polymer is translocated through the

membrane into the *trans* chamber. As the membrane is illuminated with an extended laser beam on the *trans* side, on which the gold coating is grafted, the molecules can be observed leaving the pores. In contrast, molecules in the *cis* chamber and inside the pore are dark since they are not within the illuminated volume. Finally, the fluorescence of the molecules vanishes due to bleaching and optical defocusing once they move away from the membrane. This two-chamber construction is located above the lens of the fluorescence microscope. The sample can be moved in all three directions by a stage control system with an XY-drive with µm-accuracy and a Z-drive with nm-accuracy. The stage control system is operated by the software ImageJ. The transported molecules are observed by an operating software (Andor SOLIS for imaging) that is connected to the EMCDD camera.

4.3.9.2 *Membrane preparation and polymer grafting*

We pretreated the nanoporous membranes, again following the protocol of Auger *et al.* [191, 192]. The commercially available track-etched membranes (Whatman) consist of a 6-10 µm-thick polycarbonate layer and have cylindric holes (pores) with a nominal diameter of 50 or 200 nm and a density of 1-6 $\cdot$ 10^8 pores/cm^2. To visualize the translocation of molecules through the pores, we vapor deposited a gold layer of 50 nm thickness after a pre-treatment of low-intensity ionic pickling. Gold was evaporated, using a pressure below 10^{-6} Pa, and deposited at a rate of 0.2 nm/s. The rate and thickness of the deposition were monitored by a quartz balance.

The polymer grafting (Table 2) on top of the gold layer used electro-grafting, i.e connection between the polymers and the gold surface via covalent bounds generated by diazonium salt reduction [244, 245]. Polymers used in this article were poly(2-methyl-2-oxazoline)s (PMeOx) and poly(2-*n*-propyl-2-oxazoline)s (P*n*PrOx) of various number-average degrees of polymerization (X_n, number of repeat units). In the next step, a covalent bond between the polymer and the gold surface was formed by reduction of the diazonium salt. A detailed protocol for polymer synthesis and electro-grafting can be found in Supplementary Information Section 4.3.10.1 and Section 4.3.10.2.

4.3.9.3 *Sample preparation*

For all experiments, we used a tris(hydroxymethyl)aminomethane (Tris) and ethylenediaminetetraacetic acid (EDTA) based buffer (TE buffer), made from Tris-HCl (Sigma-Aldrich) and EDTA (Sigma-Aldrich), pH 7.5. We used Lambda-DNA (Invitrogen) which is a double-stranded linear DNA from bacteriophage λ, (*E. coli*) consisting of 48,502 base pairs (32,300 kDa). This DNA is commercially available as a solution of 500 µg/mL in 10 mM Tris-HCl and 1 mM EDTA . The diameter of the DNA molecules is about 2 nm while the contour length (maximum length of the molecule) is about 16 µm. The DNA molecules were fluorescently labeled with YOYO-1 (Life Tech). For the stationary heating experiments, we introduced 100 µL TE buffer mixed with 2 µL DNA-YOYO mix in the *cis* chamber and 500 µL TE buffer in the *trans* chamber.

As a model of the viral capsid, we used capsids from Adeno-Associated Virus serotype 8 (AAV-8). More precisely, recombinant AAV-8 capsids were produced and purified as described previously [246]. Briefly, HEK-293 cells were co-transfected with a helper plasmid (pDG8), containing both rep2-cap8 and the

adenoviral helper genes, and the AAV2-CMV-GFP vector plasmid (encoding for GFP under the control of the cytomegalovirus (CMV) promoter). Particles were purified from cell lysates on a double CsCl gradient and dialyzed. The concentration of the final AAV-8 sample was determined using qPCR and was equal to $1.4 \cdot 10^{12}$ µg/mL. Fluorescent labeling was achieved using YOYO-1, which was diluted 1500 in the AAV-8 solution (labeling required incubation for 10 min at room temperature). Serum Fetal Bovin (FSB) was added to 10% of the final virus solution.

DNA or virus samples were placed in the *cis* chamber. To apply specific temperatures, we made use of a temperature control system (Pecon, Temp-Controller 2000-2). This system allows us to heat a metal ring that is located around the objective. As the objective is connected by a drop of water to the *trans* chamber, which in turn is filled with buffer that is in contact with the membrane, we have the possibility to indirectly heat the membrane. The applied temperature at the level of the heater was chosen to be 50 °C. After the temperature control system had reached this temperature, we waited for 60 minutes to make sure that the whole system is heated up to sufficiently high temperature. The temperature of the buffer in the *trans* chamber was checked to be higher than 30 °C using a thermometer with a long and flexible probe that is placed on the side of the inner edge of the *trans* chamber so that it is in contact with the liquid inside. Thereafter, we switched off the heat supply and let the system cool down while taking one video every minute. With the acquisition of a video, we also measured and noted the temperature of the liquid in the *trans* chamber.

For varying pressure experiments, we introduced 100 µL TE buffer mixed with 2 µL DNA-YOYO mix in the *cis* chamber and 500 µL TE buffer in the *trans* chamber. The applied pressure was changed between 0 mbar and 150 mbar using the pressure control system. After setting a pressure value at the control system, we waited 3 minutes to let the system adapt. Then, we took four videos in a row at constant pressure. The measurements were either performed at room temperature or while heating the system as explained for the stationary heating experiment.

4.3.9.4 *Data analysis*

To determine the translocation frequency, the single-molecule translocation events appearing in the video are counted manually. Translocation events are visible as bright spots on the otherwise dark background (the membrane is only slightly auto-fluorescent). The frequency f is then calculated as the number of events N observed during one video sequence divided by the number of pores present in one film NP times the acquisition time $t_{acq} = 15$ s. N_P can be calculated as the pore density $\rho = 6\text{-}10 \cdot 10^8$ pores/cm^2 times the observed area 150 µm × 150 µm:

$$f = \frac{N}{N_p \cdot t_{acq}} = \frac{N}{\rho A \cdot t_{acq}} \tag{25}$$

Further data analysis was carried out using custom MATLAB routines. For the analysis of the stationary heating experiments, we plotted the number of translocation events as a function of time and the measured temperature. As the temperature was taken at the edge of the *trans* chamber, the noted temperature differs from the actual temperature of the membrane, but we assumed that these two temperatures are not far from each other. The resulting curves were

normalized by setting the starting frequency value to one. Subsequently, the temperature-frequency curves were fitted by an error function defined as:

$$erf(x) = \frac{2}{\sqrt{\pi}} \int_0^x \exp(-t^2) dt \tag{26}$$

We note that the use of an error function is not motivated by a specific physical model, but just provides a convenient expression to provide an accurate mathematical fit. For varying pressure experiments, we took the mean value of the number of translocation events of the four videos recorded at the same pressure. This value was then represented as a function of the applied pressure and fitted using the suction model [191]. In this theoretical framework, the frequency of translocation f can be written as

$$f = k \cdot \left(\frac{P}{P_c}\right) \cdot \exp\left(\frac{-P_c}{P}\right) \tag{27}$$

with k being constant, P the applied pressure, and P_c the critical pressure. By fitting this equation to our data points, we were able to obtain values for k and P_c. Here, we were mainly interested in P_c, the minimum pressure that is required to transport the molecule through the pore.

4.3.10 *Supplementary tables, figures, and notes*

4.3.10.1 *Polymer synthesis and characterization of synthesized polymers*

The polymerization of 2-alkyl-2-oxazolines was accomplished through a process of Cationic Ring Opening Polymerization (CROP), which was well-controlled [247, 248]. Polymer's structure and the reaction recap are represented in Supplementary Figure 28. Polymers used in this article were poly(2-methyl-2-oxazoline)s (PMeOx) and poly(2-n-propyl-2-oxazoline)s (P*n*PrOx). A description of the chemical mechanism for the PMeOx polymerization is also depicted in Supplementary Figure 29. The mechanism is similar for the P*n*PrOx polymerization since only the structure of the monomer changes (see Supplementary Figure 28).

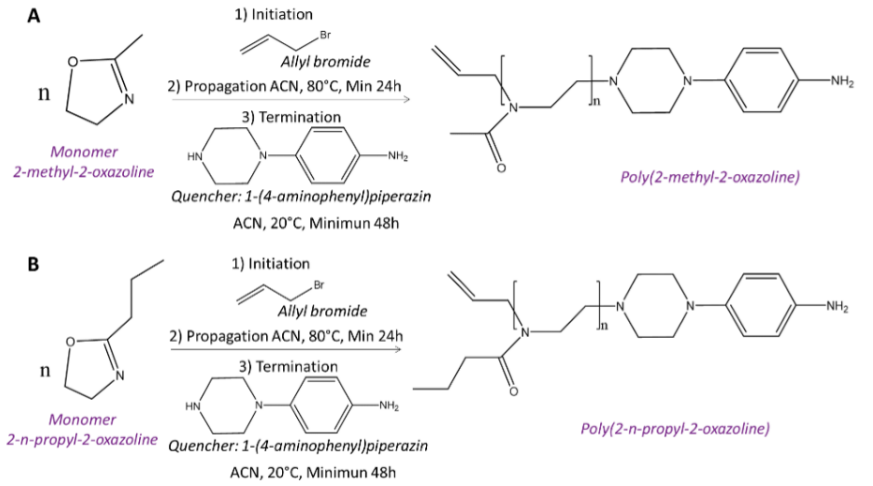

Figure 28: Balance equation for the polymerization reaction of A) PMeOx and B) P*n*PrOx.

Polymer synthesis

Polymers used in this article were PMeOx and P*n*PrOx of various polymerization degrees (X_n). The polymerization of 2-alkyl-2-oxazolines was well-controlled. The reagents of the polymerization were:

- Initiator: Allyl bromide (AlBr, 99%, Sigma Aldrich)
- Monomers: 2-methyl-2-oxazoline (98%, Sigma Aldrich), 2-n-propyl-2-oxazoline (97%, TCI)
- Terminating agent: 1-(4-aminophenyl)piperazine (97%, Sigma Aldrich). It was chosen in order to introduce an aminophenyl group at the end of the polymer chain.

Those reagents and the solvent (acetonitrile, ACN, Sigma Aldrich) were first cryo-distilled over calcium hydride to remove any trace of water. The reaction was carried out in ACN at 80°C under inert atmosphere. The reagents were introduced in the following order: initiator, ACN, and then the monomer. After a variable time (depending on the expected degree of polymerization), the terminating agent in solution in DMF was introduced in the reaction medium

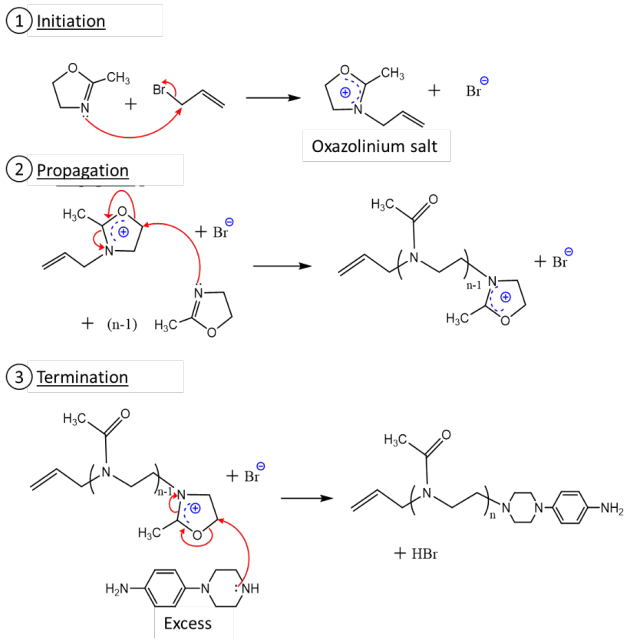

Figure 29: Polymerization mechanism for PMeOx (Cationic Ring Opening Polymerization, ionic mechanism). (1) Initiation: it consists in the nucleophilic attack of the non-bonding doublet of the nitrogen atom of the monomer on the electrophilic site of the initiator and generates an oxazolinium salt. (2) Propagation: the oxazolinium salt undergoes a nucleophilic attack of the monomer. This attack is done on carbon 5, which induces the opening of the ring. (3) Termination: it is based on the addition of the deactivating agent (1-(4-aminophenyl)piperazine). The nucleophilic part (aniline side) attacks the carbon 5, which generates polymer chains whose active center is deactivated.

in excess. The polymers were then dialyzed using a regenerated cellulose membrane (Repligen, Spectra/Pore 6, Standard Regenerated Cellulose, cut-off 1000 Da) against methanol.

Polymer characterization

The polymers were characterized using ^{1}H NMR (Bruker Nanobay 300 MHz, in CDCl3 solvent) and Size Exclusion Chromatography (SEC, in N,N-dimethylformamide, with poly(methyl methacrylate) standards).

^{1}H NMR

The spectrometer used was the Bruker Nanobay 300 MHz. The solutions of polymers were prepared at 30 mg/mL with CDCl3 (Euriso-TOP). The spectra were processed with the MestReNova software. The calibration of the spectrum was performed with the signal of the solvent here of CDCl3, which appears as a singlet at 7.26 ppm. The attribution of the protons and their chemical displacement were shown for two examples in the Supplementary Figure 30: PMeOx (X_n = 387) and P*n*PrOx (X_n = 538).

Steric Exclusion Chromatography, SEC

The mobile phase used was N,N-dimethylformamide (DMF, Sigma Aldrich) at 60 °C and the SEC was performed with a PSS GRAM 100 nm (8×300 mm; separation limits: 1 to 1000 kg · mol^{-1}) coupled to a differential refractive

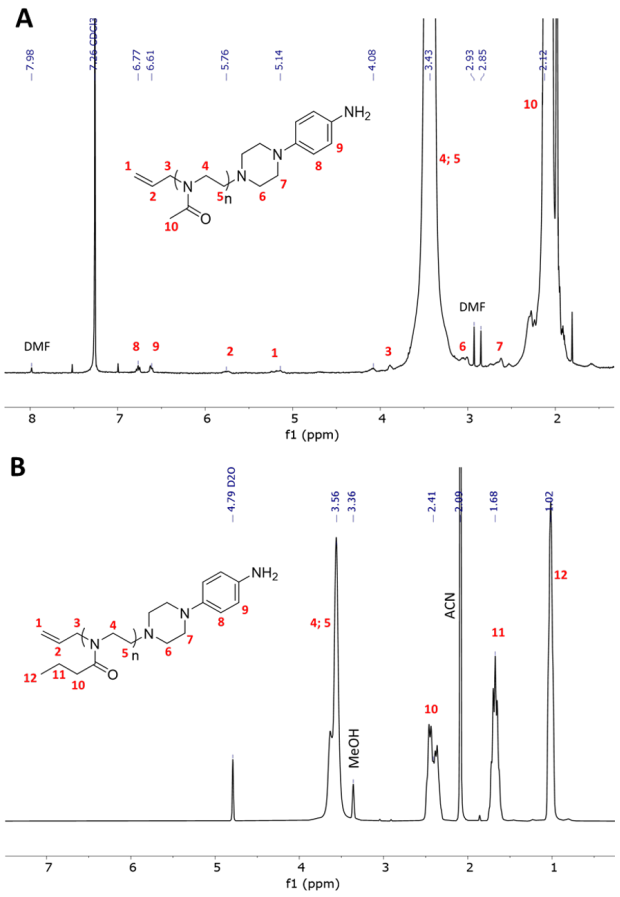

Figure 30: ^{1}H NMR of A) PMeOx (X_n = 387) and B) P*n*PrOx (X_n = 538). The assignment of the protons was given in red and their chemical displacement in blue.

index (RI) detector. The degree of polymerization (X_n) and the dispersity (Đ) of the polymers were calculated using calibration standards in PMMA (polymethylmethacrylate). Examples of SEC chromatograms for PMeOx (X_n = 387) and P*n*PrOx (X_n = 538) were given in Supplementary Figure 31. The final degree of polymerization (X_n) was obtained by averaging the polymerization degree from the data of ^{1}H NMR and the data from SEC. The results are presented in Table 3 and 4, respectively for PMeOx and P*n*PrOx.

4.3.10.2 *Electro-chemical grafting protocol*

First, a diazonium salt was generated *in situ* from the aminophenyl end of the polymers in the presence of an acid ($HClO_4$) and a nitrite compound ($NaNO_2$) [244]. Then, the formation of a covalent bond between the polymer and the gold surface was achieved by reduction of the diazonium salt. Grafting was accomplished by cyclic voltammetry, scanning the membrane between 0 and -0.8 V/$E_{Ag^+/Ag}$ at a scan rate of 0.1 V/s. Several cycles were performed (10 to 20 depending on the membranes).

Grafting characterization

Voltammograms

We used a probe with an external sphere probe that is sensitive to surface states:

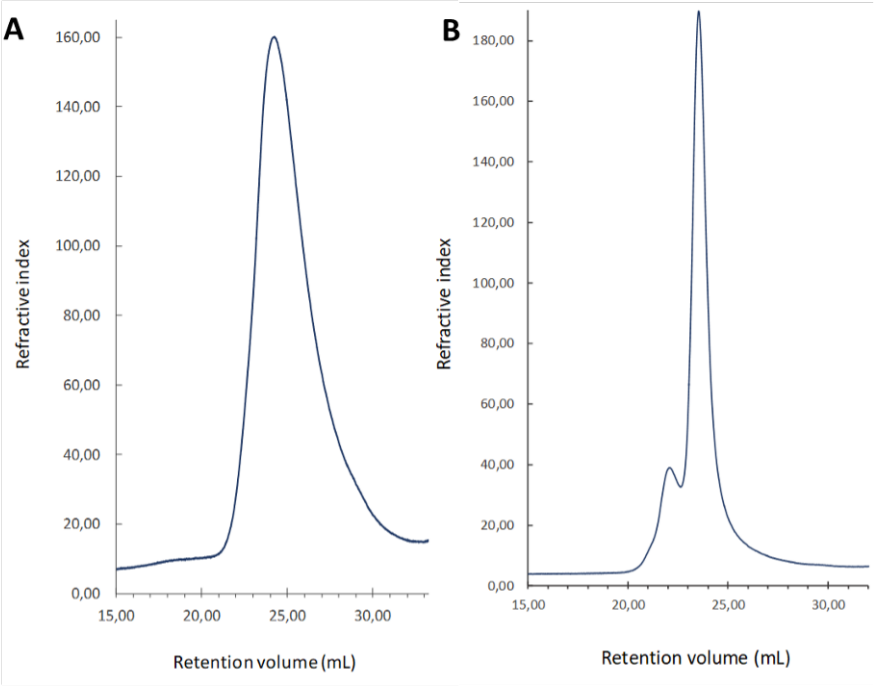

Figure 31: Chromatograms of A) PMeOx (X_n = 387) and B) P*n*PrOx (X_n = 538).

X_n (theory)[a]	X_n (NMR)[b]	X_n (SEC)[c]	X_n (average)[d]	Đ[c]
54	57	64	61	1.30
59	81	85	83	1.35
176	174	182	178	1.38
530	–	387	387	1.71

Table 3: Characterization of PMeOx. [a] $X_n = ([\text{MeOx}]_0 \times \rho(\text{MeOx})) / [\text{AlBr}]_0$ with ρ(MeOx) corresponding to MeOx conversion. [b] determined by ^{1}H NMR from signals of allyl protons and methylene protons from the polymer backbone. [c] Đcorresponds to polymer dispersity determined by SEC in DMF, PMMA standards. [d] average between NMR and SEC values.

X_n (theory)[a]	X_n (NMR)[b]	X_n (SEC)[c]	X_n (average)[d]	Đ[c]
39	32	34	33	1.12
30	51	64	59	1.08
176	226	194	210	1.2
530	–	538	538	1.31

Table 4: Characterization of P*n*PrOx. [a] $X_n = ([n\text{PrOx}]_0 \times \rho(n\text{PrOx})) / [\text{AlBr}]_0$ with $\rho(n$PrOx) corresponding to *n*PrOx conversion. [b] determined by ^{1}H NMR from signals of allyl protons and methylene protons from the polymer backbone. [c] Đcorresponds to polymer dispersity determined by SEC in DMF, PMMA standards. [d] average between NMR and SEC values.

ferrocenemethanol (FcMeOH). The membranes were characterized before and

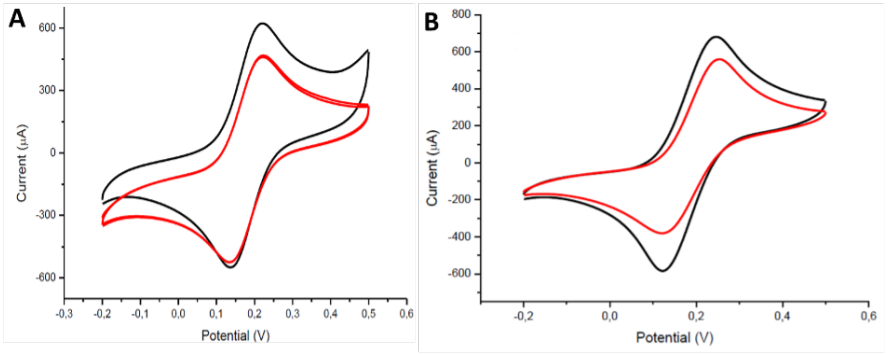

Figure 32: Voltammograms with FcMeOH before (black) and after (red) grafting for a gold nanoporous surface (pores 50 nm) grafted with A) PMeOx ($X_n = 61$) and B) P*n*PrOx ($X_n = 33$)

after grafting. For this purpose, an aqueous solution containing 1 mM of FcMeOH, and 0.1 M of lithium perchlorate ($LiClO_4$, acting as electrolyte) was prepared. The solution was added to the electro-chemical cell, and after degassing under Argon for about ten minutes, a first voltammogram before grafting was recorded (scan rate 0.1 V/E_{Ag}). After grafting, the same mother solution of FcMeOH is used, following an identical process to characterize the surface. Examples of voltammograms are given in Supplementary Figure 32. The evolution of the voltammogram before and after grafting allows to conclude qualitatively that there was indeed a modification of the surface after grafting.

X-Ray photoelectron spectrometry
XPS relies on the photoelectric effect and allows to measure elemental composition within the surface of a material. The analysis of XPS spectra allow to obtain the percentage of each element on the surface studied. Here we calculate the ratio N/O, C/O, CN and C/Au to evidence the presence of the grafting. An example of XPS surface from a nanoporous gold membrane

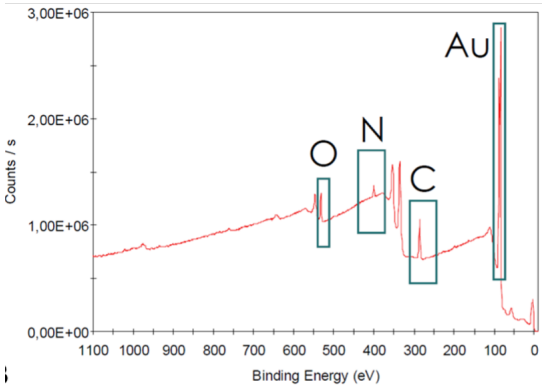

Figure 33: X-ray photoelectron spectrometry (XPS) spectrum for a nanoporous gold surface (pores 50 nm in diameter) grafted with PMeOx (X_n=178).

(pores of 50 nm in diameter) and grafted with PMeOx ($X_n = 178$) is given in Supplementary Figure 33 and Table 5. The results obtained by XPS allow

to validate the presence of a grafting. To go further and observe the grafted membranes, measurements were also realized by AFM in liquid medium (see Supplementary Information Section 4.3.10.9).

Ratio	C/N	C/O	N/O	C/Au
Theory (monomer MeOx)	4	4	1	–
Experimental data	5.9	4.0	0.7	7.0

Table 5: X-ray photoelectron spectrometry (XPS) data analysis for a nanoporous gold surface (pores 50 nm in diameter) grafted with PMeOx (X_n=178).

4.3.10.3 *Combined illumination and heating using a fluorescence lamp*

A precise determination of the temperature of the membrane during the heating by the fluorescence lamp is difficult in our system, but we can propose a rough estimate from the parameters of our illumination. At steady state our lamp delivers a power density of ∼0.5 mW/nm on the membrane. The gold film adsorption in the range of wavelength used in this study is 50% on a 10 nm interval around the plasmon resonance. If we assume that the polycarbonate membrane plays the role of a perfect insulator and that the thermal relaxation is due to thermal conduction through the water we obtain that the temperature change of gold during heating would be in the range of $\Delta T = (\Delta x \cdot q)/k$. With $k = 0.6$ W/m, the thermal conductivity of water, $\Delta x = 100$ µm the gradient length, q ∼5 mW the incident power, we obtained ΔT ∼42 °C. This order of magnitude is in good agreement with the fact that optical illumination enable to cross the critical transition.

4.3.10.4 *Normalized and averaged translocation frequencies*

4.3.10.5 *Theoretical description of the gating phenomenon*

Our theoretical description of the gating phenomenon is based on the work of Halperin *et al.* [242] on grafted polymer chain collapse in poor solvent and the suction model. The general idea of this theoretical procedure is to determine the radius of the polymer coil and use it to determine the translocation frequency.

The configuration of the grafted chains is modeled by a mean field theory. We define N as the number of monomer units per chain, R as the polymer coil radius, and a the monomer unit size. We consider the free energy F as composed of two main contributions: F_{el} that accounts for the elongational entropy of the chains and F_{mix} that accounts for the interaction of the monomer units with the solvent and with the other monomer units. In this case, Halperin *et al.* have shown that:

$$F = F_{el} + F_{mix} \tag{28}$$

$$\frac{F_{el}}{k_B T} = \alpha^2 - \log(\alpha) \tag{29}$$

$$\frac{F_{mix}}{k_B T} = \int_{coil} c + \frac{1}{2}\nu a^3 c^2 + \frac{1}{6}\omega a^6 c^3 \tag{30}$$

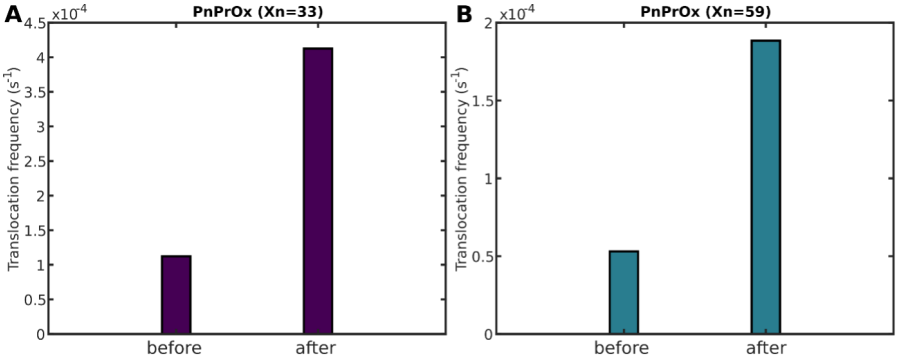

Figure 34: Comparison between the averaged translocation frequency before and after local heating. Using a fluorescent lamp, we were able to heat the membrane sufficiently locally to open the nanopores and allow transport. We exposed the surface of the membrane visible to the camera to the light source only briefly (2 min), which is already enough to exceed the LCST when we start the experiment at room temperature (20 °C). The translocation frequency was measured before illumination (label 'before') and after illumination by the fluorescent lamp (label 'after'). In all cases, the illumination is off during the frequency measurement. For both the P*n*PrOx ($X_n = 33$) grafting (A) and the P*n*PrOx ($X_n = 59$) grafting (B), the translocation frequency is increased by about 440%.

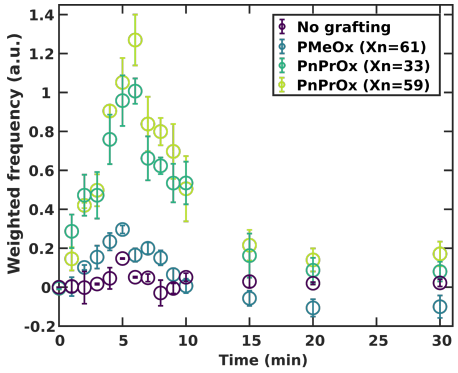

Figure 35: Normalized and averaged translocation frequency as a function of time after heating the system for different grafted pores. At t = 0 the system is shortly heated by inserting high-temperature buffer (70 °C) into the trans chamber. This leads to an increase in temperature of the system, which in turn increases the translocation frequency; after ∼5 min, the system relaxes back to room temperature and the translocation frequency decreases again as a result. We normalized and weighted the translocation frequency by the increase between starting frequency and maximum frequency. Polymer grafting: no polymer grafting (purple), PMeOx $X_n = 61$ (blue), P*n*PrOx $X_n = 33$ (dark green), P*n*PrOx $X_n = 59$ (light green).

where $\alpha = \mathrm{R}/\mathrm{R}_0$ is the expansion factor, R is the coil radius of the grafted polymer, R_0 is the radius of the ideal coil (i.e., in theta solvent), c is the monomer units concentration, ν is the second virial coefficient and ω is the third virial coefficient.

In our case where the polymer exhibits an LCST, the second virial coefficient ν is negative for low temperature and positive for high temperature, i.e. it changes sign at the theta temperature. In the vicinity of θ, the LCST, ν may be written as:

$$\nu = \nu_0 \cdot \frac{\theta - T}{\theta} \tag{31}$$

In the range of temperatures considered here, the third virial ω can be considered to be constant and positive.

We consider the regime where the chains are grafted in the mushroom regime. In this case, D the grafting distance between to polymer is larger than the coil radius ($D > R$). We obtain after integration of F_{mix} on the volume of the coil:

$$\frac{F}{k_B T} = N + \nu N^{1/2} \alpha^{-3} + \omega \alpha^{-6} + \alpha^2 - \log(\alpha) \tag{32}$$

In order to determine the equilibrium configuration, F is then minimized numerically and the corresponding α^* is measured. The effective radius of the pore R_{eff} is then given by:

$$R_{eff} = R_{pore} - \alpha^* R_0 \tag{33}$$

with R_{pore} the pore radius without grafting.

The frequency of translocation can then be determined with the suction model [241]. In this model, the energy landscape for a tongue of a flexible polymer subjected to flow injection into the pore. It concludes that a critical flow $J_c = k_B T/\eta$ is sufficient to induce the translocation of any given polymer in any nanopore. This flow is determined by the energy balance between the confinement of the polymer necessary to enter into the pore and the driving force induced by the flow of solvent that creates a drag force on the monomers. This critical phenomenon appears as soon as the radius of gyration of the polymer is larger than the pore diameter. Using Poiseuille law it can be associated to a critical pressure P_c. We have shown that in this framework the frequency of translocation for any pressure difference P is given by:

$$f = k \cdot \frac{P}{P_c} \exp\left(\frac{-P_c}{P}\right) \tag{34}$$

where k is a numerical factor determined by the geometry of the nanoporous membrane (pore density, homogeneity). Knowing the hydrodynamical resistance of the pore and the critical flow J_c it can be shown that:

$$P_c = \frac{8 k_B T \cdot L}{\pi R_{eff}^4} \tag{35}$$

with L the thickness of the nanoporous membrane. Combining with the previous expressions it follows that:

$$f = k \cdot \left(\frac{R_{eff}}{R_{pore}}\right)^4 \cdot \frac{P}{P_c^0} \exp\left(\frac{-P_c^0}{P}\left(\frac{R_{pore}}{R_{eff}}\right)^4\right) \tag{36}$$

with P_c^0 the critical pressure without polymer grafting i.e $R_{eff} = R_{pore}$. A numerical solving procedure to determine the frequency of translocation is then achieved for each temperature and various values of ω. The range of ω and ν values were chosen to be compatible with the literature [249]. The other parameters were chosen as: $R_0 = 2.5$ nm, $R_{pore} = 25$ nm, $N = 100$, $a = 0.428$ nm. We observe in each case that the frequency of translocation as function of the temperature presents a sharp transition between no translocation at low temperature to full transmission at high temperature. The sharpness of the transition is dominated by the influence of the third virial coefficient ω that is related to the chemical nature of the monomer (lateral groups).

4.3.10.6 *Molecular weight effect on critical pressure*

We checked the dependence between R_{eff}, the effective radius, and P_c, the critical pressure observed during translocation experiments, with a well-studied, flexible, and hydrophilic polymer (Polyethylene glycol terminated by a thiol function, PEG-thiol, with a molecular mass ranging from 356 Da to 20 kDa). Briefly, polymers were grafted onto the gold surface of the membrane at room temperature in presence of TCEP (5 mM) for 3h. After rinsing with buffer solution, the frequency of translocation was measured as a function of pressure. The resulting frequency versus pressure curves were fitted with the suction model and the critical pressure P_c was extracted for each grafting. The scaling of the radius of gyration of PEG with the molar mass is well established [250]. and can be described as a polymer in good solvent. In each case, R_{eff} was thus determined from a scaling law $R_{eff} = R_{pore} - aN^{0.6}$ with a, the monomer size of PEG and N, the number of monomers. We observed a power law dependence of the critical pressure P_c with the effective radius (predicted as previously from an ideal coil model) with an exponent $\alpha = -3.9 \pm 0.2$. This result, predicted by the suction model, confirms that when grafted with flexible and hydrophilic polymers the energy barrier of translocation through the pore is dominated by the entropic confinement of the DNA molecule.

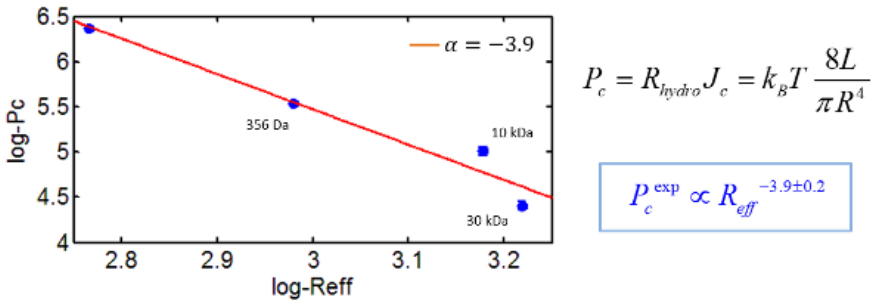

Figure 36: Effect of polymer length on the critical pressure. The critical pressure for DNA translocation through PEG-grafted membrane is shown as a function of the effective radius R_{eff}.

4.3.10.7 *Discussion on thermophoresis, viscosity, and shear effects*

In order to limit the number of possible interpretations of the observed phenomena we detailed here orders of magnitude of some additional phenomena:

Shear stress effects
Shear forces may impact the morphology of the grafted layer and shear may reduce the effective thickness of the grafted layer. Nevertheless, this effect will occur for speed flows, which are much higher than the one of the present study. Indeed, as stated in Ref. [251], Weissenberg number Wi in the range of 0.1 to 1 would be necessary for this effect. In our system we can estimate $Wi = \gamma \cdot \lambda$ with γ the shear rate and, λ the relaxation time of polymer. If we assume, that the shear rate is $\gamma = v/h$ (where v is the speed of the flow and h is the width of the speed gradient) and that the relaxation time is given by the Zimm time of the polymer, we obtain that: $Wi = 0.01 - 0.02$ in our system, which are much smaller than the critical Weissenberg number necessary to induce conformational change of the grafted polymer.

Thermophoresis
The order of magnitude of thermophoresis impact can be estimated from previous studies. A modified Peclet number comparing thermal transport due to thermophoresis and thermal diffusion [252] is given by: Pe(thermophor) = $a \cdot S_T \cdot \nabla T$ where a is the size of the object i.e., the radius of gyration in the case of DNA, ∇T is the temperature gradient between the two compartment and S_T is the Soret coefficient, a constant that has been already measured for DNA [253]. In our case, with $\nabla T = 106$ ° C/m, $a = 0.8$ µm and S_T ∼0.4, we obtain Pe(thermophor) ∼0.32. This demonstrates the small influence of thermophoresis compared to regular diffusion in our system.

Density and viscosity effects
We may assume that the effect of temperature on water would affect its viscosity and density. In the range of temperature where the critical transition is observed this would correspond to a change in viscosity of 13% and change in density of 0.2%. These changes would impact the drag force on the polymer network and DNA by a similar factor. Such a small effect cannot be observed by our experimental design and would lead to a gradual increase of the translocation frequency for an increasing temperature whereas a sharp transition is observed in our work.

4.3.10.8 *Averaging effects on frequency versus pressure and frequency versus temperature curves*

Frequency-pressure curves presented in the article (Figure 26A, 4B), were based on the averaging of data on different experiments. An example of the different individual experiments used for this averaging process is given below for 4 polymers: PMeOx ($X_n = 61$, $X_n = 83$) and P*n*PrOx ($X_n = 33$, $X_n = 59$). Frequency-temperature curves presented in the article (Figure 24B), were based on the averaging of data on different experiments. An example of the different individual experiments used for this averaging process is given below for two polymers: P*n*PrOx ($X_n = 33$) and P*n*PrOx ($X_n = 59$).

4.3.10.9 *SEM and AFM nanopore characterization*

Scanning electron microscopy, SEM
SEM images were performed to ensure that the gold deposition did not obstruct or alter the pore dimensions. Supplementary Figure 39 shows an SEM image of a track-etched membrane after metallization, taken on the electron microscopy platform of the Condorcet building of Paris Diderot University. The membrane was broken by cryofracture (cooled at -80 °C and then fracture) to make the

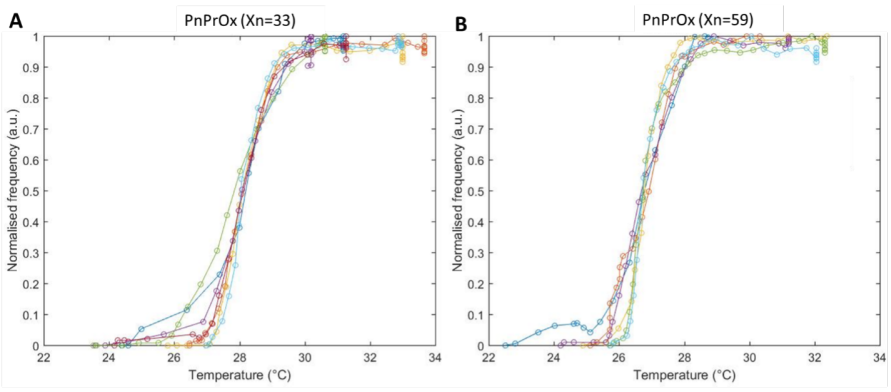

Figure 37: Unaveraged curves representing the normalized translocation frequency of λ-DNA as a function of temperature for different grafted pores: A) PnPrOx ($X_n = 33$) and B) PnPrOx ($X_n = 59$). For A) and B) each color corresponds to a different experiment based on the same grafted membranes. Pore diameter (42 ± 0.5) nm. Applied pressure: 80 mbar.

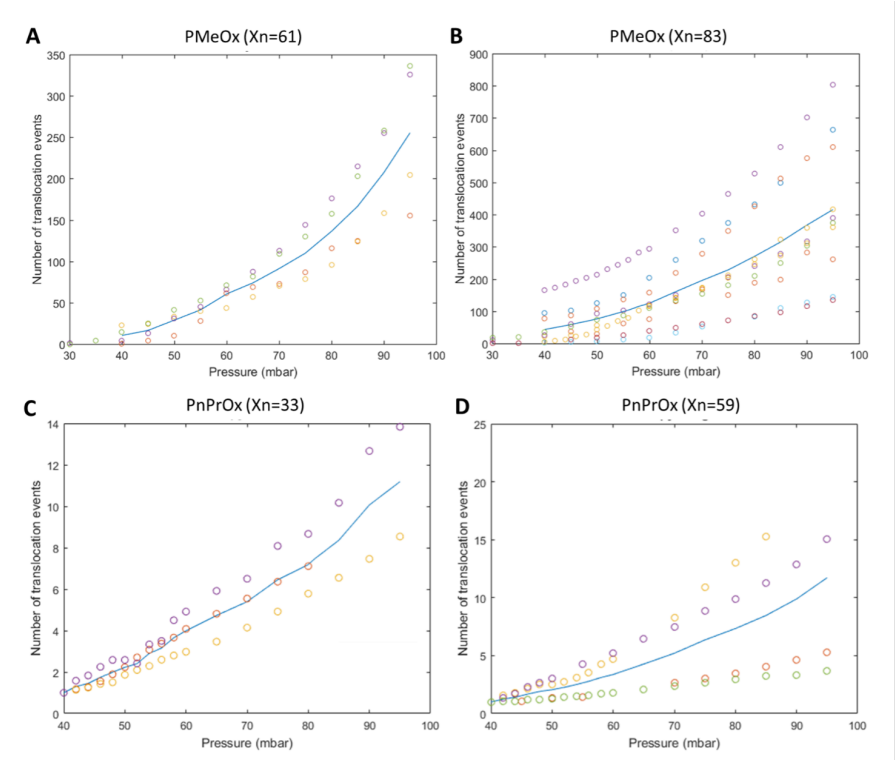

Figure 38: Unaveraged curves representing the normalized translocation frequency of λ-DNA as a function of pressure for different grafted pores: A) PMeOx ($X_n = 61$), B) PMeOx ($X_n = 83$), C) PnPrOx ($X_n = 33$) and D) PnPrOx ($X_n = 59$). For C) and D), the experiments were performed at high temperature (T = 30 °C > LCST). The colors correspond to a different experiment based on the same grafted membranes. The blue curve represents the average. Pore diameter (42 ± 0.5) nm.

cross-sectional image. This can explain the distortions observed. The pores were not obstructed by the gold deposition, and they were cylindrical. The results from the measurement of the pore radius based on SEM images were shown in Table 6. The deviations from the nominal values are in agreement with those given by the manufacturer before gold deposition (Whatman, GE Healthcare).

Nominal pore Ø (+0%, -20%), given by furnisher (Whatman, GE Healthcare) (before gold deposition)	Ø measured by SEM (after gold deposition)
50 nm	(42 ± 0.5) nm
200 nm	(220 ± 1.8) nm

Table 6: Pore diameters determined by SEM measurements. Averaging over 200 pores.

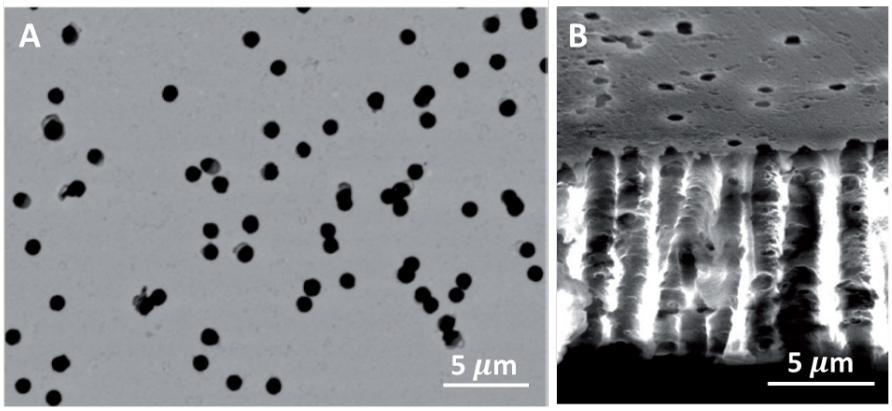

Figure 39: SEM images of 50 nm naked nanopores after gold deposition. A) Top view. B) Cross section view (made by cryofracture).

AFM in liquid environment

To characterize the nanoporous membranes and polymer graftings, we used AFM. The AFM used was Bruker Nanoscope multimode 8 (scan E). In order to be in similar experimental conditions than during our nanopore experiments, we used peak force mode in liquid (tip Scan Asyst Fluid +, $k = 0.759$ N/m). The different nanoporous membranes (naked or grafted) were sticked on a teflon ring with the help of a double-sided tape. The buffer used was Tris-EDTA (pH = 7.5), as described in Material and Methods (Sample Preparation). For P*n*PrOx, tests were realized for a buffer temperature: $T_{room} = 23$ °C. Because of the thermal heating of the membrane by the laser of the AFM system it is not possible to observe directly the process of opening and closing of the pores with this method.

The pore diameter was measured using the toolbox of Image J. Table 7 groups the values for the different data. Supplementary Figure 40 to 41 are examples of AFM images for naked and grafted membranes (with PMeOx and P*n*PrOx). For both types of polymers, we observed that grafted nanopores exhibit a significantly smaller diameter than naked pores. Nevertheless, given the limited resolution of this measurement caused by both experimental and image analysis factors (non-flatness of the membrane, AFM tip dilation at the border of the

pore) it was not possible to extract a precise measurement of the grafted layer in the pore. Beyond this limitation, this methodology validates the presence of polymer grafting in the nanopores.

	Naked (N = 102)	Grafted PMeOx (X_n = 387) (N = 87)	Grafted P*n*PrOx (X_n = 538) T_{room} (N = 64)
Pore Ø	(195 ± 19) nm	(145 ± 30) nm	(147 ± 18) nm

Table 7: Pore diameters determined by AFM measurements. Averaging over N pores.

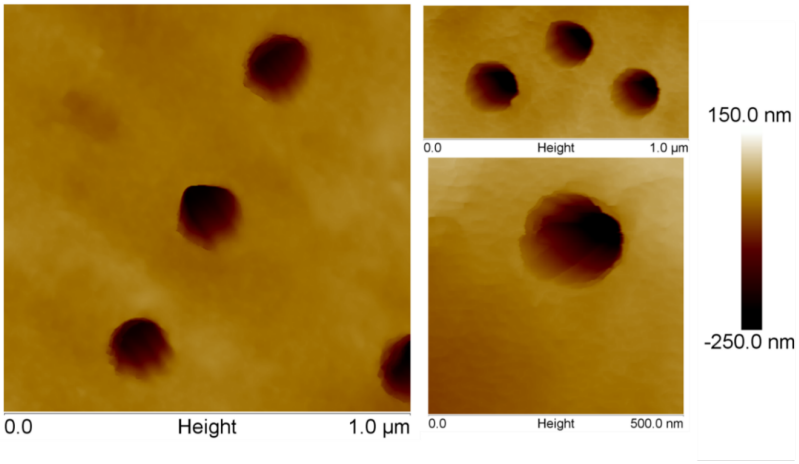

Figure 40: Typical AFM images of naked nanopores (polycarbonate covered with 50 nm-thick layer of gold). Nominal pore diameter 200 nm.

4.3.10.10 *Non-normalized frequency-temperature curves*

Frequency-temperature curves presented in the article (Figure 24B), were based on the averaging of data on different experiments and then on the normalization of the frequency in order to be able to compare the curves between them and with the proposed model. Examples of raw data for different individual experiments are given below for the transport of both λ-DNA and viral capsids.

4.3.10.11 *Stability of the grafting*

To test the stability of the grafting over time, we performed experiments on the same membrane with a time span of about 6 months. During this period, the membrane was stored in water at 4 °C. Typically, the membranes were used during a period of 2 to 4 months.

4.3.10.12 *Video example*

Example of a video corresponding to the translocation of λ-DNA trough 50 nm pores grafted with PMeOx (X_n = 178). Applied pressure: 70 mbar. This is a raw video before any data analysis.

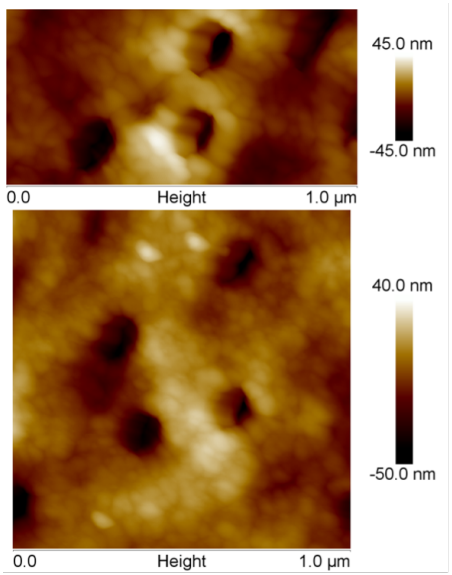

Figure 41: Typical AFM images of nanopores (polycarbonate covered with 50 nm-thick layer of gold) grafted with PMeOx ($X_n = 387$). Nominal naked pore diameter 200 nm.

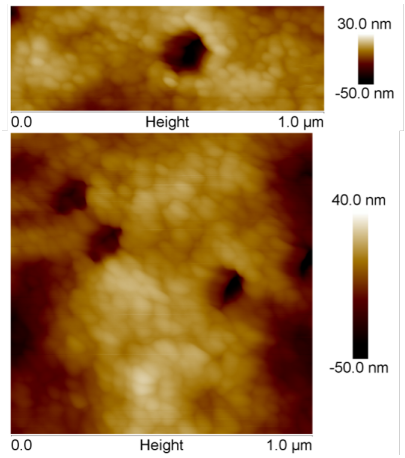

Figure 42: Typical AFM images of nanopores (polycarbonate covered with 50 nm-thick layer of gold) grafted with P*n*PrOx ($X_n = 538$). Nominal naked pore diameter 200 nm.

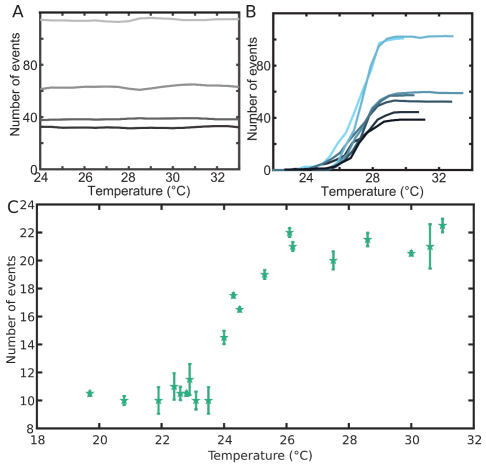

Figure 43: Non-normalized frequency temperature curves. Evolution of the number of events as a function of temperature. A) Translocation of λ-DNA through a naked membrane (pore diameter (42 ± 0.5) nm, applied pressure 80 mbar). B) Translocation of λ-DNA through a grafted membrane with P*n*PrOx (X_n = 33) (pore diameter (42 ± 0.5) nm, applied pressure 80 mbar). C) Translocation of AAV viral particles through a grafted membrane with P*n*PrOx (X_n = 210) (pore diameter (220 ± 1.8) nm, applied pressure: 4 mbar).

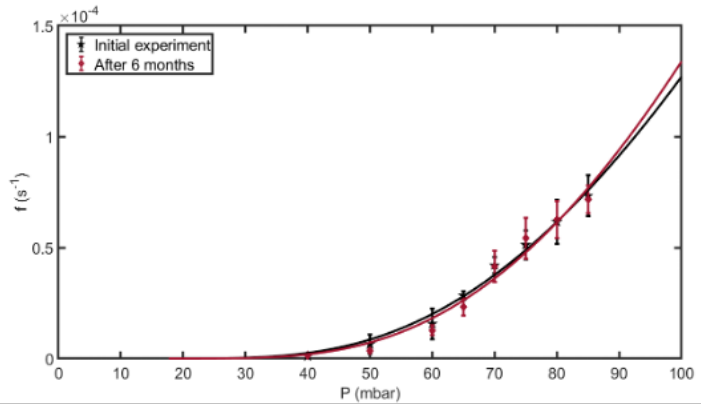

Figure 44: Stability test on grafting membrane. Evolution of the translocation frequency (f) as a function of the applied pressure (P) for λ-DNA through a membrane of 50 nm diameter nanopores and grafted with PMeOx (X_n = 178). The experiment was performed at time zero after grafting of the membrane (initial experiment, in black) and after a period of 6 months (in red) during when the membrane was stored in water at 4 °C. The solid lines correspond to the suction model.

5

AFM TIP RECONSTRUCTION AND IMAGE CORRECTION USING A 3D DNA ORIGAMI FIDUCIAL

5.1 DNA ORIGAMI RULERS

The self-assembly DNA origami technique – introduced in Section 2.2.2 – is a bottom-up nanofabrication approach, which is based on the complementarity of Watson-Crick base pairing. The collective behaviour of staple strands binding to the scaffold strand allows the construction of customary designed 2D and 3D nanostructures. Such collective phenomena are also closely related to the phenomenon of phase transitions. It is a characteristic feature of phase transitions that at the transition, properties of the system become independent of the microscopic details of the system and a collective behaviour arises [33, 254]. In this sense, the assembly of DNA origami from a mix of DNA strands to an compound structure, can also be seen as a phase transition.

Using the robust, effective, and flexible DNA origami technique, various nano-objects can be assembled in precise and predefined patterns [96]. One application of this versatile technique is DNA origami nanorulers, nanometer-sized reference structures built to check the achievable resolving power of a microscope or to estimate the size of observed structures in specimens, making them valuable training and test samples for a broad range of setups. They allow to demonstrate the capabilities of various biophysical and nanotechnological methods and, in addition, for objective characterization of different imaging techniques and experimental comparability between laboratories and instruments. In recent years, such DNA origami nanorulers have been developed for a variety of microscopy methods, including optical microscopy, electron microscopy, and AFM. To do so, the unique properties of DNA origami, including atomic precision, bio-compatibility, reproducibility, and designability, are used to generate point light sources, brightness references, nanophotonic test structures, and alignment tools for various microscopy techniques [255].

Over the last years, many advances have been made in the field of super-resolution microscopy [155, 157–159, 258–265]. Today, it is possible resolve even distances far below the Abbé limit, resulting in high-resolution images of biological and non-biological nanosystems. Nevertheless, in addition to the technical advances in the field, measures for objective characterization of fluorescence imaging techniques are needed to ensure not only high-resolution, but also high-precision results of these imaging techniques. DNA origami nanorulers meet these requirements and thus enable realistic replication of various microscopy experiments. For example, they can help distinguish between two point light sources as required by established resolution criteria. In addition to being able to quantitatively characterize microscopy techniques, DNA origami nanotubes have become a positive control, calibration tool, and practice sample in super-resolution microscopy [255]. DNA origami structures used as reference systems for fluorescence microscopy are usually equipped with staple strands modified with markers (e.g. fluorescent dyes or nanoparticles). Since the precise position of each staple strand in the DNA origami structure is well-known, also the exact position of the marker is known, making DNA

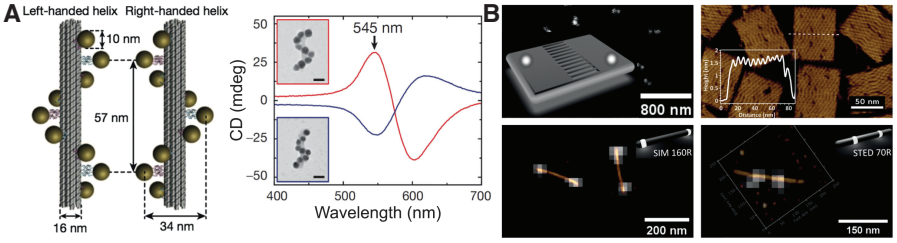

Figure 45: DNA origami nanorulers. (a) Left: 24-helix bundle DNA origami with gold nanoparticles (left- and right-handed nanohelices). Right: corresponding circular dichroism (CD) spectra of left-handed (red) and right-handed nanohelices (blue). The insets depict TEM images of the corresponding nanostructures (scale bars are 20 nm) [256]. (b) Top left: Sketch of a rectangular DNA origami (GATTA-AFM) with design-positions for the two fluorophores. In the background is a STED image of the corresponding nanotubes. Top right: fast amplitude modulation AFM topograph of the DNA origami lattice structure (z-range: 2 nm). Bottom: Optical correlation of sequentially acquired STED and AFM images of two different nanorulers (GATTAquant GmbH) with corresponding sketches [257]. Figure taken from Ref. [255].

origami nanorulers atomically precise measuring rulers for a wide variety of imaging methods (Figure 45) [255].

5.2 AFM TIP DECONVOLUTION AND BLIND TIP RECONSTRUCTION

Also for scanning probe microscopy techniques like AFM, nanorulers can be used as helpful reference structures for quantitative AFM analysis, for example to test and optimize the achievable resolution under various imaging conditions [257]. However, unlike optical microscopy imaging techniques, scanning probe microscopy techniques must account for an additional source of error, the finite size of the tip used as a probe to scan over the sample. Since scanning probe microscopy tips are not infinitely sharp, the resulting images are only approximations of the specimen surface. These tip-induced distortions are significant when the size of the features is comparable to the tip size, hence particularly for small objects.

To correct for these tip-induced distortions, a treatment of the interaction between tip and surface as a geometric exclusion can be made. In other words, an estimate of the tip geometry as accurate as possible is needed, to reduce the limitations of a finite size tip. This estimate can subsequently be used to reconstruct the true specimen shape from its measured image. There have been many different approaches to estimate the tip geometry, one of the most robust algorithms is called blind tip reconstruction (Figure 46). In this method, an outer bound on the tip geometry is determined from an image of an object without a priori knowledge of the object's actual geometry [266].

In AFM imaging, a nanometer-sized tip is moved over the sample surface to create a height image of this surface. Mathematically, the tip-surface interaction

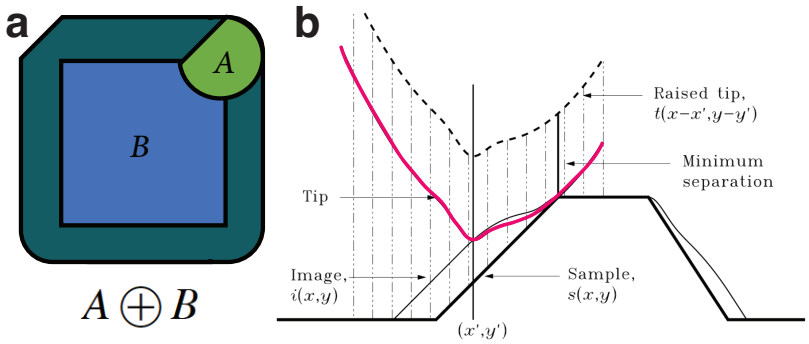

Figure 46: (a) Basic principle of a dilation of two objects A and B. (b) AFM topographic imaging. The AFM tip approaches the specimen surface until it makes contact at one or more points. Once in contact, the position of the tip apex determines the image height. Mathematically, the AFM image can be described as a dilation of the tip with the surface. Figure taken from Ref. [266]. Courtesy of NIST.

can be described as a dilation (Figure 46). A dilation of two sets A and B, with b element of B and a element of A, is defined as

$$A \bigoplus B = \bigcup_{b \in B} (A + b) \tag{37}$$

Geometrically, this can be thought of as A being centered over each b in B. Then the area swept by A is the dilation $A \bigoplus B$. So the top of the dilation $T[A \bigoplus B](x, y)$ is then accordingly the maximum of the two tops ranging over all (u, v) in the domain of the function.

$$T[A \bigoplus B](x, y) = \max_{(u,v)}[a(x - u, v - y) + b(u, v)] \tag{38}$$

The dilation can be translated into AFM imaging as depicted in Figure 46. If $i(x, y)$ is the function describing the image area, $s(x, y)$ the function of the sample, and $t(x, y)$ the function describing the tip, when the tip is shifted from (x, y) to the point (x', y'), the shifted tip is described by $t(x - x', y - y')$. The tip is positioned above the specimen surface and then lowered until it gets in contact with the surface at one or more points. So the amount it must be lowered is equal to the minimum distance between the tip and the sample surface and the apex marks the height of the image at (x', y'):

$$i(x', y') = -\min_{(x,y)} [t(x - x', y - y') - s(x, y)] \tag{39}$$

Since $-\min[a] = \max[-a]$ and with a change of variables, $x \equiv x' - u$ and $y \equiv y' - v$, this equation can be rewritten as

$$i(x', y') = \max_{(u,v)} [s(x' - u, y' - v) - t(-u, -v)] \tag{40}$$

By then defining the new function, $p(x, y) \equiv -t(-x, -y)$, which can be seen as a reflection of the tip through the origin, Equation 40 becomes

$$i(x, y) = \max_{(u,v)} [s(x - u, y - v) + p(u, v)] \tag{41}$$

By comparing this to the definition of a dilation (Equation 38), it ultimatively follows that

$$I = S \bigoplus P \tag{42}$$

So AFM imaging can indeed be described as a dilation of the specimen surface by the AFM tip.

In the following publication, I will apply the mathematical concept of blind tip reconstruction in order to characterize the used AFM tip and subsequently use this knowledge to reconstruct the AFM image. To this end, I will present a newly developed type of DNA origami nanoruler, namely a 3D DNA origami fiducial marker, which can be used as a reference system for AFM tip characterization and image reconstruction. The fiducial is designed to have very sharp features and heights comparable to a wide range of biological and non-biological nanostructures to make it an ideal system for blind tip reconstruction. Because the used design is based on DNA origami technique, the fiducial exhibits very sharp edges, which make tip characterization and image reconstruction more precise and accurate as compared to state-of-the-art tip characterizers. In addition, I will demonstrate that the fiducial can be co-deposited with other samples, which allows for *in situ* tip characterization. Thus, tip damage and degradation typical of *ex situ* characterizers are avoided and adaptive evaluation when the tip shape changes during scanning is made possible. The fiducial can be co-deposited with biological macromolecules and synthetic colloids, on a variety of surfaces, and from a wide range of aqueous solutions. For the broad spectrum of samples studied, the corrected images yield smaller and narrower width distributions than the uncorrected images, proving the tremendous versatility of this method. Taken together, this new DNA origami fiducial structure enables accurate AFM tip characterization and image reconstruction, is easy to use, provides reliable and quantitative results, and is widely applicable, which makes it a new useful tool for high-resolution AFM imaging.

5.3 DNA ORIGAMI FIDUCIAL FOR ACCURATE 3D AFM IMAGING

DNA origami fiducial for accurate 3D AFM imaging

By

Pauline J. Kolbeck[1,2,3], Mihir Dass[1,2], Irina V. Martynenko[1,2,*], Relinde J. A. van Dijk-Moes[3], Kelly J. H. Brouwer[3], Alfons van Blaaderen[3], Willem Vanderlinden[1,2,3], Tim Liedl[1,2], and Jan Lipfert[1,2,3,*]

[1,2] Department of Physics and Center for NanoScience, LMU Munich, Amalienstrasse 54, 80799 Munich, Germany
[3] Department of Physics and Debye Institute for Nanomaterials Science, Utrecht University, Princetonplein 1, 3584 CC Utrecht, The Netherlands
[*] Corresponding authors

published in

ACS Nano Letters (2023), Vol. 23, No. 4, 1236-1243

My contribution to this publication was co-designing the project, planning and performing AFM measurements, analyzing the resulting data, and writing the manuscript with input from all authors.

5.3.1 *Abstract*

AFM is a powerful technique for imaging molecules, macromolecular complexes, and nanoparticles with nanometer-resolution. However, AFM images are distorted by the shape of the tip used. These distortions can be corrected if the tip shape can be determined by scanning a sample with features sharper than the tip and higher than the object of interest. Here we present a 3D DNA origami structure as fiducial for tip reconstruction and image correction. Our fiducial is stable under a broad range of conditions and has sharp steps at different heights that enable reliable tip reconstruction from as few as ten fiducials. The DNA origami is readily co-deposited with biological and non-biological samples, achieves higher precision for the tip apex than polycrystalline samples, and dramatically improves the accuracy of the lateral dimensions determined from the images. Our fiducial thus enables accurate and precise AFM imaging for a broad range of applications.

5.3.2 *Introduction*

AFM is a powerful technique to visualize nano- to micrometer-scale structures with sub-nanometer resolution [161]. Consequently, AFM imaging is frequently used in a broad range of applications, ranging from solid-state physics, to nanofabrication, photonics, material science, and the life sciences [268–274]. In particular, AFM imaging has provided unprecedented insights into the structure of biological macromolecules and their complexes [275–282]. For the interpretation and modeling of the imaged structures, high-resolution AFM images that reflect the true sample dimensions are desirable. However, AFM images are distorted due to the finite size of the AFM tip, resulting in a dilation of image features similar to the convolution of optical images by the point-spread-function of the imaging system [272]. In general, as long as the tip is much sharper than the feature under observation, the measured profile will closely resemble the true shape. Yet, if the sample contains features whose aspect ratio is comparable to that of the tip, distortions due to the finite size of the tip become significant. To correct for the distortions introduced by the tip one can, in principle, estimate the tip geometry and use it to correct the image and estimate the true specimen shape [266, 283–285]. Unfortunately, the exact shape of most commercial AFM tips is not precisely known. Moreover, the tip shape is variable, even within the same batch of tips, and can also change during the measurement due to wear or contamination of the tip while imaging.

There are several approaches to determining the AFM tip shape. Villarrubia showed mathematically that the best possible estimate of the tip shape is achieved using a method called 'blind tip reconstruction' [266]. The approach is based on exploiting features of the AFM image as broadened, inverted replicas of the tip. The fidelity and quality of this tip reconstruction depend on the calibration sample containing features with similar or greater sharpness than those of the tip. There are commercially available calibration samples, for example polycrystalline or silicon standards with features sharper than the tip [286] or nanofabricated tip characterizers [287]. Inconveniently, these types of calibration samples must be measured either before or after the actual measurement of interest. In addition, since these types of calibration samples are typically very hard, the shape of the tip is prone to change due to wear when the sample is scanned, which will deteriorate or invalidate the resulting

tip reconstruction [284]. In addition, measuring separate calibration samples cannot correct for changes in tip shape during measurement.

Consequently, it is desirable to use an internal marker, i.e., a reference sample that is co-deposited with the sample of interest. Using an internal reference sample has the advantage that the tip can be characterized during the measurement, which is experimentally convenient and ensures that reference sample and the sample of interest are imaged with identical parameters, since e.g., molecular deformations depend on the AFM imaging mode, the applied force, and the imaging medium. A common internal marker for biological samples is dsDNA [282, 288, 289], since it is easy to prepare and handle, biocompatible, and well characterized. However, using DNA as a reference sample only works well for samples with a maximum height similar to DNA (1-2 nm depending on the measurement method and force), whereas for higher structures the tip is not sufficiently characterized, since the tip reconstruction requires calibration features of the same height as the sample of interest. Another choice for internal, non-destructive markers are virus particles, e.g. the rod-shaped tobacco mosaic virus (TMV) [290], or inorganic nanoparticles [291, 292]. However, these are significantly higher than many biologically relevant samples and do not exhibit sharp features, which limits the quality of a blind tip reconstruction.

To overcome these limitations, we present a DNA origami fiducial that provides a 3D reference sample for AFM tip reconstruction with sharply defined steps of different heights and a height profile well matched for use with a broad range of macromolecular complexes (up to 18 nm). The DNA origami technique enables the self-assembly of large numbers of identical nanostructures at the molecular scale [95, 96], with customized geometry and almost atomistic structural detail [293, 294]. The resulting nanostructures have been shown to be robust and stable in a variety of conditions and are used in a large range of applications [295–302]. In particular, DNA origami structures have been used as molecular rulers [255] for fluorescence [303, 304] and super-resolution microscopy [305]. For AFM imaging, a single-layer rectangular sheet DNA structure has been used as a size reference and positioning platform [297, 306, 307]. Yet, the previous structures are not suitable for tip characterization because of their low height and lack of sharply defined features in the z-dimension.

Our DNA origami fiducial combines several characteristics that make it well-suited for blind tip reconstruction: the structural features of DNA origami structures have been characterized with high resolution, its designed structure contains flat faces in the x-y direction and sharp edges in the z direction, creating a four-step staircase from 1 – 2 to 15 – 20 nm, well-matched to typical macromolecular complexes. The fact that it consists of DNA makes it fully biocompatible and enables straightforward surface deposition alongside other biological macromolecules. In addition, we show that our fiducial can be deposited on various surfaces including bare mica, poly-L-lysine (PLL)-coated mica, and aminopropylsilatrane (APS)-coated mica and imaged both dry and in liquid. Taken together, our fiducial enables straightforward AFM image correction for a wide range of nanostructures.

5.3.3 *Results*

5.3.3.1 *Design of the DNA origami fiducial structure*

We designed the staircase-like nanostructure built of eight layers of parallel helices arranged on a square lattice [293, 308] (Figure 47a and Supplementary Figure 52). The designed length (L1) of the structure is 200 base pairs, the

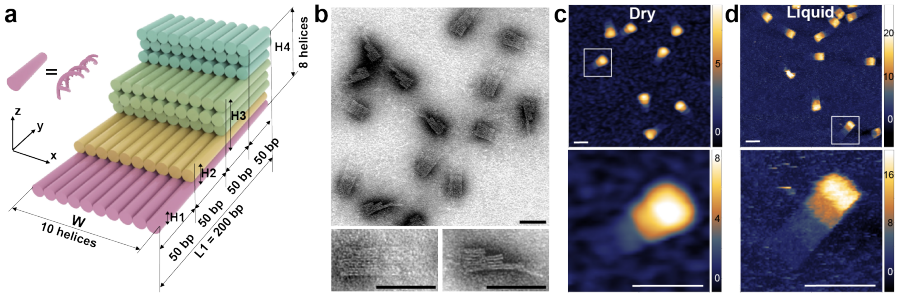

Figure 47: Design of the DNA origami fiducial structure and visualization by TEM and AFM imaging. Design of the 3D DNA origami structure used as a fiducial for AFM imaging. a) Schematic of the designed 3D structure including the design dimensions. The colors represent the different levels. b) Negative-stain TEM images of the fiducial structures confirm the correct assembly and dimensions (a detailed dimension analysis is shown in Supplementary Figure 53). The lower images are zoom-ins of two exemplary structures. c) AFM height image of the fiducial structures obtained by imaging on APS mica after drying. The upper and lower image both have a resolution of 0.5 pixel/nm. The lower image is a zoom-in of the upper image (white box). d) AFM height image of the fiducial structures obtained by imaging on APS mica in liquid. Both images have a resolution of 1 pixel/nm. The lower image is a zoom-in of the upper image (white box). The scale bars in all panels are 50 nm. The z-ranges are indicated in nm by the scale bars on the right.

maximum height (H4) is eight helices and the width (W) ten helices. For the design purposes, we model DNA helices as a cylinder with a diameter of 2 nm (helix diameter in B-form DNA is 2 nm) and a length of 0.34 nm per base pair. Using these parameters and assuming close packing, the approximate size of the designed structure is $68 \times 20 \times 16$ nm^3 (L1 $\times$ W $\times$ H4).

We vary the number of DNA helices in the layers to obtain four discrete steps with equal areas and heights of one, two, five, and eight helices. Therefore, the fiducial structure features different heights between 2 nm and 18 nm, which cover a height range suitable for a broad range of samples, including other DNA origami structures [293, 309, 310] and biological samples [279, 282, 311–313]. Critically, the structure provides sharp and defined vertical edges, which is desirable for a reliable AFM tip estimation via blind tip reconstruction.

5.3.3.2 *Confirmation of correct folding and visualization of the fiducial structures*

We folded the fiducial structures in Tris/EDTA/$MgCl_2$ buffer, purified excess DNA staple strands, and imaged them with negative-stain TEM (Figure 47b).

The fiducial structures appear as rectangular four-"stair" structures with visible striations running along the length of the fiducial, confirming the direction of the DNA helices. The observed structures lay in different orientations on the surface, while defective or deformed fiducials were not observed, which confirms successful and high-yield assembly of our fiducial structures. Using the TEM images, we analyze the dimensions of the fiducial structures (Supplementary Figure 53) and find L1 = (71.7 ± 3) nm, H4 = (19 ± 1.2) nm, and W = (23 ± 1.2) nm, indicating an effective diameter of the DNA helices of (2.3 ± 0.1) nm (Table 8). The effective diameter of DNA helices in 3D DNA origami may vary significantly depending on the DNA origami design, type of packing of the adjacent helices in lattices, number of connecting crossovers and position of nicks [314–316]. In addition, the spacing of helices depends on solution conditions, like pH, temperature, and in particular ion concentration, as the highly negatively charged helices tend to repel each other electrostatically [78] resulting in "swelling" of the structures [314, 315]. Our value from TEM analysis is in good agreement with the value determined previously under similar conditions for a multi-layer origami also by TEM (2.25 nm) [316] and is close to but slightly smaller than the values determined by small-angle X-ray scattering (SAXS) in free solution (∼2.7 nm) [315] and cryo-EM structure modeling (∼2.6 nm) [317].

Next, we imaged the fiducial structures by AFM both *in situ* (i.e., fully hydrated under buffered solution) and after drying in air. For dry AFM measurements (Figure 47c), we investigated different surface deposition strategies: bare mica, APS mica, and PLL mica. All surface deposition strategies result in overall similar images, however, with slight differences in the exact dimensions (Supplementary Figure 54). Notably, almost all fiducials have the expected shapes and are oriented with their large flat face on the substrate's surface, exposing the staircase feature to the AFM tip, which is also the preferred orientation for our purposes (Supplementary Figure 54d). The heights of the steps are almost a factor of 2 lower compared to the heights obtained via TEM (Supplementary Figure 55 and Table 8), which is expected for dry AFM measurements [318]. Furthermore, it is apparent from the AFM images that the lateral x-y dimensions are distorted, in particular the higher features of the staircase appear wider than the lower features (Figure 47c), which is expected due to the finite size and conical shape of the tip. In AFM images obtained in liquid (Figure 47d), we see different orientations of the fiducial structure on the surface, however the flat side of the staircase is still attached to the bottom most frequently (Supplementary Figure 54d). Compared to the dry measurements, the structures are significantly higher and appear less distorted, resulting in dimensions closer to those measured in the TEM images. Overall, the images obtained in liquid appear "crisper", with higher resolution, which is likely due to the lower interaction forces between the tip and the sample [163, 283].

5.3.3.3 *Fiducial structures enable AFM tip characterization via blind tip reconstruction and subsequent correction for the finite AFM tip size*

To test the performance of our DNA origami fiducial structure for estimation of the 3D shape of the AFM tip during measurement, we deposited DNA origami fiducial structures on APS mica and imaged a large field of view (Supplementary Figure 54c). We then use the features of the DNA origami

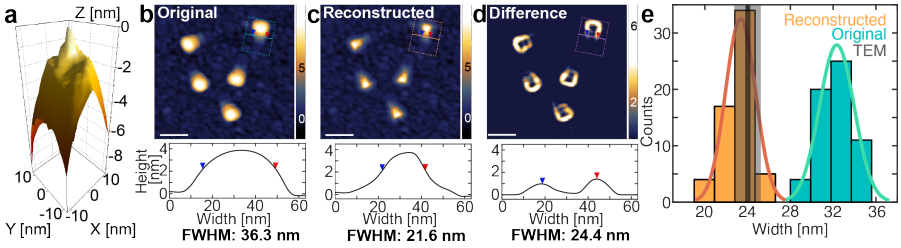

Figure 48: AFM tip characterization and finite tip size correction using the fiducial. a) Estimate of the AFM tip shape obtained by blind reconstruction using the image shown in Supplementary Figure 54c. b) Top: AFM height image of the fiducial structures on APS mica imaged dry with a resolution of 1 pixel/nm. Bottom: height profile of one exemplary molecule, averaged along the fiducial's long axis (as indicated in the AFM image). Arrows indicate the full width at half maximum (FWHM) [319]; the apparent width is significantly larger than the expected width from the design of ∼22.5 nm and the width measured in negative stain TEM, (23.0 ± 1.2) nm. c) The same image as in panel b after reconstruction based on the tip shape in panel a from blind tip reconstruction. The apparent width now is much closer to what is expected from the design. d) Difference image visualizing the effect of image deconvolution. Scale bars are 50 nm and z-ranges are indicated in nm on the right. e) Width distribution from AFM images before (turquoise) and after (orange) image reconstruction. The solid lines are Gaussian fits. The width of (32.3 ± 1.6) nm (mean ± std) is corrected to (23.3 ± 1.4) nm after correcting for the finite tip size. The corrected value is in excellent agreement with the designed width and the width measured in negative stain TEM indicated by a dark gray vertical line and std in light grey (see Table 8 for a detailed dimension comparison).

fiducials to perform blind tip reconstruction following the protocol of Villarrubia [266] implemented in the image analysis software SPIP or Gwyddion (Figure 48a; see Supporting Information for details, including an example image and step-by-step instructions on how to perform the image reconstruction). We note that the blind tip reconstruction does not require exact knowledge of the reference structure shape, but only requires the fiducial to have sharp and high enough features. In a next step, we use this tip estimate to correct a zoom-in of the same AFM image scanned with the same tip (Figure 48b,c). To assess the effectiveness of this method, we determine the width of the fiducial structure before and after correction and find that the width is reduced from 32.3 nm to 23.3 nm (Figure 48e), which is much closer to the width of the origami design (Figure 47a) and the width measured in TEM images (Supplementary Figure 53). To highlight the finite tip size correction, we also calculate a difference image of the corrected image and the original image (Figure 48d), which shows that especially the widths of the higher steps of the staircase are significantly overestimated in the original image. We note that while the tip size correction procedure does reduce the measured width of the structures imaged in liquid, the final size is still wider than what is observed from corrected AFM images in air or from TEM imaging, but in agreement, within experimental error, with the helix spacing from SAXS (∼2.7 nm) [314,

315] (Table 8). The difference in observed lateral width per helix, (2.33 ± 0.14) nm vs. (2.88 ± 0.29) nm/helix after tip shape correction for images in air and in liquid, respectively, is consistent with the view that origami structures swell in solution, due to electrostatic repulsion [314, 315].

5.3.3.4 *Evaluation of the number of fiducial structures required for reliable tip reconstruction*

We next investigate how many fiducial structures are sufficient to get a good estimate of the AFM tip shape. From an image with 114 fiducial structures in total (Figure 49a), we selected between 1 and 100 structures for the blind tip reconstruction. For each number of structures, we randomly selected (with

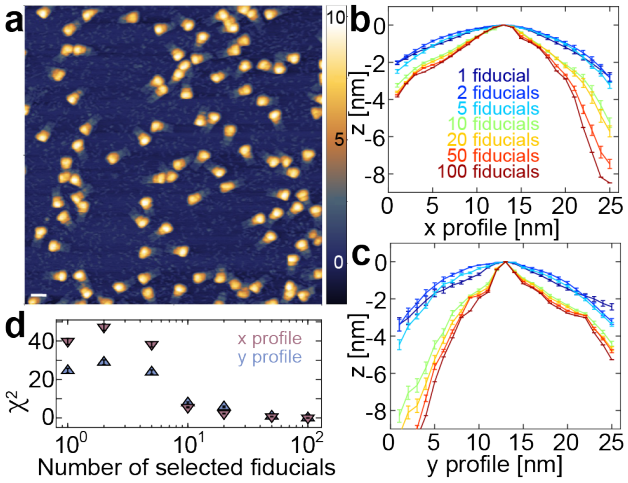

Figure 49: AFM tip characterization using different numbers of fiducials. a) AFM height image of fiducial structures (114 in total) imaged in dry AFM mode on APS mica with a resolution of 1 pixel/nm. The scale bar is 50 nm and the z-range is indicated in nm on the right. b) Estimate of the AFM tip shape x-profile obtained by using between 1 and 100 fiducials for the blind tip reconstruction in the image shown in panel a. For each graph, 20 sets of fiducials were randomly selected, with repeats. c) AFM tip shape y-profile, analogous to panel b. d) χ^2 of the x- and y-profiles shown in panels b and c as a function of the number of selected fiducials compared to the estimate using 100 fiducials with $\chi^2 = \sum_i \frac{(profile_i - profile_{100})^2}{profile_{100}}$. The symbols and error bars are the mean ± std over the 20 sets of randomly chosen fiducials. Error bars are smaller than symbols in some cases.

repeats) 20 sets of fiducial structures as inputs for the tip reconstruction. The resulting x- and y-profiles of the estimated tip shape (Figure 49b,c) converge towards the final tip shape result (100 fiducial structures, dark red line) for ≥10 fiducials (Figure 49d). The results suggest that using a minimum of 10 fiducials for blind tip reconstruction is sufficient for an acceptable tip estimate, for example for a 1×1 µm^2 image this requires a fiducial concentration of ∼1 nM.

5.3.3.5 *Comparison of tip characterization using our fiducial or a polycrystalline sample*

Having established an effective method of finite-size tip correction using a DNA origami fiducial structure, we compare our method to correction using an external polycrystalline tip characterization sample (PA01 AFM Tip Evaluation Sample, NanoAndMore GmbH, Germany). We characterized five different AFM cantilevers (FASTSCAN-A, Bruker, USA; which are used throughout the study) both using our fiducial as well as a polycrystalline sample (Supporting Figure S5). Interestingly, we find that for a sharp tip (Supporting Figure S5a–c) we get an extremely good estimate of the very edge of the tip when using the DNA fiducial, almost identical to the vendor specifications and better than the estimate obtained with the polycrystalline sample. The advantage of the polycrystalline sample is that it can characterize a larger z-range of the tip (20 – 30 nm instead of 5 – 10 nm for the fiducial sample). For a contaminated or blunt tip (Supporting Figure S5d,e), both samples give equally poor results. The results highlight significant tip-to-tip variation even for fresh tips from the same batch. While the polycrystalline sample has the advantage of presenting features with a greater range of heights, for the height that is accessible with our DNA origami fiducial, the DNA fiducial provides a higher-resolution tip reconstruction.

5.3.3.6 *Co-deposition of fiducial structures allows reconstructing the size of a 24-helix bundle DNA origami structure*

We next test the application of our fiducial *in situ* by co-deposition with another structure of interest. We deposited an equimolar mixture of the fiducial sample and a 24-helix bundle DNA origami (24-HB; Figure 50a). In a 1×1 μm^2 image (1024×1024 pixels), we select 25 fiducial structures for blind tip reconstruction to ensure convergence of the tip estimate (Figure 50b,c). We then use the tip to correct the dimensions of the 24-HBs (Figure 50d–f). The width of the 24-HB is (22.1 ± 1.8) nm (mean ± std; Figure 50f) in the original image, which is significantly larger than the expected width from the design of (15.5 ± 1.0) nm. In contrast, in the corrected image, we find a width of (16.3 ± 1.6) nm, very close to the value expected from the design. The results suggest that co-deposition of our fiducial provides a convenient and straightforward way to obtain accurate, high-resolution, tip-corrected images.

5.3.3.7 *In situ image correction for DNA-protein complexes*

To demonstrate the applicability of our method to macromolecular complexes beyond DNA origami, we co-deposit our fiducial with dsDNA and a DNA-interacting protein (IN). We find that the fiducial is bio-compatible and preserves its shape despite the presence of DNA-interacting proteins (Figure 51a). Here again, we observed that the widths of DNA, protein, and protein-DNA complexes are reduced after image reconstruction. As a proof of principle, we compared the DNA width before and after reconstruction and find that it reduces significantly from ∼5.1 nm to ∼2.9 nm (Figure 51b,c), which is much closer to 2 nm, the crystallographic width of dsDNA.

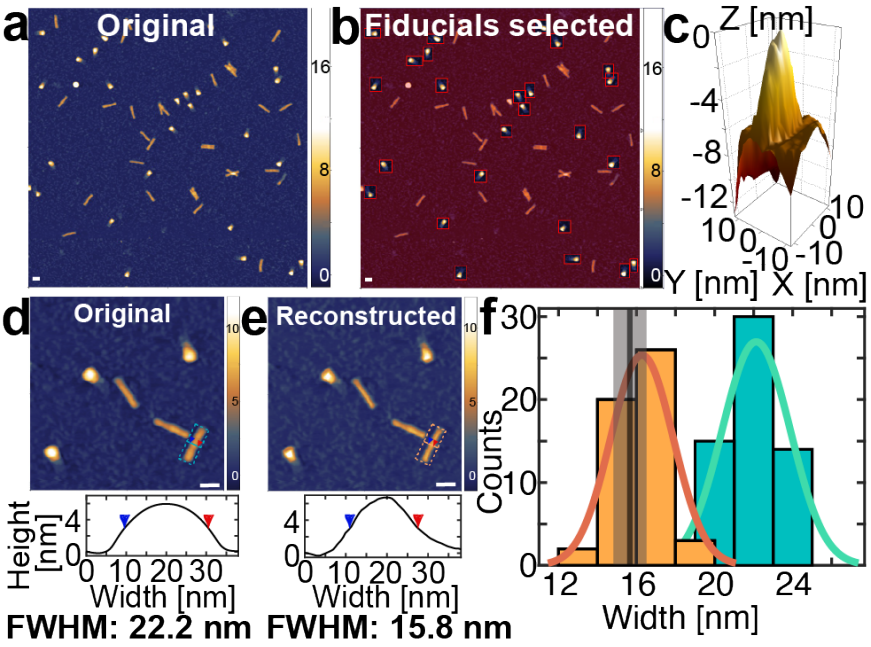

Figure 50: Fiducials enable accurate AFM measurements of a 24-helix bundle DNA origami structure. a) AFM height image of the fiducial structures co-deposited with a DNA origami 24-helix bundle (24-HB) structure, both at a concentration of 1 nM, deposited on APS mica and measured dry with a resolution of 1 pixel/nm. b) Same image as in panel a, with the 25 fiducial structures highlighted by red boxes. The image sections highlighted by the boxes are used for blind tip shape reconstruction. c) Tip shape obtained from blind tip reconstruction using the fiducial samples marked in panel b. d) Top: zoom-in on a different spot of the same sample shown in panel a, the resolution is 2 pixel/nm. Bottom: height profile of the raw AFM image of an exemplary 24-HB. Arrows indicate the FWHM; the apparent width of 22.2 nm is significantly larger than the expected width from the design of ∼15.5 nm. e) Top: the same image as in panel d, after reconstruction based on the tip shape from blind tip reconstruction shown in panel c. All scale bars are 50 nm and z-ranges are indicated in nm on the right. Bottom: height profile of the reconstructed AFM image of the same 24-HB. f) Width distribution from AFM images before (turquoise) and after (orange) image reconstruction. The solid lines are Gaussian fits. The width of (22.1 ± 1.8) nm (mean ± std) is corrected to (16.3 ± 1.6) nm by finite tip size correction. This value is in excellent agreement with the designed width of (15.5 ± 1.0) nm, indicated by a dark gray vertical line and std in light gray.

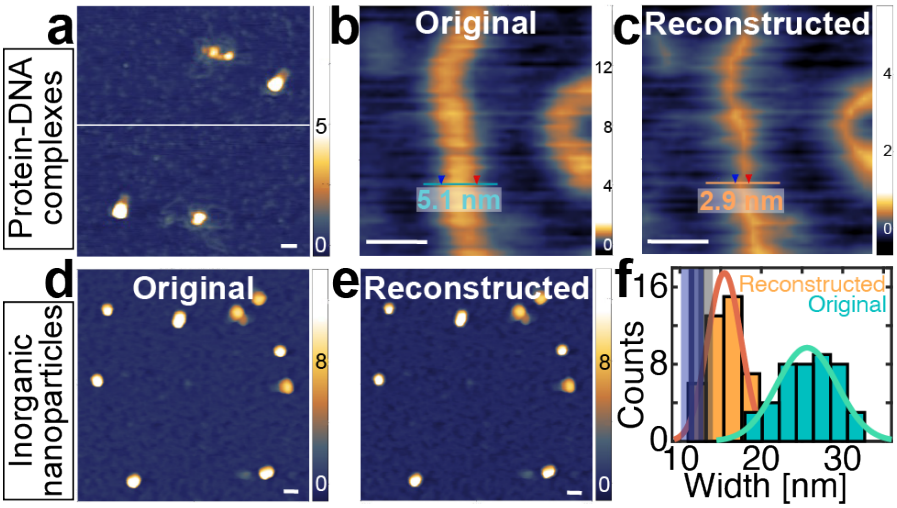

Figure 51: Fiducials enable accurate AFM measurements of DNA protein complexes and inorganic nanoparticles. a) AFM height image of the fiducial structures co-deposited with DNA-protein complexes (DNA length 4.8 kbp; protein HIV-1 integrase) deposited on APS mica and measured dry with a resolution of 0.4 pixel/nm. b) Zoom-in on a different spot of the same sample shown in panel a, the resolution is 1.4 pixel/nm. The apparent DNA width of 5.1 nm is significantly larger than the expected DNA width of 2 nm. c) The same image as in panel b, after reconstruction based on the tip shape from blind tip reconstruction. The DNA width in the reconstructed AFM image is much closer to the expected DNA width of 2 nm. The scale bars are 10 nm and z-ranges are indicated in nm on the right. d) AFM height image of the fiducial structures co-deposited with SiO_2 nanoparticles, both at a concentration of 1 nM, deposited on APS mica and measured dry with a resolution of 1 pixel/nm. e) The same image as in panel d, after reconstruction based on the tip shape from blind tip reconstruction using the co-deposited fiducials. The scale bars are 50 nm and z-ranges are indicated in nm on the right. f) Width distribution from AFM images before (turquoise) and after (orange) image reconstruction. The solid lines are Gaussian fits. The width of (25.6 ± 3.7) nm (mean ± std) is corrected to (15.5 ± 2.1) nm by finite tip size correction. This value is much closer to the AFM imaged height (12.6 ± 1.4) nm (mean ± std), indicated with a dark grey vertical line and the standard deviation in light grey, and also to the width measured in TEM, (11.5 ± 1.2) nm, indicated by a dark blue vertical line and the standard deviation in light blue.

5.3.3.8 *Height and width analysis of inorganic nanoparticles*

Next, we test our fiducial structure for *in situ* image reconstruction of inorganic nanoparticles. We co-deposited SiO_2 nanoparticles with our fiducial. Similar as for the biological samples, the apparent widths of the silica nanoparticles are significantly larger than the widths in the corrected image (Figure 51d–f). After image reconstruction, the width is reduced from (25.6 ± 3.7) nm (mean ± std) to (15.5 ± 2.1) nm, which is much closer to the width measured in TEM images (11.5 ± 1.2) nm (Supplementary Figure 57a,b) and also to the height of the particles measured in AFM, (12.6 ± 1.4) nm (Supplementary Figure 57c,d). After image correction, the AFM-determined width and height measurements and the TEM-derived widths are in overall approximate agreement, as would be expected for spherical particles. The fact that the dimensions from the TEM analysis are still slightly smaller than AFM derived values might be due to the fact that the ultra-high vacuum used during TEM imaging leads to a small reduction in particle size [163]. The remaining small difference between AFM-determined width and height might stem from imperfections in the image correction, from slight compression of the particle by the AFM cantilever, or could be due to the fact that particles are not perfectly spherical and tend to adhere to the surface with their larger side. Additionally, we observed that the width distribution becomes smaller after image reconstruction (Figure 51f) while the height distribution stayed the same within error (Supplementary Figure 57d). The reduction in the variance of the width distribution is likely due to an asymmetry of the tip, such that the widths of the particles are distributed wider in the original image than in the reconstructed image.

5.3.4 *Conclusion*

In conclusion, we have established a method to correct for the finite size of the AFM tip and its specific shape while scanning a sample, employing a DNA origami staircase structure as a fiducial for AFM image calibration. We demonstrate that our fiducial structures are versatile and biocompatible, can be deposited on various surfaces including bare mica, APS mica, and PLL mica, and can be imaged in liquid or dry. This allows straightforward surface co-deposition with samples of interest, and we demonstrate the broad applicability of the method by imaging DNA origami structures, DNA-protein complexes, and silica nanoparticles. In all cases, the blind tip reconstruction using our fiducial allows for subsequent correction of images for finite tip size, which enables much more accurate determination of sample dimensions than uncorrected images. We show that as few as 10 fiducial structures are sufficient for a good tip estimate. Also, we demonstrate that to characterize the very edge of the tip of FASTSCAN-A cantilevers, the fiducial sample gives a better estimate of the effective tip shape than a commercial polycrystalline characterization sample (Supporting Figure S5). In addition, we provide a detailed step-by-step protocol on how to perform the analysis with SPIP or Gwyddion (Methods Section 5.3.9 and Supplementary Figure 58). Taken together, our method enables accurate, straightforward, and user-friendly AFM image correction.

We anticipate many new applications coming within reach by using DNA origami structures as fiducials for 3D AFM image calibration. We note that the design of the DNA origami structure could be altered or extended for specific purposes, for example by addition of additional steps or attachment

of fluorescent dyes. A combination with fluorescent markers has the potential to enable simultaneous use of the fiducial as a tip shape and fluorescence calibration [255, 303–305, 320, 321]. Another research direction would be to go beyond imaging and to use the fiducial as a mechanical stiffness marker to study the compliance of biomolecules to indentation forces [322], e.g. to probe the effects of silicification [323, 324] or other functionalization. Soft biological materials are deformed by interactions with the AFM tip and our fiducial structure could provide a convenient reference to take these effects into account while correcting images. Further, structures on or within the fiducial could be used to quantify and optimize resolution of AFM images, in addition to concurrently correcting the lateral dimensions. We, therefore, anticipate that our fiducial marker will provide a multi-modal calibration platform for a range of applications.

5.3.5 *Author Contributions*

P.J.K. and W.V. designed this study. M.D. and I.M. designed, assembled, and purified DNA origami samples; R.J.A.v.D-M., K.J.H.B., and A.v.B. synthesized and characterized silica nanoparticles; P.J.K. and W.V. performed AFM measurements and analyzed the data. T.L. and J.L. supervised research; P.J.K. and J.L. wrote the manuscript with input from all authors.

5.3.6 *Funding*

This work was supported by the Deutsche Forschungsgemeinschaft (DFG, German Research Foundation) through SFB 863, Project 111166240 A11 and by Utrecht University.

5.3.7 *Notes*

The authors declare no competing financial interest.

5.3.8 *Acknowledgements*

We thank Thomas Nicolaus for laboratory assistance, Diogo Saraiva, Lisa Tran, Steven de Feyter and Aidin Lak for helpful discussions, and Arthur Ermatov for critical reading of the manuscript.

5.3.9 *Materials and Methods*

5.3.9.1 *DNA origami design and assembly*

The DNA origami AFM fiducial structure was designed using caDNAno [294] (design schematics in Supplementary Figure 52). The staircase-like structure consists of eight layers of parallel helices packed on a square lattice. The designed length of the structure is 200 base pairs, the width is ten helices. The number of DNA helices in the layers is varied to obtain four discrete steps with equal x-y areas and heights of one, two, five, and eight helices. Sequences and the caDNAno design of the DNA origami AFM fiducial structure can be found as AFMRuler.xls and AFMRuler.json as a part of the zip archive AFMRuler.zip in the Supporting Information. The x-y dimension of each step in our design

is approximately 17 nm×20 nm (50 base pair × 10 helices), which provides a sufficient number (> 20 points per height plateau) of independent measurement points for calibration [316] and ensures mechanical stability during the AFM measurement. We used the square lattice geometry and corrected the design for internal twist [325] to obtain a flat surface of the 'stairs'.

Design-specific staple strands were purchased from IDT Technologies, the scaffold strand p8634 was produced from M13 phage replication in E. coli. Scaffold strand and staple strands were mixed at 1:5 scaffold:staple ratio with target concentrations of 30 nM and 150 nM (each staple), respectively in 10 mM Tris Base, 1 mM EDTA buffer with 18 mM magnesium chloride (TE/Mg^{2+}). 50 µL volumes of staple/scaffold mixture were heated up to 65 °C for 5 min and annealed from 65 °C to 20 °C at -0.2 °C/min in a PCR machine. The DNA origami structures were purified from excess staples using 100 kD molecular weight cut-off filters (Amicon Ultra-0.5 Centrifugal Filter Units with Ultracel-100 membranes). The 24-helix-bundle (24HB) structure [315] was folded in a similar fashion using the p8064 scaffold strand and purified using the PEG precipitation method adapted from Wagenbauer *et al.* [326].

5.3.9.2 *TEM sample preparation and imaging*

5 µL of sample solution was incubated for 30 s – 5 min, depending on concentration, on glow discharged TEM grids (formvar/carbon, 300 mesh Cu; Ted Pella) at room temperature. After incubation on the grids, the sample was wicked off by bringing the grid into contact with a filter paper strip. Samples containing DNA origami went through an additional staining step with a 2% uranyl formate aqueous solution containing 25 mM sodium hydroxide. After incubating and wicking the sample off, a 5 µL drop of staining solution (2% uranyl formate aqueous solution containing 25 mM sodium hydroxide) was applied to the grid, immediately wicked off, followed by applying another 5 µL drop of staining solution. This drop was allowed to incubate on the grid for 10 seconds and then wicked off. The grid was allowed to dry for 5 minutes before imaging. Imaging was performed with a JEM1011 transmission electron microscope (JEOL) operated at 80 kV.

5.3.9.3 *Synthesis of silica nanoparticles*

Silica particles were synthesized with a one-step synthesis based on previous literature [327, 328]. All glassware was etched of residual silica via a base bath (2 – 3 days in a saturated solution of KOH in isopropanol, rinsed with milliQ water). The particles were synthesized as follows: in a 500 mL 1-neck flask, 181 mg (6 mM) L-arginine (98%, Sigma-Aldrich) were dissolved in 169 mL milliQ water. The mixture was heated to 30 °C and stirred slowly (200 rpm). After 1 h, 11.2 mL (49 mmol) TEOS (tetraethoxysilane; 98%, Sigma-Aldrich) was added slowly via the wall and a two layered system formed (top: TEOS, bottom: water). The reaction mixture was stirred for 1 week to complete the synthesis. The resulting particles were stored at room temperature in the dark and used without further processing.

5.3.9.4 *AFM sample preparation*

For the AFM samples, we deposited 20 µL of a buffered solution (10 mM Tris Base, 12.5 mM MgCl2,1 mM EDTA, pH 8.35; AFM buffer) containing the

fiducial structures (at different concentrations between 1 and 10 nM) either on freshly cleaved bare muscovite mica or on aminopropylsilatrane (APS)-coated mica or poly-L-lysine coated mica. The sample was incubated 5 minutes before washing with 20 mL milliQ water and drying with a gentle stream of filtered argon gas. The APS coating was performed following the protocol from Shlyakhtenko *et al.* [329]. The poly-L-lysine coated mica was prepared as described previously [281] by depositing 20 µL 0.01%-poly-L-lysine on freshly cleaved muscovite mica for 30 seconds and subsequently rinsing the surface with 30 mL of milliQ water before drying with a gentle stream of filtered argon gas.

For the liquid measurements, 2.5 mL of the buffered solution was added to the sample after incubation. For the co-deposited samples, we pre-mixed the fiducial structures with the corresponding sample (at varying concentrations between 1 and 10 nM) prior to deposition in AFM buffer. The samples were incubated, washed, and dried as described above.

For the DNA-protein complex sample, we first mixed linearized plasmid pU3U5 (4.751 kbp; Mini-HIV DNA, see Cherepanov *et al.* [330]) with HIV-1 integrase in sodium buffer (10 mM Tris-HCl, 90 mM NaCl; 5 mM MgCl2) to a final concentration of 1 ng/µL DNA and 1 µM of protein. Next, we added the fiducial structures at a final concentration of 1 nM and deposited 20 µL of the mixture on APS-coated mica. The sample was incubated, washed, and dried as described above.

5.3.9.5 *AFM imaging*

The dry AFM images were recorded in tapping mode at room temperature using the Nanowizard Ultraspeed 2 (JPK, Berlin, Germany) with silicon tips (FASTSCAN-A, drive frequency 1400 kHz, tip radius 5 nm, Bruker, Billerica, Massachusetts, USA). Images were scanned over different fields of view and with various pixel sizes (indicated for each image) with a scanning speed of 5 Hz. The free amplitude varied from 20 to 30 nm. The amplitude setpoint was set to 80% of the free amplitude and adjusted to maintain good image resolution.

The liquid AFM images were recorded in peak-force tapping mode at room temperature, also using the Nanowizard Ultraspeed 2 (JPK, Berlin, Germany) with silicon tips (BL-AC40TS, drive frequency 25 kHz in water, tip radius 10 nm, Olympus, Tokyo, Japan). Images were scanned over different fields of view and with various pixel sizes (indicated for each image). The peak force was set to 200 pN. For some measurements we use an external polycrystalline tip characterization sample (PA01 AFM Tip Evaluation Sample, NanoAndMore GmbH, Wetzlar, Germany) with hard sharp pyramidal nanostructures with base length in the range 50-100 nm and height 50-150 nm, and radius of curvature of the sharpest edges below 5 nm.

5.3.9.6 *AFM image analysis*

For this work, postprocessing of AFM data was performed in the software SPIP (v.6.4, Image Metrology, Hørsholm, Denmark), which has implemented blind peak reconstruction as well as image deconvolution following Villarrubia's protocol [266]. We note that while we used SPIP for all image processing, other AFM post-processing softwares, such as Gwyddion, have also incorporated

blind tip reconstruction routines with implementations very similar to SPIP. Here, we will give detailed instructions for tip characterization and image reconstruction for SPIP and Gwyddion. An example of a fiducial image recorded with a FASTSCAN-A cantilever can be found in Image-Reconstruction-Example-SPIP-Gwyddion.zip as Supporting Data, the resulting reconstructed images are also shown in Supplementary Figure 58.

AFM postprocessing with SPIP

First, the images were flattened (Modify → Global leveling) and line-wise leveled (Modify → Linewise leveling). Next, the tip was characterized via blind tip reconstruction. To this end, we either used the entire image or (in case of co-deposition or contamination of the sample) selected a subset of fiducial structures (General → Area of interest). Next, we used the tip characterization tool (Analyze → Tip) and specified the tip size in x and y as number of pixels (Tip characterization → Size X and Y). For FASTSCAN-A cantilevers, we took the manufacturer's specified tip radius of 12 nm as a starting point for the blind tip reconstruction (for example, for a FASTSCAN-A cantilever with a tip diameter of 24 nm and an image resolution of 1.6 nm/pixel, the tip size would correspond to 15 pixels). We typically used 5 iterations (more iterations did not to improve tip reconstruction in our experience, but could be an option for troubleshooting the procedure, e.g. for a particularly challenging sample). The resulting tip shape was saved (Tip characterization → Save tip) and then loaded (Tip characterization → Load tip) to correct (Tip characterization → Deconvolute) the same or another image scanned by the same tip. Here, too, the tip size had to be adjusted to the corresponding size in pixel so that the resolution is not lost (Tip characterization → Size X and Y). As a useful quality control, SPIP also calculates an uncertainty map. In this map, the areas of the image where the tip did not touch the surface in a single point, but in multiple points (so not with the tip apex but with the side), are highlighted in red, so that, for example, a larger area is shown in red when a blunt tip is used than when the same area was scanned with a sharp tip.

AFM postprocessing with Gwyddion

Gwyddion is an open source software for scanning probe microscopy data visualization and analysis (http://gwyddion.net/). Post-processing of AFM data in Gwyddion works very similarly to SPIP. Tip reconstruction in Gwyddion using the blind tip reconstruction algorithm is described in detail in the Gwyddion online user guide: http://gwyddion.net/documentation/user-guide-en/tip-convolution-artefacts.html. In brief, the images first need to be flattened (Data process → Level → Plane level) and line-wise leveled (Data process → Correct data → Align rows (Polynomial degree 2, Direction: horizontal)). In the case of co-deposition, at least 10 fiducials are selected with one or several masks (Tools → Edit mask (Mode: add selection to mask)). As a prerequisite for blind tip reconstruction, the tip is first modeled (Data Process → SPM modes → Tip → Model tip) using the manufacturer's tip specifications (for example for a FASTCAN-A cantilever, Tip type: pyramid, Number of sides: 3, Tip slope: 15°, Tip rotation: 0°, Tip apex radius: 10 nm). Next, the tip is characterized using the blind tip estimation algorithm (Data Process → SPM modes → Tip → Blind Estimation). The blind tip estimation window opens where the related data (the previously modeled tip) is chosen and the tip size in pixel is specified. The tip size in pixel is given by the resolution (in pixel/nm) multiplied by the size of the tip (in nm; which can be e.g. obtained from the vendor's specifications). The resolution of the image can be viewed in Tools → Statistical quantities. The noise suppression threshold was set to

100 pm, this value strongly depends on the sample and image quality and can be adjusted according to the noise level.

We recommend to first carry out partial tip estimation and to use the result as input for the full tip estimation run. First, partial tip estimation, which uses only a limited number of the highest points in the image, is applied (Blind tip estimation → Run partial), and then full tip estimation (Blind tip estimation → Run full), which uses the entire image. This way, the results of the partial tip estimation are used as a starting point for the full estimation and the speed of the full tip estimation is improved. The tip is saved automatically (after clicking Ok). Next, the estimated tip shape is used to correct the same or another image (Data Process → SPM modes → Tip → Surface reconstruction) - note that the scan pixel size needs to be the same as tip image pixel size (the physical pixel size can be matched manually: Data Process → Basic Operations → Resample → Match pixel size). Also in Gwyddion, a certainty map can be calculated to view the areas that were not scanned by the apex of the tip but with a side of the tip (Data Process → SPM Modes → Tip → Certainty Map). We note, that in our experience the blind tip reconstruction in Gwyddion depends more strongly on the starting values (model tip) than the implementation in SPIP.

5.3.10 *Supplementary table and figures*

Parameter	Design	TEM	Dry AFM	Liquid AFM
Width W	10 helices	23±1.2 nm	32.3±1.6 nm (orig.) 23.3±1.4 nm (recon.)	30.0±2.2 nm (orig.) 28.8±2.9 nm (recon.)
Height H1	1 helix	–	0.65±0.3 nm	0.55±0.4 nm
Height H2	2 helices	5.3±0.8 nm	2.1±0.4 nm	2.0±0.5 nm
Height H3	5 helices	12±1 nm	5.4±0.4 nm	9.4±1.4 nm
Height H4	8 helices	19±1.2 nm	8.0±0.4 nm	15.9±1.1 nm
Interhelical spacing	–	2.3±0.1 nm	1.1±0.2 nm	2.0±0.2 nm

Table 8: Dimension analysis of the DNA origami fiducial structure. Comparison of the design dimensions to the dimensions measured in TEM, dry AFM, and liquid AFM. Not all features were consistently visible in the different techniques and are therefore not listed. For the TEM data, the mean and standard deviation are listed. Details about the analysis and the raw data can be found in Supplementary Figure 52. For the dry and liquid AFM data, Gaussians are fitted to the data (Supplementary Figure 55) and here the mean and standard deviation of the distribution are listed. We note that the height values are averaged over the full width of the structure.

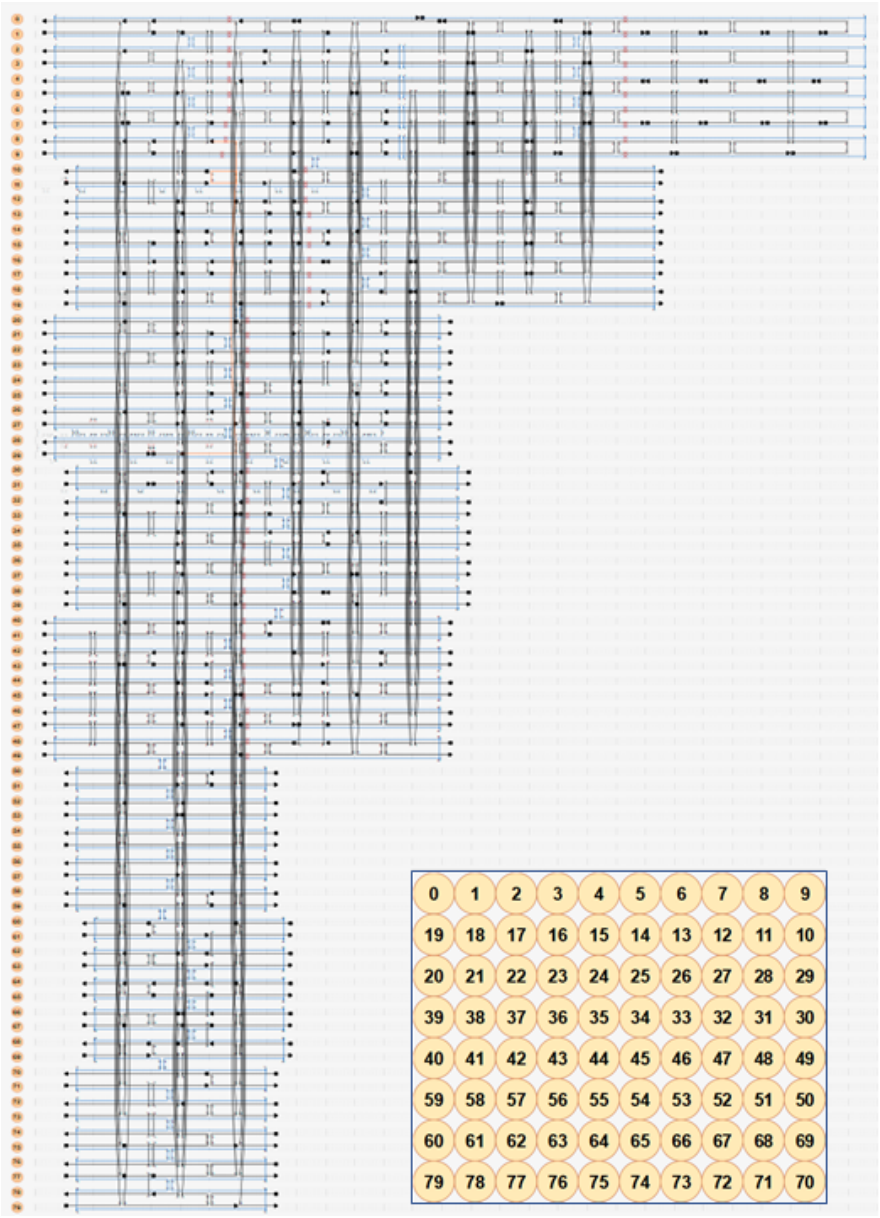

Figure 52: CaDNAno layout of the DNA origami AFM fiducial structure design. The DNA origami AFM fiducial structure was designed using the open-source software caDNAno [294]. The structure consists of four levels, the first two comprising one DNA layer each, the second and fourth three layers each, resulting in a total of eight layers. The DNA helices are arranged in parallel on a square lattice.

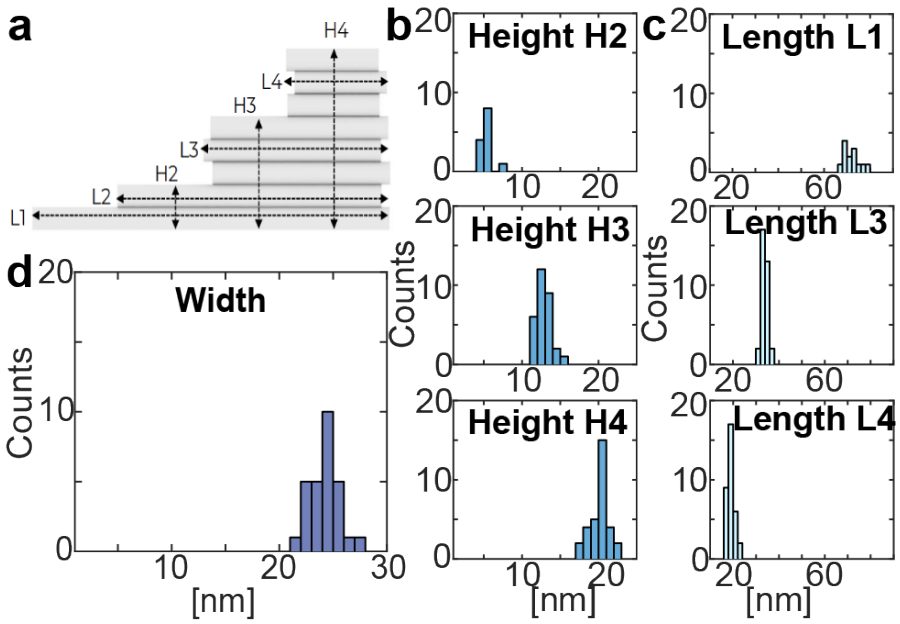

Figure 53: Dimension analysis of the fiducial structures based on TEM images. a) Design of the fiducial structure indicating the design dimensions and labelling of the lengths and heights. b) Height distribution for the 3 highest levels of the fiducial (the lowest level H1 was not visible in the TEM images; see Table 8 for a detailed dimension comparison). c) Length distribution for the levels 1, 3, and 4 of the fiducial (length L2 was not clearly visible in the TEM images). d) Width distribution of the fiducial.

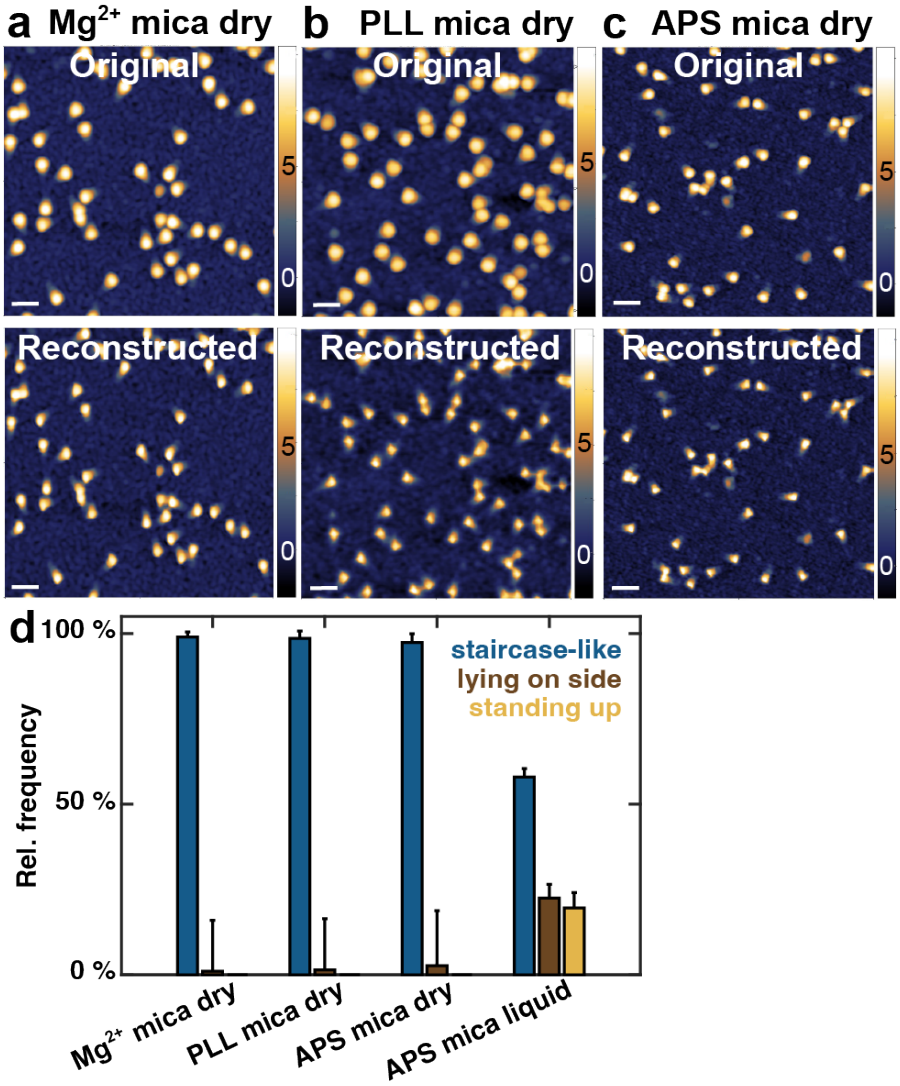

Figure 54: Comparison of AFM images obtained with different surfaces deposition approaches. a) Top: AFM height image of fiducial structures at a concentration of 10 nM deposited on a) Mg^{2+} mica, b) PLL mica, c) APS mica, after drying in air. Bottom: Same images as in top row after reconstruction. The scale bars are 100 nm. The z-ranges are indicated in nm by the scale bars on the right. We note that the variability in image quality visible in the data is mostly due to tip-to-tip variability and not systematically dependent on the deposition method. d) Relative frequency of deposition orientations for Mg^{2+} mica dry, PLL mica dry, APS mica dry, and APS mica liquid. For all tested deposition strategies, the staircase-like orientation is preferred. Only for AFM images acquired in liquid, fiducials lying on their sides or standing upright were also observed in relevant quantities. For all conditions, > 300 fiducials from at least three independent measurements were analyzed. The error bars were obtained from counting statistics.

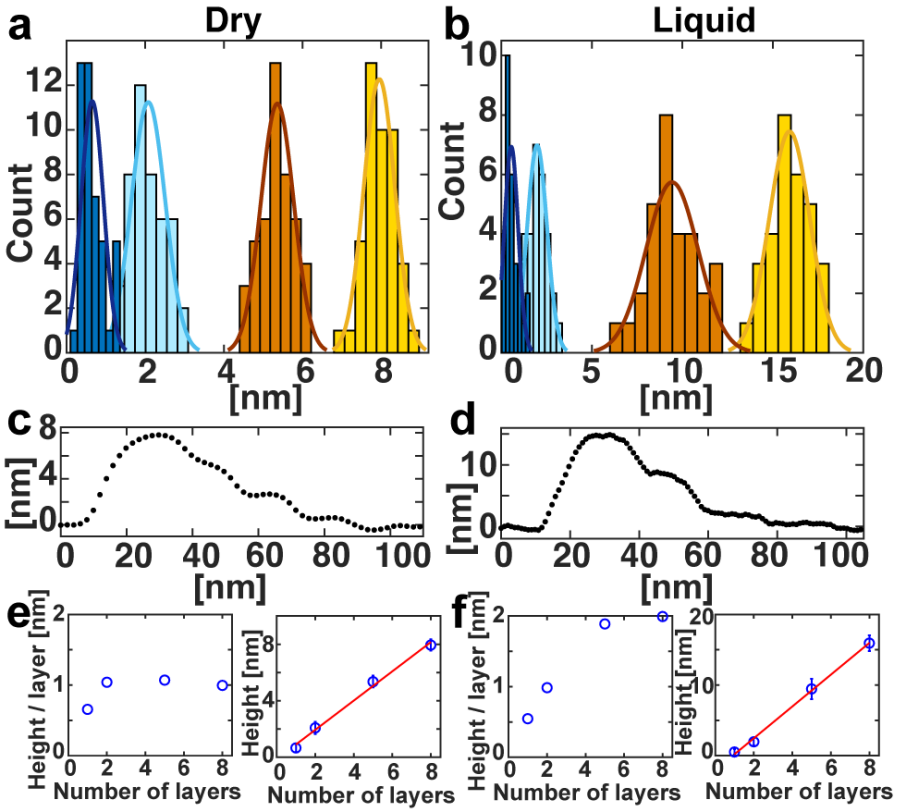

Figure 55: Dimension analysis of the fiducial structures based on AFM images. a) Height distribution for the 4 different levels of the fiducial from dry AFM images and Gaussian fits (solid lines) with Gaussians. b) Height distribution for the 4 different levels of the fiducial from liquid AFM images and Gaussian fits (solid lines). See Table S1 for a detailed dimension comparison. c) One exemplary fiducial height profile from dry AFM imaging. d) One exemplary fiducial height profile from liquid AFM imaging. e) Height per DNA layer and total height as a function of the number of DNA layers in the DNA origami for dry AFM imaging. f) Height per DNA layer and global height as a function of the number of DNA layers in the DNA origami for liquid AFM imaging. The red lines in e and f indicate linear fits. The reported heights are averaged over the full width of the structure. Consequently, the height values represent averages over the helices and the gaps between helices and are, therefore, lower than what the diameter of DNA.

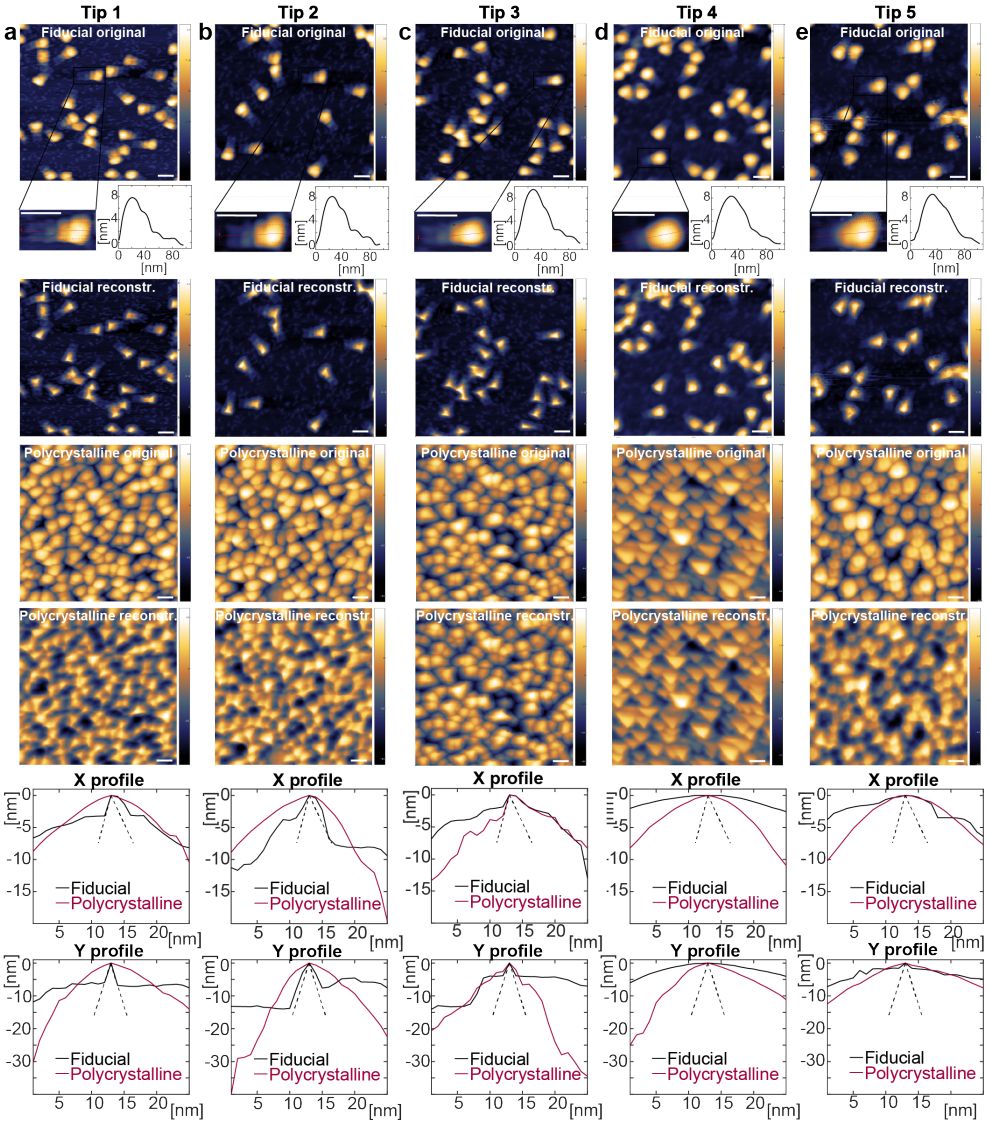

Figure 56: AFM tip characterization using different AFM FASTSCAN-A cantilevers. a) Top: AFM height image of fiducial structures at a concentration of 5 nM on APS mica, measured dry. Total image size is 500×500 nm2 and 512×512 pixels. The scale bars are 50 nm. The z-ranges are indicated in nm by scale bars on the right. One exemplary fiducial structure is shown as a zoom-in as well as its height profile underneath. Third row: Reconstructed image of the AFM image shown in the first row. Fourth row: scan of a polycrystalline AFM with the same tip. Total image size is 1×1 µm2 and 1024×1024 pixels. Fifth row: Reconstructed image of the AFM image shown in the forth row. The scale bars are 50 nm. The z-ranges are indicated in nm by scale bars on the right. Sixth and seventh row: AFM tip shape (height profile along x and y) obtained from blind tip reconstruction using the fiducial sample or the polycrystalline sample, respectively. As a reference, the tip opening angles stated by the vendor are co-plotted as dashed lines. b) - e) Analogous to panel a for different FASTSCAN-A tips from the same batch. The data suggest considerable variation between tips; Tips used for panels a and b enabled high-resolution images and reconstructed tip shapes using our fiducial are close to vendor specifications. Tips used for panels c–e appeared less sharp and gave only lower-resolution images.

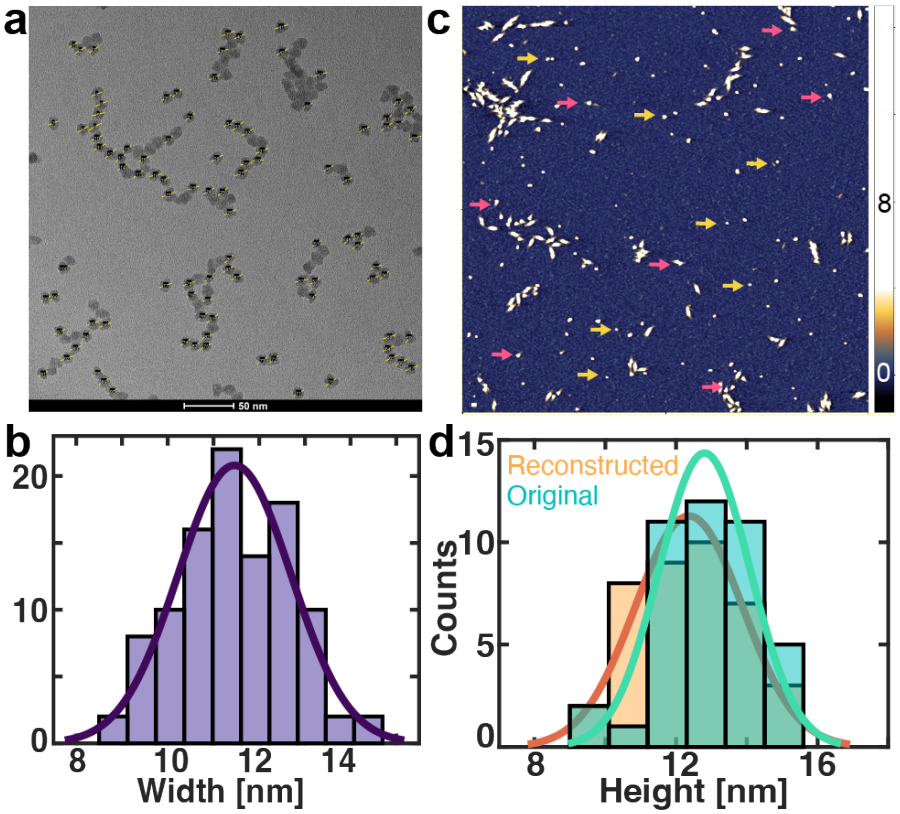

Figure 57: Width analysis of SiO_2 nanoparticles based on TEM images and co-deposition with fiducial structures in AFM with height analysis. a) TEM image of SiO_2 nanoparticles to determine size and shape. Yellow lines indicate cross-sections used for size analysis. b) Width distribution of the SiO_2 nanoparticles from the TEM image shown in panel a with a mean and standard deviation of (11.5 ± 1.2) nm. c) AFM height image of the fiducial structures co-deposited with SiO_2 nanoparticles, both at a concentration of 1 nM, deposited on APS mica and measured dry with a resolution of 1 pixel/nm. Exemplary fiducials and nanoparticles are indicated with magenta and yellow arrows, respectively. The scale bar is 50 nm. The z-range is indicated in nm by the scale bar on the right. d) Height distribution from AFM images before (turquoise) and after (orange) image reconstruction. The solid lines are Gaussian fits. The mean height in the original image of (12.8 ± 1.3) nm (mean ± std) does not change within error after image reconstruction (12.4 ± 1.5) nm by finite tip size correction.

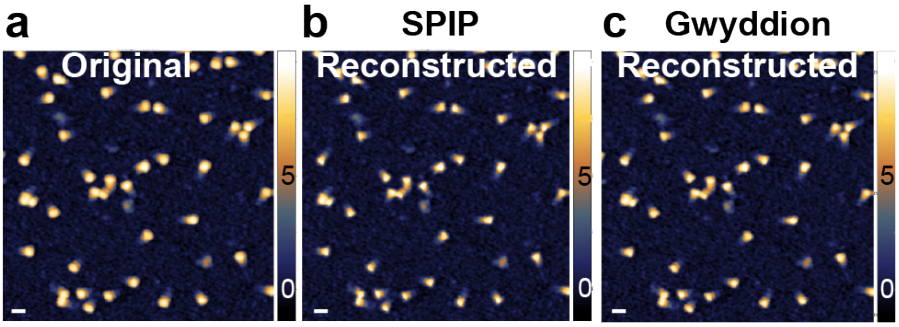

Figure 58: Comparison of AFM image reconstruction softwares. a) AFM height image of fiducial structures at a concentration of 10 nM deposited on APS mica, after drying in air (same image as shown in Supplementary Figure 54c top). b) The image from panel a after reconstruction with the software SPIP (same image as shown in Supplementary Figure 54c bottom). c) The image from panel a after reconstruction with the software Gwyddion. The scale bars are 50 nm. The z-ranges are indicated in nm by the scale bars on the right. The three images shown in this figure are provided as Supplementary Data in the file Image-Reconstruction-Example-SPIP-Gwyddion.zip.

6

DNA COMPACTION BY HIV-1 INTEGRASE

6.1 DNA CONFINEMENT IN THE REPLICATION CYCLE OF HIV

As introduced in Chapter 2, especially in countries of the Global South, the impact of HIV and AIDS on people's lives is enormous. To this end, inhibition of viral proteins has been studied for several decades now as a useful approach for prophylaxis and intervention of AIDS. HIV relies on its own viral proteins as well as cellular proteins called co-factors to complete its replication cycle [331]. After entering the human cell by interacting with cellular receptors and co-receptors, the viral RNA is reverse transcribed into a double-stranded vDNA. After reverse transcription, the vDNA together with viral and host proteins forms the PIC. This nucleoprotein complex is then transported to the nucleus where it is targeted to the host chromatin and the viral protein IN catalyzes the insertion of the viral genome into the host genome.

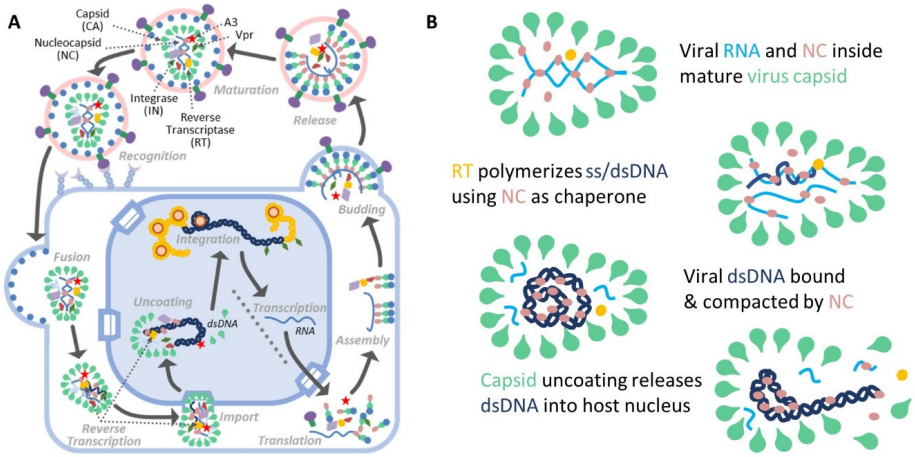

Figure 59: Overall view of the role of the nucleocapsid protein in the HIV replication cycle. (A) The nucleocapsid protein is critical for several steps in the life cycle of HIV, e.g., for packaging viral RNA into the capsid. Additionally, the nucleocapsid protein also acts as a chaperone for reverse transcription of viral RNA into DNA and binds and aggregates vDNA with high affinity. (B) The nucleocapsid protein binds and condenses viral DNA during reverse transcription. To fit the entire vDNA of ∼10 kbp into the viral capsid, the DNA must be considerably compressed. Once the capsid uncoats, the vDNA and viral proteins are released into the host cell nucleus. Figure taken from Ref. [332].

The virus capsid contains the viral genome (two viral RNAs), viral proteins (including IN, reverse transcriptase, nucleocapsid protein, and others), as well as several host proteins. While early experiments assumed that the capsid disintegrates soon after entering the host cell [331, 333], recent studies have shown that the intact HIV capsid is transported through the NPC into the nucleus where reverse transcription occurs within the fully intact viral capsid

[140, 322, 332, 334, 335]. This in turn raises the question of how a nearly 10 kbp viral DNA genome can be stably packed into a narrow capsid with a diameter similar to the persistence length of dsDNA and at the same time remain accessible for transcription [336]. Several viral proteins are thought to play a role in this process, e.g., nucleocapsid protein [332, 337–339] (Figure 59), but the exact mode of operation is not fully understood. While the relative progression of reverse transcription and capsid uncoating are well studied and to a large extent understood, the mechanisms and timing of uncoating remain obscure. One possible scenario might be that the synthesis of full-length proviral DNA exerts sufficient pressure on the capsid to cause forcible disassembly (i.e., uncoating) [332, 335]. However, in order to fully grasp the relationship between reverse transcription progression, internal DNA pressure, capsid deformation, and capsid de-shelling, knowledge of the conformation of the rigid proviral DNA within the virus core is needed.

6.2 THE VIRAL PROTEIN HIV-1 INTEGRASE AND ITS ROLE IN DNA COMPACTION

Retroviral integration, i.e. the covalent insertion of a copy of DNA containing the viral genome into the host genome, is the critical step in retroviral replication and a necessary requirement for productive infection [313, 330, 340–344]. However, to reach this point, the viral genome must first be transported to the nucleus. This is complicated by the size limitation of the viral capsid, which requires the vDNA to be stably contained within a narrow capsid with diameter similar to the persistence length of dsDNA, as discussed in the previous section. It is likely, that viral proteins play an important role in DNA compaction and preservation in the viral capsid. While the strand transfer reaction assembles an IN multimer at the vDNA ends, it was found that the PIC comprises approximately 150 – 250 copies of IN, more than 10-fold the amount of IN monomers needed for integration catalysis [343, 345, 346]. This raises the question of why the virus invests in packing so much excess IN? Might IN serve an additional functional role beyond integration catalysis in the compaction of the vDNA in the narrow viral capsid? Yet, until now, neither the exact protein composition nor the DNA folding mechanisms within this narrow compartment are well characterized or understood [332, 337–339].

In this work, I focus on the viral protein IN, which is a major component of the PIC, and propose a role for IN beyond catalysis: vDNA compaction. I use AFM imaging to show that IN induces flexible bends and oligomerizes on DNA. IN can compact DNA at sizes comparable to vDNA into particles capable of dynamic bridging and looping, enabling conformational plasticity that provides a pathway for efficient compaction of the viral genome. I quantify DNA compaction as a function of IN concentration, ionic strength, and DNA length. Importantly, I will show that compaction occurs in two distinct concentration regimes, and results in the formation of biphasic condensates which are consistent in size with *in vivo* super-resolution fluorescence microscopy images of infected PICs containing fluorescently labeled IN [347]. Using AFM-based elasticity mapping I will further reveal that the formed assemblies feature are hard core surrounded by a soft shell. Lastly, I will use magnetic tweezers to unravel individual condensates and show that remarkably low forces (<1 pN) are sufficient to resolve IN-DNA condensates. The de-compaction occurs in

bursts interspersed with pauses representing a kinetic barrier towards disassembly. Together, the results support a model wherein IN compacts the viral genome in distinct biphasic condensates that are held together by two different types of interaction forces. It is possible that IN might extend its functionality – i.e., catalytic versus structural – by adopting different roles depending on the environment.

6.3 HIV INTEGRASE COMPACTS VIRAL DNA INTO BIPHASIC CONDENSATES

HIV integrase compacts viral DNA into biphasic condensates

By

Pauline J. Kolbeck[1,2,3], Marjolein de Jaeger[3], Margherita Gallano[1,2], Tine Brouns[4,5], Sebastian F. Konrad[1,2], Steven De Feyter[4], Frauke Christ[5], Zeger Debyser[5], Laura Filion[3], Willem Vanderlinden[1,2,3,*] and Jan Lipfert[1,2,3,*]

[1,2] Department of Physics and Center for NanoScience, LMU Munich, Amalienstrasse 54, 80799 Munich, Germany
[3] Department of Physics and Debye Institute for Nanomaterials Science, Utrecht University, Princetonplein 1, 3584 CC Utrecht, The Netherlands
[4] Division of Molecular Imaging and Photonics, KU Leuven, Belgium
[5] Department of Pharmaceutical and Pharmacological Sciences, KU Leuven, Belgium
[*] Corresponding authors

In preparation.

My contribution to this publication was designing and performing AFM and MT measurements, analyzing the resulting data, and co-writing the manuscript with input from all authors.

6.3.1 *Abstract*

Viruses replicate within changing and often hostile micro-environments of their host cell and must do so using a limited arsenal of protein machinery. HIV completes the early cellular stages of infection, i.e. reverse transcription of the single stranded RNA genome to a dsDNA copy, within the context of a protecting capsid while travelling through the cytoplasm to the cell nucleus. The boundaries set by the capsid imply a gradual buildup in pressure during reverse transcription, and at the same time hinder uptake of host-derived agents to compact the genome. In this work, we identify the viral enzyme IN to compact genomic length vDNA mimetics. Under physiologically relevant conditions, IN-compacted genomes are consistent in size with those found for PICs in infected cells. Using a range of single molecule techniques, combined with coarse grained simulations, we demonstrate that compaction occurs in two stages. In a first stage, integrase tetramers form DNA bridges that assemble into rosette structures that are thermodynamically and mechanically stable. In a second stage the extruding DNA loops condense onto the rosette core to form a disordered outer layer that is thermodynamically and mechanically unstable. Notably however, the core complex is susceptible towards allosteric IN inhibitors (ALLINIs), whereas the diffuse outer layer is not. Together, our data suggest that IN has a structural role in vDNA compaction and highlight the importance to explore inhibitors targeting disordered IN-DNA interactions.

6.3.2 *Introduction*

To establish infection, HIV traverses multiple cellular micro-environments of human host cells, using only a limited arsenal of viral proteins. HIV infects non-dividing cells, and viral particles must enter the cell nucleus to perform integration, thereby irreversibly establishing a provirus in the human genome. While the molecular structures and mechanisms of reverse transcription [340, 341] and integration [313, 330, 342–344] are reasonably well understood, the composition and structural assembly of the large nucleoprotein complexes wherein they occur, i.e. the reverse transcription complex and the PIC respectively, remain obscure.

Recent work has dramatically impacted our view on the intracellular nature of the virus particle: in contrast to previous belief, HIV transport towards the nucleus occurs within the confines of a (largely) intact viral capsid [140, 142]. This new insight infers that reverse transcription takes place in a nanocontainer that requires to constrain increasing mechanical stresses due to the conversion of single-stranded HIV RNA into a stiffer double-stranded copy DNA (cDNA) of the HIV genome. Therefore, a molecular framework has to be present to buffer the extensive mechanical strain on the capsid.

In this context, it was found that the estimated copy-number of the viral protein IN in PICs [345] is $\sim$150 – 250, at least one order of magnitude larger than the number of IN (4 – 16 copies [343, 346]) required for intasome assembly and catalysis of integration. This raises the question of how such large excess of IN is beneficial during the replication cycle. Indeed, IN serves a functional role during the late stages of HIV replication, in particular during viral assembly and maturation through binding to viral RNA [151]. Furthermore, IN plays a critical role in the process of capsid uncoating [348], and IN mutants defective for non-specific DNA binding are impaired for nuclear import [349] and reverse

transcription [350], suggesting a critical role of IN within the cytoplasmic viral capsid during the early stages of infection.

Here, we demonstrate an additional functional role of IN by showing that IN effectively induces compaction of vDNA mimetics under physiologically relevant conditions. Dimensions of the resulting condensates agree favorably with those of PICs purified from [134] or within the infected cell [347]. Our data, obtained by single molecule force microscopy and spectroscopy techniques, and complemented with coarse-grained polymer simulations, suggest a bridging-induced attraction mechanism that features an on-pathway rosette intermediate preceding full collapse. The fully collapsed condensates retain the mechanically robust rosette core and a diffuse visco-elastic outer layer, reminiscent of current models of eukaryotic genome folding [351] – albeit at a length scale many orders of magnitude shorter. Importantly, we demonstrate a differential susceptibility towards allosteric IN inhibitors (ALLINIs) for the rosette folding intermediate versus the fully collapsed condensate.

6.3.3 *Results*

6.3.3.1 *IN binds viral DNA ends with moderate selectivity*

Binding of IN to vDNA ends underlies catalysis of integration. Here, we use AFM imaging to quantify the selectivity of recombinant IN for the specific ends in short viral cDNA mimics (Figure 60A), as a function of the level of 3'-end processing. We determine the position of the bound IN complexes with respect to the nearest DNA end in IN-DNA nucleoprotein complexes (Figure 60B and Supplementary Figure 67), which enables to estimate the selectivity of end-binding [352]: $S = \frac{P_{end}}{P_{background}}$. We first investigated binding of IN to the 491 bp cDNA mimic in buffer containing 1 mM Mg^{2+} and find a selectivity $S = 64 \pm 13$ (34 out of 159 complexes end-bound; errors were estimated from counting statistics using standard error propagation; Figure 60C).

Next, we studied binding in buffer wherein Mg^{2+} is replaced by Ca^{2+} to impede catalysis of 3'-end processing [134]. Under these conditions, we find a reduced selectivity $S = 19 \pm 7$ (9 out of 122 complexes end-bound; Figure 60C). Last, we quantify binding to HIV DNA mimetics with 3' pre-processed ends. In this case, we find a highly elevated selectivity, $S = 256 \pm 15$ (53 out of 129 complexes end-bound). Thus, the selectivity of binding to the specific blunt HIV ends increases by more than 10-fold by catalysis of 3'-end processing. Nevertheless, binding selectivity overall is only moderate; the probability of binding to a random position in genomic length vDNA ($\sim 8 - 9$ kbp) is $1 - 2$ orders of magnitude larger than binding to the specific ends.

6.3.3.2 *IN unspecific binding infers DNA bending and looping*

As most IN-DNA complexes bind to internal sequences, i.e., non-sequence specifically, we investigate whether non-specific binding alters DNA structure. We quantify IN-induced DNA bending (Figure 60E,F) and find that the distribution is much broader and shifted to larger bend angles at positions where IN is bound, as compared to the distribution of naked DNA bends. At higher ionic strength (250 mM NaCl, 5 mM $MgCl_2$), the fraction of complexes with small bend angles decreases with respect to complexes with large bend angles (Figure 60F). This suggests the presence of (at least) two binding modes:

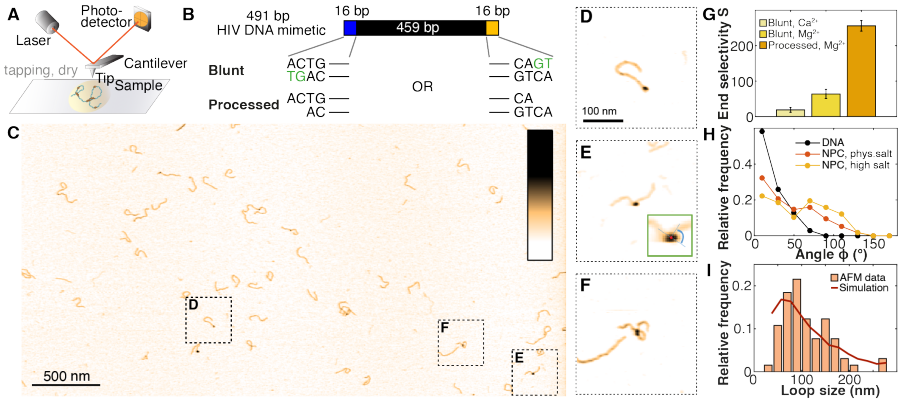

Figure 60: IN specific and aspecific binding to HIV DNA mimetics. A. Schematic representation of the experimental set up for AFM imaging experiments. B. Schematic of the 491 bp DNA we use to mimic the HIV cDNA, both as a blunt ended or as a 3'-preprocessed substrate. C. Overview AFM topograph of the 491 bp DNA in the presence of 100 nM IN. Color range is 1.5 nm. D. HIV DNA mimetic with end-bound IN. E. HIV DNA mimetic with IN bound at internal sites and definition of bend angle (inset). F. HIV DNA mimetic with IN-mediated DNA looping. G. Selectivity for end-binding over binding to internal sites in the mimetic as a function of 3'-end processing and buffer conditions. The binding site size is assumed to be 16 bp. H. Bend angle distribution measured at 10 nm length scale for bare DNA and IN-DNA nucleoprotein complexes (NPCs) deposited from near-physiological salt buffer (50 mM NaCl, 1 mM $MgCl_2$, 10 mM Tris-HCl pH = 7.4; N = 232) or high salt buffer (250 mM NaCl, 5 mM $MgCl_2$, 10 mM Tris-HCl pH = 7.4; N = 109). I. Histogram of the loop size distribution obtained from measurements on 1 kbp HIV DNA mimetic. The loop size distribution obtained from simulations (see main text for details) with r = 6 nm is co-plotted (red line).

a first mode that is salt-sensitive and minimally invasive, and a second binding mode that is less sensitive to ionic strength and infers strong DNA bending.

Beyond bending, a small fraction (∼5% of all internally bound complexes) forms synapses, i.e., intramolecular DNA loops mediated by IN (Figure 60G). Using a longer vDNA mimetic (1000 bp) and otherwise identical conditions (100 nM IN), the fraction of looped DNA increases to (30 ± 5)% of all internally bound nucleoprotein complexes (N = 93). This increase is consistent with the expectation that looping is facilitated by the longer DNA lengths, since ∼500 bp corresponds to only ∼4 times the bending persistence length of DNA.

Quantifying the loop size distribution (Figure 60H), we find the most probable loop size to be ∼85 nm (∼250 bp), which is significantly smaller than what is expected for a hypothetical DNA looping back on itself (i.e. at zero separation between the DNA ends the optimal loop size is ∼160 nm or ∼500 bp). Comparing the experimentally observed loop size distribution [353] to Monte Carlo (MC) simulations (Figure 60H), we find that loop sizes are consistent with the expected distribution with a distance between the DNA strands in the synapse of ∼6 nm. A distance constraint of ∼6 nm strongly suggests that the synapse is formed by IN tetramers, in which the DNA binding interfaces in the C-terminal

domains are brought closer together as compared to IN dimers [354], which is the dominant oligomeric species in the unbound state (Supplementary Figure 67). Together, our results demonstrate that IN binding to random positions along the DNA is prevalent and can alter DNA conformation by bending and looping.

6.3.3.3 *Two-stage compaction of genomic length viral DNA*

To investigate how IN unspecific binding affects DNA of lengths similar to the HIV genome, we titrate linearized mini-HIV DNA [330] (3.4 kbp, 4.8 kbp, 9.1 kbp) with IN and quantify the resulting complexes using AFM (Figure 61A and Supplementary Figure 68 and 69). To directly relate the conformations of adsorbed complexes to their solution state, we used conditions that infer kinetic trapping (i.e., a 3D-2D projection).

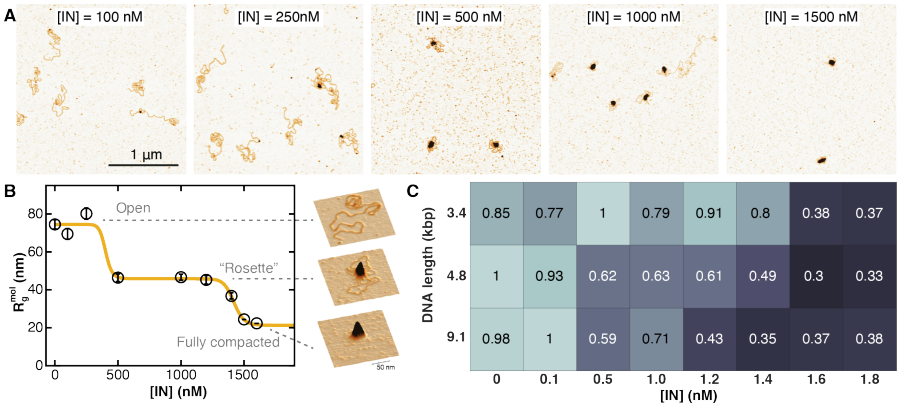

Figure 61: IN compacts of long viral DNA mimetics in biphasic condensates. A. AFM topographs of the 4.8 kbp DNA in the presence of (from left to right) 100 nM, 250 nM, 500 nM 1000 nM, 1500 nM IN. B. Radius of gyration of the nucleoprotein complex for 4.8 kbp DNA at 60 mM ionic strength as a function of [IN]. The data reveal two distinct compaction transitions and are fitted by a double-Hill-fit: the first transition from open state to rosette state occurs at $\sim$ 500 nM, the second transition from rosette state to fully compacted state at $\sim$ 1100 nM. Representative AFM images are shown on as insets on the right. C. Phase diagram showing the normalized radius of gyration of the nucleoprotein complexes (relative to the maximum radius of gyration) formed as a function of [IN] and DNA length. With increasing DNA length the compaction transitions shift to lower IN concentration. Intriguingly, at a DNA length $>$ 3.4 kbp a biphasic compaction transition is observed, whereas at a DNA length of 3.4 kbp, the transition occurs in one step.

We first used a 4.8 kbp mini-HIV DNA [330] for titration with IN in the concentrations range [IN] = 0 – 2 µM (Figure 61A and Supplementary Figure 76). At IN concentrations of 100 – 500 nM, we observe localized IN binding and IN-induced looping. Increasing the concentration to [IN] = 500 – 1200 nM results in the formation of large nucleoprotein complexes featuring a central nucleoprotein core surrounded by naked DNA loops. Because of their appearance, we refer to these complexes as "rosettes". At even higher IN concentrations (1200 – 2000 nM), the DNA is further compacted, and the

nucleoprotein complexes are predominantly in conformations wherein the DNA is no longer visible. On occasion, these intramolecular complexes self-associate to form large conglomerates comprising multiple DNA copies (Supplementary Figures 68F and 69E,F).

We quantified DNA compaction upon titration of mini-HIV DNA with IN by automated analysis of the height-weighted 2D radius of gyration:

$$R_g = \sqrt{\frac{\sum_{i=1}^{n} h_i \cdot s_i^2}{\sum_{i=1}^{n} h_i}} \tag{43}$$

where s_i is the distance of pixel i with respect to the molecular center of mass, and h_i is the height value in pixel i. Consistent with the qualitative observations of DNA-IN complex geometries, the R_g data reveal that IN significantly compacts DNA in two successive, highly cooperative transitions: a first transition occurs at [IN] ~400 nM and reduces R_g by approximately 40% (from 75 nm at [IN] $\leq$ 250 nM, to 45 nm for [IN] = 500 – 1200 nM). A second transition is observed at [IN] ~1400 nM, and further reduces R_g ~two-fold (Figure 61).

Condensation of nucleic acids with proteins and the formation of nucleoprotein complexes is in general often dependent on the ionic strength of the solution [78]. Therefore, we systematically varied the salt concentration in our sample (Supplementary Figure 70 and 71) and constructed a phase diagram of condensate formation as a function of salt and IN concentration (Figure 61C and Supplementary Figure 72). The data show that both rosette formation and full collapse are disfavored by high salt concentration, but occur under physiologically relevant conditions.

Having characterized the compaction behavior of a 4.8 kbp HIV DNA mimic, we next explore how DNA length alters IN-induced condensation (Supplementary Figure 68 and 69). We find that the degree of compaction is independent of the DNA contour length and reduces R_g approximately 3-fold at full compaction. Nevertheless, the critical concentrations for the compaction transitions increases for shorter contour lengths (Figure 61C and Supplementary Figure 73). Most notably, full compaction of the 3.4 kbp HIV mimetic occurs in a single transition (i.e., the rosette state is no longer observed), in contrast to the biphasic behavior observed for 4.8 kbp and 9.1 kbp DNA. This observation is consistent with predictions of a simple scaling argument [355] that estimates optimal balancing of bending energy with the entropy loss due to looping: DNA segments longer than about 3 kbp are required to observe stochastic bridging. Last, the radius of gyration of the fully compacted state for 9.1 kbp DNA (approximately the length of the viral genome) is ~32 nm, close to the Stokes' radius found for purified PICs [134] (28 nm) and in agreement with the molecular dimensions of PICs in infected cells [347]. Thus, quantitative AFM analysis indicates that genomic length vDNA is compacted via two distinct transitions into condensates with dimensions that are in quantitative agreement with those found in infected cells.

6.3.3.4 *Simulations suggest bridging-mediated attraction mechanism with a critical role for IN-IN interactions*

To obtain a mechanistic understanding of how local interactions lead to DNA compaction, we turn to Monte Carlo (MC) simulations (Figure 62). In our simulations, DNA is modeled as a chain of non-overlapping beads, each

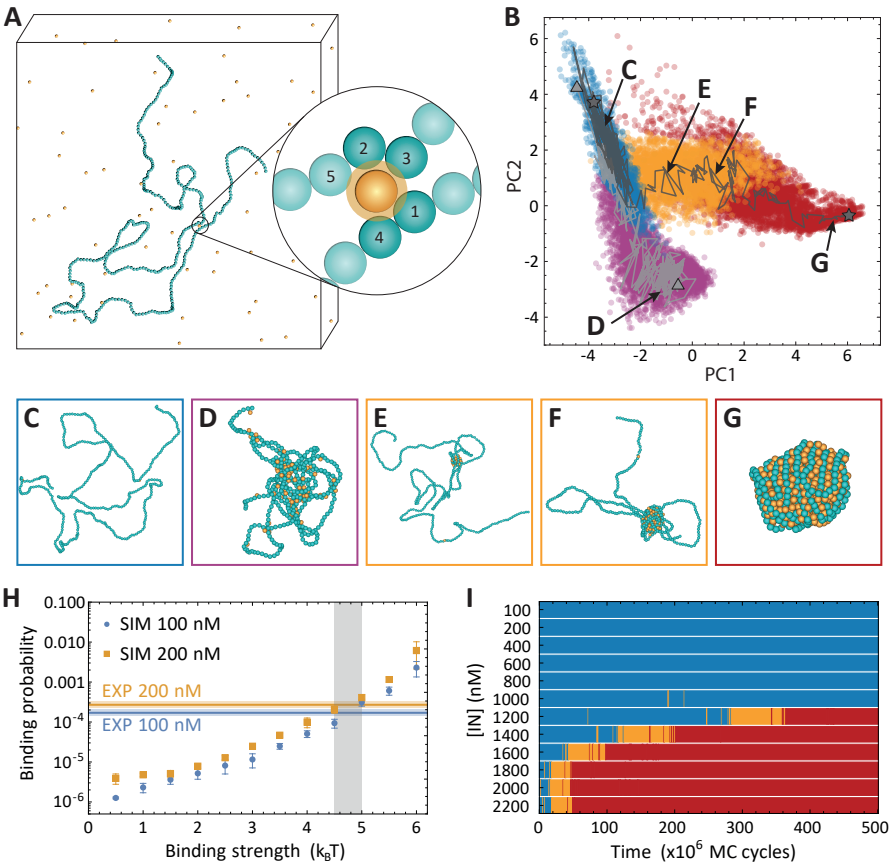

Figure 62: Monte Carlo (MC) simulations show that IN protein-protein interactions modulate biphasic compaction. A. Schematic representation of the experimental setup for MC simulations. DNA beads (16 bp) are colored in light blue, free IN beads (same size) are colored in red, and bound IN beads (same size) are colored in dark blue. The box size is not to scale. B. Principal component-analysis (PCA) gives rise to several "sub-phenotypes" of DNA-IN complexes (depicted as different colors. Without IN-IN interaction, the left path is taken (triangles at start and end point), here no rosette intermediates are formed. Only if IN-IN interactions are added (right path; stars at start and end point), rosette formation (orange) as well as full compaction (red) are possible. C. – G. Snapshots of simulated 4.8 kbp DNA in presence of increasing [IN]. H. IN-DNA binding strength (in k_BT) as a function of binding probability for 100 nM and 200 nM IN determined experimentally from AFM images and from MC simulations. The crossing area of experiment and simulations allows to estimate the IN-DNA interaction free energy, 4.5 – 5 k_BT. I. Averaged compaction states (same color code as in panel B) for varying IN concentrations, well in line with the experimental data (Figure 61).

representing 16 bp (equal to the approximate binding site size of IN) joined by springs. To reproduce the experimentally determined bending stiffness of DNA, a bending potential is added which penalizes sharp kinks between subsequent springs. IN is similarly modeled as beads of equal size. We capture

the (assumed) tetrahedral nature of IN by introducing a maximum valence of 4: each IN bead can bind to at most four DNA beads (see methods Section 6.3.10.10). We determine the interaction strength of IN binding to a single DNA segment to be $\epsilon = 5\ k_BT$ by direct quantitative comparison to experimental data (Figure 62H). We perform both simulations where IN only binds to DNA and simulations that include both IN-DNA and IN-IN binding. The IN concentration is controlled via a semi-grand canonical ensemble (see methods Section 6.3.10.10) to ensure that the concentration of free IN remains roughly constant during the simulation.

We analyze the output of extensive simulations with different interactions parameters and identify states and the pathways between states by principal component analysis of 15 different structural parameters and a Gaussian mixture model (see methods Section 6.3.10.10). A key result is that we observe distinct pathways in the presence and absence of IN-IN interactions: MC simulations that only include IN-DNA binding, but no IN-IN interactions exhibit DNA compaction, but fail to reproduce the two-phase compaction and the experimentally observed rosette structures. In contrast, if IN-IN interactions are included, we observe transitions and structures that are in quantitative agreement with the experimental observations (Figure 62C–G,I). In summary, our simulations demonstrate that a simple model that includes both IN-DNA and tetrameric IN interactions can quantitatively reproduce the observed DNA compaction.

6.3.3.5 *IN-DNA condensates feature a rigid core surrounded by a soft coat*

The MC simulations suggest that the rosette state is an on-pathway intermediate to the fully collapsed condensate. To test this prediction experimentally, and to obtain insights into the mechanical properties of the condensates, we employ AFM-based force-volume mapping [356, 357].

In this modality, a full force-distance curve (i.e., an approach and retract cycle) is recorded in every pixel of the image. Localized interaction forces on the tip are recorded as it moves towards and away from the sample surface and can be directly correlated to the sample topography (Figure 63A). We analyze approach force curves to extract the indentation stiffness k, the retract curve to quantify elastic deformation energy ΔG_{Elast}, and the hysteresis between both curves to obtain a measure of plastic deformation ΔG_{Plast}. From the elastic and plastic contributions to the deformation free energy, we can quantify the dimensionless visco-elasticity index

$$\eta = 1 - \frac{\Delta G_{Elast}}{\Delta G_{Elast} + \Delta G_{Plast}} \tag{44}$$

which equals zero for a perfectly elastic deformation (all bonds broken during indentation are reformed during the stress release). In contrast, $\eta = 1$ for a completely viscous deformation (none of the bonds broken during indentation are reformed during the stress release).

We first perform force-volume mapping on complexes in the rosette state (Figure 63B and D) and find the approach and retract curves to be uniform across the nucleoprotein core, and to exhibit little hysteresis. The values of k, ΔG_{Elast}, and ΔG_{Plast} are pooled and averaged per complex (N = 5). We find a mean stiffness $\langle k \rangle = 31 \pm 7$ pN/nm (error is the standard deviation) and a

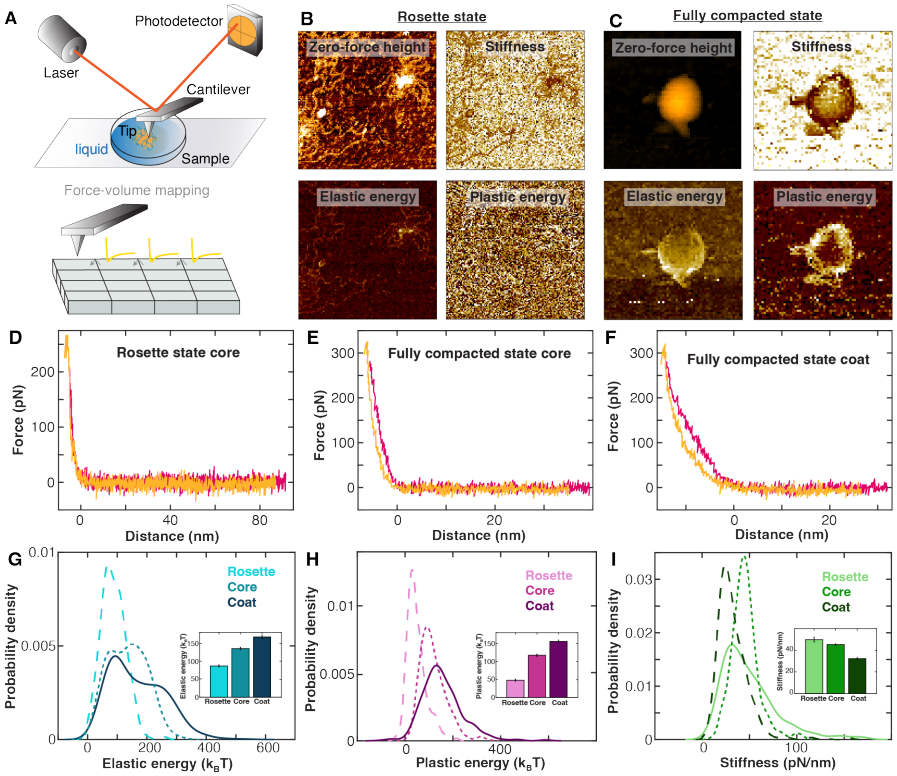

Figure 63: AFM Force-volume based multiparametric imaging of IN-DNA condensates. A. Schematic depiction of AFM setup for force-volume-mapping. B. Multiparametric imaging results of a condensate in the rosette state, all recorded in the same scan: zero-force height, stiffness, elastic energy, plastic energy (image size 500 × 500 nm^2). C. Same as in panel B for a IN-DNA condensate in the fully compacted state (image size 250 × 250 nm^2). Our results show that fully condensed condensates feature a dense core surrounded by a soft layer with visco-elastic properties. D – F. Exemplary force-separation curve for the inner part ('core') of a rosette sate condensate (panel D), the 'core' of a fully compacted state condensate (panel E), and the outer part ('coat') of a fully compacted state condensate (panel F). The approach curve is colored in yellow, the retract curve in pink. G – I. Probability density for the elastic energy (panel G), plastic energy (panel H), and stiffness (panel I) each for the for the 'core' of the rosette sate condensate, the 'core' of the fully compacted state condensate, and the 'coat' of the fully compacted state condensate.

mean visco-elasticity index $\langle\eta\rangle = 0.34 \pm 0.07$ for the core of the rosette state of the condensate.

In a second set of experiments, we use force-volume mapping on fully collapsed condensates (Figure 63C, E, and F; N = 5). In contrast to force curves recorded on rosettes, we consistently observe substantial hysteresis between approach and retract curves. Furthermore, we find the overall slopes of the force curves to vary depending on their radial position: at constant peak forces, larger indentations are observed near the edges of the condensates. Indentation curves do not show breakthrough events, and because one would expect decreased

indentations due to finite AFM tip size effects near steep topographic features we interpret the spatially resolved features in the condensates to result from complex material properties [358, 359]. The spatially resolved stiffness map is used to identify a "core" and outer layer or "coat". We pool force curves in the core and we use values of k, ΔG_{Elast}, and ΔG_{Plast}. to quantify $\langle k \rangle = 53 \pm 8$ pN/nm (error is standard deviation) and a mean visco-elasticity index $\langle \eta \rangle = 0.48 \pm 0.09$ over the different condensates. An analogous treatment for force curves recorded on the condensate coats, gives quantify $\langle k \rangle = 29 \pm 2$ pN/nm (error is SD) and a mean visco-elasticity index $\langle \eta \rangle = 0.55 \pm 0.08$.

We conclude that the elastic energy, plastic energy, and stiffness of the core of the rosette state, the core of the fully compacted state condensate, and the coat of the fully compacted condensate vary considerably (Figure 63G–I). Fully collapsed condensates feature a rigid core and diffuse outer layer, consistent with the biphasic compaction mechanism observed by titration *ex situ*. Thus, the nucleoprotein complex stabilizing the rosette is preserved on full collapse, which might involve the compaction of the DNA loops that are extruded from the intermediate rosette state.

The stiffness on indentation is related to the density and dissociation rate of bonds, while the visco-elasticity index relates to the association rate of bonds within the indented region. The complex material properties are therefore expected to be strongly dependent on the timescale of the experiment. Provided that the time frame for stress application and release is ∼5 ms, the intrinsic dynamics is expected to occur on a significantly slower time scale.

6.3.3.6 *Force spectroscopy of IN-DNA confirms biphasic structure and reveals glassy dynamics of compacted loops*

To investigate the dynamics and stability of IN-DNA condensates, we performed MT force spectroscopy experiments. In our assay, we tethered linear DNA molecules (21 kbp) between the flow cell surface and superparamagnetic beads (Figure 64A). Using external magnets, we can apply precisely calibrated stretching forces to the tethered molecules. To investigate the forces involved in IN-DNA condensation, we first introduced IN (2 µM) in the MT flow cell to interact with the tethered DNA molecules under very low stretching forces ($F < 0.01$ pN) for 10 min to allow for condensate formation, and then apply stretching forces to mechanically probe the stability and structure of the condensate (Figure 64B). In control experiments with bare DNA, the DNA extension increases essentially instantaneously (< 0.1 s) upon increasing the force to the full extension of DNA at the given force (Supplementary Figure 77). In contrast, after formation of IN-DNA condensates, the extension only increases very gradually upon applying force. During force-induced extension, we observe slow increases of the extension, interspersed by long ($>$ min) pauses at constant extension (Figure 64B).

We quantify the extension time traces at constant force by determining the dwell times between extension events and for the extensions events i) the total increase in tether length for each event and ii) the extension velocity (Figure 64C). The increase in length per extension event shows a distribution that closely matches the loop distributions observed by AFM imaging and MC simulations (Figure 64D), which suggests that individual extension events correspond to the release of compacted loops.

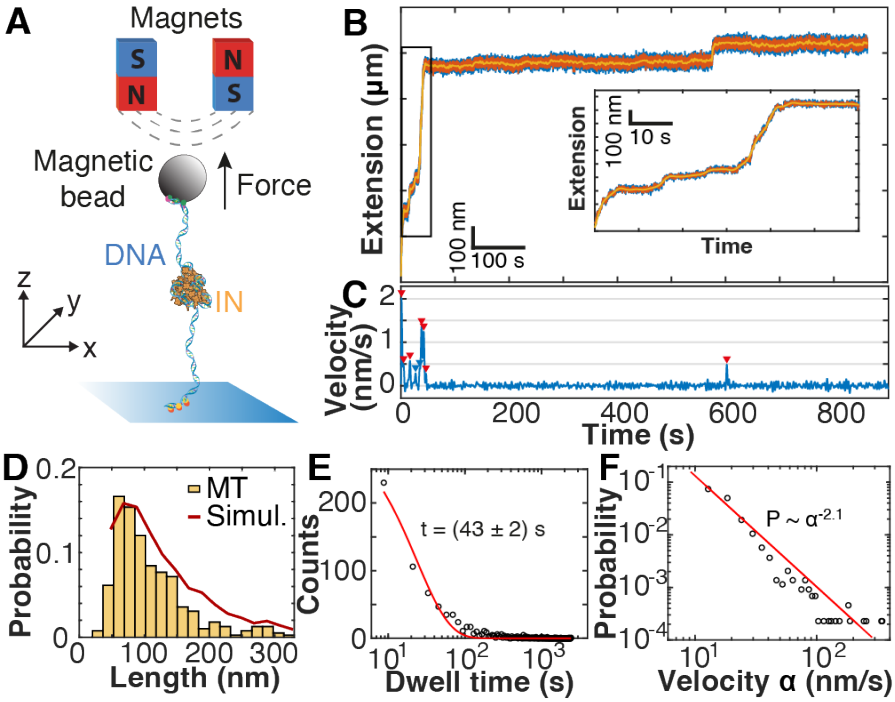

Figure 64: Single-molecule MT measurements show dynamics of force-induced condensate unfolding. A. Schematic depiction of the MT force spectroscopy measurements. 21 kbp DNA is tethered between a flow cell surface and small magnetic beads and (partially) compacted by IN. External magnets enable the application of precisely calibrated stretching forces. B. Exemplary extension curve over time at a constant force of 2 pN. Raw data (blue) recorded at 58 Hz and data smoothed using a Butterworth filter (red/orange). C. Numerical derivative of the smoothed extension time trace shows velocity bursts. D. Burst size distribution. For comparison, the simulation data (red line; same as already shown in Figure 60I) are depicted. E. Dwell times between extension bursts. The resulting dwell time distribution is fitted by an exponential decay with a half time of (43 ± 2) s. F. Extension bursts velocities. The broad distribution of velocities suggests a high heterogeneity of interactions inside the condensate. The data is best fit by a power law with exponent -2.1.

The dwell times between extension events follow approximately a single exponential distribution with a lifetime of (43 ± 2) s at 1 pN (Figure 64E), suggesting that the interactions that form DNA loops are robust and stabilize the condensate. Consistent with this view, we find that at forces up to 5 pN, the majority of DNA tethers (∼80%) does not reach of the extension expected for bare DNA even after 30 min, suggesting that even at 5 pN the majority of condensates remain only partially resolved (Supplementary Figure 79B).

The extension velocities are much smaller than what would be expected for the release of free DNA loops [360, 361] and show a broad velocity distribution (Figure 64F), suggesting that IN-compacted DNA loops are released under forces of ∼1 pN, but that the release is slowed down by protein interactions that cause an effective friction and exhibit glassy dynamics, consistent with the viscose nature of the soft coat region observed by AFM probing. The dynamic

and reversible nature (Supplementary Figure 78 and 80) of the interactions involved in loop compaction is further evidenced by the fact that at very low forces (< 0.5 pN), we observe slow increases and decreases in DNA extension at constant force (Supplementary Figure 79A and 80).

6.3.3.7 *Allosteric IN inhibitors interact differentially with rosettes versus collapsed condensates*

Titration of IN with DNA, mechanical property mapping, and force-jump experiments indicate that the core is thermodynamically and mechanically more robust as compared to the coat of the condensates. Further, our combined experimental and simulation data suggest that interactions in the core are mediated by IN tetramers and higher order assemblies thereof. As IN tetramers are the preferred target for allosteric IN inhibitors [361] we aim to test the susceptibility of condensates in the rosette and fully compacted states, towards inhibitor CX14442 [362].

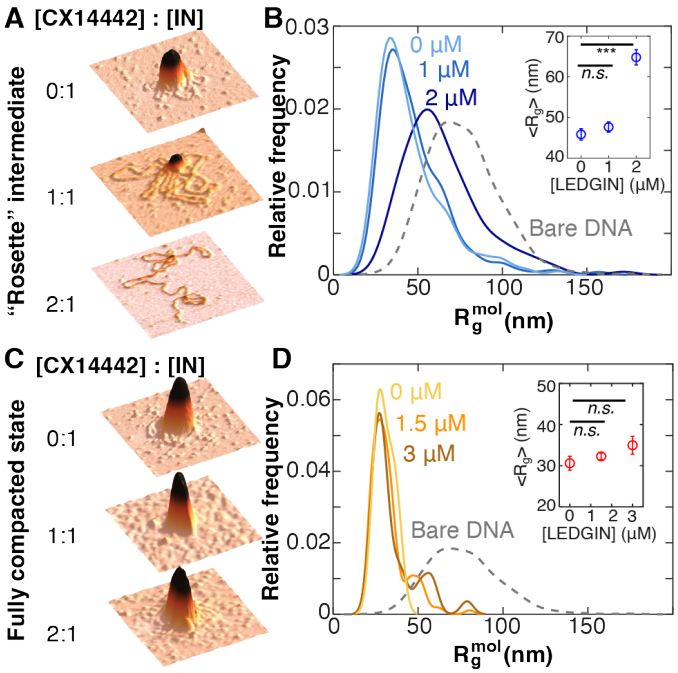

Figure 65: Allosteric IN inhibitors (ALLINIs) affect compaction behavior of long vDNA mimetics. A. AFM topographs of the 4.8 kbp DNA in the presence of 1000 nM IN (rosette state) and no, 1000 nM, 2000 nM ALLINIs. ALLINIs were added after complex formation. B. R_g-distributions for the 1000 nM IN and no, 1000 nM, 2000 nM ALLINIs. As a reference, the distribution for bare DNA is shown as well. With increasing [ALLINI] less compaction is observed. C. AFM topographs of the 4.8 kbp DNA in the presence of 1500 nM IN (fully compacted state) and no, 1500 nM, 3000 nM ALLINIs. ALLINIs were added after complex formation. D. R_g-distributions for the 1500 nM IN and no, 1500 nM, 3000 nM ALLINIs. As a reference, the distribution for bare DNA is shown as well. Even at high [ALLINI], the fully compacted IN-DNA complexes are not broken by the ALLINIs.

In a first set of experiments, we introduced CX14442 at 1 and 2 µM, at a fixed [IN] = 1 µM. At 1:1 [CX14442]:[IN] ratio, the typical single nucleoprotein cluster of the rosette conformations appears partly disintegrated (Figure 65A), and we quantify the radius of gyration of the nucleoprotein core to statistically assess changes with respect to the absence of inhibitor (Figure 65B). Despite the significant changes in cluster size and integrity, we find no significant changes in compaction of the condensate, as assessed by the radius of gyration of the condensate. At 2:1 [CX14442]:[IN] ratio, the rosette core is disintegrated completely: individual IN are bound along the DNA contour yet do net exhibit bridging interactions. Consistently, we find significant changes in cluster size and integrity, as well as significant changes in compaction of the condensate.

In a second set of experiments, we introduced CX14442 at 1.5 and 3 µM, at a fixed [IN] = 1.5 µM. Strikingly, independent of the CX14442 concentration, the nucleoprotein assemblies retain their fully compacted conformations akin to those found in the absence of inhibitor (Figure 65C). Consistently, we find no significant changes in cluster size, or in terms of compaction of the condensate (Figure 65D). We see a similar effect when adding CX14442 before complex formation (Supplementary Figure 81).

We draw the following conclusions from these experimental results: first, the fact that at 1.5 µM IN no visible changes are observed, rules out that the major effect of CX14442 is due to the loss of IN in inactive aggregates, which is the inhibitor's mode of action at high IN concentrations [151, 332]. Second, the differential effect of CX14442 on rosette formation and the fully collapsed state indicate that the protein-protein and/or protein-DNA interactions involved are different for the different compaction stages, and further establish that specific IN tetramer-tetramer interactions are important in the assembly of rosettes. Third, the fact that the strong and dense core complex is susceptible to allosteric IN inhibitors, while the diffuse outer layer is not, shows that thermodynamic and mechanical stability do not necessarily correlate with drug susceptibility.

6.3.4 *Conclusion*

In this work, we used single molecule biophysics experiments in combination with Monte Carlo simulations, to analyze nucleoprotein condensates formed between viral cDNA mimics and recombinantly expressed IN. IN can induce (flexible) DNA bends and DNA loops. Furthermore, DNA-bound IN complexes were found to be larger than unbound complexes, suggesting that DNA binding induces conformational changes leading to higher order oligomerization. At concentrations 500 – 1000 nM, IN induces formation of large DNA complexes with multiple DNA loops extending from the center, that we refer to as rosettes. At higher IN concentrations 1000 – 1500 nM, a second compaction transition occurs in which the extruding loops of the rosette structure collapse onto the core of the condensate and full compaction is achieved. The resulting fully collapsed condensates drastically (∼30-fold) reduce the volume occupied by the viral genome (Figure 66A).

In addition, our data indicate that in the fully collapsed condensate, a rigid central core is surrounded by a diffuse outer layer. It is interesting to note that this architecture resembles a polymer brush, the model that similarly describes the folding of eukaryotic chromosomes that are order of magnitude larger. Importantly, we experimentally demonstrate that the core and outer layer IN-

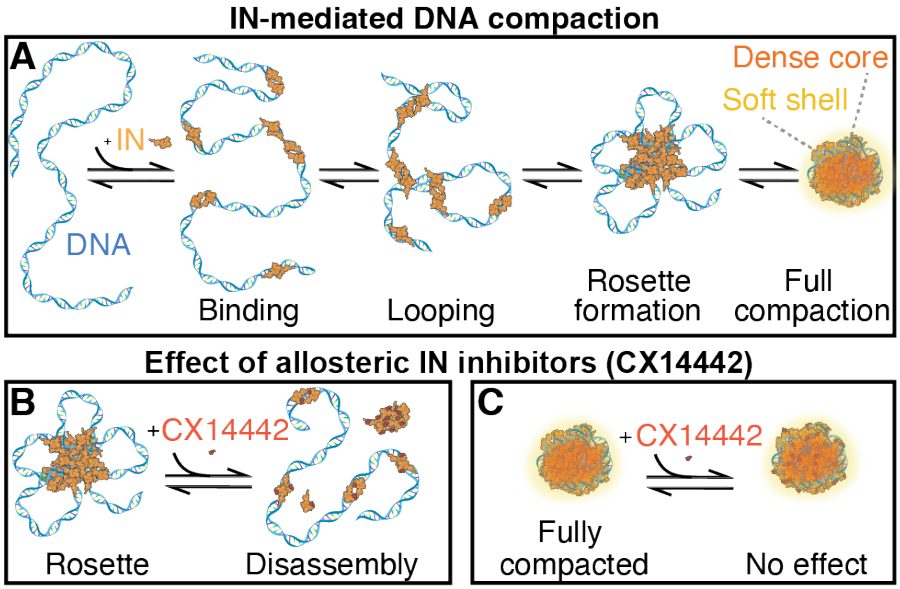

Figure 66: Model for IN-mediated DNA compaction. A) Schematic model of DNA compaction by IN. At increasing IN concentrations, the protein binds to the DNA and can form DNA loops. At intermediate concentration, loop-extruding complexes, so-called rosettes, form. At high IN concentrations, full compaction occurs. The DNA compaction is reversible. B) Allosteric IN inhibitors (CX14442) can de-compact rosettes. C) Allosteric IN inhibitors (CX14442) cannot de-compact fully compacted IN-DNA condensates.

DNA complexes interact differently with the allosteric IN inhibitor CX14442: while the core complex dissolves in a CX14442 concentration-dependent manner, the coat is not susceptible to CX14442 in the concentration range probed (Figure 66B,C).

6.3.5 *Discussion*

Provided that our experiments give a very reductionist view of HIV DNA genome compaction, it is important to evaluate potential relevance with regards to viral condensates in the infected cell. In this regard, the size of IN-DNA condensates *in vitro* compare very favorably to sizes found by super-resolution microscopy *in vivo* and to those of PICs purified from infected cells [347]. In addition, *in vivo* IN plays a crucial role during capsid uncoating [348], and IN mutants defective for non-specific DNA binding are impaired for nuclear import [349] and reverse transcription [363]. Thus, it appears that IN plays a critical role within the cytoplasmic viral capsid during the early stages of infection. Maybe, these effects involve an architectural role for IN as a DNA compaction agent – similar to the established role of IN during folding of the RNA genome in nascent virus particles [151]. Nevertheless, we stress that our data do not rule out the involvement of other DNA interacting viral proteins that have been shown to induce DNA compaction *in vitro*, such as the nucleocapsid [332, 339] and Vpr proteins [364].

Last, we are convinced that the highly quantitative approaches will be highly instrumental towards future efforts aiming to unravel the molecular mechanisms governing retroviral nucleoprotein condensation. These methods could enable further establishing the role of IN and other DNA-binding viral proteins in compaction of vDNA. We especially anticipate breakthrough insights into PIC architecture by combining bottom-up (i.e. reconstitution) and top-down (i.e. purification) approaches. Similarly, it would be intriguing to also study the effects of IN on HIV RNA compaction, which has an established biological role during virus maturation. Last, we expect our experimental platform to be valuable for the in-depth mechanistic investigation of strand transfer and allosteric inhibitors of IN on DNA compaction, and potentially uncover the mode of action of future inhibitors targeting disordered phases of IN and its condensates.

6.3.6 *Author Contributions*

W.V. designed this study. Z.D. and F.C. purified and provided the IN protein and the allosteric IN inhibitor; M.d.J. and L.F. ran simulations; P.J.K., T.B. and W.V. performed AFM measurements and analyzed the resulting data; S.F.K. provided code for analyzing the AFM data; P.J.K. and M.G. performed MT measurements and W.V., P.J.K., and M.G. analyzed the resulting MT data; W.V. and J.L. supervised research; W.V., J.L., and P.J.K. wrote the manuscript with input from all authors.

6.3.7 *Funding*

This work was supported by the Deutsche Forschungsgemeinschaft (DFG, German Research Foundation) through SFB 863, Project 111166240 A11 and by Utrecht University.

6.3.8 *Notes*

The authors declare no competing financial interest.

6.3.9 *Acknowledgements*

We thank Ben Bekaert and Michael Hafner for initial measurements, Thomas Nicolaus for laboratory assistance, and Rinske Alkemade, Frank Smallenburg, Gerhard Blab, Paulo Onuchic, Wolfgang Ott, and Arthur Ermatov for helpful discussions.

6.3.10 *Materials and Methods*

6.3.10.1 *HIV integrase expression & purification*

For all experiments, we used His-tagged HIV-1 integrase (IN) recombinantly expressed from pKB-IN6H250 and purified as described previously [365–369]. The small-molecule allosteric IN inhibitor CX14442 was synthesized as described previously by Christ *et al.* [370].

6.3.10.2 *AFM imaging with short DNA*

The AFM samples are prepared by incubating 2.5 ng/µL viral cDNA mimics (491 bp and 1000 bp DNA with 16 bp terminal sequences corresponding to viral U3 and U5 ends; ScaI linearized miniHIV plasmid [330] and recombinant (C-terminal His-tag) IN at different concentrations, in high sodium buffer (10 mM Tris-HCl pH= 7.6; 250 mM NaCl; 5 mM $MgCl_2$) and at 37 ° C for 30 min, and subsequent 5-fold dilution in low sodium buffer (10 mM Tris-HCl pH= 7.6; 50 mM NaCl; 5 mM $MgCl_2$) just prior to drop-casting onto poly-L-lysine-modified mica. After allowing adsorption for 30 s, mica substrates were rinsed with milliQ water and dried using a gentle flow of filtered N_2 or argon, respectively. AFM imaging was performed in amplitude-modulation ("tapping") mode in air using a Nanoscope IV Multimode AFM.

6.3.10.3 *AFM imaging with long DNA*

Using Gibson assembly and blunt end cloning (described in greater detail in Section 3.4 in Chapter 3 in this thesis) we generated three viral cDNA mimics (3437 bp, 4751 bp, 9112 bp) from the miniHIV parental plasmid [330]. All three exhibit two 180 bp terminal sequences corresponding to viral U3 and U5 ends. The plasmids are linearized using the cutting enzyme ScaI (NEB). The AFM samples are prepared by incubating 5 ng/µL DNA and IN at different concentrations in high sodium buffer (HSB; 250 mM NaOAc, 25 mM Tris, 5 mM $Mg(OAc)_2$) at room temperature, and subsequent 5-fold dilution in 25 mM Tris (changes in temperature and incubation time did not show significantly different compaction behavior, see Supplementary Figures 74 and 75). The sample was deposited on freshly cleaved aminopropylsilatrane (APS)-modified mica. The sample was incubated for 30 seconds before being washed with 20 mL of MilliQ water and dried with a gentle stream of filtered argon gas.

After sample preparation, AFM images were acquired in tapping mode at room temperature using a Nanowizard Ultraspeed 2 (JPK, Berlin, Germany) AFM with silicon tips (FASTSCAN-A, drive frequency 1400 kHz, tip radius 5 nm, Bruker, Billerica, Massachusetts, USA). Images were scanned over (5 × 5) μm^2 or smaller areas at a scan speed of 5 Hz. The free amplitude was adjusted to the complex heights, usually 20 nm. The amplitude set point was set to 80% of the free amplitude and adjusted to maintain good image resolution.

Force-volume experiments were performed in aqueous buffer (50 mM NaOAc, 25 mM Tris, 1 mM $Mg(OAc)_2$) using the Nanowizard Ultraspeed 2 (JPK, Berlin, Germany) this time with silicon tips (BL-AC40TS, drive frequency 25 kHz in water, tip radius 10 nm, Olympus, Tokyo, Japan). Cantilever spring constant and optical lever sensitivity were determined by fitting the frequency spectrum of thermal fluctuation, using a Lorentzian function. Imaging uses a peak force of 300 pN, loading rate of 2 µm/s, and a sampling rate of 20 kHz. Images were scanned over different fields of view and with pixel sizes between 4 and 10 nm (indicated for each image).

6.3.10.4 *AFM data analysis*

The post-processing of the AFM data was carried out using SPIP software (v.6.4, Image Metrology, Hørsholm, Denmark) to smooth and line-correct the images. Next, the images were analyzed using custom-written Python code to

determine the radii of gyration for the core of the IN-DNA clusters and the clusters themselves.

6.3.10.5 *Analysis of AFM based force-volume map data*

Processing of force volume maps was performed using MountainsSPIP v9 (Digital Surf) software, and includes baseline z-correction using a first order polynomial, and x-alignment of the curves using the approach segment of the force curves. The contact point for x-alignment is taken the first crossing of the deflection (y-)axis. The measured piezo height is converted to lateral tip position by correction for the bending of the cantilever. To this end the cantilever deflection (measured in units of length) is subtracted from the piezo height.

Individual force curves were analyzed in terms of stiffness, elastic deformation energy, and plastic deformation energy. Stiffness k was determined by taking the slope of a linear fit to the approach segment within the force regime of 0 – 200 pN. Elastic deformation energy ΔG_{Elast}, (defined as the area enclosed by the retract segment above the x-axis, i.e. at zero force), and the plastic deformation energy ΔG_{Plast}. (defined as the area enclosed by the approach segment above the y-axis), were used to define a visco-elasticity index

$$\eta = 1 - \frac{\Delta G_{Elast}}{\Delta G_{Elast} + \Delta G_{Plast}} \tag{45}$$

Maps of the spatially resolved stiffness, and deformation energies were generated and used to identify and extract areas corresponding to nucleoprotein complexes. The pixel values were pooled per particle and the midpoint of the Abott-Firestone curve (i.e. at 50% material ratio) was used to determine means and standard deviations. Significance tests used two-sample t-tests.

6.3.10.6 *Magnetic tweezers setup*

The MT experiments were carried out using a custom-built MT setup that has been described previously by Kriegel *et al.* [173]. In brief, two magnets (5 × 5 × 5 mm3; W-05-N50-G, Supermagnets, Switzerland) are mounted vertically [172, 371] on a movable arm with two motors, a translational one (M-126.PD2 motor with C-863.11-Mercury controller, PI, Germany) and a rotational one (C-150.PD motor with C-863.11-Mercury controller, PI, Germany) to control the rotation and z-position of the magnets, respectively. The setup is controlled by Lab-VIEW software (National Instruments) which has been described previously by Cnossen *et al.* [176].

The magnets are placed above a flow cell, which was constructed from two glass cover slips (24 × 60 mm, Carl Roth, Germany). The lower cover slip was pre-functionalized with (3-glycidoxypropyl)trimethoxysilane (abcr GmbH, Germany) as described by Kriegel *et al.* [174]. The silanized slides were then covered with 75 µL of a 5000-fold diluted stock solution of polystyrene beads (Polysciences, USA) in ethanol (Carl Roth, Germany) and slowly air dried to later serve as reference beads for drift correction. The upper cover slip was equipped with two holes of ∼1 mm in diameter, drilled with a laser cutter to allow for fluid exchange in the flow cell. To this end, the outlet of the flow cell was connected via an adapter piece to a peristaltic pump (ISM832C, Ismatec). The lower and upper cover slips were assembled with a single layer of parafilm

(Carl Roth, Germany), pre-cut to form a ∼50 µL channel connecting the inlet and outlet ports of the flow cell, on a heating plate at ∼80 °C for 30 s.

After flow cell preparation, 100 µL of 200 µg/mL anti-digoxigenin (abcam, Germany) in 1× phosphate-buffered saline (PBS) was introduced into the flow cell and incubated overnight. The flow cell was then rinsed with 800 µL of 1× PBS and passivated with BSA (25 mg/mL; Carl Roth, Germany) for 1 hour to minimize non-specific interactions. The flow cell was then again rinsed with 1 mL of 1× PBS to remove any residual material.

6.3.10.7 *DNA constructs and magnetic beads for magnetic tweezers*

For the MT experiments, we used a 21-kb DNA construct, prepared as described previously by Kriegel *et al.* [174]. The two ends of the DNA segments were provided with handles (∼600 bp) containing several biotins and several digoxigenins, respectively, to bind magnetic beads and the bottom surface of the flow cell. As magnetic beads we used streptavidin-coated M270 beads (with a diameter of 2.8 µm) and MyOne beads (with a diameter of 1 µm; both purchased from Thermo Fisher Scientific, Germany). We attached the DNA construct to the magnetic beads by incubating 0.5 µL picomolar DNA stock solution and 13 µL beads in case of M270 beads or 2 µL in case of MyOne beads in 200 µL PBS for 30 seconds. The DNA-bead solution was then introduced into the flow cell to allow the multiple digoxigenin-anti digoxigenin bonds to form on the surface. The flow cell was then rinsed with 1 mL of 1× PBS to remove any unbound DNA tethers.

6.3.10.8 *Magnetic tweezers measurements*

Before starting the actual experiment, the DNA-bound beads were tested for being attached to a single DNA tether (and not multiple) and their torsional constraints by measuring their response to force and torque. Beads bound to the flow cell surface via multiple DNA tethers were excluded from further analysis. Nicked as well as supercoiled tethers were included in the analysis. In the next step, the length of the DNA tethers was checked by changing the force from 5 pN to < 0.1 pN. At 5 pN the DNA constructs are stretched to $> 95\%$ of the contour length, whereas at < 0.1 pN they feel almost no force, therefore this force is used as a reference for zero tether extension. We keep only tethers that show the expected contour length (∼7 µm)t. After selecting the DNA tethers for the experiment, the flow cell was flushed with 800 µL of low sodium buffer (LSB, 25mM Tris-HCl pH= 7.6; 5mM MgCl2; 50 mM $MgCl_2$), followed by 50µL of 2 mM IN diluted in LSB flushed at 1.7µL/min, while holding the magnet to apply a force of 5 pN onto the beads. Subsequently, the force was lowered to let the tethers relax and to obtain a control value of the tether length at 1 pN for the analysis. The magnets were next moved completely up to apply a very low force (> 0.1pN) to allow for IN-DNA interaction. After ∼5 min, the magnet was moved again closer to the flow cell to create a sudden force jump to a specific constant force (e.g. 0.5 pN, 1 pN, 2 pN, or 5pN, respectively). The z-extension of the DNA tethers was monitored over several hours or until full extension of the DNA tethers were reached.

6.3.10.9 *Analysis of magnetic tweezers data*

Magnetic tweezers data were analyzed using custom written code in Matlab (R2022a, Mathworks). The individual tethers time traces were drift corrected using the x,y,z-coordinates of reference beads, de-spiked by linear interpolation using the build-in data cleaner app, and smoothed using a Butterworth filter. The resulting extension-time traces are differentiated to yield velocity-time traces, and subsequently analyzed using the peak finder function. Dwell times are calculated from successive peak locations, burst velocities are evaluated at the peak maximum, and burst sizes are calculated by peak integration.

6.3.10.10 *Monte Carlo simulations*

We simulated the DNA-IN interaction using coarse-grained Monte Carlo (MC) simulations. For this, we modelled the DNA via a beads-on-a-string model with a bead size of 16 bp of DNA. The DNA beads interact via an excluded-volume interaction to prevent overlapping, and subsequent beads are connected by springs. To reproduce the experimentally determined bending stiffness of DNA, we introduce a bending potential which penalizes sharp kinks between subsequent springs. The IN proteins are modelled as beads of the same size as the DNA beads. They can bind to DNA beads via an isotropic, short-ranged binding potential, and the (assumed) tetrahedral nature of IN is captured by imposing a maximum valence of 4, i.e. each IN bead can bind to at most four DNA beads. To determine the binding strength between IN and DNA, we measure the binding probability of IN to DNA as a function of the binding strength. From comparison to experimental data, the binding strength of IN to DNA was determined to be 5 k_BT (see main text and Figure 62 for details).

In order to investigate the role of the IN-IN interaction in the IN-induced compaction of DNA, we considered two cases for IN-IN interaction: (i) a purely excluded-volume interaction (same as for the DNA beads), and (ii) an excluded-volume interaction with some added short-ranged attraction. For both cases, we performed multiple simulations for a range of IN concentrations and DNA lengths. In all simulations, the DNA was simulated in the canonical ensemble, while we simulated the IN in the grand-canonical ensemble. This ensured that depletion of the free IN was suppressed. From the simulations, we obtained time series showing different compaction pathways. To classify these pathways and the individual states along these pathways, we developed an unsupervised machine learning pipeline. For this we composed a training data set of several thousand snapshots from these time series. Then, for each snapshot in the data set, we computed 15 different parameters which captured the structural configuration of the DNA-IN complex. Next, we used principal component analysis (PCA) to reduce the dimensionality of the 15-dimensional input. We found that 3 dimension were sufficient to retain all important features of the input data. Furthermore, we observed distinct clusters in this 3D principle component distribution. Hence, we used a clustering algorithm – in this case a Gaussian mixture model (GMM) – to provide an unsupervised and objective clustering of the 3D space into seven categories for (compacted) DNA-IN complexes. Using the trained unsupervised machine learning pipeline, we then classified every configuration of each time series.

6.3.11 *Supplementary figures*

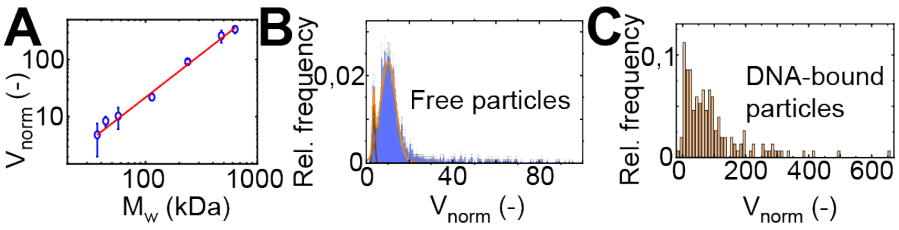

Figure 67: DNA binding triggers IN higher-order oligomerization. A. Calibration curve of protein volumes normalized by the volume of co-deposited free DNA as a function of known protein molecular weights (errors are standard deviation of the protein volume distributions). Interestingly, the volumes of protein particles measured by AFM scale non-linearly with molecular weight Mw, but are well-described by a power law fit: $V_{NORM} = 0.0198^{0.0291}_{0.0105} \times Mw^{1.52^{1.61}_{1.43}}$ (for $Mw \leq 632$ kDa; $\chi^2_{red} = 1.14$) despite correcting for the finite size of the AFM tip by using the volume per nanometer length of co-adsorbed DNA. This is in contrast to a previous report [272] that found a linear relation ($V_{norm} \propto Mw$), though for non-globular proteins with heights not exceeding that of the DNA fiducial marker. B. Histogram of normalized protein volumes of free IN particles ($n_{tot} = 2305$). The data are well-described by a double Gaussian fit ($\chi^2_{red} = 0.85$). Nevertheless, ~17% of the total population is not covered by the fit at higher measured volumes. We deduce molecular weights of the two different populations $Mw1 = 30 \pm 14$ kDa (8%) and $Mw2 = 60 \pm 54$ kDa (75%) (errors reflect uncertainty due to propagation of fit parameter uncertainties for the calibration curve, and from the standard deviation of the Gaussian fit to the volume distribution), suggesting a small fraction of IN monomers ($Mw = 32$ kDa) and a dominant fraction of IN dimers ($Mw = 64$ kDa), in agreement with previous *in vitro* reports [354, 372, 373]. We note that the population centered at $V_{norm} \approx 10$ (assigned to IN dimers) is very broad. This could be due to the existence of diverse dimeric forms [374], which are differently affected by AFM tip convolution. C. Histogram of normalized protein volumes of DNA-bound IN particles ($n_{tot} = 152$). In this case, assigning the oligomeric state is complicated by the additional volume of DNA inside the complex. We have addressed this complication by quantifying the volume of the entire protein-DNA complex and subtracted the average volume of surrounding free DNA molecules. We find the resulting protein volume distribution to be significantly broader and shifted to larger volumes as compared to the DNA-unbound IN population. We speculate that higher-order IN oligomerization triggered by DNA binding might result from large-scale structural rearrangements of IN on DNA binding [145, 375, 376].

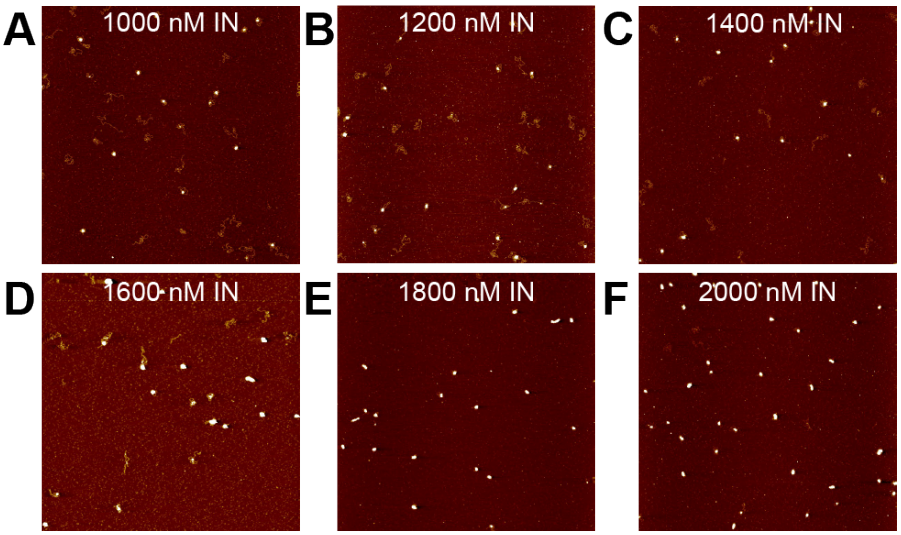

Figure 68: 3.4 kbp DNA compaction by IN. The compaction of 3.4 kbp DNA is very similar to 4.8 kbp DNA except for the fact that there is no rosette state observed but the compaction occurs in one single step. A. – F. Overview AFM topographs (5 µm × 5 µm) of the 3.4 kbp DNA in the presence of IN in concentrations ranging from 1000 nM to 2000 nM.

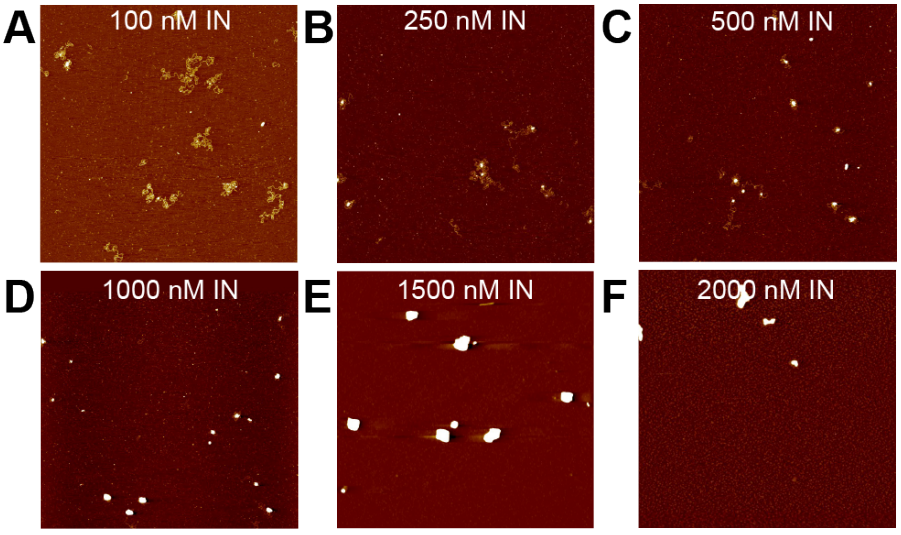

Figure 69: 9.1 kbp DNA compaction by IN. The compaction of 9.1 kbp DNA is very similar to 4.8 kbp DNA. A. – F. Overview AFM topographs (5 µm × 5 µm) of the 9.1 kbp DNA in the presence of IN in concentrations ranging from 100 nM to 2000 nM.

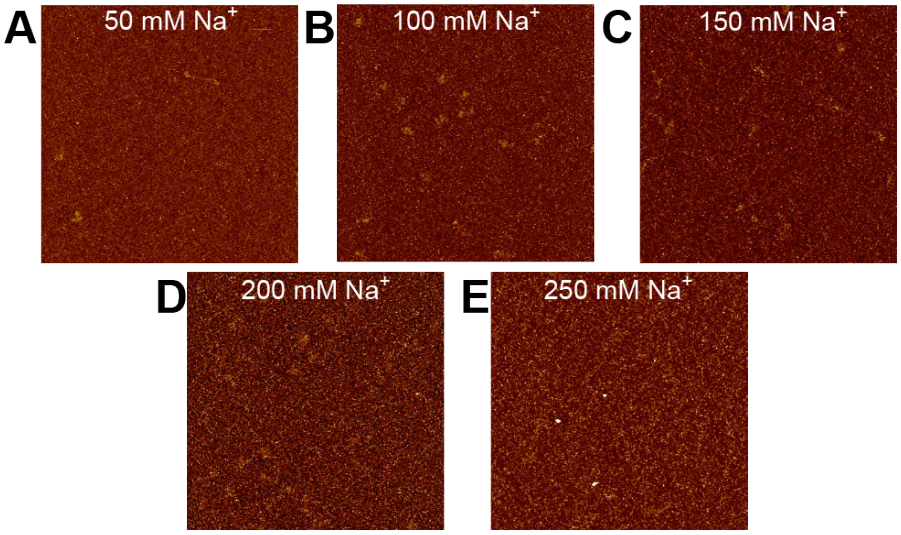

Figure 70: DNA incubated with 2000 nM IN without dilution step at different sodium concentrations. A. – F. Overview AFM topographs (5 µm × 5 µm) of the 4.8 kbp DNA in the presence of 2000 mM IN at sodium concentrations ranging from 50 nM to 250 mM. Without the incubation step, no DNA compaction is observed.

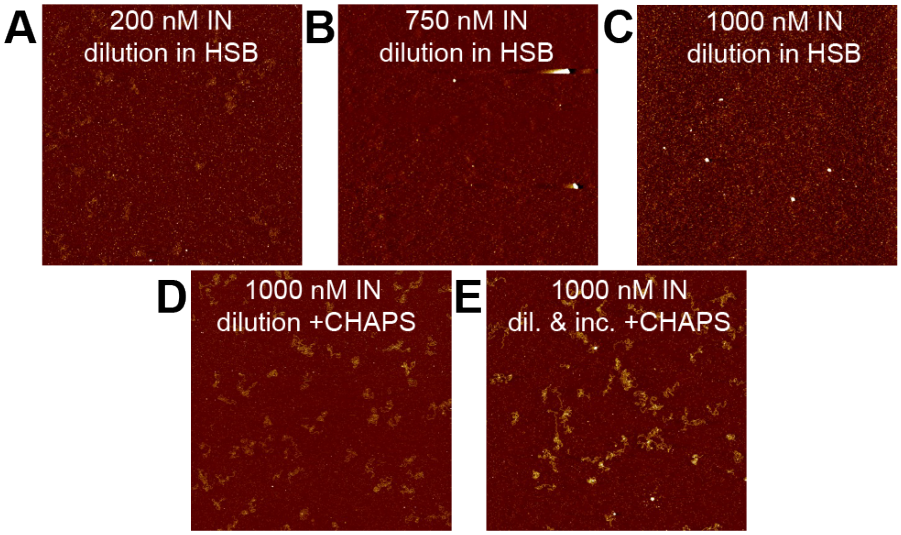

Figure 71: DNA incubated with IN with dilution step but at different ionic strength or in addition of CHAPS. A. – C. Overview AFM topographs (5 µm × 5 µm) of 4.8 kbp DNA in the presence of varying IN concentrations (200, 750, and 1000 nM). After incubation, the IN-DNA mix is not diluted with a low-salt buffer, but instead with HSB (250 mM Na^+, 5mM Mg^{2+}). No DNA compaction is observed. D. Overview AFM topographs (5 µm × 5 µm) of 4.8 kbp DNA in the presence of 1000 nM IN concentrations (200, 750, and 1000 nM). After incubation, the IN-DNA mix is diluted with LSB to which CHAPS ((3-[(3-Cholamidopropyl)dimethylammonio]-1-propanesulfonate)) was added. E. Same as in panel D but also during the incubation step CHAPS was added. No DNA compaction is observed.

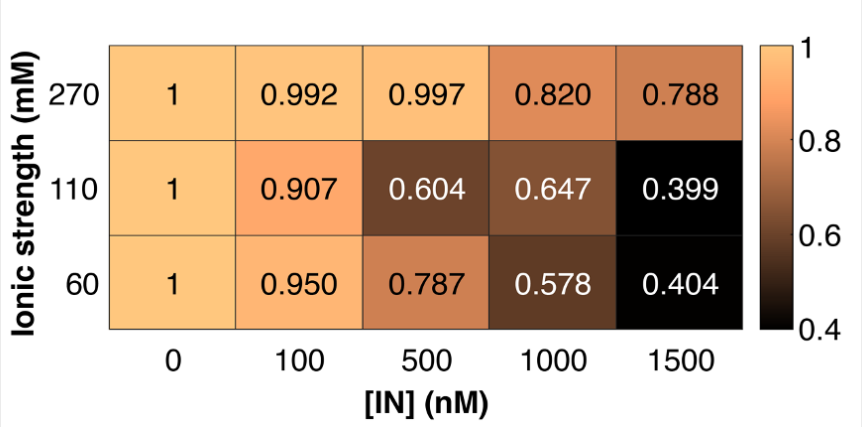

Figure 72: Phase diagram depicting the normalized relative radius of gyration of the nucleoprotein complexes formed as a function of [IN] and ionic strength of the solution. At high ionic strength, compaction is significantly less than lower ionic strength and no full compaction is reached even at high [IN].

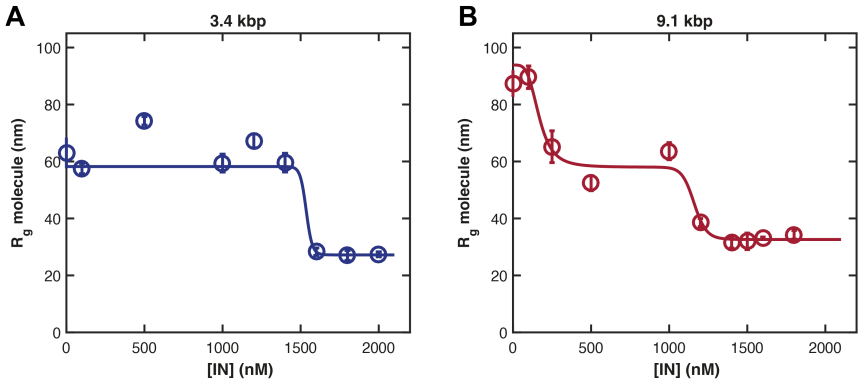

Figure 73: Radius of gyration of the nucleoprotein complex for 3.4 and 9.1 kbp DNA at 60 mM ionic strength as a function of [IN]. A. The data for the 3.4 kbp DNA (see Supplementary Figure 68) reveal only one compaction transition at ∼1500 nM. It is therefore fitted by a single-Hill-fit. B. The data for the 9.1 kbp DNA (see Supplementary Figure 69) show two distinct compaction transitions and are fitted by a double-Hill-fit: the first transition from open state to rosette state occurs at ∼300 nM, the second transition from rosette state to fully compacted state at ∼1100 nM.

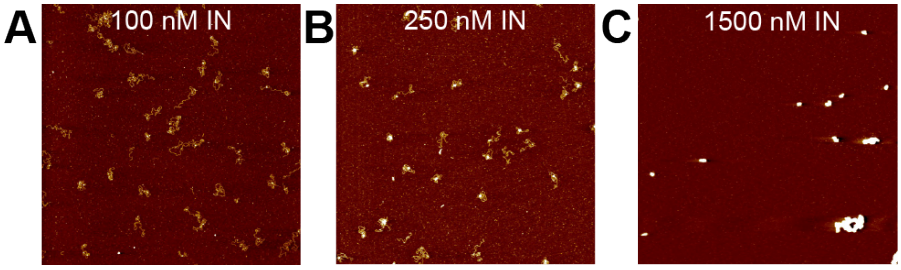

Figure 74: Incubation of the IN-DNA mix at 37 °C instead of room temperature. A. - C. Overview AFM topographs (5 µm × 5 µm) of the 4.8 kbp DNA in the presence of 100, 250, and 1500 nM IN incubated at 37 °C for 30 minutes before deposition. Since no effect of the incubation temperature on the compaction behavior was observed, the incubation was carried out at room temperature for all experiments shown in this work for convenience.

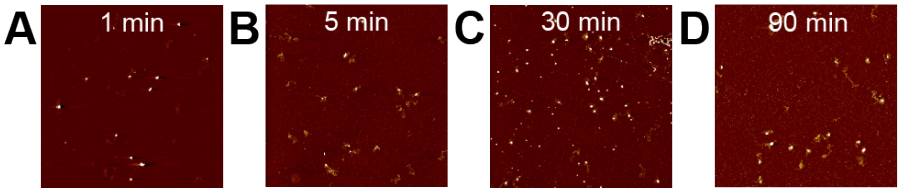

Figure 75: Different incubation times of DNA and IN. A. - D. Overview AFM topographs (5 µm × 5 µm) of the 4.8 kbp DNA in the presence of 500 nM IN for different incubation times (1 min – 90 min) before deposition. Since no effect of the incubation time on the compaction behavior was observed, the incubation time was set to 5 min for all experiments shown in this work for convenience.

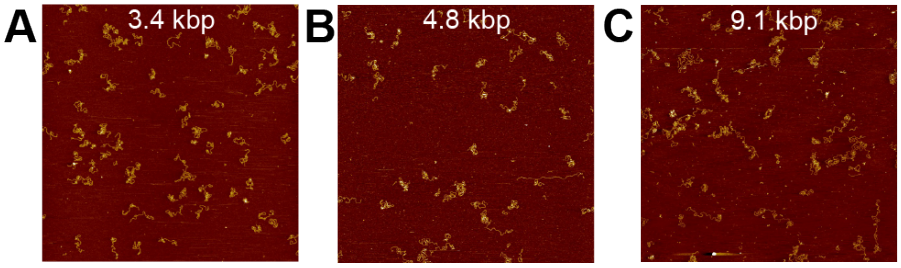

Figure 76: Bare DNA in 50 mM Na^+, 1 mM Mg2+. A. Overview AFM topograph (5 µm × 5 µm) of the 3.4 kbp DNA without IN B. Same as in panel A for 4.8 kbp DNA. C. Same as in panel A for 9.1 kbp DNA.

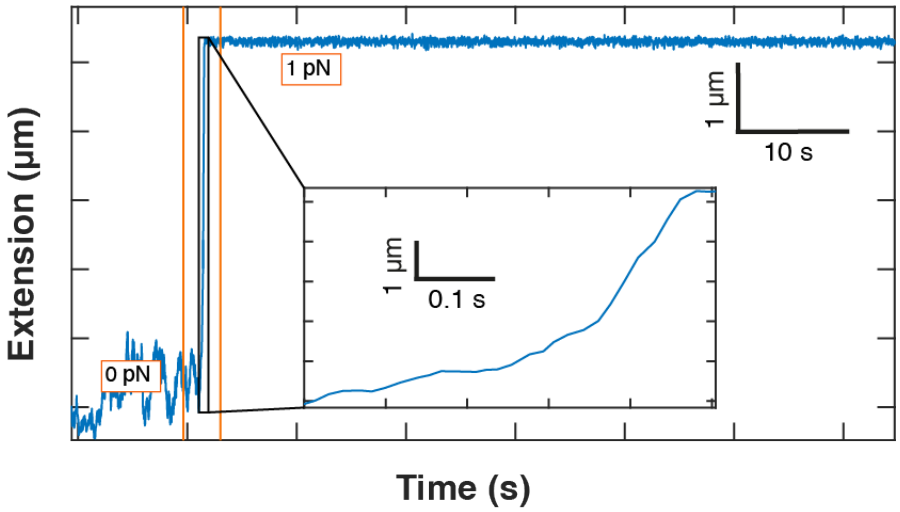

Figure 77: Exemplary MT extension curve over time at a constant force of 1 pN in the absence of IN.

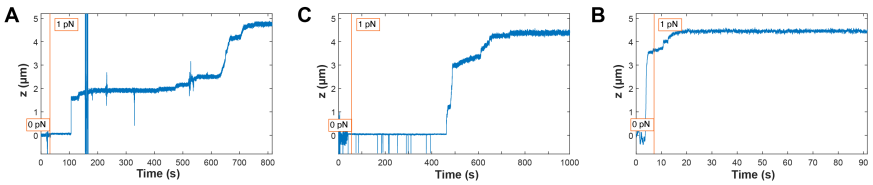

Figure 78: Series of three MT extension curves over time at a constant force of 1 pN and in the presence of 2 µM IN. The three extension curves were recorded in succession for the same DNA tether showing the reversibility of the system.

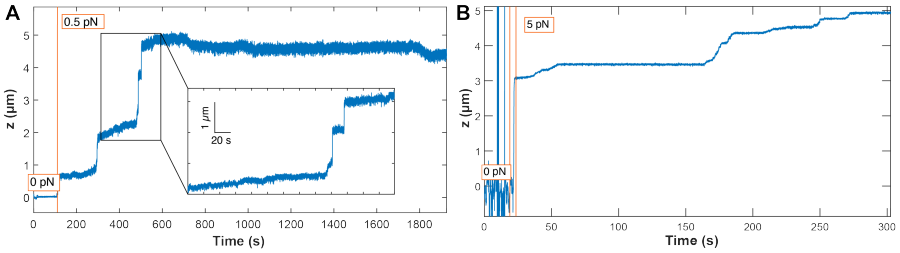

Figure 79: Exemplary MT extension curves over time at a constant force and in the presence of 2 µM IN. A. F = 0.5 pN B. F = 5 pN.

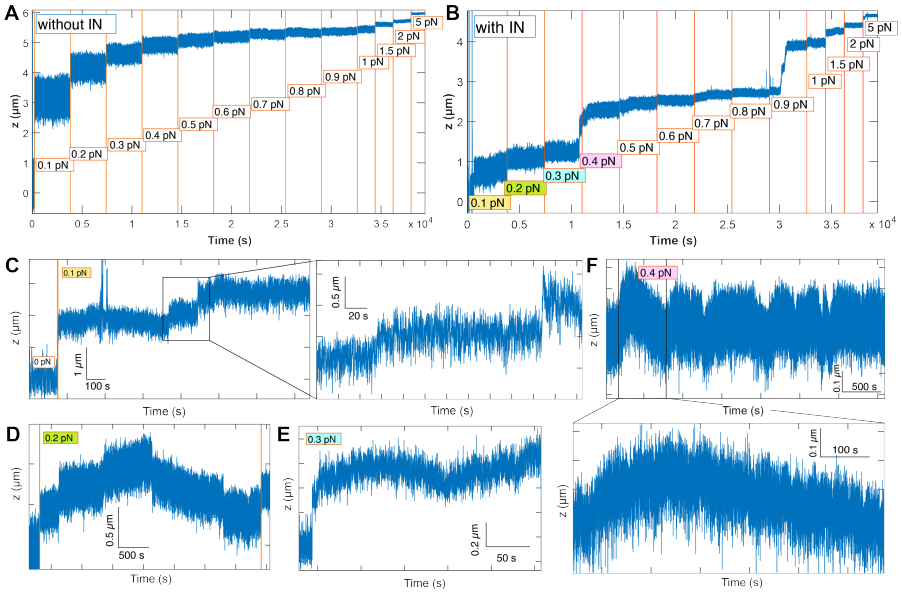

Figure 80: Exemplary MT force extension curve over time with constant force plateaus. A. MT force-extension curve ranging from 0.1 to 5 pN recorded in the absence of IN. B. MT force-extension curve ranging from 0.1 to 5 pN recorded in the presence of 2 µM IN. C. Zoom in at 0.1 pN including an additional zoom to visualize the broad fluctuations. D. Zoom in at 0.2 pN showing de-compaction and compaction of several hundred nanometers. E. Zoom in at 0.3 pN. E. Zoom in at 0.4 pN including an additional zoom to visualize the continuous compaction and de-compaction at constant force. The zooms for the individual force plateaus in panel C – F are not from the same trace shown in panel B.

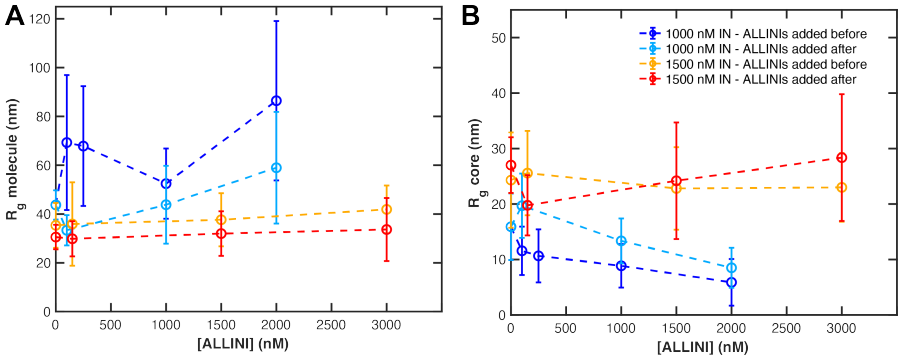

Figure 81: Effect of adding allosteric inhibitors (ALLINIs) to IN-DNA condensates before and after compaction. A. Radius of gyration for the entire molecule for the rosette state (1000 nM IN) and the fully compacted state (1500 nM IN) for varying [ALLINI] and for adding the ALLINIs before or after the compaction reaction. B. Same as in panel A for the radius of gyration for the core of the condensates.

7

CONCLUSIONS AND OUTLOOK TO FUTURE WORK

In summary, I have studied three different systems in this thesis, which – to a greater or lesser degree – involve a phase transition. Such phase transitions reflect spontaneous transformations of collective organization. They occur in each case when the system undergoes a change of state characterized by a transition in the value of the order parameter. This occurs at the critical value of a control parameter that affects the state of the system. From the fact that these phase transitions occur in very different biological systems, we learn that living systems make extensive use of phase transitions in ensuring their proper working. The American physicist and author Mark Buchanan wrote 2019 in a *Nature Physics* article about biological transitions:

> Perhaps nothing is more crucial for living organisms than to maintain precise spatial control over their biochemical processes [39].

In the light of evolution, it is known that organisms take advantage of mechanisms that allow compartmentalization of complex systems, which is often done by phase separation. But there are many more phase transitions that biology uses to its benefit. Another example is the behavior of so-called active matter, such as the swarming of bacteria on a hard surface. Here, too, phase transitions reflect spontaneous transformations of collective organization. Taken together, phase transitions in complex systems thus represent a strongly evolving and yet always surprising field of research with innumerable facets [39].

In this thesis, I answered three research questions, all of which revolve around the topic of *phase transitions in linear polymers*. In the first results chapter of this thesis (Chapter 4), I presented a thermally switchable nanopore for macromolecular transportation. The toggle switch to open or close the pore for translocation is based on a phase transition of LCST polymers grafted inside the nanopore. Because of this unique property of the pore, I was able to create a system that allows selective nanoscale transport for DNA and, in particular, viruses. The used LCST polymers are specifically designed for this application. Therefore, also the grafted pore could be adapted user-specific, for example the underlying nanopore could be enlarged to enable specific and controlled transport of larger cargo. Then also the grafted polymers could be adapted to maintain the toggle switch between an open and a completely closed pore. In the direction of smaller molecules I have already sought to expand the range of cargo macromolecules. To this end, I have worked with the small protein bovine serum albumin (BSA) and the simple sugar dextran and have been able to show for both molecules in ensemble fluorescence measurements that selective transport through thermally switchable nanopores is possible even for these very small cargo molecules. This shows how diverse the possible areas of use for this gating system are already now. And moreover, building on the work done so far, customized, efficient, reliable and cost-effective nanogates for applications ranging from pharmaceutical processing and drug sensitivity testing to drinking water treatment and waste disposal in agriculture, industry, and research come within reach.

The focus of the second result chapter (Chapter 5) was a newly designed DNA origami structure. The precise organization of biological and non-biological materials in 3D-space at the nanoscale holds great opportunities for a variety of applications in structural biology, sustainable energy, photonics, electronics, biophysics, medicine, and more. Therefore, DNA nanotechnology research revolves around the question of how to develop more powerful methods that provide greater precision and higher resolution. In this regard, the bottom-up nanotechnology DNA origami has emerged as a technique with unprecedented capabilities for self-assembly of rationally designed nanostructures, which are fully addressable with nanometer precision. This makes DNA origami a promising platform for the precise organization of other functional materials for applications in a variety of fields. In this work, I designed a DNA origami structure as fiducial for high-precision AFM imaging, which has several advantages over existing methods: it can be co-deposited for *in situ* tip characterization, avoiding the tip damage and wear typical of *ex situ* tip characterizers, and it allows adaptive evaluation as the tip shape changes during scanning. I demonstrated the versatility of this method by applying it to biological macromolecules and synthetic nanoparticles on a variety of surfaces and in a wide range of aqueous solutions. Taken together, this newly developed DNA origami fiducial structure enables AFM tip characterization and image reconstruction, is easy to use, provides reliable and quantitative results, and is widely applicable. I am confident that the presented fiducial structure will become a useful tool for high-resolution AFM imaging. Building on the published work, I aspire to enlarge the field of applications for our DNA origami fiducial structure for AFM imaging. Most importantly, since the structure is built from DNA origami, it can easily be modified and adapted to meet user-specific requirements. For example, additional steps could be added or the existing steps could be altered. Structures on or within the fiducial could be used to quantify and optimize the resolution of AFM images while correcting for lateral dimensions. With this, it is possible to add fluorescent dyes and/or additional staple strands for DNA PAINT (point accumulation in nanoscale toppography) [260, 377, 378] in order to expand the AFM fiducial as a simultaneous alignment tool for correlation microscopy [255, 303–305, 320, 321]. Recent break-throughs in "super-super resolution" microscopy [265] and in the intrinsically high resolution of AFM imaging [273] have the potential to enable sub-nm resolution in both the AFM and optical channels, in a new type of "super-super-super resolution" imaging. Another possible research direction would be to go beyond imaging and apply the fiducial as a mechanical stiffness reference marker for biomolecules under force [322]. Soft biological materials are deformed by interaction with the AFM tip, and our reference structure can provide a convenient reference to account for these effects when correcting images. Together with Willem Vanderlinden and Hemani Chhabra I am therefore currently working on an application of the same fiducial structure to study the stiffness of multilayer DNA origami with the ultimate goal of establishing a stiffness standard for biomolecules, their complexes, and various other types of nanostructures. With this, for example the effects of silicification [323, 324, 379] or other fictionalizations could be studied. Moreover, one could determine areas inside a molecular complex or nanostructure with increased or decreased local stress. This would enable to localize for example target points for antiviral drugs or to detect defects in nanostructures. Taken together, I expect the presented fiducial structure to provide a multimodal calibration

platform for a variety of applications within and beyond bionanotechnology, paving the way for accurate multidimensional AFM measurements.

In the third result chapter (Chapter 6), I studied in detail the compaction of vDNA by the viral protein IN. Using AFM imaging, I was able to show that IN binding locally alters the structure of the DNA by bending, looping, and bridging. By quantifying the viral genome compaction as a function of IN concentration, ionic strength, and DNA length, I could show that compaction occurs in two distinct concentration regimes, and results in the formation of supramolecular structures consistent with super-resolution microscopy *in vivo*. AFM-based elasticity mapping further revealed that condensates feature a relatively rigid core surrounded by a "fuzzy" coating, which is significantly more compliant towards indentation forces. Together, these results imply that IN compacts the viral genome into biphasic condensates that are held together by two different types of interaction forces. The results further suggest that IN might extend its functionality – i.e., catalytic versus structural – by adopting different roles depending on the environment. I assume that this system is not an isolated case in this way, but that there are many other proteins that fulfill other tasks in addition to their previously known role. Therefore, I hope that the interaction of the protein IN with DNA will serve as a model system through which other unknown protein functions can be discovered and a deeper understanding of protein-DNA interactions and the phasic behavior involved can be achieved. As a follow-up or extension to the work presented so far, it would be interesting to study the effects of IN on RNA, since vDNA is only the reverse-transcribed form of the original RNA genome of HIV. Also, the allosteric IN inhibitor tested in this work is only one exemplary drug, it would be instructive to compare the obtained results to the outcomes from using other allosteric IN inhibitors to obtain a deeper understanding of the molecular mode of action of these small molecules. Furthermore, by testing DNA-binding deficient mutants of IN, more insight into the DNA-binding interface of IN could be gained. It has been shown that the double mutant R263A/K264A is 10-20 fold less efficient at 3'-processing and strand transfer *in vitro* [349]. In addition, a mutation of a stretch of three amino acids R262, R263 and K264 was found to completely abolish aspecific DNA binding [380, 381]. With this, an improved characterization of the minimal DNA-binding domain of IN would be possible paving the way for specifically adapted drugs or vaccination approaches.

A

DEVELOPED AND OPTIMIZED PROTOCOLS

In the course of my PhD, I have developed, refined, or optimized various protocols for laboratory work steps and analyses. I would like to describe these protocols in the following.

A.1 ATOMIC FORCE MICROSCOPY PROTOCOLS

A.1.1 *AFM mica surface preparation*

As described in Section 3.1.3, we normally use muscovite mica as substrate for AFM imaging. To get a flat an clean mica surface, in a first step, a 25 mm round mica sheet (SPI-Chem Mica Grade V-1 25mm Discs, 0.275 to 0.325 mm, Item 01925-MB, SPI supplies) is cleaved either with a fresh scalpel or with adhesive tape. To facilitate adsorption of (negatively charged) DNA (complexes) on the mica surface, a positive spacing layer must be provided between the sample and the negatively charged mica. I used three different approaches to achieve this:

1. Use of a buffer containing divalent, positively charged ions such as magnesium
2. Addition of a positively charged layer of poly-L-lysine (PLL):
    - In preparation, clean a pair of inverted tweezers with isopropanol in sonicator for 15 min
    - Add 20 µL 0.01% PLL (Sigma Aldrich, catalog number: P0879 – diluted to 0.01% in milliQ water) centrally to the cleaved mica surface
    - Let incubate for 30 sec while holding the mica horizontally using (clean) inverted tweezers
    - Remove unbound PLL by washing the sheet gently with 50 mL milliQ water using the contents of the two syringes filled with 25 mL each
    - Make sure the sample is always covered by at least a small layer of liquid
    - Dry the PLL mica with a gently gas flow (argon or nitrogen), start in the center then go the the edges
    - If needed, remove leftover liquid with a dust-free tissue (Kimtech, catalog number: 5511)
3. Addition of a positively charged layer of aminopropylsilatrane (APS):
    - In preparation, make a stock solution from crystalline APS
        - Let the tube with APS crystals stand on the bench at room temperature for at least 1 hour (otherwise the crystal will soak water when you open the tube)
        - Prepare 50 mL stock solution of 50 mM APS in milliQ water: weigh 0.5809 g APS (MW: 232.36 g/mol) and dissolve in 50 mL milliQ water by turning the glass bottle a few times

  - Store the bottle in the fridge (4 °C)
- Dilute stock solution 300x in a glass beaker: 500 µL APS stock solution + 150 mL milliQ water
- Cleave mica plate from both sides with a fresh scalpel and place in appropriate Teflon holder (capacity for up to 10 mica disks)
- Place the Teflon holder into the beaker with the APS solution and let stand for 30 min at room temperature
- Rinse thoroughly with milliQ water by introducing the Teflon holder subsequently into three 1 L beakers filled with 750 m milliQ water (using a cleaned tweezers), each time moving 30x up and down with the holder
- Take the Teflon holder in your hand and rinse the mica disk(s) again thoroughly under the milliQ system next to the sink
- Dry the APS mica with a gently gas flow (argon or nitrogen)
- The APS mica sheets can be stored for a few hours in a dry and clean Teflon holder in a glass box filled with argon and sealed with parafilm (Carl Roth, catalog number: H666.1)

A.1.2 *AFM sample preparation*

AFM sample preparation for dry AFM measurements

After mica surface preparation, the sample is added to the dry (coated) mica. In the case of bare DNA, I typically used a concentration of 0.5 – 1 ng/µL and a volume of 15 – 30 µL. After incubating for 30 sec, the sheet is washed by adding 20 µL of milliQ water to the surface. Subsequently, mica is dried by a gently flow of argon or nitrogen and stored in a clean, labeled petri dish (3 or 5.5 mm; Carl Roth, catalog number: 0690.1) sealed with parafilm.

AFM sample preparation for liquid AFM measurements

For liquid AFM measurements, sample preparation is similar but has some variations. As a prerequisite for sample preparation, the liquid cells for imaging have to be prepared first. To this end, a small Petri dish (3 mm) is glued with its flat side centered on a glass slide with optical adhesive (Norland, 1 oz. NOA 68 (36-427) bottle, Edmund Optics). A 12 mm round mica plate (SPI-Chem Mica Grade V-1 12mm Discs, 0.275 to 0.325 mm, Item 01926-MB, SPI supplies) is then glued flat and centered in the Petri dish with the same glue. To solidify the glue, the liquid cell is then incubated for 30 min under a UV lamp (4 W, $\lambda = 366$ nm) at a distance of 3 cm. The liquid cell can then be used directly or stored at room temperature for several months in a dust free environment.

As described above (Section A.1.1) for dry measurements, the mica is then cleaved with adhesive tape. If an intermediate layer of PLL is added, the same concentration, quantity and working steps as for dry AFM measurements are used, except that the entire liquid cell is used instead of the mica plate during washing. With APS mica, the stock solution is not diluted in a beaker, but directly in the liquid cell. Here, a volume of 3 mL (1:300 stock solution in milliQ water) is used. After incubation at room temperature for 30 minutes, the liquid cell is washed with 500 mL of milliQ water and dried with a gentle gas stream (argon or nitrogen). The sample is then applied and after incubation

(approximately 3 – 5 minutes, varies from sample to sample), 2.5 mL of the buffered solution is added to the sample.

A.1.3 *AFM imaging*

The AFM images presented in this thesis are all recorded using a Nanowizard Ultraspeed 2 (JPK, Berlin, Germany) AFM. Different types of measurements are possible with this machine.

AFM imaging under dry conditions

A detailed and well-illustrated description of imaging with the Nanowizard Ultraspeed 2 by my former colleague Sebastian Konrad can be found in Ref. [382].

Before starting an AFM measurement under dry conditions, the following steps are conducted:

1. Setup preparation

- Prepare the (dry) sample by gluing the prepared mica centered on a glass cover slide using double sided tape and place the cover slide
- Install the glass slide with the mica plate on the sample holder of the AFM
- Start the AFM software (JPK SPM Desktop software)
- Choose imaging mode (e.g. AC mode fast imaging for fast scanning in air)
- Mount cantilever holder on holder support (make sure that the upper surface is level so that the tip does not fall off later) and tighten it in the support
- Install cantilever (e.g. FASTSCAN-A (drive frequency 1400 kHz, tip radius 5 nm, Bruker, Billerica, Massachusetts, USA)) centered in cantilever holder using Carbon tip tweezers
- Make sure the tip of the cantilever is located above the reflecting part of the cantilever holder
- Tighten the cantilever in the cantilever holder with the screw on the back of the holder (not too tight)
- Carefully carry the cantilever holder on the holder support to the AFM, and transfer the cantilever holder from the holder support to the AFM head; to insert the cantilever holder, use the position of the holder with the tip of the cantilever facing up, and then rotate the holder 90° clockwise to lock its position (same mechanism as for the holder support)
- Connect the cable from the cantilever holder to the fast scanning piezo (HG) on the right above the cantilever holder
- Mount the AFM head on the AFM stage; starting at the rear, place the feet in clockwise direction

2. Calibration

- Insert the filter on the side of the microscope to block the laser light and switch on the lamp (the switch is located at the rear left of the microscope)

- Next, bring the cantilever in focus by carefully moving the stage in y-direction using the 'navigate' tab of the program and by focusing the microscope using the big screw on the right of the optical microscope
- Next, align the cantilever by moving the stage in x-y-direction until the green cross in the screen is located at the tip of the cantilever; the corresponding screws are the gray ones on the right of the setup (also labeled accordingly)
- Switch off the lamp and remove the filter to see the laser; then align the laser using the upper black screws on the right and front right of the setup (also labeled); first move the laser to a position somewhere on the cantilever using the image in the right box of the program; then focus on the sum signal (bar on the very right of the program) and move the laser gently to maximize it; for FASTSCAN-A cantilevers, a sum signal between 1.3 and 1.5 is typical
- Align the detector such that the maximum of the signal is in the center of the quadrant detector using the black screws on the left and front left of the setup (also labeled) by moving the detector until the red point is in the center of the four quadrants to maximize it
- To calibrate the cantilever (based on the thermal noise spectrum), insert the information about the used cantilever and the measuring conditions (23 °C, air) in the computer program, then thermally excite the cantilever and check whether the detected resonance frequency is close to the value stated by the vendor
- If the found spring constant or resonance frequency are very far off or no resonance frequency is found, re-install the cantilever or change it
- Switch to the 'Acquire data' tap to scan the cantilever for its resonance frequency; select 'AC Feedback Mode Wizard' and type in the estimated drive frequency of the cantilever (around 1400 kHz for FASTSCAN-A cantilevers) and select start and end frequencies around 20% below/above that value; select a drive amplitude (free amplitude) appropriate for the expected height of the sample (a bit above the expected height, e.g. 5 nm for bare AFM, 20 – 30 nM for AFM-IN complexes); when clicking on '∞', the software excites the cantilever and finds it's resonance frequency (the highest peak, should be in the area around the estimated drive frequency)
- Zoom in on the highest peak and position the courser cross on the left flank of the peak slightly next to the peak at a target amplitude of about 90% of the maximum amplitude; then close the window
- If needed, manually approach the cantilever (carefully, always check by eye, steps of 500 – 100 µm)

3. Initiation of the measurement

- Switch on the stable table and the active isolation (located under the microscope) and close the box of the AFM
- By default, the largest z-scanner should be selected (6.3 µm), if not, click on options → scanners → z-scanners and select the 6.3 µm scanner
- Click on 'approach' (arrow downwards on top left of the program window)
- Once the surface is reached, the approach process automatically stops

- Click on 'withdraw' (arrow downwards on top left of the program window) to slightly remove the cantilever from the surface
- Change the z-scanner by clicking on options → scanners → z-scanners and select the 2.1 µm HG scanner (for fast scanning)
- The 'AC Feedback Mode Wizard' automatically opens; click on '∞' to verify the resonance peak again, as the cantilever resonance may have changed under the influence of the nearby surface
- Go to 'Setup experiment' tab to select appropriate imaging parameters: relative setpoint ∼80 – 90 %, gain ∼1500, scan size ∼1 – 5 µm, pixels ∼256 – 4096, line rate ∼1 – 6 Hz; the most suitable values for these parameters vary greatly depending on the type and condition of the AFM tip, the nature of the sample and the desired resolution, and must be adapted to the specific situation
- After that, the measurement can be started by going to the 'Acquire data' tab and clicking on 'scan' (arrow to the right on top left of the program window)

AFM imaging under wet conditions

For AFM imaging in liquid, the procedures are similar to those for measurements in dry conditions. Therefore, I will mainly discuss the differences between the two methods in the following:

- To reduce drift, place the buffer to be used for the measurements (imaging buffer) in the AFM box several hours before recording so that it can adapt to the temperature there
- In the AFM software, choose a liquid imaging mode (e.g. peakforce tapping – biomolecules in liquid or force volume maps – biomolecules in liquid)
- Mount a cantilever suited for liquid AFM measurements (e.g. AC-40) as described for dry measurements; it's not necessary to use the cantilever holder with the fast-scanning option since this is not needed for measuring under wet conditions
- After introducing the cantilever holder to the AFM head and fixating it, carefully wet the tip of the cantilever with a few droplets of imaging buffer using a pipette
- Install the home-built liquid cell containing the sample and 2 – 3 µL imaging buffer on the sample holder of the AFM
- Mount the AFM head as described before on the AFM stage
- Align the cantilever, laser, and detector as described before
- Calibrate the cantilever based on the thermal noise spectrum, insert the information about the used cantilever and the measuring conditions (23°C, liquid) in the computer program, then thermally excite the cantilever and check whether the detected resonance frequency is close to the value stated by the vendor
- If needed, carefully approach the cantilever manually
- Switch on the stable table and the active isolation (located under the microscope) and close the box of the AFM

- Use the largest z-scanner (6.3 µm) for approaching, then switch to a smaller scanner as soon as the surface is reached
- Go to 'Setup experiment' tab to select appropriate imaging parameters
  - for peak force tapping: setpoint 0.1 – 0.2 nN, IGain 400 z, PGain 0.0048, frequency 3125 Hz, amplitude 20 – 30 nm (depending on sample height), scan size ∼1 – 5 µm, pixels ∼256 – 4096, line rate ∼1 – 2 Hz (∼2 taps per pixel); again these parameters need to be adjusted depending on the specific measurement
  - for force volume mapping: setpoint 0.1 – 0.2 nN, z length 0.1 µm, z speed 2 µm/s, z resolution 20 px/nm contact time 0 s, contact type 'constant force', scan size ∼1µm, pixels ∼128 – 256, line rate ∼1 – 2 Hz (∼2 taps per pixel); again these parameters need to be adjusted depending on the specific measurement
- Start the measurement by clicking on 'scan' (as for AFM measurements under dry conditions)

A.1.4 *AFM image analysis*

I used the software SPIP (v.6.4, Image Metrology, Hørsholm, Denmark) for AFM data postprocessing. The software is very user-friendly and has already blind peak reconstruction as well as image deconvolution implemented. As an open-source alternative, I rarely also used Gwyddion (http://gwyddion.net/) for AFM post-processing which works very similar to SPIP.

AFM postprocessing with SPIP

- Flatten the image (Modify → Global leveling)
- Level the image line-wise (Modify → Linewise leveling)
- If needed, characterize the tip via blind tip reconstruction [266]
  - Select relevant area of the image, e.g. co-deposited fiducials (General → Area of interest)
  - Open tip characterization (Analyze → Tip), insert parameters of the tip used as starting values (Tip characterization → Size X and Y)
  - Click on 'characterize'
  - Save resulting tip shape
- With the characterized tip shape and size, the same image or other images can then be corrected (deconvoluted)
  - Open tip deconvolution (Tip characterization → Deconvolute)
  - Adjust the starting parameters for the tip size as before
  - Click on 'deconvolute'
- Save the resulting image(s) as ascii files

AFM postprocessing with Gwyddion

- Flatten the image (Data process → Level → Plane level)
- Level the image line-wise (Data process → Correct data → Align rows (Polynomial degree 2, Direction: horizontal))
- If needed, characterize the tip via blind tip reconstruction [266]
  - Select relevant area of the image, e.g. co-deposited fiducials (Tools → Edit mask (Mode: add selection to mask))
  - Model the tip using the manufacturer's tip specifications (Data Process → SPM modes → Tip → Model tip)
  - Characterize the tip (Data Process → SPM modes → Tip → Blind Estimation)
  - The 'Blind tip estimation' window opens automatically; choose the previously modeled tip as related data and specify the tip size in pixel
  - Run partial tip estimation (Blind tip estimation → Run partial)
  - Run full tip estimation (Blind tip estimation → Run full)
  - Click 'okay' to save the tip
- With the characterized tip shape and size, the same image or other images can then be corrected (Data Process → SPM modes → Tip → Surface reconstruction)
  - Open tip deconvolution (Tip characterization → Deconvolute)
  - Adjust the starting parameters for the tip size as before
  - Click on 'deconvolute'
- Save the resulting image(s) as ascii files

A.2 MAGNETIC TWEEZERS PROTOCOLS

A.2.1 *MT flow cell preparation*

The following magnetic tweezers protocols are also given in a similar way in Ref. [383].

Ideally, prepare flow cells (usually ∼6 in parallel) at least 1 day before starting a new measurement series.

1. Preparation

- Place coverslides (24 x 60 mm, Carl Roth, Germany) with holes (pre-processed using a laser cutter to introduce two openings with a radius of 1 mm each which serve as liquid inlet and outlet openings; top slides) in a suited coverslide holder and put the holder in glass box
- Add a mix of 50% milliQ water and 50% isopropanol (Carl Roth, Germany) until the slides are fully covered in liquid
- Seal the box with parafilm and sonicate for 15 min in ultrasonic bath
- Mix 1 µL of polystyrene beads (Polysciences, USA) in 5 mL ultra clean ethanol (Carl Roth, Germany; 99.8% pure)
- Vortex briefly and then sonicate for 15 min
- Take Epoxy-silane top-coverslides (pre-coated with (3-Glycidoxypropyl)-trimethoxysilane (abcr GmbH, Germany) by Tom; top slides) and put each in one 50 mL falcon tube
- Re-fill the box with the remaining Epoxy-silane coverslides with argon under the flowhood to avoid contamination, then close with parafilm

2. Flow cell production

- Pre-heat the heating plate to ∼80°C
- Lay bottom slides down flat on a dust-free tissue and cover with the prepared polystyrene bead solution (about 100 µL)
- Put a lid on top and let them dry for about one hour at room temperature
- Take the box with the top slides from the sonicator and dry the slides one by one using a gently stream of nitrogen gas (avoid using sharp tweezers)
- Cut parafilm according to a prepared template and stick it on top of the top slides so that the inlets are left open
- Put bottom slide on top (with the polystyrene bead coated side facing downwards) and place both in between two cleaned glass slides
- Heat for about 30 sec on the heating plate to seal the two slides together, press gently with a pipette tip if needed
- Store the flow cells (one by one) in labelled falcon tubes

3. Flow cell measurement preparation

- Clean the flow cell holder by sonication for 20 minutes and dry all parts (don't clean screws)
- Introduce the flow cell into the flow cell holder and carefully but firmly tighten the screws
- Spin down two tubes of 50 µL 100 µg/mL anti-digoxigenin (Roche, Switzerland) in 1x PBS for 5 min at 13000 rpm in table top centrifuge
- Add both anti-digoxigenin tubes to the flow cell
- Insert a bit less than 100 µl from the upper part of the tube into one inlet (with the pipette tip touching the ground of the inlet), then slowly insert a bit less than 100 µl into the other inlet (with the pipette tip at the border of the inlet)
- Close the inlet and the outlet of the flow cell with parafilm (to avoid air bubble formation in the flow cell as a consequence of evaporation)
- Incubated overnight (at least 12 h)
- At the MT setup, add a droplet of immersion oil to the objective
- Carefully place the flow cell holder on top of the objective and fixate with screws
- Remove the parafilm from the inlet and the outlet and connect the pumping system
- Rinse the flow cell with 1 mL of 1x PBS
- Passivate using 1 mL of a commercial passivation mix (BlockAid Blocking Solution, Thermoscientific) or 1 mL of 25 mg/mL bovine serum albumin (Carl Roth, Germany) for at least 1 h in order to minimize non-specific interactions
- Rinse the flow cell with 1 mL of 1x PBS

A.2.2 *DNA constructs and magnetic beads*

For the MT measurements, I either used a 7.9-kbp DNA construct or a 21-kbp DNA construct, prepared as described previously [371, 384]. In brief, PCR-generated DNA fragments (∼600 base pair) were labeled with multiple biotin and digoxigenin groups and ligated to the target DNA to bind magnetic beads and the flow cell surface, respectively.

As magnetic beads I used either 1.0 µm diameter MyOne magnetic beads or 2.7 µm diameter M-270 magnetic beads (Life Technologies, USA), both streptavidin coated. To attach the DNA construct to the magnetic beads, the following steps are necessary:

- Take magnetic beads from fridge and vortex the tube for about 1 min (tend to stick together)
- Wash the magnetic beads
  - Put 2 µL MyOne beads (or 10 µL M-270 beads) in a low binding 1.5 mL tube and add 150 µL 1x Phosphate-buffered saline (Sigma-Aldrich, USA; PBS)

  - Pipette strongly up and down or vortex the tube for a few seconds to mix the beads and PBS
  - Place tube in magnet holder to move magnetic beads to one side of the tube; wait for about 30 sec; remove 145 µL from the tube and quickly add 145 µL fresh PBS
  - Repeat the previous two steps twice
- Add 0.5 µL 7.9-kpb DNA (or 2.5 µL 21-kpb DNA) to the beads and drop tube on the bench to mix (from now on, treat the tube carefully to avoid breaking the DNA)
- Incubate about 5-10 minutes while carefully tapping the tube

Afterwards, 50 µL of bead-coupled DNA constructs are introduced into the MT flow cell and allowed to bind for 5 min. Then, to flush out unbound beads, the flow cell is rinsed with at least 2 mL PBS, and the magnet is mounted to constrain the supercoiling density of the tethers and to apply an upward force on the beads.

A.2.3 *MT experimental preparation and quality tests*

Before starting the measurement, the software is started and parameters are set, and the beads are selected and tested.

1. Software initiation

- Open the software parts one after another from left to right as placed on the computer desktop
- PI micromove (controls piezo): tick 'servo on' for both (height and turning); then press on left arrow: 'start up axes' → 'pos limit' → 'close'; 'start up axes' → 'advanced' → 'ok' → 'ok' → 'close'; close program
- PI nanocapture (connected to piezo): tick 'servo on'; close program
- Bead tracker main program (labview): start by clicking on the arrow in the left upper corner; three windows open: bead tracker main, experiment program, motorUI.vi (here set focal depth piezo to 50)

2. Magnet installation and offset determination

- Select file path in the software (usually named by date)
- Bring flow cell surface in focus by moving the stage up or down using the big golden screw underneath the objective
- Select the polystyrene beads in the field of view as reference beads
- Save beadlist and note reference beads in lab book
- Screw in magnet (small golden screw in front)
- Switch on LED (about 60 mA)
- Click 'magnet all up' in software
- Determine magnet offset:
  - Go down with magnet first in steps of 3 mm, then 0.1 or 0.05 mm (as soon as close to surface)

  - When close to flow cell surface: look at flow cell image in software to see magnet touching the surface
  - Go 0.1 mm up from this point and note the value as magnet offset
- Click 'magnet all up' and remove magnet again

3. Bead selection and Z-lookup table

- Change piezo such that moving/tumbling beads are the only ones in focus
- Select all moving/tumbling beads and safe beadlist (not too close to the edges, otherwise program might crush)
- Choose size of the ROI around the beads (about 90 to 110 µm)
- Generate Z-lookup table (Z-LUT):
  - Move magnet to 1mm
  - Change piezo to get moving/tumbling beads in focus
  - Set piezo about 5 steps higher than this
  - Click 'set current piezo as start z'
  - Click 'generate Z-LUT'
  - 'ok' → 'ok' → 'ok'
- Move piezo to centre of Z-LUT (5 steps up)

3. Bead testing

1. Length test
   - Set path and call experiment 'length1'
   - Move magnet to 0.5 mm (F = 5 pN)
   - Click on 'start experiment'
   - Change magnet position from 0.5 mm to 12 mm and then back to 0.5 mm
   - Click on 'abort experiment'
   - Examine traces to see whether the length of the DNA tethers is fine (between 2 and 3 mm is acceptable)
2. Rotation test
   - Set path and call experiment 'rot'
   - Move magnet to 0.5 mm (F = 5 pN)
   - Set magnet velocity to 5 turns per sec
   - Click on 'start experiment'
   - Rotate to -25, then back to 0
   - Change magnet position from 0.5 mm to 4 mm (F = 0.5 pN)
   - Rotate to +25, then back to 0
   - Click on 'abort experiment'
   - Change magnet position from 4 mm to 0.5 mm
   - Rotate back to 0
   - Look at traces to find 'good beads': discard double-tethers (go up and down at high force, negative coiling), discard nicked tethers (don't go down at low force, positive coiling)

Delete unwanted beads and perform a second length test, save the bead list and do not change it from now on. Afterwards, the measurement can be started.

A.3 ZERO-MODE WAVEGUIDE PROTOCOLS

A.3.1 *ZMW nanoporous membrane preparation*

In preparation for the ZMW experiments, I pre-treated commercially available track-edged membranes (Whatman) consisting of a 6 µm-thick polycarbonate layer with cylindric pores with a diameter of 50 nm and a density of $6 \cdot 10^8$ pores/cm^2.

A gold layer with a thickness of 50 nm is grafted on top of the membrane to allow for zero-mode waveguiding at a length scale smaller than the wavelength of the illuminating light. The gold deposition procedure on the track-edged membranes is realised via gold sputtering in a clean room using an evaporator coupled to an electron beam accelerator.

- Arrange the track-etched membranes on the sample holder and fixate them with metal rings of the same diameter as the membranes on which the rods are supported
- Pump air out of the evaporation chamber ($p \leq 10^{-6}$ Pa) to create a vacuum
- Perform low intensity ionic pickling to remove impurities from membrane
- Start gold deposition (speed of 0.2 nm/s)
- Stop process after 4 min 10 sec to get a gold layer thickness of 50 nm

Following this, the polymer grafting onto the gold layer is achieved via electrografting by Dihia Benaoudia (Itodys, Paris Diderot University).

A.3.2 *Fluorescent sample labelling*

A.3.2.1 *DNA labelling*

For the ZMW DNA translocation experiments, I use λ DNA (Invitrogen), linear double-stranded bacteriophage DNA (*Escherichia coli*) consisting of 48502 base pairs (32 300 kDa) with 5' single-strand terminations of 12 additional base pairs (the λ-DNA can therefore circularise spontaneously). For the labelling of the DNA, the following components are combined in one tube:

- 1 mL TE buffer (10 mM Tris-HCl and 1 mM EDTA)
- 1 µL λ-DNA (c = 0.5 µg/µL in TE buffer)
- 0.3 µL YOYO-1 (Life Tech, 200 µL solution at a 1 mM concentration in dimethylsulfoxyde)

Let the mixture incubate at room temperature for 30 min, then the produced DNA-YOYO mix is stored in the fridge (4 °C).

Track-etched or ion-tracked signifies that the pores in the membrane are made by subjecting a µm thick polymer film (e.g., polycarbonate or polyester) to a high energy (on the order of MeV/u) bombardment of heavy ions (^{170}Au, ^{206}Pb, ^{238}U). As the ions permeate the membrane, they ionize the material, lose their energy, and leave a latent track. After the track has been created, the irradiated material can be etched faster than the starting material with a corrosive agent adapted to the employed polymer (e.g. sodium carbonate for polycarbonate), thus creating pores in place of the tracks.

A.3.2.2 *Virus labelling*

For the fluorescent labelling of the virus samples for ZMW translocation experiments, the following components are combined in one tube:

- 3 µL adeno-associated virus 9 (AAV9; produced in the lab of Anna Salvetti, CRCL Lyon; stored at -80°C in PBS)
- 0.7µL YOYO-1
- 1 mL TE buffer

The labeling procedure is performed as described in the following steps:

1. Combine AAV9 and the YOYO-1 at the bottom of the tube
2. Let incubate for 15 minutes
3. Add the TE buffer
4. Store in fridge (4 °C)

A.3.3 *Experimental preparation*

Before starting the ZMW for nanopores experiment, the sample and the setup need to be prepared.

- Add a droplet of water on top of the objective
- Place the *cis* chamber on top (so that it's in contact with the water droplet)
- Prepare the *trans* chamber
  - Take a Nanion screw cap with a glass bottom with a pre-drilled 0.1 mm hole
  - Enlarge hole to about 2 mm diameter by piercing it with a sharp tweezers tip
  - Cut out a 3 mm diameter circular part of the membrane (prepared as explained in Section A.3.1)
  - Glue onto the enlarged hole using a biocompatible silicon glue (Silcomet JS 533 rouge, Loctite)
  - Let glue dry for ∼1 h
- Add sample to the inside of the *trans* chamber (e.g., a mix of DNA and buffer)
- Close the *trans* chamber from above by screwing it to a lid that is connected to the pressure control system using a thin tube
- Place *trans* chamber on top of the *cis* chamber

To start the ZMW measurement, the setup components must be launched.

- Switch on the computer, the laser, and the shutter control system
- Test the settings (laser beam and its optical path have to be well positioned to ensure that the beam is parallel when leaving the lens)
- When not using the laser, close the shutter to protect the EMCCD camera

- Use the camera software to control the Peltier element to cool down the camera to -60 °C (to reduce thermal noise)
- In camera software: set acquisition mode to kinetic, frequency to maximal value (frame transfer), and electron multiplier gain to 300
- Switch on the other parts of the setup (pressure control system and stage control system)

A.3.4 *Data acquisition*

I perform six different types ofZMW measurements: five single-molecule measurements (1. – 5.) and one ensemble measurement (6.)

1. Transient heating experiments:
   Measure translocation frequency of DNA by briefly heating up the system. While applying a constant pressure, the frequency of translocation as a function of temperature is measured
2. Stationary heating experiments:
   Measure translocation frequency of DNA while gradually cooling down the system
3. Short-time heating experiments:
   Briefly heat the membrane to visualise the opening and closing behaviour of the pores
4. DNA translocation by varying pressure experiments:
   Measure the translocation frequency of DNA as a function of applied pressure to determine the thickness of the grafted polymer layer
5. Virus translocation by varying pressure experiments:
   Measure the pressure dependency of virus translocation
6. Small molecule translocation experiments:
   Examine the characteristics of translocation of bio-objects smaller than DNA diffusing through the porous membrane (ensemble measurement)

In preparation for the experiments, the *trans* and *cis* chambers are prepared as described in the following table (Table 9): After filling the liquids into the

	***trans* chamber**	***cis* chamber**
1.	100 µL TE buffer + 2 µL DNA-YOYO mix	500 µL TE buffer
2.	100 µL TE buffer + 2 µL DNA-YOYO mix	500 µL TE buffer
3.	100 µL TE buffer + 2 µL DNA-YOYO mix	500 µL TE buffer
4.	100 µL TE buffer + 2 µL DNA-YOYO mix	500 µL TE buffer
5.	50 µL TE buffer	250 µL AAV9-YOYO mix
6.	50 µL TE buffer	500 µL TE buffer + 50 µL dextran / 10 µL BSA

Table 9: Components inserted into the two chambers of the setup for the different types of ZMW experiments.

two chambers, the two chambers are brought into contact by placing the *trans* chamber on top of the *cis* chamber.

To find a suitable location on the membrane for the ZMW experiments, the following steps are accomplished:

- Manually change the focus of the microscope until the membrane can be seen in focus in the camera program
- Move the stage vertically until the camera is focused on an area in the center of the membrane (minimum tilt of the membrane)

In single molecule experiments, single translocation events across the membrane are observed and analyzed. To this end, multiple images are acquired in a short time frame (image acquisition interval: 30 ms) in real time with an image resolution of 512 x 512 pixels in a 150 µm x 150 µm area observed by the EMCCD camera. The resulting videos consist of a sequence of 500 frames, corresponding to a video length of 15 seconds.

For the experiments examining diffusive transport of small molecules through nanopores (6.), I use either 50 µL dextran (Thermo Fisher Scientific) at a concentration of $4 \cdot 10^{-4}$ µg/µL ($\widehat{=}$ 100 nM) or 10 µL bovine serum albumin (BSA, Thermo Fisher Scientific) at a concentration of 20 µg/mL ($\widehat{=}$ 300 nM). Both dextran and BSA are purchased labelled with Alexa Fluor 488 (Thermo Fisher Scientific).

The steps involved in the different types of ZMW-nanopore experiments are outlined below:

1. Transient heating experiments
   - Set pressure to 80 mbar (and keep constant over experiment)
   - Record one video at the chosen location as a reference point before starting the experiment
   - Remove buffer in *cis* chamber (T $\approx$ 20°C) using a syringe
   - Replace liquid by 50 °C-buffer again using a syringe
   - Record one video every minute for the following 30 minutes
2. Stationary heating experiments
   - Add temperature control system (Pecon, TempController 2000-2) to setup (metal ring around the objective)
   - Set temperature control system to 50°C
   - Wait for 60 minutes to make ensure that the whole system is heated up to a fairly constant temperature
   - Check temperature of the buffer in the *cis* chamber (should be $\geq$ 30 °C) using a thermometer with a long and flexible probe placed on the side of the inner edge of the *cis* chamber
   - Start experiment while the temperature control system is still heating up the system
   - For first 5 minutes: record a video every minute, then one video after 10 minutes and one video after 15 minutes
   - Switch off the heat supply and let the system cool down while taking one video every minute

Dextran is a complex branched glucan (polysaccharide made of many glucose molecules) with a molar mass of 3 kDa.
BSA is a small protein with a length of 583 amino acids with a molecular weight of 66.463 kDa.

- When recording a video, also measure and note the temperature of the liquid in the chamber

3. Short-time heating experiments
   - Add use the fluorescent lamp to heat the membrane to setup
   - Set pressure to 80 mbar (and keep constant over experiment)
   - Record one video at the chosen location as a reference point before starting the experiment
   - Switch illumination source of the setup from routinely used laser to the fluorescent lamp
   - Heat membrane for 2 minutes
   - Change illumination back to laser
   - Record another video
4. DNA translocation by varying pressure experiments
   - Start experiment
   - Change applied pressure between 0 mbar and 150 mbar using the pressure control system
   - After setting a pressure value at the control system, wait 3 minutes to let the system adopt
   - Always take four videos in a row at constant pressure
5. Virus translocation experiments
   - Invert pressure system so that the flow drives the particles from the *cis* chamber to the *trans* chamber (facilitates detection of the viruses which are smaller than the λ-DNA)
   - Change pressure between 0 and 100 mbar
   - After setting a pressure value at the control system, wait 3 minutes to let the system adopt
   - Always take two videos in a row at constant pressure
6. Small molecule translocation experiments
   - Start experiment by taking a picture of the observed area to measure the mean intensity of the field of view using the camera program
   - Repeat this every minute for the following 60 minutes

A.3.5 *Data analysis*

To determine the translocation frequency, the translocation events appearing in the video (visible as bright spots on the otherwise dark background) are counted by hand. The frequency f is then calculated as the number of events N observed during one video sequence divided by the number of pores present in one film N_p times the acquisition time t = 15 s. N_p can be calculated as the pore density $\rho = 6 \cdot 10^8$ pores/cm^2 times the observed area 150 µm x 150 µm, so

$$f = \frac{N}{N_p t} = \frac{N}{\rho \cdot A \cdot t} \tag{46}$$

For the analysis of the ensemble experiments, the camera program is used to determine the overall mean fluorescent intensity of the recorded images.

A.4 MOLECULAR CLONING PROTOCOLS

A.4.1 *DNA design*

Parts of the following DNA protocols are also given in a similar way in Ref. [383].

For this work, I used different-length DNA with 180-base pair ends identical to the viral DNA ends HIV to test the length dependence of DNA compaction by IN. As a starting point, I used the mini-HIV plasmid pU3U5 (Figure 82) [330] and shortened or enlarged the plasmid to obtain two more plasmid sizes:

- pU3U5 small (3.437 kbp)
- pU3U5 original (4.751 kbp)
- pU3U5 large (9.112 kbp)

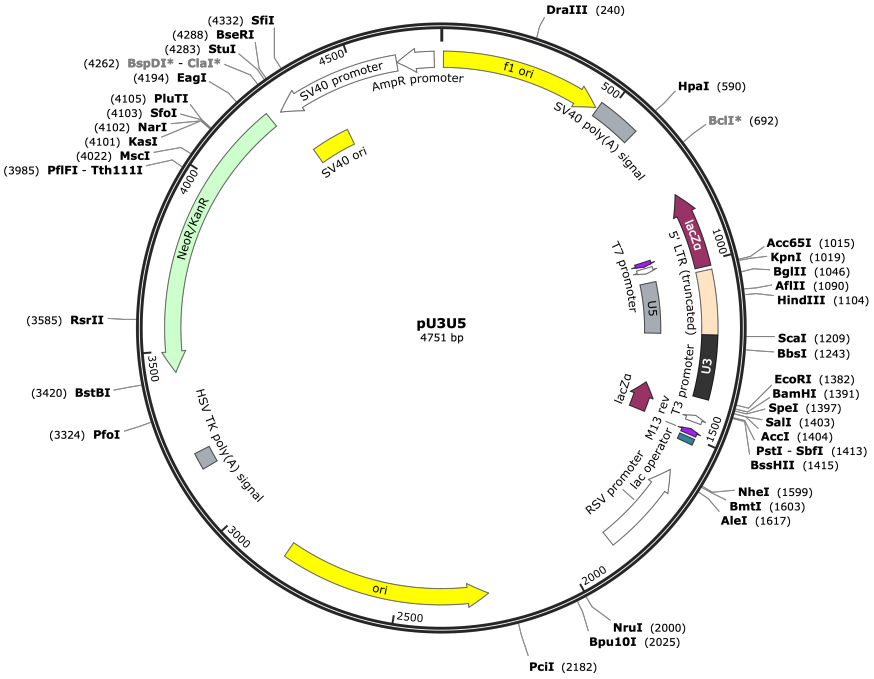

Figure 82: Map of the plasmid pU3U5, 4751 base pairs. Important sequences are highlighted in colour, such as the origin of replication (ori), the antibiotic resistance to neomycin and kanamycin, the lacZa that produces the lacZa fragment of β-galactosidase, and the U3 and U5 domains, sequences identical to the viral ends of HIV, 180 base pairs each. Created by SnapGene.

I used blunt-end cloning to get the 3.4 kbp pU3U5 (Figure 83) and Gibson assembly to get the 9.1 kbp pU3U5 (Figure 84). To view and design DNA sequences, the software SnapGene was used. The individual processes are explained in the following, the sequencing results can be found in the appendix in Section B.

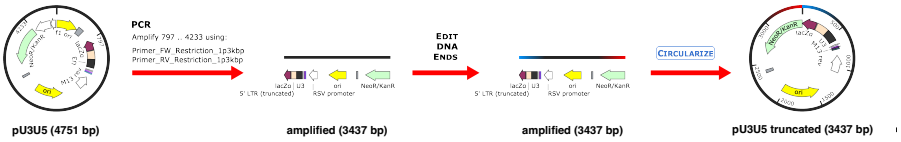

Figure 83: Map and blunt-end-cloning process to reduce the size of the pU3U5 plasmid from 4.751 kbp to 3.437 kbp. Created by SnapGene.

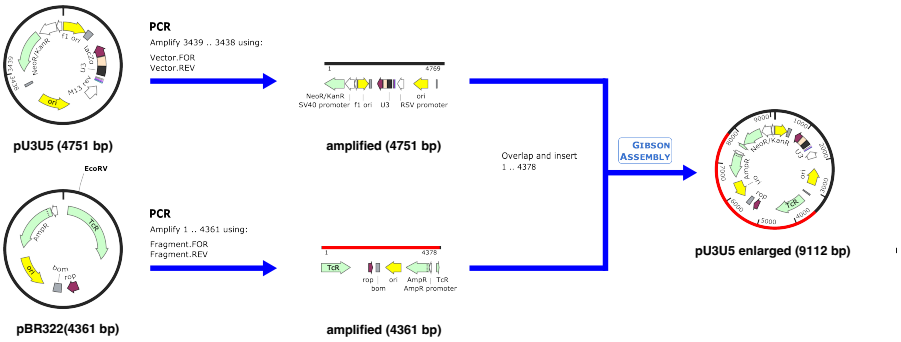

Figure 84: Map and Gibson assembly process to enlarge the size of the pU3U5 plasmid from 4.751 kbp to 9.112 kbp. Created by SnapGene.

A.4.2 *Polymerase chain reaction*

The first step that is done to produce a truncated or enlarged version of pU3U5 is a PCR. As a prerequisite, the needed primers are designed with the help of SnapGene. For the 3.4 kbp plasmid, the used primers are:

- Forwards primer: ATGATTGAACAAGATGGATTGCACGCAGGT
- Reverse: TTAAAAATTGGATCTCCATTCGCCATTCAGGCTGC

For the 9.1 kbp plasmid, two primers are needed to linearize and amplify the two Gibson fragments. The first fragment is created from a PCR from pU3U5 plasmid:

- Forwards primer 1: CTTGCGGGATTCAGAAGAACTCGTCAAGAAG-GCGATAGAAGGC
- Reverse primer 1: TGGACGATGCGGGACTCTGGGGTTCGAAAT-GAC

The second fragment is created from a PCR from pBR322 plasmid:

- Forwards primer 2: GTCCCGCATCGTCCATTCCGACAGCATCGCC
- Reverse primer 2: GTTCTTCTGAATCCCGCAAGAGGCCCGG

For the PCR, the necessary components – the DNA template, the primers, the DNA polymerase and the nucleotides – are combined in one tube:

- 10 µL Phusion HF PCR Master Mix (NEB, catalogue number: M0531S)
- 1 µL DNA ($c \approx 100$ ng/µL)
- 1 µL forwards primer ($c = 10$ ng/µL)
- 1 µL reverse primer ($c = 10$ ng/µL)
- 7 µL milliQ water

The content of the tube is briefly mixed and then place it in a preheated PCR machine. The PCR machine program is described in Table 10.

Process	Temperature	Duration	Repetition
Preheating	98°C	∞ (manual start)	1x
Initialisation	98°C	120 sec	1x
Denaturation	98°C	10 sec	35x
Annealing	55°C	10 sec	
Extension	72°C	36 sec	
Final extension	72°C	5 sec	1x
Final hold	8°C	∞ (manual stop)	1x

Table 10: Steps of the PCR process. The denaturation, annealing, and extension steps are repeated 30x.

The PCR's success is checked via gel electrophoresis:

- Weigh 0.5 g Broad Range Agarose (Carl Roth, item number: T846.3; agarose)
- Combine with 50 mL TAE 1x buffer (40 mM Tris, 20 mM NaAc waterfree and 1 mM EDTA; TAE) in Erlenmeyer flask to get a 1% agarose gel
- Heat the agarose-TAE mixture in the microwave until just before the boiling point
- Mix thoroughly with a magnetic stirrer until the agarose is dissolved in the buffer
- Prepare gel electrophoresis mould (check the levelness by means of a bubble level)
- Add 1.8 µL Roti Safe (Carl Roth, order number: 3865.1) to the prepared mould
- Introduce the hot agarose-TAE to the mould
- Mixed with the Roti Safe using a pipette tip
- Insert a cleaned comb into the corresponding retainer of the mould
- Let cool down and solidify for at least 30 minutes
- Fill electrophoresis chamber with enough TAE to cover the gel
- Mix the PCR product with Gel Loading Dye Purple (6x) (NEB, catalogue number: B7024S; gel loading dye): 5 µL DNA + 1 µL loading dye
- Load in small chambers of the gel
- Add 5 µL 2 log DNA ladder into the last chamber of the gel (as a size standard)
- Run gel electrophoresis for 20 minutes, at a constant voltage of 120 V
- Visualize the gel using a Gel Doc XR+ System

A.4.3 *Blunt-end cloning*

For the reduced-size version of pU3U5, after PCR, the ends of the shorter linearized DNA need to be ligated together. This is achieved via blunt-end cloning (BEC), where ligation is performed first followed by transformation.

For the blunt end cloning ligation, the following components are combined in one tube:

- 1.0 µL CutSmart Buffer (NEB, catalogue number: B7204S; 50 mM Potassium Acetate, 20 mM Tris-acetate, 10 mM Magnesium Acetate, 100 ng/µL BSA, pH 7.9 at 25°C)
- 1.0 µL Adenosine 5'-Triphosphate 10mM (NEB, catalogue number: P0756S; ATP)
- 0.5 µL PEG-6000 average M_n 6000 (Carl Roth, order number: 0158.4; Poly(ethylene glycol))
- 1.0 µL DpnI (NEB, catalogue number: R0176S)
- 1.0 µL T4 DNA-Ligase (NEB, catalogue number: M0202S)
- 4.5 µL unpurified PCR product (c ≈ 100 ng/µL)

After stirring the tube briefly, it is placed in a preheated PCR machine and the program is started:

- 15 minutes at 37 °C
- 45 minutes at 22 °C
- 5 minutes at 80 °C

The results are again checked via gel electrophoresis (following the protocol described in the previous section (Section A.4.2)).

For the BEC transformation, one aliquot (50 µL) of competent *E. coli* cells (NEB, catalogue number: B7204S) is taken from the fridge (-80 °C) and place it on ice to allow for thawing. A small amount (1 µL) of the DNA (c ≈ 1 ng/µL) to be cloned is added to the aliquot and mixed thoroughly. Then, the following steps are performed (Table 11):

Process	**Place and/or temperature**	**Duration**
1. Cooling	on ice (0°C)	30 min
heat shocking	water bath (42°C)	60 sec
2. Cooling	on ice (0°C)	120 sec
Cell relaxation by adding 900 µL SOC medium	room temperature	
Incubation	shaking incubator (37 °C)	60 min

Table 11: Steps of the BEC transformation process. The used SOC medium is Super Optimal broth with Catabolite repression (Thermofisher, catalogue number: 15544034, without antibiotics). For the final incubation, the shaking incubator is set to 850 rpm.

Next, some of the transformed cells are plated onto a LB agar plate containing the antibiotic Kanamycin to allow for selective bacterial growth (only correctly transformed cells):

- Perform the following steps under a sterile fume hood (also disinfect all used materials beforehand)
- Add ∼15 small glass beads to the agar plate
- Add 100 µL of the cells prepared in the previous step to the agar plate
- Move the glass beads gently on the agar plate
- Remove glass beads in the appropriate container
- Incubate the agar plates at 37 °C overnight

A.4.4 *Gibson assembly*

For the enlarged-size version of pU3U5, two sequences from two different plasmids are prepared via PCR first. Then, in a next step, the two linearized DNAs need to be combined into one DNA. I used Gibson assembly 3.4 to achieve this:

- Add 1 µL DpnI (NEB, catalogue number: R0176S) per PCR tube
- Incubate in PCR cycler at 37°C overnight (or at least 1 h)
- Heat samples in pre-heated PCR cycler at 80°C for 5 minutes
- Heat samples in pre-heated PCR cycler
- Conduct PCR cleanup (use 30 µL milliQ water in the last step)
- Check concentration in nanodrop

Using the concentration estimation from the nanodrop, the appropriate concentrations for the two fragments of the Gibson assembly can be calculated:

$$V_{backbone} = \frac{N_{bp} \cdot 0.65\, g/mol \cdot 0.03\, pmol}{c_{DNA}} \tag{47}$$

$$V_{inset} = \frac{N_{bp} \cdot 0.65\, g/mol \cdot 0.09\, pmol}{c_{DNA}} \tag{48}$$

with N_{bp} the number of base pairs in the DNA fragment and c_{DNA} the concentration of the DNA fragment (determined via nanodrop measurement).

For the Gibson assembly, the following components are combined in one tube:

- 10 µL Gibson Mastermix (aliquot with other PCR-Mastermixes, name: 'HiFi Mastermix')
- Calculated volume of backbone DNA ($V_{backbone}$)
- Calculated volume of inset DNA (V_{inset})
- Fill up to 20 µL with milliQ water

Gently tap the tubes, and spin them down in a table top centrifuge. Then incubate in a PCR cycler for 1 h at 50°C, then place on ice. After that, the Gibson assembly transformation is performed analogously as described for the BEC transformation

A.4.5 *DNA storage*

After overnight incubation, individual colonies have grown on the agar plate. To obtain *E. coli* cells with identical genetic information, one individual colony is selected and its cells are amplified. To do so, the following steps are performed under a sterile fumehood:

- Prepare a tube containing 6 mL agar (incl. Kanamycin resistance)
- Selected a colony from the plate
- Transferred the colony to the tube by gently touching it with a pipette tip and then drop the tip into the tube with the agar solution
- Incubate the *E. coli* solution overnight in a shaker (200 rpm, 37°C)

Closed and sealed agar plates can be kept at 4 °C for several days or even weeks. To store the DNA for longer, it is advisable to prepare a gycerol stock that is stored at -80 °C. The required steps are again performed under a sterile fumehood:

- Prepare glycerol stock tube (special tube with screw cap) and label it with label maker
- Add 500 µL glycerol (80%)
- Add 1000 µL *E. coli* solution
- Mix the tube by inverting 4 to 6 times
- Store the stock in the refrigerator at -80 °C and note its location

A.4.6 *DNA purification*

To extract the vector DNA out of the *E. coli* cells, I typically used the QIAprep Spin Miniprep Kit (Qiagen, catalogue number: 27104) and a microcentrifuge. In preparation for the DNA extraction, the cells are inoculated (again under fumehood):

- Add 5000 µL culture medium (LB medium) with added antibiotics (ratio 1000:1) to a tube
- Add a pipette tip that has previously been introduced to the frozen glycerol stock
- Place the tube in a shaker at 37 °C overnight with slightly opened cover
- Centrifuge the tube for 15 minutes at 15000 rpm ($\widehat{=}$ 3220g) in a large centrifuge (a pellet of *E. coli* should form at the bottom of the tube)

Subsequently, the DNA purification is performed as described in Table 12 (all steps are executed at room temperature). The success of the DNA purification is then checked using a photometer (nanodrop).

Process	**Addition**
Resuspension	250 µL P1 buffer
Transfer to a new tube	
1. Lysis reaction	250 µL P2 buffer
2. Lysis reaction	350 µL P3 buffer
Centrifuge for 10 min at 13000 rpm	
Transfer to spin column	
Washing	750 µL PE buffer
Centrifuge for 60 sec at 13000 rpm	
Final centrifugation	
Centrifuge for 60 sec at 13000 rpm	
Transfer to a new microcentrifuge tube	
Elution	50 µL milliQ water
Incubate for 60 sec	
Centrifuge for 60 sec at 13000 rpm	

Table 12: Steps of DNA purification using a commercial spin miniprep kit. The washing step (incl. centrifugation) can be repeated 2 – 5 times to improve the purity of the sample.

B

SEQUENCES OF NEWLY DESIGNED PLASMIDS

The truncated and enlarged versions of pU3U5 were prepared custom for this work (as described in section A.4), and since this preparation has not been done previously, the obtained plasmids were sequenced. In the following, only the top strands are given.

B.1 SEQUENCING RESULT OF THE PLASMID PU3U5 RESTRICTED TO 3.437 KBP

AAGGGCGATCGGTGCGGGCCTCTTCGCTATTACGCCAGCTGGCG
AAAGGGGGATGTGCTGCAAGGCGATTAAGTTGGGTAACGCCAGG
GTTTTCCCAGTCACGACGTTGTAAAACGACGGCCAGTGAATTGTA
ATACGACTCACTATAGGGCGAATTGGGTACACTTACCTGGTACCT
GTACTGGGTCTCTCTGGTTAGACCAGATCTGAGCCTGGGAGCTCT
CTGGCTAACTAGGGAACCCACTGCTTAAGCCTCAATAAAGCTTGC
CTTGAGTGCTTCAAGTAGTGTGTGCCCGTCTGTTGTGTGACTCTG
GTAACTAGAGATCCCTCAGACCCTTTTAGTCAGTGTGGAAAATCT
CTAGCAGTACTGGAAGGGCTAATTCACTCCCAAAGAAGACAAGAT
ATCCTTGATCTGTGGATCTACCACACACAAGGCTACTTCCCTGAT
TAGCAGAACTACACACCAGGGCCAGGGGTCAGATATCCACTGACC
TTTGGATGGTGCTACAAGCTAGTACCAGTTGAGCCAGATAAGATA
GAATTCTTTGGATCCACTAGTGTCGACCTGCAGGCGCGCGAGCTC
CAGCTTTTGTTCCCTTTAGTGAGGGTTAATTTCGAGCTTGGCGTA
ATCAAGGTCATAGCTGTTTCCTGTGTGAAATTGTTATCCGCTCAC
AATTCCACACAATATACGAGCCGGAAGTATAAAGTGTAAAGCCTG
GGGTGCCTAATGAGTGAGCTAACTCACAGTAATTGCGGCTAGCC
AGGTGCACACCAATGTGGTGAATGGTCAAATGGCGTTTATTGTAT
CGAGCTAGGCACTTAAATACAATTATCTCTGCAATGCGGTATTCA
GTGGTTCGTCCAATCCATGTCAGACCCGTCTGTTGCCTTCCTAAT
AAGGCACGATCGTACCACCTTACTTCCACCAATCGGCATGCACGG
TGCTTTTTCTCTCCTTGTAAGGCATGTTGCTAACTCATCGTTACC
ATGTTGCAAGACTACAAGAGTATTGCATAAGACTACATTTCCCCC
TCCCTATGCAAAAGCGAAACTACTATATCCTGAGGGGACTCCTAA
CCGCGTACAACCGAAGCCCCGCTTTTCGCCTAAACACACCCTAGT
CCCCTCAGATACGCGTATATCTGGCCCGTACATCGCGAAGCAGCG
CAAAACGCCTAACCCTAAGCAGATTCTTCATGCAATTGTCGGTCA
AGCCTTGCCTTGTTGTAGCTTAAATTTTGCTCGCGCACTACTCAG
CGACCTCCAACACACAAGCAGGGAGCAGATGCATGGCGGTAATA
CGGTTATCCACAGAATCAGGGGATAACGCAGGAAAGAACATGTG
AGCAAAAGGCCAGCAAAAGGCCAGGAACCGTAAAAAGGCCGCGT
TGCTGGCGTTTTTCCATAGGCTCCGCCCCCCTGACGAGCATCACA
AAAATCGACGCTCAAGTCAGAGGTGGCGAAACCCGACAGGACTA
TAAAGATACCAGGCGTTTCCCCCTGGAAGCTCCCTCGTGCGCTCT
CCTGTTCCGACCCTGCCGCTTACCGGATACCTGTCCGCCTTTCTC
CCTTCGGGAAGCGTGGCGCTTTCTCATAGCTCACGCTGTAGGTAT
CTCAGTTCGGTGTAGGTCGTTCGCTCCAAGCTGGGCTGTGTGCAC
GAACCCCCCGTTCAGCCCGACCGCTGCGCCTTATCCGGTAACTAT

CGTCTTGAGTCCAACCCGGTAAGACACGACTTATCGCCACTGGCA
GCAGCCACTGGTAACAGGATTAGCAGAGCGAGGTATGTAGGCGG
TGCTACAGAGTTCTTGAAGTGGTGGCCTAACTACGGCTACACTAG
AAGAACAGTATTTGGTATCTGCGCTCTGCTGAAGCCAGTTACCTT
CGGAAAAAGAGTTGGTAGCTCTTGATCCGGCAAACAAACCACCG
CTGGTAGCGGTGGTTTTTTTGTTTGCAAGCAGCAGATTACGCGCA
GAAAAAAAGGATCTCAAGAAGATCCTTTGATCTTTTCTACGGGGT
CTGACGCTCAGTGGAACGAAAACTCACGTTAAGGGATTTTGGTCA
TGAGATTATCAAAAAGGATCTTCACCTAGATCCTTTTAAATTAAA
AATGAAGTTTTAAATCAATCTAAAGTATATATGAGTAACCTGAGG
CTATGGCAGGGCCTGCCGCCCCGACGTTGGCTGCGAGCCCTGGG
CCTTCACCCGAACTTGGGGGGTGGGGTGGGGAAAAGGAAGAAAC
GCGGGCGTATTGGCCCCAATGGGGTCTCGGTGGGGTATCGACAG
AGTGCCAGCCCTGGGACCGAACCCCGCGTTTATGAACAAACGACC
CAACACCGTGCGTTTTATTCTGTCTTTTTATTGCCGTCATAGCGC
GGGTTCCTTCCGGTATTGTCTCCTTCCGTGTTTCAGTTAGCCTCC
CCCTAGGGTGGGCGAAGAACTCCAGCATGAGATCCCCGCGCTGG
AGGATCATCCAGCCGGCGTCCCGGAAAACGATTCCGAAGCCCAAC
CTTTCATAGAAGGCGGCGGTGGAATCGAAATCTCGTGATGGCAG
GTTGGGCGTCGCTTGGTCGGTCATTTCGAACCCCAGAGTCCCGCT
CAGAAGAACTCGTCAAGAAGGCGATAGAAGGCGATGCGCTGCGA
ATCGGGAGCGGCGATACCGTAAAGCACGAGGAAGCGGTCAGCCC
ATTCGCCGCCAAGCTCTTCAGCAATATCACGGGTAGCCAACGCTA
TGTCCTGATAGCGGTCCGCCACACCCAGCCGGCCACAGTCGATGA
ATCCAGAAAAGCGGCCATTTTCCACCATGATATTCGGCAAGCAGG
CATCGCCATGGGTCACGACGAGATCCTCGCCGTCGGGCATGCTCG
CCTTGAGCCTGGCGAACAGTTCGGCTGGCGCGAGCCCCTGATGCT
CTTCGTCCAGATCATCCTGATCGACAAGACCGGCTTCCATCCGAG
TACGTGCTCGCTCGATGCGATGTTTCGCTTGGTGGTCGAATGGG
CAGGTAGCCGGATCAAGCGTATGCAGCCGCCGCATTGCATCAGCC
ATGATGGATACTTTCTCGGCAGGAGCAAGGTGAGATGACAGGAG
ATCCTGCCCCGGCACTTCGCCCAATAGCAGCCAGTCCCTTCCCGC
TTCAGTGACAACGTCGAGCACAGCTGCGCAAGGAACGCCCGTCGT
GGCCAGCCACGATAGCCGCGCTGCCTCGTCTTGCAGTTCATTCAG
GGCACCGGACAGGTCGGTCTTGACAAAAAGAACCGGGCGCCCCT
GCGCTGACAGCCGGAACACGGCGGCATCAGAGCAGCCGATTGTC
TGTTGTGCCCAGTCATAGCCGAATAGCCTCTCCACCCAAGCGGCC
GGAGAACCTGCGTGCAATCCATCTTGTTCAATCAT

B.2 SEQUENCING RESULT OF THE PLASMID PU3U5 ENLARGED TO 9.112 KBP

CACCTGACGCGCCCTGTAGCGGCGCATTAAGCGCGGCGGGTGTG
GTGGTTACGCGCAGCGTGACCGCTACACTTGCCAGCGCCCTAGCG
CCCGCTCCTTTCGCTTTCTTCCCTTCCTTTCTCGCCACGTTCGCC
GGCTTTCCCCGTCAAGCTCTAAATCGGGGGCTCCCTTTAGGGTTC
CGATTTAGTGCTTTACGGCACCTCGACCCCAAAAAACTTGATTAG
GGTGATGGTTCACGTAGTGGGCCATCGCCCTGATAGACGGTTTTT
CGCCCTTTGACGTTGGAGTCCACGTTCTTTAATAGTGGACTCTTG
TTCCAAACTGGAACAACACTCAACCCTATCTCGGTCTATTCTTTT
GATTTATAAGGGATTTTGCCGATTTCGGCCTATTGGTTAAAAAAT
GAGCTGATTTAACAAAAATTTAACGCGAATTTTAACAAAATATTA

ACGCTTACAATTTACGCGTTAAGATACATTGATGAGTTTGGACAA
ACCACAACTAGAATGCAGTGAAAAAAATGCTTTATTTGTGAAATT
TGTGATGCTATTGCTTTATTTGTAACCATTATAAGCTGCAATAAA
CAAGTTAACAACAACAATTGCATTCATTTTATGTTTCAGGTTCAG
GGGGAGGTGTGGGAGGTTTTTTAAAGCAAGTAAAACCTCTACAA
ATGTGGTATGGCTGATTATGATCATGAACAGACTGTGAGGACTG
AGGGGCCTGAAATGAGCCTTGGGACTGTGAATCTAAAATACACA
AACAATTAGAATCAGTAGTTTAACACATTATACACTTAAAAATTG
GATCTCCATTCGCCATTCAGGCTGCGCAACTGTTGGGAAGGGCGA
TCGGTGCGGGCCTCTTCGCTATTACGCCAGCTGGCGAAAGGGGG
ATGTGCTGCAAGGCGATTAAGTTGGGTAACGCCAGGGTTTTCCCA
GTCACGACGTTGTAAAACGACGGCCAGTGAATTGTAATACGACTC
ACTATAGGGCGAATTGGGTACACTTACCTGGTACCTGTACTGGGT
CTCTCTGGTTAGACCAGATCTGAGCCTGGGAGCTCTCTGGCTAAC
TAGGGAACCCACTGCTTAAGCCTCAATAAAGCTTGCCTTGAGTGC
TTCAAGTAGTGTGTGCCCGTCTGTTGTGTGACTCTGGTAACTAGA
GATCCCTCAGACCCTTTTAGTCAGTGTGGAAAATCTCTAGCAGTA
CTGGAAGGGCTAATTCACTCCCAAAGAAGACAAGATATCCTTGAT
CTGTGGATCTACCACACACAAGGCTACTTCCCTGATTAGCAGAAC
TACACACCAGGGCCAGGGGTCAGATATCCACTGACCTTTGGATGG
TGCTACAAGCTAGTACCAGTTGAGCCAGATAAGATAGAATTCTTT
GGATCCACTAGTGTCGACCTGCAGGCGCGCGAGCTCCAGCTTTTG
TTCCCTTTAGTGAGGGTTAATTTCGAGCTTGGCGTAATCAAGGTC
ATAGCTGTTTCCTGTGTGAAATTGTTATCCGCTCACAATTCCACA
CAATATACGAGCCGGAAGTATAAAGTGTAAAGCCTGGGGTGCCT
AATGAGTGAGCTAACTCACAGTAATTGCGGCTAGCCAGGTGCACA
CCAATGTGGTGAATGGTCAAATGGCGTTTATTGTATCGAGCTAG
GCACTTAAATACAATTATCTCTGCAATGCGGTATTCAGTGGTTCG
TCCAATCCATGTCAGACCCGTCTGTTGCCTTCCTAATAAGGCACG
ATCGTACCACCTTACTTCCACCAATCGGCATGCACGGTGCTTTTT
CTCTCCTTGTAAGGCATGTTGCTAACTCATCGTTACCATGTTGCA
AGACTACAAGAGTATTGCATAAGACTACATTTCCCCCTCCCTATG
CAAAAGCGAAACTACTATATCCTGAGGGGACTCCTAACCGCGTAC
AACCGAAGCCCCGCTTTTCGCCTAAACACACCCTAGTCCCCTCAG
ATACGCGTATATCTGGCCCGTACATCGCGAAGCAGCGCAAAACGC
CTAACCCTAAGCAGATTCTTCATGCAATTGTCGGTCAAGCCTTGC
CTTGTTGTAGCTTAAATTTTGCTCGCGCACTACTCAGCGACCTCC
AACACACAAGCAGGGAGCAGATGCATGGCGGTAATACGGTTATC
CACAGAATCAGGGGATAACGCAGGAAAGAACATGTGAGCAAAAG
GCCAGCAAAAGGCCAGGAACCGTAAAAAGGCCGCGTTGCTGGCG
TTTTTCCATAGGCTCCGCCCCCCTGACGAGCATCACAAAAATCGA
CGCTCAAGTCAGAGGTGGCGAAACCCGACAGGACTATAAAGATA
CCAGGCGTTTCCCCCTGGAAGCTCCCTCGTGCGCTCTCCTGTTCC
GACCCTGCCGCTTACCGGATACCTGTCCGCCTTTCTCCCTTCGGG
AAGCGTGGCGCTTTCTCATAGCTCACGCTGTAGGTATCTCAGTTC
GGTGTAGGTCGTTCGCTCCAAGCTGGGCTGTGTGCACGAACCCC
CCGTTCAGCCCGACCGCTGCGCCTTATCCGGTAACTATCGTCTTG
AGTCCAACCCGGTAAGACACGACTTATCGCCACTGGCAGCAGCCA
CTGGTAACAGGATTAGCAGAGCGAGGTATGTAGGCGGTGCTACA
GAGTTCTTGAAGTGGTGGCCTAACTACGGCTACACTAGAAGAAC
AGTATTTGGTATCTGCGCTCTGCTGAAGCCAGTTACCTTCGGAAA
AAGAGTTGGTAGCTCTTGATCCGGCAAACAAACCACCGCTGGTAG

CGGTGGTTTTTTTGTTTGCAAGCAGCAGATTACGCGCAGAAAAAA
AGGATCTCAAGAAGATCCTTTGATCTTTTCTACGGGGTCTGACGC
TCAGTGGAACGAAAACTCACGTTAAGGGATTTTGGTCATGAGATT
ATCAAAAAGGATCTTCACCTAGATCCTTTTAAATTAAAAATGAAG
TTTTAAATCAATCTAAAGTATATATGAGTAACCTGAGGCTATGGC
AGGGCCTGCCGCCCCGACGTTGGCTGCGAGCCCTGGGCCTTCACC
CGAACTTGGGGGGTGGGGTGGGGAAAAGGAAGAAACGCGGGCGT
ATTGGCCCCAATGGGGTCTCGGTGGGGTATCGACAGAGTGCCAG
CCCTGGGACCGAACCCCGCGTTTATGAACAAACGACCCAACACCG
TGCGTTTTATTCTGTCTTTTTATTGCCGTCATAGCGCGGGTTCCT
TCCGGTATTGTCTCCTTCCGTGTTTCAGTTAGCCTCCCCCTAGGG
TGGGCGAAGAACTCCAGCATGAGATCCCCGCGCTGGAGGATCAT
CCAGCCGGCGTCCCGGAAAACGATTCCGAAGCCCAACCTTTCATA
GAAGGCGGCGGTGGAATCGAAATCTCGTGATGGCAGGTTGGGCG
TCGCTTGGTCGGTCATTTCGAACCCCAGAGTCCCGCATCGTCCAT
TCCGACAGCATCGCCAGTCACTATGGCGTGCTGCTAGCGCTATAT
GCGTTGATGCAATTTCTATGCGCACCCGTTCTCGGAGCACTGTCC
GACCGCTTTGGCCGCCGCCCAGTCCTGCTCGCTTCGCTACTTGGA
GCCACTATCGACTACGCGATCATGGCGACCACACCCGTCCTGTGG
ATCCTCTACGCCGGACGCATCGTGGCCGGCATCACCGGCGCCACA
GGTGCGGTTGCTGGCGCCTATATCGCCGACATCACCGATGGGGA
AGATCGGGCTCGCCACTTCGGGCTCATGAGCGCTTGTTTCGGCGT
GGGTATGGTGGCAGGCCCCGTGGCCGGGGGACTGTTGGGCGCCA
TCTCCTTGCATGCACCATTCCTTGCGGCGGCGGTGCTCAACGGCC
TCAACCTACTACTGGGCTGCTTCCTAATGCAGGAGTCGCATAAGG
GAGAGCGTCGACCGATGCCCTTGAGAGCCTTCAACCCAGTCAGCT
CCTTCCGGTGGGCGCGGGGCATGACTATCGTCGCCGCACTTATGA
CTGTCTTCTTTATCATGCAACTCGTAGGACAGGTGCCGGCAGCGC
TCTGGGTCATTTTCGGCGAGGACCGCTTTCGCTGGAGCGCGACGA
TGATCGGCCTGTCGCTTGCGGTATTCGGAATCTTGCACGCCCTCG
CTCAAGCCTTCGTCACTGGTCCCGCCACCAAACGTTTCGGCGAGA
AGCAGGCCATTATCGCCGGCATGGCGGCCGACGCGCTGGGCTAC
GTCTTGCTGGCGTTCGCGACGCGAGGCTGGATGGCCTTCCCCATT
ATGATTCTTCTCGCTTCCGGCGGCATCGGGATGCCCGCGTTGCAG
GCCATGCTGTCCAGGCAGGTAGATGACGACCATCAGGGACAGCT
TCAAGGATCGCTCGCGGCTCTTACCAGCCTAACTTCGATCATTGG
ACCGCTGATCGTCACGGCGATTTATGCCGCCTCGGCGAGCACATG
GAACGGGTTGGCATGGATTGTAGGCGCCGCCCTATACCTTGTCT
GCCTCCCCGCGTTGCGTCGCGGTGCATGGAGCCGGGCCACCTCGA
CCTGAATGGAAGCCGGCGGCACCTCGCTAACGGATTCACCACTCC
AAGAATTGGAGCCAATCAATTCTTGCGGAGAACTGTGAATGCGCA
AACCAACCCTTGGCAGAACATATCCATCGCGTCCGCCATCTCCAG
CAGCCGCACGCGGCGCATCTCGGGCAGCGTTGGGTCCTGGCCAC
GGGTGCGCATGATCGTGCTCCTGTCGTTGAGGACCCGGCTAGGC
TGGCGGGGTTGCCTTACTGGTTAGCAGAATGAATCACCGATACG
CGAGCGAACGTGAAGCGACTGCTGCTGCAAAACGTCTGCGACCT
GAGCAACAACATGAATGGTCTTCGGTTTCCGTGTTTCGTAAAGTC
TGGAAACGCGGAAGTCAGCGCCCTGCACCATTATGTTCCGGATCT
GCATCGCAGGATGCTGCTGGCTACCCTGTGGAACACCTACATCTG
TATTAACGAAGCGCTGGCATTGACCCTGAGTGATTTTTCTCTGGT
CCCGCCGCATCCATACCGCCAGTTGTTTACCCTCACAACGTTCCA
GTAACCGGGCATGTTCATCATCAGTAACCCGTATCGTGAGCATCC

TCTCTCGTTTCATCGGTATCATTACCCCCATGAACAGAAATCCCC
CTTACACGGAGGCATCAGTGACCAAACAGGAAAAAACCGCCCTTA
ACATGGCCCGCTTTATCAGAAGCCAGACATTAACGCTTCTGGAGA
AACTCAACGAGCTGGACGCGGATGAACAGGCAGACATCTGTGAA
TCGCTTCACGACCACGCTGATGAGCTTTACCGCAGCTGCCTCGCG
CGTTTCGGTGATGACGGTGAAAACCTCTGACACATGCAGCTCCCG
GAGACGGTCACAGCTTGTCTGTAAGCGGATGCCGGGAGCAGACA
AGCCCGTCAGGGCGCGTCAGCGGGTGTTGGCGGGTGTCGGGGCG
CAGCCATGACCCAGTCACGTAGCGATAGCGGAGTGTATACTGGCT
TAACTATGCGGCATCAGAGCAGATTGTACTGAGAGTGCACCATAT
GCGGTGTGAAATACCGCACAGATGCGTAAGGAGAAAATACCGCA
TCAGGCGCTCTTCCGCTTCCTCGCTCACTGACTCGCTGCGCTCGG
TCGTTCGGCTGCGGCGAGCGGTATCAGCTCACTCAAAGGCGGTA
ATACGGTTATCCACAGAATCAGGGGATAACGCAGGAAAGAACAT
GTGAGCAAAAGGCCAGCAAAAGGCCAGGAACCGTAAAAAGGCCG
CGTTGCTGGCGTTTTTCCATAGGCTCCGCCCCCCTGACGAGCATC
ACAAAAATCGACGCTCAAGTCAGAGGTGGCGAAACCCGACAGGA
CTATAAAGATACCAGGCGTTTCCCCCTGGAAGCTCCCTCGTGCGC
TCTCCTGTTCCGACCCTGCCGCTTACCGGATACCTGTCCGCCTTT
CTCCCTTCGGGAAGCGTGGCGCTTTCTCATAGCTCACGCTGTAGG
TATCTCAGTTCGGTGTAGGTCGTTCGCTCCAAGCTGGGCTGTGTG
CACGAACCCCCCGTTCAGCCCGACCGCTGCGCCTTATCCGGTAAC
TATCGTCTTGAGTCCAACCCGGTAAGACACGACTTATCGCCACTG
GCAGCAGCCACTGGTAACAGGATTAGCAGAGCGAGGTATGTAGG
CGGTGCTACAGAGTTCTTGAAGTGGTGGCCTAACTACGGCTACAC
TAGAAGGACAGTATTTGGTATCTGCGCTCTGCTGAAGCCAGTTAC
CTTCGGAAAAAGAGTTGGTAGCTCTTGATCCGGCAAACAAACCAC
CGCTGGTAGCGGTGGTTTTTTTGTTTGCAAGCAGCAGATTACGC
GCAGAAAAAAAGGATCTCAAGAAGATCCTTTGATCTTTTCTACGG
GGTCTGACGCTCAGTGGAACGAAAACTCACGTTAAGGGATTTTG
GTCATGAGATTATCAAAAAGGATCTTCACCTAGATCCTTTTAAAT
TAAAAATGAAGTTTTAAATCAATCTAAAGTATATATGAGTAAACT
TGGTCTGACAGTTACCAATGCTTAATCAGTGAGGCACCTATCTCA
GCGATCTGTCTATTTCGTTCATCCATAGTTGCCTGACTCCCCGTC
GTGTAGATAACTACGATACGGGAGGGCTTACCATCTGGCCCCAGT
GCTGCAATGATACCGCGAGACCCACGCTCACCGGCTCCAGATTTA
TCAGCAATAAACCAGCCAGCCGGAAGGGCCGAGCGCAGAAGTGG
TCCTGCAACTTTATCCGCCTCCATCCAGTCTATTAATTGTTGCCG
GGAAGCTAGAGTAAGTAGTTCGCCAGTTAATAGTTTGCGCAACG
TTGTTGCCATTGCTGCAGGCATCGTGGTGTCACGCTCGTCGTTTG
GTATGGCTTCATTCAGCTCCGGTTCCCAACGATCAAGGCGAGTTA
CATGATCCCCCATGTTGTGCAAAAAAGCGGTTAGCTCCTTCGGTC
CTCCGATCGTTGTCAGAAGTAAGTTGGCCGCAGTGTTATCACTCA
TGGTTATGGCAGCACTGCATAATTCTCTTACTGTCATGCCATCCG
TAAGATGCTTTTCTGTGACTGGTGAGTACTCAACCAAGTCATTCT
GAGAATAGTGTATGCGGCGACCGAGTTGCTCTTGCCCGGCGTCA
ACACGGGATAATACCGCGCCACATAGCAGAACTTTAAAAGTGCTC
ATCATTGGAAAACGTTCTTCGGGGCGAAAACTCTCAAGGATCTTA
CCGCTGTTGAGATCCAGTTCGATGTAACCCACTCGTGCACCCAAC
TGATCTTCAGCATCTTTTACTTTCACCAGCGTTTCTGGGTGAGCA
AAAACAGGAAGGCAAAATGCCGCAAAAAAGGGAATAAGGGCGAC
ACGGAAATGTTGAATACTCATACTCTTCCTTTTTCAATATTATTG

AAGCATTTATCAGGGTTATTGTCTCATGAGCGGATACATATTTGA
ATGTATTTAGAAAAATAAACAAATAGGGGTTCCGCGCACATTTCC
CCGAAAAGTGCCACCTGACGTCTAAGAAACCATTATTATCATGAC
ATTAACCTATAAAAATAGGCGTATCACGAGGCCCTTTCGTCTTCA
AGAATTCTCATGTTTGACAGCTTATCATCGATAAGCTTTAATGCG
GTAGTTTATCACAGTTAAATTGCTAACGCAGTCAGGCACCGTGTA
TGAAATCTAACAATGCGCTCATCGTCATCCTCGGCACCGTCACCC
TGGATGCTGTAGGCATAGGCTTGGTTATGCCGGTACTGCCGGGC
CTCTTGCGGGATTCAGAAGAACTCGTCAAGAAGGCGATAGAAGG
CGATGCGCTGCGAATCGGGAGCGGCGATACCGTAAAGCACGAGG
AAGCGGTCAGCCCATTCGCCGCCAAGCTCTTCAGCAATATCACGG
GTAGCCAACGCTATGTCCTGATAGCGGTCCGCCACACCCAGCCGG
CCACAGTCGATGAATCCAGAAAAGCGGCCATTTTCCACCATGATA
TTCGGCAAGCAGGCATCGCCATGGGTCACGACGAGATCCTCGCCG
TCGGGCATGCTCGCCTTGAGCCTGGCGAACAGTTCGGCTGGCGC
GAGCCCCTGATGCTCTTCGTCCAGATCATCCTGATCGACAAGACC
GGCTTCCATCCGAGTACGTGCTCGCTCGATGCGATGTTTCGCTTG
GTGGTCGAATGGGCAGGTAGCCGGATCAAGCGTATGCAGCCGCC
GCATTGCATCAGCCATGATGGATACTTTCTCGGCAGGAGCAAGGT
GAGATGACAGGAGATCCTGCCCCGGCACTTCGCCCAATAGCAGCC
AGTCCCTTCCCGCTTCAGTGACAACGTCGAGCACAGCTGCGCAAG
GAACGCCCGTCGTGGCCAGCCACGATAGCCGCGCTGCCTCGTCTT
GCAGTTCATTCAGGGCACCGGACAGGTCGGTCTTGACAAAAAGA
ACCGGGCGCCCCTGCGCTGACAGCCGGAACACGGCGGCATCAGA
GCAGCCGATTGTCTGTTGTGCCCAGTCATAGCCGAATAGCCTCTC
CACCCAAGCGGCCGGAGAACCTGCGTGCAATCCATCTTGTTCAAT
CATGCGAAACGATCCTCATCCTGTCTCTTGATCGATCTTTGCAAA
AGCCTAGGCCTCCAAAAAAGCCTCCTCACTACTTCTGGAATAGCT
CAGAGGCCGAGGCGGCCTCGGCCTCTGCATAAATAAAAAAAATTA
GTCAGCCATGGGGCGGAGAATGGGCGGAACTGGGCGGAGTTAGG
GGCGGGATGGGCGGAGTTAGGGGCGGGACTATGGTTGCTGACTA
ATTGAGATGCATGCTTTGCATACTTCTGCCTGCTGGGGAGCCTGG
GGACTTTCCACACCTGGTTGCTGACTAATTGAGATGCATGCTTTG
CATACTTCTGCCTGCTGGGGAGCCTGGGGACTTTCCACACCCTAA
CTGACACACATTCCACAGCTGGTTCTTTCCGCCTCAGGACTCTTC
CTTTTTCAATATTATTGAAGCATTTATCAGGGTTATTGTCTCATG
AGCGGATACATATTTGAATGTATTTAGAAAAATAAACAAATAGG
GGTTCCGCGCACATTTCCCCGAAAAGTGC

BIBLIOGRAPHY

[1] K. Stierstadt. "Phasenübergänge in Physik und Biologie: I. Phasenübergänge im thermodynamischen Gleichgewicht und ihre Bedeutung für physiologische Vorgänge im menschlichen Körper." In: *Physikalische Blätter* 34.7 (1978), pp. 304–316. ISSN: 0031-9279. DOI: https://doi.org/10.1002/phbl.19780340702 (cit. on p. 1).

[2] K. Stierstadt. "Phase Transitions in Physics and Biology." In: *Physics Bulletin* 30.1 (1979), p. 15. ISSN: 0031-9112. DOI: 10.1088/0031-9112/30/1/020 (cit. on pp. 1, 4, 6).

[3] P. Papon, J. Leblond, and P. H. E. Meijer. *The physics of phase transitions: Concepts and applications*. 2006, pp. 1–409. DOI: 10.1007/3-540-33390-8 (cit. on pp. 1, 5).

[4] D. G. Lev, K. E. Gubbins, R. Radhakrishnan, and M. Sliwinska-Bartkowiak. "Phase separation in confined systems." In: *Reports on Progress in Physics* 62.12 (1999), p. 1573. ISSN: 0034-4885. DOI: 10.1088/0034-4885/62/12/201 (cit. on pp. 1, 4).

[5] D. van Delft. "The Cryogenic Laboratory of Heike Kamerlingh Onnes: An Early Case of Big Science." In: *History of Artificial Cold, Scientific, Technological and Cultural Issues*. Ed. by K. Gavroglu. Dordrecht: Springer Netherlands, 2014, pp. 65–81. ISBN: 978-94-007-7199-4. DOI: 10.1007/978-94-007-7199-4_4 (cit. on p. 1).

[6] H. K. Onnes. ""Further experiments with liquid helium."" In: *Through Measurement to Knowledge: The Selected Papers of Heike Kamerlingh Onnes 1853–1926*. Ed. by K. Gavroglu and Y. Goudaroulis. Dordrecht: Springer Netherlands, 1991, pp. 201–220. ISBN: 978-94-009-2079-8. DOI: 10.1007/978-94-009-2079-8_10 (cit. on p. 1).

[7] The Nobel Foundation. *The Nobel Prize in Physics 1903*. 1913 (accessed November 21, 2023). URL: https://www.nobelprize.org/prizes/physics/1913/summary/ (cit. on p. 1).

[8] L. Landau. "Theory of the Superfluidity of Helium II." In: *Physical Review* 60.4 (1941), pp. 356–358. DOI: 10.1103/PhysRev.60.356 (cit. on pp. 1, 2).

[9] The Nobel Foundation. *The Nobel Prize in Physics 1962*. 1962 (accessed August 24, 2023). URL: https://www.nobelprize.org/prizes/physics/1962/summary/ (cit. on p. 2).

[10] A. J. Leggett. "Superfluidity." In: *Reviews of Modern Physics* 71.2 (1999), S318–S323. DOI: 10.1103/RevModPhys.71.S318 (cit. on p. 2).

[11] The Nobel Foundation. *The Nobel Prize in Physics 1982*. 1982 (accessed August 24, 2023). URL: https://www.nobelprize.org/prizes/physics/1982/summary/ (cit. on pp. 2, 3).

[12] M. Niss. "History of the Lenz–Ising Model 1950–1965: from irrelevance to relevance." In: *Archive for History of Exact Sciences* 63.3 (2009), pp. 243–287. ISSN: 1432-0657. DOI: 10.1007/s00407-008-0039-5 (cit. on pp. 2, 3).

[13] K. G. Wilson. "Critical phenomena in 3.99 dimensions." In: *Physica* 73.1 (1974), pp. 119–128. ISSN: 0031-8914. DOI: https://doi.org/10.1016/0031-8914(74)90229-8 (cit. on pp. 2, 3).

[14] K. G. Wilson. "The renormalization group and critical phenomena." In: *Reviews of Modern Physics* 55.3 (1983), pp. 583–600. DOI: 10.1103/RevModPhys.55.583 (cit. on pp. 2, 3).

[15] Hamish Johnston. *My favourite Nobel prize: a universal theory for phase transitions*. September 24, 2019 (accessed August 25, 2023). URL: https://physicsworld.com/a/my-favourite-nobel-prize-a-universal-theory-for-phase-transitions/ (cit. on p. 3).

[16] The Nobel Foundation. *The Nobel Prize in Physics 2016*. October 2016 (accessed August 25, 2023). URL: https://www.nobelprize.org/prizes/physics/2016/summary/ (cit. on p. 3).

[17] J. M. Kosterlitz and D. J. Thouless. "Long range order and metastability in two dimensional solids and superfluids. (Application of dislocation theory)." In: *Journal of Physics C: Solid State Physics* 5.11 (1972), p. L124. ISSN: 0022-3719. DOI: 10.1088/0022-3719/5/11/002 (cit. on p. 3).

[18] J Kosterlitz and D Thouless. "Order, metastability and phase transitions in two-dimensional systems." In: *Journal of Physics C* 6 (1973), pp. l181–1203 (cit. on p. 3).

[19] D. J. Thouless, M. Kohmoto, M. P. Nightingale, and M. den Nijs. "Quantized Hall Conductance in a Two-Dimensional Periodic Potential." In: *Physical Review Letters* 49.6 (1982), pp. 405–408. DOI: 10.1103/PhysRevLett.49.405 (cit. on p. 3).

[20] F. D. M. Haldane. "Continuum dynamics of the 1-D Heisenberg antiferromagnet: Identification with the O(3) nonlinear sigma model." In: *Physics Letters A* 93.9 (1983), pp. 464–468. ISSN: 0375-9601. DOI: https://doi.org/10.1016/0375-9601(83)90631-X (cit. on p. 3).

[21] F. D. M. Haldane. "Nonlinear Field Theory of Large-Spin Heisenberg Antiferromagnets: Semiclassically Quantized Solitons of the One-Dimensional Easy-Axis Néel State." In: *Physical Review Letters* 50.15 (1983), pp. 1153–1156. DOI: 10.1103/PhysRevLett.50.1153 (cit. on p. 3).

[22] I. Langmuir. "Oscillations in Ionized Gases." In: *Proceedings of the National Academy of Sciences* 14.8 (1928), pp. 627–637. DOI: 10.1073/pnas.14.8.627 (cit. on p. 4).

[23] A. Einstein. "Quantentheorie des einatomigen idealen Gases. Zweite Abhandlung." In: *Albert Einstein: Akademie-Vorträge*. 2005, pp. 245–257. ISBN: 9783527608959. DOI: https://doi.org/10.1002/3527608958.ch28 (cit. on p. 4).

[24] U. Stroth. *Plasmaphysik*. Vieweg+Teubner, 2018. ISBN: 978-3-8348-1615-3. DOI: 10.1007/978-3-8348-8326-1 (cit. on p. 4).

[25] S. O. Demokritov, V. E. Demidov, O. Dzyapko, G. A. Melkov, A. A. Serga, B. Hillebrands, and A. N. Slavin. "Bose–Einstein condensation of quasi-equilibrium magnons at room temperature under pumping." In: *Nature* 443.7110 (2006), pp. 430–433. ISSN: 1476-4687. DOI: 10.1038/nature05117 (cit. on p. 4).

[26] "Preface." In: *Les Houches*. Ed. by J.-P. Bouchaud, M. Mézard, and J. Dalibard. Vol. 85. Elsevier, 2007, pp. xvii–xx. ISBN: 0924-8099. DOI: https://doi.org/10.1016/S0924-8099(07)80007-2 (cit. on p. 4).

[27] R. Monasson. "Course 1 Introduction to phase transitions in random optimization problems." In: *Les Houches*. Ed. by J.-P. Bouchaud, M. Mézard, and J. Dalibard. Vol. 85. Elsevier, 2007, pp. 1–65. ISBN: 0924-8099. DOI: https://doi.org/10.1016/S0924-8099(07)80008-4 (cit. on p. 4).

[28] S. Boeynaems, S. Alberti, N. L. Fawzi, T. Mittag, M. Polymenidou, F. Rousseau, J. Schymkowitz, J. Shorter, B. Wolozin, L. Van Den Bosch, et al. "Protein Phase Separation: A New Phase in Cell Biology." In: *Trends in Cell Biology* 28.6 (2018), pp. 420–435. ISSN: 0962-8924. DOI: 10.1016/j.tcb.2018.02.004 (cit. on pp. 4–6).

[29] L.-P. Bergeron-Sandoval, N. Safaee, and S. W. Michnick. "Mechanisms and consequences of macromolecular phase separation." In: *Cell* 165.5 (2016), pp. 1067–1079. ISSN: 0092-8674 (cit. on pp. 4, 5).

[30] J.-G. Young, G. St-Onge, E. Laurence, C. Murphy, L. Héebert-Dufresne, and P. Desrosiers. "Phase Transition in the Recoverability of Network History." In: *Physical Review X* 9.4 (2019), p. 041056. DOI: 10.1103/PhysRevX.9.041056 (cit. on p. 4).

[31] J. Rau and J. Rau. "182Phase Transitions." In: *Statistical Physics and Thermodynamics: An Introduction to Key Concepts*. Oxford University Press, 2017, p. 0. ISBN: 9780199595068. DOI: 10.1093/oso/9780199595068.003.0008 (cit. on pp. 4, 5).

[32] H. Nishimori, G. Ortiz, H. Nishimori, and G. Ortiz. "1Phase transitions and critical phenomena." In: *Elements of Phase Transitions and Critical Phenomena*. Oxford University Press, 2010, p. 0. ISBN: 9780199577224. DOI: 10.1093/acprof:oso/9780199577224.003.0001 (cit. on pp. 4, 5).

[33] C. F. Lee and J. D. Wurtz. "Novel physics arising from phase transitions in biology." In: *Journal of Physics D: Applied Physics* 52.2 (2019), p. 023001. ISSN: 0022-3727. DOI: 10.1088/1361-6463/aae510 (cit. on pp. 4–6, 89).

[34] R. Franzosi and M. Pettini. "Theorem on the Origin of Phase Transitions." In: *Physical Review Letters* 92.6 (2004), p. 060601. DOI: 10.1103/PhysRevLett.92.060601 (cit. on pp. 4, 5).

[35] P. A. Fleury. "Phase Transitions, Critical Phenomena, and Instabilities." In: *Science* 211.4478 (1981), pp. 125–131. DOI: 10.1126/science.211.4478.125 (cit. on p. 4).

[36] A. A. Hyman, C. A. Weber, and F. Jülicher. "Liquid-Liquid Phase Separation in Biology." In: *Annual Review of Cell and Developmental Biology* 30.1 (2014), pp. 39–58. ISSN: 1081-0706. DOI: 10.1146/annurev-cellbio-100913-013325 (cit. on pp. 5, 6).

[37] D. M. Mitrea and R. W. Kriwacki. "Phase separation in biology; functional organization of a higher order." In: *Cell Communication and Signaling* 14.1 (2016), p. 1. ISSN: 1478-811X. DOI: 10.1186/s12964-015-0125-7 (cit. on p. 5).

[38] E. F. W. Heffern, H. Huelskamp, S. Bahar, and R. F. Inglis. "Phase transitions in biology: from bird flocks to population dynamics." In: *Proceedings of the Royal Society B: Biological Sciences* 288.1961 (2021), p. 20211111. DOI: doi:10.1098/rspb.2021.1111 (cit. on pp. 5, 6).

[39] M. Buchanan. "Biological transitions." In: *Nature Physics* 15.1 (2019), pp. 2–2. ISSN: 1745-2481. DOI: 10.1038/s41567-018-0393-4 (cit. on pp. 5, 151).

[40] V. N. Uversky. "Biological Liquid-Liquid Phase Separation, Biomolecular Condensates, and Membraneless Organelles: Now You See Me, Now You Don't." In: *International Journal of Molecular Sciences* 24.17 (2023), p. 13150. ISSN: 1422-0067 (cit. on p. 5).

[41] Y. Shin and C. P. Brangwynne. "Liquid phase condensation in cell physiology and disease." In: *Science* 357.6357 (2017), eaaf4382. DOI: 10.1126/science.aaf4382 (cit. on pp. 5, 6).

[42] Jennifer Baily. *It's not just a phase (separation)*. November 6, 2019 (accessed August 25, 2023). URL: https://bioscope.ucdavis.edu/2019/11/06/its-not-just-a-phase-separation/ (cit. on p. 6).

[43] The Nobel Foundation. *The Nobel Prize in Physics 1991*. October 1991 (accessed March 5, 2023). URL: https://www.nobelprize.org/prizes/physics/1991/summary/ (cit. on p. 9).

[44] P.-G. de Gennes. "Soft matter (Nobel lecture)." In: *Angewandte Chemie International Edition in English* 31.7 (1992), pp. 842–845. ISSN: 0570-0833 (cit. on p. 9).

[45] M. Daoud and C. E. Williams. *Soft matter physics*. Springer, 1999. ISBN: 3540648526 (cit. on p. 9).

[46] F. Brochard Wyart and P. G. de Gennes. "Viscosity at small scales in polymer melts." In: *The European Physical Journal E* 1.1 (2000), pp. 93–97. ISSN: 1292-8941. DOI: 10.1007/s101890050011 (cit. on p. 9).

[47] P.-G. De Gennes and P.-G. Gennes. *Scaling concepts in polymer physics*. Cornell university press, 1979. ISBN: 080141203X (cit. on pp. 9, 10).

[48] H. Staudinger, H. Johner, R. Signer, G. Mie, and J. Hengstenberg. "Der polymere Formaldehyd, ein Modell der Zellulose." In: *Zeitschrift für Physikalische Chemie* 126U.1 (1927), pp. 425–448. DOI: doi:10.1515/zpch-1927-12628 (cit. on p. 10).

[49] H. Staudinger and E. Ochiai. "Über hochpolymere Verbindungen." In: *57. Mitteilung. Viscositätsmessungen an Lösungen von Fadenmolekülen* 158A.1 (1932), pp. 35–55. DOI: doi:10.1515/zpch-1932-15803 (cit. on p. 10).

[50] R. Phillips, J. Kondev, J. Theriot, and H. Garcia. *Physical biology of the cell, Chapter 1*. Garland Science, 2012. ISBN: 0429168837 (cit. on pp. 10, 14).

[51] A. Vologodskii. *Biophysics of DNA*. Cambridge University Press, 2015. ISBN: 9781316239889 (cit. on pp. 10, 12, 13, 15, 19, 22, 25, 26).

[52] W. Kuhn. "Über die Gestalt fadenförmiger Moleküle in Lösungen." In: *Kolloid-Zeitschrift* 68.1 (1934), pp. 2–15. ISSN: 1435-1536. DOI: 10.1007/BF01451681 (cit. on p. 10).

[53] O. Kratky and G. Porod. "Röntgenuntersuchung gelöster fadenmoleküle." In: *Recueil des Travaux Chimiques des Pays-Bas* 68.12 (1949), pp. 1106–1122. ISSN: 0165-0513 (cit. on p. 11).

[54] M. D. Frank-Kamenetskii. "Biophysics of the DNA molecule." In: *Physics Reports* 288.1-6 (1997), pp. 13–60. ISSN: 0370-1573 (cit. on pp. 12, 18, 19, 26).

[55] P. J. Flory. *Principles of polymer chemistry*. Cornell university press, 1953. ISBN: 0801401348 (cit. on pp. 13, 19).

[56] B. Alberts, A. Johnson, J. Lewis, M. Raff, K. Roberts, and P. Walter. *Molecular Biology of the Cell, 5th edition, Chapter 4*. New York, USA and Abingdon, UK: Garland Science, Taylor and Francis Group, 2008. Chap. DNA Replication, Repair, and Recombination (cit. on pp. 14, 50, 53).

[57] National Human Genome Research Institute. *DEOXYRIBONUCLEIC ACID (DNA)*. May 16, 2023 (accessed May 19, 2023). URL: https://www.genome.gov/genetics-glossary/Deoxyribonucleic-Acid (cit. on p. 14).

[58] R. E. Franklin and R. G. Gosling. "Evidence for 2-Chain Helix in Crystalline Structure of Sodium Deoxyribonucleate." In: *Nature* 172.4369 (1953), pp. 156–157. ISSN: 1476-4687. DOI: 10.1038/172156a0 (cit. on p. 15).

[59] R. E. Franklin and R. G. Gosling. "Molecular Configuration in Sodium Thymonucleate." In: *Nature* 171.4356 (1953), pp. 740–741. ISSN: 1476-4687. DOI: 10.1038/171740a0 (cit. on p. 15).

[60] J. D. Watson and F. H. C. Crick. "Molecular Structure of Nucleic Acids: A Structure for Deoxyribose Nucleic Acid." In: *Nature* 171.4356 (1953), pp. 737–738. ISSN: 1476-4687. DOI: 10.1038/171737a0 (cit. on p. 15).

[61] M. Cobb and N. Comfort. "What Rosalind Franklin truly contributed to the discovery of DNA's structure." In: *Nature* 616.7958 (2023), pp. 657–660. ISSN: 0028-0836 (cit. on pp. 15, 21).

[62] M. H. Wilkins. "Molecular Configuration of Nucleic Acids: From extensive diffraction data and molecular model building a more detailed picture is emerging." In: *Science* 140.3570 (1963), pp. 941–950. ISSN: 0036-8075 (cit. on p. 15).

[63] J. D. Griffith. "DNA Structure: Evidence from Electron Microscopy." In: *Science* 201.4355 (1978), pp. 525–527. DOI: doi:10.1126/science.663672 (cit. on p. 15).

[64] T. Zettl, R. S. Mathew, S. Seifert, S. Doniach, P. A. B. Harbury, and J. Lipfert. "Absolute Intramolecular Distance Measurements with Angstrom-Resolution Using Anomalous Small-Angle X-ray Scattering." In: *Nano Letters* 16.9 (2016), pp. 5353–5357. ISSN: 1530-6984. DOI: 10.1021/acs.nanolett.6b01160 (cit. on p. 15).

[65] F. H. Crick. "The genetic code - yesterday, today, and tomorrow." In: *Cold Spring Harbor symposia on quantitative biology*. Vol. 31. Cold Spring Harbor Laboratory Press, pp. 3–9. ISBN: 0091-7451 (cit. on p. 16).

[66] F. H. Crick. "On protein synthesis." In: *Symp Soc Exp Biol* 12 (1958), pp. 138–63. ISSN: 0081-1386 (Print) 0081-1386 (cit. on p. 16).

[67] G. Litwack. "Chapter 10 - Nucleic Acids and Molecular Genetics." In: *Human Biochemistry*. Ed. by G. Litwack. Boston: Academic Press, 2018, pp. 257–317. ISBN: 978-0-12-383864-3. DOI: https://doi.org/10.1016/B978-0-12-383864-3.00010-7 (cit. on pp. 16, 51).

[68] A. Telesnitsky and S. P. Goff. "Reverse Transcriptase and the Generation of Retroviral DNA." In: *Retroviruses*. Ed. by J. M. Coffin, S. H. Hughes, and H. E. Varmus. Cold Spring Harbor (NY): Cold Spring Harbor Laboratory Press Copyright 1997, Cold Spring Harbor Laboratory Press., 1997 (cit. on p. 16).

[69] S. B. Smith, L. Finzi, and C. Bustamante. "Direct Mechanical Measurements of the Elasticity of Single DNA Molecules by Using Magnetic Beads." In: *Science* 258.5085 (1992), pp. 1122–1126. DOI: doi:10.1126/science.1439819 (cit. on pp. 17, 18).

[70] C. Bustamante, J. F. Marko, E. D. Siggia, and S Smith. "Entropic elasticity of lambda-phage DNA." In: *Science* 265.5178 (1994), pp. 1599–1600. ISSN: 0036-8075 (cit. on pp. 17–19).

[71] S. B. Smith, Y. Cui, and C. Bustamante. "Overstretching B-DNA: The Elastic Response of Individual Double-Stranded and Single-Stranded DNA Molecules." In: *Science* 271.5250 (1996), pp. 795–799. DOI: doi:10.1126/science.271.5250.795 (cit. on p. 17).

[72] T. R. Strick, J.-F. Allemand, D. Bensimon, A. Bensimon, and V. Croquette. "The Elasticity of a Single Supercoiled DNA Molecule." In: *Science* 271.5257 (1996), pp. 1835–1837. DOI: doi:10.1126/science.271.5257.1835 (cit. on pp. 17, 46, 47).

[73] K. R. Chaurasiya, T. Paramanathan, M. J. McCauley, and M. C. Williams. "Biophysical characterization of DNA binding from single molecule force measurements." In: *Physics of Life Reviews* 7.3 (2010), pp. 299–341. ISSN: 1571-0645. DOI: https://doi.org/10.1016/j.plrev.2010.06.001 (cit. on p. 18).

[74] J. F. Marko. "Biophysics of protein-DNA interactions and chromosome organization." In: *Physica A: Statistical Mechanics and its Applications* 418 (2015), pp. 126–153. ISSN: 0378-4371. DOI: https://doi.org/10.1016/j.physa.2014.07.045 (cit. on pp. 18, 26).

[75] P. J. Flory and M. Volkenstein. "Statistical mechanics of chain molecules." In: *Biopolymers* 8.5 (1969), pp. 699–700. ISSN: 0006-3525. DOI: https://doi.org/10.1002/bip.1969.360080514 (cit. on p. 19).

[76] S. R. Gallagher. "Quantitation of DNA and RNA with Absorption and Fluorescence Spectroscopy." In: *Current Protocols in Human Genetics* 00.1 (1994), A.3D.1–A.3D.8. ISSN: 1934-8266. DOI: https://doi.org/10.1002/0471142905.hga03ds00 (cit. on p. 19).

[77] J. B. Schimelman, D. M. Dryden, L. Poudel, K. E. Krawiec, Y. Ma, R. Podgornik, V. A. Parsegian, L. K. Denoyer, W.-Y. Ching, N. F. Steinmetz, et al. "Optical properties and electronic transitions of DNA oligonucleotides as a function of composition and stacking sequence." In: *Physical Chemistry Chemical Physics* 17.6 (2015), pp. 4589–4599. ISSN: 1463-9076. DOI: 10.1039/C4CP03395G (cit. on p. 19).

[78] J. Lipfert, S. Doniach, R. Das, and D. Herschlag. "Understanding nucleic acid-ion interactions." In: *Annu Rev Biochem* 83 (2014), pp. 813–41. ISSN: 0066-4154 (Print) 0066-4154. DOI: 10.1146/annurev-biochem-060409-092720 (cit. on pp. 19–21, 98, 129).

[79] M. Gouy. "Sur la constitution de la charge électrique à la surface d'un électrolyte." In: *J. Phys. Theor. Appl.* 9.1 (1910), pp. 457–468 (cit. on p. 19).

[80] D. L. Chapman. "LI. A contribution to the theory of electrocapillarity." In: *The London, Edinburgh, and Dublin philosophical magazine and journal of science* 25.148 (1913), pp. 475–481. ISSN: 1941-5982 (cit. on p. 19).

[81] F. Fogolari, A. Brigo, and H. Molinari. "The Poisson-Boltzmann equation for biomolecular electrostatics: a tool for structural biology." In: *Journal of Molecular Recognition* 15.6 (2002), pp. 377–392. ISSN: 0952-3499. DOI: https://doi.org/10.1002/jmr.577 (cit. on p. 20).

[82] P. Debye and E. Hückel. "Zur Theorie der Elektrolyte. I. Gefrierpunktserniedrigung und verwandte Erscheinungen." In: *Physikalische Zeitschrift* 24.9 (1923), pp. 185–206 (cit. on p. 20).

[83] The Nobel Foundation. *The Nobel Prize in Chemistry 1986*. 1936 (accessed February 19, 2023). URL: https://www.nobelprize.org/prizes/chemistry/1936/debye/biographical/ (cit. on p. 20).

[84] T. Markovich, D. Andelman, and R. Podgornik. "Charged Membranes: Poisson-Boltzmann Theory, The DLVO Paradigm, and Beyond." In: *Handbook of lipid membranes*. CRC Press, 2021, pp. 99–128. ISBN: 0429194072 (cit. on p. 20).

[85] G. S. Manning. "Limiting Laws and Counterion Condensation in Polyelectrolyte Solutions II. Self-Diffusion of the Small Ions." In: *The Journal of Chemical Physics* 51.3 (1969), pp. 934–938. ISSN: 0021-9606. DOI: 10.1063/1.1672158 (cit. on p. 21).

[86] G. S. Manning. "Limiting laws and counterion condensation in polyelectrolyte solutions: IV. The approach to the limit and the extraordinary stability of the charge fraction." In: *Biophysical Chemistry* 7.2 (1977), pp. 95–102. ISSN: 0301-4622. DOI: https://doi.org/10.1016/0301-4622(77)80002-1 (cit. on p. 21).

[87] G. S. Manning. "The molecular theory of polyelectrolyte solutions with applications to the electrostatic properties of polynucleotides." In: *Quarterly Reviews of Biophysics* 11.2 (1978), pp. 179–246. ISSN: 0033-5835. DOI: 10.1017/S0033583500002031 (cit. on p. 21).

[88] T. Vuletić, S. D. Babić, D. Grgicin, D. Aumiler, J. Rädler, F. Livolant, and S. Tomić. "Manning free counterion fraction for a rodlike polyion: Aqueous solutions of short DNA fragments in presence of very low added salt." In: *Physical Review E* 83.4 (2011), p. 041803. DOI: 10.1103/PhysRevE.83.041803 (cit. on p. 21).

[89] J. Zhang, F. Li, and D. Yang. "DNA: From Carrier of Genetic Information to Polymeric Materials." In: *Transactions of Tianjin University* 25.4 (2019), pp. 301–311. ISSN: 1995-8196. DOI: 10.1007/s12209-019-00188-w (cit. on pp. 21, 24).

[90] R. P. Feynman. "Plenty of Room at the Bottom." In: *APS annual meeting*. 1959 (cit. on pp. 21, 22).

[91] N. C. Seeman. "Nucleic acid junctions and lattices." In: *Journal of Theoretical Biology* 99.2 (1982), pp. 237–247. ISSN: 0022-5193. DOI: https://doi.org/10.1016/0022-5193(82)90002-9 (cit. on p. 22).

[92] N. C. Seeman. "DNA in a material world." In: *Nature* 421.6921 (2003), pp. 427–431. ISSN: 1476-4687. DOI: 10.1038/nature01406 (cit. on p. 22).

[93] B. Saccà and C. M. Niemeyer. "DNA Origami: The Art of Folding DNA." In: *Angewandte Chemie International Edition* 51.1 (2012), pp. 58–66. ISSN: 1433-7851. DOI: https://doi.org/10.1002/anie.201105846 (cit. on p. 22).

[94] C. Lin, Y. Liu, and H. Yan. "Designer DNA Nanoarchitectures." In: *Biochemistry* 48.8 (2009), pp. 1663–1674. ISSN: 0006-2960. DOI: 10.1021/bi802324w (cit. on p. 22).

[95] N. C. Seeman. "An overview of structural DNA nanotechnology." In: *Molecular biotechnology* 37.3 (2007), p. 246. ISSN: 1073-6085 (cit. on pp. 22, 96).

[96] P. W. K. Rothemund. "Folding DNA to create nanoscale shapes and patterns." In: *Nature* 440.7082 (2006), pp. 297–302. ISSN: 1476-4687. DOI: 10.1038/nature04586 (cit. on pp. 23, 89, 96).

[97] D. Fu, R. Pradeep Narayanan, A. Prasad, F. Zhang, D. Williams, J. S. Schreck, H. Yan, and J. Reif. "Automated design of 3D DNA origami with non-rasterized 2D curvature." In: *Science Advances* 8.51 (2022), eade4455. DOI: doi:10.1126/sciadv.ade4455 (cit. on p. 23).

[98] H. Yan, T. H. LaBean, L. Feng, and J. H. Reif. "Directed nucleation assembly of DNA tile complexes for barcode-patterned lattices." In: *Proceedings of the National Academy of Sciences* 100.14 (2003), pp. 8103–8108. DOI: doi:10.1073/pnas.1032954100 (cit. on p. 23).

[99] S. Dey, C. Fan, K. V. Gothelf, J. Li, C. Lin, L. Liu, N. Liu, M. A. D. Nijenhuis, B. Saccà, F. C. Simmel, et al. "DNA origami." In: *Nature Reviews Methods Primers* 1.1 (2021), p. 13. ISSN: 2662-8449. DOI: 10.1038/s43586-020-00009-8 (cit. on p. 24).

[100] J. Huang, S. Gambietz, and B. Saccà. "Self-Assembled Artificial DNA Nanocompartments and Their Bioapplications." In: *Small* n/a.n/a (2022), p. 2202253. ISSN: 1613-6810. DOI: https://doi.org/10.1002/smll.202202253 (cit. on p. 24).

[101] A. J. Turberfield, J. C. Mitchell, B. Yurke, A. P. Mills, M. I. Blakey, and F. C. Simmel. "DNA Fuel for Free-Running Nanomachines." In: *Physical Review Letters* 90.11 (2003), p. 118102. DOI: 10.1103/PhysRevLett.90.118102 (cit. on p. 24).

[102] R. Weil and J. Vinograd. "THE CYCLIC HELIX AND CYCLIC COIL FORMS OF POLYOMA VIRAL DNA." In: *Proceedings of the National Academy of Sciences* 50.4 (1963), pp. 730–738. DOI: doi:10.1073/pnas.50.4.730 (cit. on pp. 25, 26).

[103] J. Vinograd and J. Lebowitz. "Physical and Topological Properties of Circular DNA." In: *Journal of General Physiology* 49.6 (1966), pp. 103–125. ISSN: 0022-1295. DOI: 10.1085/jgp.49.6.103 (cit. on pp. 25, 26).

[104] F. B. Fuller. "The Writhing Number of a Space Curve." In: *Proceedings of the National Academy of Sciences* 68.4 (1971), pp. 815–819. DOI: doi:10.1073/pnas.68.4.815 (cit. on p. 26).

[105] A. V. Vologodskii, S. Levene, K. V. Klenin, M. Frank-Kamenetskii, and N. R. Cozzarelli. "Conformational and thermodynamic properties of supercoiled DNA." In: *Journal of Molecular Niology* 227 (1992), pp. 1224–1243 (cit. on p. 26).

[106] A. Bates and A. Maxwell. *DNA Topology*. Oxford University Press, 2005. ISBN: 9780198567097 (cit. on p. 26).

[107] K. V. Klenin, A. V. Vologodskii, V. V. Anshelevich, A. M. Dykhne, and M. D. Frank-Kamenetskii. "Computer simulation of DNA supercoiling." In: *Journal of Molecular Biology* 217.3 (1991), pp. 413–419. ISSN: 0022-2836. DOI: https://doi.org/10.1016/0022-2836(91)90745-R (cit. on p. 26).

[108] T. C. Boles, J. H. White, and N. R. Cozzarelli. "Structure of plectonemically supercoiled DNA." In: *J Mol Biol* 213.4 (1990), pp. 931–51. ISSN: 0022-2836 (Print) 0022-2836 (Linking). DOI: 10.1016/S0022-2836(05)80272-4 (cit. on p. 26).

[109] J. H. White. "Self-linking and Gauss-integral in higher dimensions." In: *American Journal of Mathematics* 91.3 (1969), p. 693. ISSN: 0002-9327. DOI: 10.2307/2373348 (cit. on pp. 26, 27).

[110] F. Bacon. "1620. The new organon." In: *Aphorisms concerning the interpretation of nature and the kingdom of man. Venice, Italy: Typis Gasparis Gerardi* (2000) (cit. on p. 28).

[111] C. a Linne. *Caroli a Linne: systema naturae per regna tria naturae, secundum classes, ordines, genera, species, cum characteribus, differentiis, synonymis, locis*. 1768 (cit. on p. 28).

[112] M. A. Ruggiero, D. P. Gordon, T. M. Orrell, N. Bailly, T. Bourgoin, R. C. Brusca, T. Cavalier-Smith, M. D. Guiry, and P. M. Kirk. "A Higher Level Classification of All Living Organisms." In: *PLOS ONE* 10.4 (2015), e0119248. DOI: 10.1371/journal.pone.0119248 (cit. on p. 28).

[113] D. Moreira and P. López-García. "Evolution of viruses and cells: do we need a fourth domain of life to explain the origin of eukaryotes?" In: *Philos Trans R Soc Lond B Biol Sci* 370.1678 (2015), p. 20140327. ISSN: 0962-8436 (Print) 0962-8436. DOI: 10.1098/rstb.2014.0327 (cit. on p. 28).

[114] H. M. B. Harris and C. Hill. "A Place for Viruses on the Tree of Life." In: *Frontiers in Microbiology* 11 (2021). ISSN: 1664-302X. DOI: 10.3389/fmicb.2020.604048 (cit. on p. 29).

[115] A. M. S. Correa, C. Howard-Varona, S. R. Coy, A. Buchan, M. B. Sullivan, and J. S. Weitz. "Revisiting the rules of life for viruses of microorganisms." In: *Nature Reviews Microbiology* 19.8 (2021), pp. 501–513. ISSN: 1740-1534. DOI: 10.1038/s41579-021-00530-x (cit. on p. 29).

[116] T. M. Rivers. "The nature of viruses." In: *Physiological reviews* 12.3 (1932), pp. 423–452. ISSN: 0031-9333 (cit. on p. 29).

[117] F. Barré-Sinoussi. "HIV as the cause of AIDS." In: *The Lancet* 348.9019 (1996), pp. 31–35. ISSN: 0140-6736. DOI: https://doi.org/10.1016/S0140-6736(96)09058-7 (cit. on pp. 29, 30).

[118] A. Dance. "The incredible diversity of viruses." In: *Nature* 595 (2021), pp. 22–25 (cit. on p. 29).

[119] H. M. Temin and D. Baltimore. "RNA-Directed DNA Synthesis and RNA Tumor Viruses." In: *Advances in Virus Research*. Ed. by K. M. Smith, M. A. Lauffer, and F. B. Bang. Vol. 17. Academic Press, 1972, pp. 129–186. ISBN: 0065-3527. DOI: https://doi.org/10.1016/S0065-3527(08)60749-6 (cit. on pp. 29, 30).

[120] T. Ni, Y. Zhu, Z. Yang, C. Xu, Y. Chaban, T. Nesterova, J. Ning, T. Böcking, M. W. Parker, C. Monnie, et al. "Structure of native HIV-1 cores and their interactions with IP6 and CypA." In: *Science Advances* 7.47 (2021), eabj5715. DOI: doi:10.1126/sciadv.abj5715 (cit. on p. 30).

[121] M. Gottlieb, H. Schanker, P. Fan, A Saxon, and J. Weisman. *Epidemiologic Notes and Reports, Pneumocystis Pneumonia -Los Angeles*. June 1981 (accessed October 28, 2022). URL: https://www.cdc.gov/mmwr/preview/mmwrhtml/june_5.htm (cit. on p. 31).

[122] Joint United Nations Programme on HIV/AIDS (UNAIDS). *UNAIDS Global AIDS Update 2022*. 2022 (accessed October 28, 2022). URL: https://www.unaids.org/sites/default/files/media_asset/2022-global-aids-update-summary_en.pdf (cit. on p. 31).

[123] F. Barre-Sinoussi, J. C. Chermann, F. Rey, M. T. Nugeyre, S. Chamaret, J. Gruest, C. Dauguet, C. Axler-Blin, F. Vezinet-Brun, C. Rouzioux, et al. "Isolation of a T-lymphotropic retrovirus from a patient at risk for acquired immune deficiency syndrome (AIDS)." In: *Science* 220.4599 (1983), pp. 868–871 (cit. on p. 31).

[124] F. Barre-Sinoussi, A. L. Ross, and J. F. Delfraissy. "Past, present and future: 30 years of HIV research." In: *Nat. Rev. Microbiol.* 11.12 (2013), pp. 877–883 (cit. on p. 31).

[125] P. Lesbats, A. N. Engelman, and P. Cherepanov. "Retroviral DNA Integration." In: *Chem. Rev.* (2016) (cit. on pp. 31, 33–35).

[126] I. L. Shytaj and A. Savarino. "A cure for AIDS: a matter of timing?" In: *Retrovirology* 10.1 (2013), p. 145. ISSN: 1742-4690. DOI: 10.1186/1742-4690-10-145 (cit. on p. 31).

[127] R. Craigie and F. D. Bushman. "HIVDNA Integration." In: 2.7 (2012) (cit. on pp. 32–35).

[128] National Human Genome Research Institute. *Retrovirus*. June 1, 2023 (accessed June 1, 2023). URL: https://www.genome.gov/genetics-glossary/Retrovirus (cit. on p. 32).

[129] A. Engelman and P. Cherepanov. "Retroviral Integrase Structure and DNA Recombination Mechanism." In: *Microbiology Spectrum* 2.6 (2014), p. 2.6.11. DOI: doi:10.1128/microbiolspec.MDNA3-0024-2014 (cit. on pp. 32, 35, 36).

[130] A. Engelman and P. Cherepanov. *Mobile DNA, 3rd edition, Chapter 44*. Ed. by N. L. Craig, M. Chandler, M. Gellert, L. A. M., P. A. Rice, and S. Sandmeyer. Washington DC, USA: American Scociety for Microbiology, 2014. Chap. Retroviral Integrase Structure and DNA Recombination Mechanism (cit. on pp. 32, 35, 36).

[131] A. Fassati and S. P. Goff. "Characterization of intracellular reverse transcription complexes of human immunodeficiency virus type 1." In: *J. Virol.* 75.8 (2001), pp. 3626–3635 (cit. on p. 33).

[132] S. Hare, S. S. Gupta, E. Valkov, A. Engelman, and P. Cherepanov. "Retroviral intasome assembly and inhibition of DNA strand transfer." In: *Nature* 464.7286 (2010), pp. 232–236 (cit. on pp. 34, 35).

[133] B. Bowerman, P. O. Brown, J. M. Bishop, and H. E. Varmus. "A nucleoprotein complex mediates the integration of retroviral DNA." In: *Genes Dev.* 3.4 (1989), pp. 469–478 (cit. on p. 34).

[134] M. D. Miller, C. M. Farnet, and F. D. Bushman. "Human immunodeficiency virus type 1 preintegration complexes: studies of organization and composition." In: *J Virol* 71.7 (1997), pp. 5382–90. ISSN: 0022-538X (Print) 0022-538x. DOI: 10.1128/jvi.71.7.5382-5390.1997 (cit. on pp. 34, 126, 129).

[135] F. Dyda, A. B. Hickman, T. M. Jenkins, A. Engelman, R. Craigie, and D. R. Davies. "Crystal Structure of the Catalytic Domain of HIV-1 Integrase: Similarity to Other Polynucleotidyl Transferases." In: *Science* 266.5193 (1994), pp. 1981–1986. DOI: doi:10.1126/science.7801124 (cit. on pp. 34, 35).

[136] G. N. Maertens, A. N. Engelman, and P. Cherepanov. "Structure and function of retroviral integrase." In: *Nature Reviews Microbiology* 20.1 (2022), pp. 20–34. ISSN: 1740-1534. DOI: 10.1038/s41579-021-00586-9 (cit. on pp. 34–36).

[137] R. D. Schiff and D. P. Grandgenett. "Virus-coded origin of a 32,000-dalton protein from avian retrovirus cores: structural relatedness of p32 and the beta polypeptide of the avian retrovirus DNA polymerase." In: *Journal of Virology* 28.1 (1978), pp. 279–291. DOI: doi:10.1128/jvi.28.1.279-291.1978 (cit. on p. 34).

[138] T. Jacks, M. D. Power, F. R. Masiarz, P. A. Luciw, P. J. Barr, and H. E. Varmus. "Characterization of ribosomal frameshifting in HIV-1 gag-pol expression." In: *Nature* 331.6153 (1988), pp. 280–283. ISSN: 1476-4687. DOI: 10.1038/331280a0 (cit. on p. 34).

[139] L.-A. Carlson, J. A. G. Briggs, B. Glass, J. D. Riches, M. N. Simon, M. C. Johnson, B. Müller, K. Grünewald, and H.-G. Kräusslich. "Three-Dimensional Analysis of Budding Sites and Released Virus Suggests a Revised Model for HIV-1 Morphogenesis." In: *Cell Host and Microbe* 4.6 (2008), pp. 592–599. ISSN: 1931-3128. DOI: https://doi.org/10.1016/j.chom.2008.10.013 (cit. on p. 34).

[140] R. C. Burdick, C. Li, M. Munshi, J. M. O. Rawson, K. Nagashima, W.-S. Hu, and V. K. Pathak. "HIV-1 uncoats in the nucleus near sites of integration." In: *Proceedings of the National Academy of Sciences* 117.10 (2020), pp. 5486–5493. DOI: doi:10.1073/pnas.1920631117 (cit. on pp. 35, 120, 125).

[141] N.-Y. Chen, L. Zhou, P. J. Gane, S. Opp, N. J. Ball, G. Nicastro, M. Zufferey, C. Buffone, J. Luban, D. Selwood, et al. "HIV-1 capsid is involved in post-nuclear entry steps." In: *Retrovirology* 13.1 (2016), p. 28. ISSN: 1742-4690. DOI: 10.1186/s12977-016-0262-0 (cit. on p. 35).

[142] V. Zila, E. Margiotta, B. Turonová, T. G. Müller, C. E. Zimmerli, S. Mattei, M. Allegretti, K. Börner, J. Rada, B. Müller, et al. "Cone-shaped HIV-1 capsids are transported through intact nuclear pores." In: *Cell* 184.4 (2021), 1032–1046.e18. ISSN: 0092-8674. DOI: https://doi.org/10.1016/j.cell.2021.01.025 (cit. on pp. 35, 125).

[143] K. S. Jones, J. Coleman, G. W. Merkel, T. M. Laue, and A. M. Skalka. "Retroviral integrase functions as a multimer and can turn over catalytically." In: *Journal of Biological Chemistry* 267.23 (1992), pp. 16037–16040. ISSN: 0021-9258. DOI: https://doi.org/10.1016/S0021-9258(18)41960-6 (cit. on p. 35).

[144] P. Cherepanov, G. Maertens, P. Proost, B. Devreese, J. Van Beeumen, Y. Engelborghs, E. De Clercq, and Z. Debyser. "HIV-1 Integrase Forms Stable Tetramers and Associates with LEDGF/p75 Protein in Human Cells." In: *Journal of Biological Chemistry* 278.1 (2003), pp. 372–381. ISSN: 0021-9258. DOI: 10.1074/jbc.M209278200 (cit. on p. 35).

[145] Z. Zhao, C. J. McKee, J. J. Kessl, W. L. Santos, J. E. Daigle, A. Engelman, G. Verdine, and M. Kvaratskhelia. "Subunit-specific protein footprinting reveals significant structural rearrangements and a role for N-terminal Lys-14 of HIV-1 Integrase during viral DNA binding." In: *J Biol Chem* 283.9 (2008), pp. 5632–41. ISSN: 0021-9258 (Print) 0021-9258. DOI: 10.1074/jbc.M705241200 (cit. on pp. 35, 143).

[146] J. Kulkosky, K. S. Jones, R. A. Katz, J. P. Mack, and A. M. Skalka. "Residues critical for retroviral integrative recombination in a region that is highly conserved among retroviral/retrotransposon integrases and bacterial insertion sequence transposases." In: *Mol. Cell. Biol.* 12.5 (1992), pp. 2331–2338 (cit. on p. 36).

[147] G. N. Maertens, S. Hare, and P. Cherepanov. "The mechanism of retroviral integration from X-ray structures of its key intermediates." In: *Nature* 468.7321 (2010), pp. 326–329. ISSN: 1476-4687. DOI: 10.1038/nature09517 (cit. on p. 36).

[148] S. Hare, G. N. Maertens, and P. Cherepanov. "3'-processing and strand transfer catalysed by retroviral integrase in crystallo." In: *EMBO J.* 31.13 (2012), pp. 3020–3028 (cit. on p. 36).

[149] J. L. Elliott, J. E. Eschbach, P. C. Koneru, W. Li, M. Puray-Chavez, D. Townsend, D. Q. Lawson, A. N. Engelman, M. Kvaratskhelia, and S. B. Kutluay. "Integrase-RNA interactions underscore the critical role of integrase in HIV-1 virion morphogenesis." In: *Elife* 9 (2020). ISSN: 2050-084x. DOI: 10.7554/eLife.54311 (cit. on p. 36).

[150] C. W. Dobard, M. S. Briones, and S. A. Chow. "Molecular Mechanisms by Which Human Immunodeficiency Virus Type 1 Integrase Stimulates the Early Steps of Reverse Transcription." In: *Journal of Virology* 81.18 (2007), pp. 10037–10046. DOI: doi:10.1128/JVI.00519-07 (cit. on p. 36).

[151] J. J. Kessl, S. B. Kutluay, D. Townsend, S. Rebensburg, A. Slaughter, R. C. Larue, N. Shkriabai, N. Bakouche, J. R. Fuchs, P. D. Bieniasz, et al. "HIV-1 Integrase Binds the Viral RNA Genome and Is Essential during Virion Morphogenesis." In: *Cell* 166.5 (2016), 1257–1268.e12. ISSN: 0092-8674. DOI: https://doi.org/10.1016/j.cell.2016.07.044 (cit. on pp. 36, 125, 136, 137).

[152] "Beyond the diffraction limit." In: *Nature Photonics* 3.7 (2009), pp. 361–361. ISSN: 1749-4893. DOI: 10.1038/nphoton.2009.100 (cit. on pp. 37, 38).

[153] S. W. Hell and J. Wichmann. "Breaking the diffraction resolution limit by stimulated emission: stimulated-emission-depletion fluorescence microscopy." In: *Optics Letters* 19.11 (1994), pp. 780–782. DOI: 10.1364/OL.19.000780 (cit. on p. 38).

[154] M. Dyba and S. W. Hell. "Focal Spots of Size $\lambda/23$ Open Up Far-Field Florescence Microscopy at 33 nm Axial Resolution." In: *Physical Review Letters* 88.16 (2002), p. 163901. DOI: 10.1103/PhysRevLett.88.163901 (cit. on p. 38).

[155] T. A. Klar, S. Jakobs, M. Dyba, A. Egner, and S. W. Hell. "Fluorescence microscopy with diffraction resolution barrier broken by stimulated emission." In: *Proceedings of the National Academy of Sciences* 97.15 (2000), pp. 8206–8210. DOI: doi:10.1073/pnas.97.15.8206 (cit. on pp. 38, 89).

[156] The Nobel Foundation. *The Nobel Prize in Chemistry 2014*. October 2014 (accessed March 6, 2023). URL: https://www.nobelprize.org/prizes/chemistry/2014/summary/ (cit. on pp. 38, 48).

[157] E. Betzig, G. H. Patterson, R. Sougrat, O. W. Lindwasser, S. Olenych, J. S. Bonifacino, M. W. Davidson, J. Lippincott-Schwartz, and H. F. Hess. "Imaging Intracellular Fluorescent Proteins at Nanometer Resolution." In: *Science* 313.5793 (2006), pp. 1642–1645. DOI: doi:10.1126/science.1127344 (cit. on pp. 38, 48, 89).

[158] M. J. Rust, M. Bates, and X. Zhuang. "Sub-diffraction-limit imaging by stochastic optical reconstruction microscopy (STORM)." In: *Nature Methods* 3.10 (2006), pp. 793–796. ISSN: 1548-7105. DOI: 10.1038/nmeth929 (cit. on pp. 38, 89).

[159] W. E. Moerner. "New directions in single-molecule imaging and analysis." In: *Proceedings of the National Academy of Sciences* 104.31 (2007), pp. 12596–12602. DOI: doi:10.1073/pnas.0610081104 (cit. on pp. 38, 89).

[160] The Nobel Foundation. *The Nobel Prize in Physics 1986*. October 1986 (accessed December 12, 2022). URL: https://www.nobelprize.org/prizes/physics/1986/summary/ (cit. on p. 39).

[161] G. Binnig, C. F. Quate, and C. Gerber. "Atomic Force Microscope." In: *Physical Review Letters* 56.9 (1986), pp. 930–933. DOI: 10.1103/PhysRevLett.56.930 (cit. on pp. 39, 95).

[162] J. Wood. "The top ten advances in materials science." In: *Materials Today* 11.1 (2008), pp. 40–45. ISSN: 1369-7021. DOI: https://doi.org/10.1016/S1369-7021(07)70351-6 (cit. on p. 39).

[163] R. García. *Amplitude modulation atomic force microscopy*. John Wiley and Sons, 2011. ISBN: 352764394X (cit. on pp. 40–42, 98, 104).

[164] A. M. Baró and R. G. Reifenberger. *Atomic force microscopy in liquid: biological applications*. John Wiley and Sons, 2012. ISBN: 3527327584 (cit. on pp. 40–42).

[165] F. Moreno-Herrero, J. Colchero, J. Gómez-Herrero, and A. M. Baró. "Atomic force microscopy contact, tapping, and jumping modes for imaging biological samples in liquids." In: *Physical Review E* 69.3 (2004), p. 031915. DOI: 10.1103/PhysRevE.69.031915 (cit. on pp. 42, 43).

[166] A. Ortega-Esteban, I. Horcas, M. Hernando-Pérez, P. Ares, A. J. Pérez-Berná, C. San Martín, J. L. Carrascosa, P. J. de Pablo, and J. Gómez-Herrero. "Minimizing tip-sample forces in jumping mode atomic force microscopy in liquid." In: *Ultramicroscopy* 114 (2012), pp. 56–61. ISSN: 0304-3991. DOI: https://doi.org/10.1016/j.ultramic.2012.01.007 (cit. on p. 43).

[167] K. Xu, W. Sun, Y. Shao, F. Wei, X. Zhang, W. Wang, and P. Li. "Recent development of PeakForce Tapping mode atomic force microscopy and its applications on nanoscience." In: *Nanotechnology Reviews* 7.6 (2018), pp. 605–621. DOI: doi:10.1515/ntrev-2018-0086 (cit. on p. 43).

[168] A. Ashkin, J. M. Dziedzic, J. E. Bjorkholm, and S. Chu. "Observation of a single-beam gradient force optical trap for dielectric particles." In: *Opt Lett* 11.5 (1986), p. 288. ISSN: 0146-9592 (Print) 0146-9592 (Linking). DOI: 8652 [pii] (cit. on p. 45).

[169] The Nobel Foundation. *The Nobel Prize in Physics 2018*. October 2018 (accessed February 21, 2023). URL: https://www.nobelprize.org/prizes/physics/2018/summary/ (cit. on p. 45).

[170] K. C. Neuman and A. Nagy. "Single-molecule force spectroscopy: optical tweezers, magnetic tweezers and atomic force microscopy." In: *Nature Methods* 5.6 (2008), pp. 491–505. ISSN: 1548-7105. DOI: 10.1038/nmeth.1218 (cit. on p. 45).

[171] D. Dulin, J. Lipfert, M. C. Moolman, and N. H. Dekker. "Studying genomic processes at the single-molecule level: introducing the tools and applications." In: *Nature Reviews Genetics* 14.1 (2013), pp. 9–22. ISSN: 1471-0064. DOI: 10.1038/nrg3316 (cit. on pp. 46, 47).

[172] F. Kriegel, N. Ermann, and J. Lipfert. "Probing the mechanical properties, conformational changes, and interactions of nucleic acids with magnetic tweezers." In: *Journal of Structural Biology* 197.1 (2017), pp. 26–36. ISSN: 1047-8477. DOI: https://doi.org/10.1016/j.jsb.2016.06.022 (cit. on pp. 46, 47, 140).

[173] F. Kriegel, N. Ermann, R. Forbes, D. Dulin, N. H. Dekker, and J. Lipfert. "Probing the salt dependence of the torsional stiffness of DNA by multiplexed magnetic torque tweezers." In: *Nucleic Acids Research* 45.10 (2017), pp. 5920–5929. ISSN: 0305-1048. DOI: 10.1093/nar/gkx280 (cit. on pp. 46, 47, 140).

[174] F. Kriegel, W. Vanderlinden, T. Nicolaus, A. Kardinal, and J. Lipfert. "Measuring Single-Molecule Twist and Torque in Multiplexed Magnetic Tweezers." In: *Nanoscale Imaging: Methods and Protocols*. Ed. by Y. L. Lyubchenko. New York, NY: Springer New York, 2018, pp. 75–98. ISBN: 978-1-4939-8591-3. DOI: 10.1007/978-1-4939-8591-3_6 (cit. on pp. 46, 140, 141).

[175] D. Dulin, T. J. Cui, J. Cnossen, M. Docter, J. Lipfert, and N. Dekker. "High Spatiotemporal-Resolution Magnetic Tweezers: Calibration and Applications for DNA Dynamics." In: *Biophysical Journal* 109.10 (2015), pp. 2113–2125. ISSN: 0006-3495. DOI: https://doi.org/10.1016/j.bpj.2015.10.018 (cit. on p. 46).

[176] J. P. Cnossen, D. Dulin, and N. H. Dekker. "An optimized software framework for real-time, high-throughput tracking of spherical beads." In: *Review of Scientific Instruments* 85.10 (2014), p. 103712. DOI: 10.1063/1.4898178 (cit. on pp. 46, 140).

[177] A. Huhle, D. Klaue, H. Brutzer, P. Daldrop, S. Joo, O. Otto, U. F. Keyser, and R. Seidel. "Camera-based three-dimensional real-time particle tracking at kHz rates and Angström accuracy." In: *Nature Communications* 6.1 (2015), p. 5885. ISSN: 2041-1723. DOI: 10.1038/ncomms6885 (cit. on p. 46).

[178] C.-H. Chiou, Y.-Y. Huang, M.-H. Chiang, H.-H. Lee, and G.-B. Lee. "New magnetic tweezers for investigation of the mechanical properties of single DNA molecules." In: *Nanotechnology* 17.5 (2006), p. 1217. ISSN: 0957-4484. DOI: 10.1088/0957-4484/17/5/009 (cit. on p. 46).

[179] A. J. W. te Velthuis, J. W. J. Kerssemakers, J. Lipfert, and N. H. Dekker. "Quantitative Guidelines for Force Calibration through Spectral Analysis of Magnetic Tweezers Data." In: *Biophysical Journal* 99.4 (2010), pp. 1292–1302. ISSN: 0006-3495. DOI: https://doi.org/10.1016/j.bpj.2010.06.008 (cit. on p. 47).

[180] B. M. Lansdorp and O. A. Saleh. "Power spectrum and Allan variance methods for calibrating single-molecule video-tracking instruments." In: *Review of Scientific Instruments* 83.2 (2012), p. 025115. DOI: 10.1063/1.3687431 (cit. on p. 47).

[181] E. Betzig and J. K. Trautman. "Near-Field Optics: Microscopy, Spectroscopy, and Surface Modification Beyond the Diffraction Limit." In: *Science* 257.5067 (1992), pp. 189–195. DOI: doi:10.1126/science.257.5067.189 (cit. on p. 48).

[182] E. Betzig and R. J. Chichester. "Single Molecules Observed by Near-Field Scanning Optical Microscopy." In: *Science* 262.5138 (1993), pp. 1422–1425. DOI: doi:10.1126/science.262.5138.1422 (cit. on p. 48).

[183] J. K. Trautman, J. J. Macklin, L. E. Brus, and E. Betzig. "Near-field spectroscopy of single molecules at room temperature." In: *Nature* 369.6475 (1994), pp. 40–42. ISSN: 1476-4687. DOI: 10.1038/369040a0 (cit. on p. 48).

[184] L. Novotny. "Allowed and forbidden light in near-field optics. I. A single dipolar light source." In: *JOSA A* 14.1 (1997), pp. 91–104. ISSN: 1520-8532 (cit. on p. 48).

[185] L. Novotny. "Allowed and forbidden light in near-field optics. II. Interacting dipolar particles." In: *JOSA A* 14.1 (1997), pp. 105–113. ISSN: 1520-8532 (cit. on p. 48).

[186] G. M. Crouch, D. Han, and P. W. Bohn. "Zero-mode waveguide nanophotonic structures for single molecule characterization." In: *Journal of Physics D: Applied Physics* 51.19 (2018), p. 193001. ISSN: 0022-3727. DOI: 10.1088/1361-6463/aab8be (cit. on pp. 48, 49).

[187] V. V. Klimov. "Smart Design of Zero-Mode Waveguide Nanodevices for Effective Detection of Single-Molecule Fluorescence." In: *Physical Review Applied* 12.1 (2019), p. 014049. DOI: 10.1103/PhysRevApplied.12.014049 (cit. on pp. 48, 49).

[188] E. Cubukcu, S. Zhang, Y.-S. Park, G. Bartal, and X. Zhang. "Split ring resonator sensors for infrared detection of single molecular monolayers." In: *Applied Physics Letters* 95.4 (2009), p. 043113. DOI: 10.1063/1.3194154 (cit. on p. 48).

[189] A. W. Clark, A. Glidle, D. R. S. Cumming, and J. M. Cooper. "Plasmonic Split-Ring Resonators as Dichroic Nanophotonic DNA Biosensors." In: *Journal of the American Chemical Society* 131.48 (2009), pp. 17615–17619. ISSN: 0002-7863. DOI: 10.1021/ja905910q (cit. on p. 48).

[190] M. Rycenga, X. Xia, C. H. Moran, F. Zhou, D. Qin, Z.-Y. Li, and Y. Xia. "Generation of Hot Spots with Silver Nanocubes for Single-Molecule Detection by Surface-Enhanced Raman Scattering." In: *Angewandte Chemie* 123.24 (2011), pp. 5587–5591. ISSN: 0044-8249. DOI: https://doi.org/10.1002/ange.201101632 (cit. on p. 48).

[191] T. Auger, J. Mathé, V. Viasnoff, G. Charron, J.-M. Di Meglio, L. Auvray, and F. Montel. "Zero-Mode Waveguide Detection of Flow-Driven DNA Translocation through Nanopores." In: *Physical Review Letters* 113.2 (2014), p. 028302. DOI: 10.1103/PhysRevLett.113.028302 (cit. on pp. 49, 59, 60, 64, 66, 70, 71, 73).

[192] T. Auger, E. Bourhis, J. Donnez, A. Durnez, J. M. Di Meglio, L. Auvray, F. Montel, J. Yates, and J. Gierak. "Zero-mode waveguide detection of DNA translocation through FIB-organised arrays of engineered nanopores." In: *Microelectronic Engineering* 187-188 (2018), pp. 90–94. ISSN: 0167-9317. DOI: https://doi.org/10.1016/j.mee.2017.12.005 (cit. on pp. 49, 70, 71).

[193] N. Klughammer and C. Dekker. "Palladium zero-mode waveguides for optical single-molecule detection with nanopores." In: *Nanotechnology* 32.18 (2021), 18LT01. ISSN: 0957-4484. DOI: 10.1088/1361-6528/abd976 (cit. on p. 49).

[194] J Sambrook and D. W. Russell. *Molecular cloning: a laboratory manual 3rd edition*. Coldspring-Harbour Laboratory Press, 2001 (cit. on p. 50).

[195] B. Guo and Y. Bi. "Cloning PCR products." In: *PCR cloning protocols* (2002), pp. 111–119 (cit. on p. 50).

[196] J. M. S. Barlett and S. D. *A short history of the Polymerase Chain Reaction*. Ed. by J. M. S. Barlett and S. D. Vol. 226. PCR protocols, 2nd edition. Humana Press Inc., 2003, pp. 2–6 (cit. on p. 50).

[197] A. H. Lund, M. Duch, and F. Skou Pedersen. "Increased Cloning Efficiency by Temperature-Cycle Ligation." In: *Nucleic Acids Research* 24.4 (1996), pp. 800–801. ISSN: 0305-1048. DOI: 10.1093/nar/24.4.800 (cit. on p. 51).

[198] S. Valla and R. Lale. *DNA cloning and assembly methods*. Vol. 119. Springer, 2014 (cit. on p. 51).

[199] X. Zhu, G. Huang, C. Zeng, X. Zhan, K. Liang, Q. Xu, Y. Zhao, P. Wang, Q. Wang, Q. Zhou, et al. "Structure of the cytoplasmic ring of the Xenopus laevis nuclear pore complex." In: *Science* 376.6598 (2022), eabl8280. DOI: doi:10.1126/science.abl8280 (cit. on p. 53).

[200] S. Petrovic, D. Samanta, T. Perriches, C. J. Bley, K. Thierbach, B. Brown, S. Nie, G. W. Mobbs, T. A. Stevens, X. Liu, et al. "Architecture of the linker-scaffold in the nuclear pore." In: *Science* 376.6598 (2022), eabm9798. DOI: doi:10.1126/science.abm9798 (cit. on p. 53).

[201] S. Mosalaganti, A. Obarska-Kosinska, M. Siggel, R. Taniguchi, B. Turonová, C. E. Zimmerli, K. Buczak, F. H. Schmidt, E. Margiotta, M.-T. Mackmull, et al. "AI-based structure prediction empowers integrative structural analysis of human nuclear pores." In: *Science* 376.6598 (2022), eabm9506. DOI: doi:10.1126/science.abm9506 (cit. on p. 53).

[202] P. Fontana, Y. Dong, X. Pi, A. B. Tong, C. W. Hecksel, L. Wang, T.-M. Fu, C. Bustamante, and H. Wu. "Structure of cytoplasmic ring of nuclear pore complex by integrative cryo-EM and AlphaFold." In: *Science* 376.6598 (2022), eabm9326. DOI: doi:10.1126/science.abm9326 (cit. on p. 53).

[203] C. J. Bley, S. Nie, G. W. Mobbs, S. Petrovic, A. T. Gres, X. Liu, S. Mukherjee, S. Harvey, F. M. Huber, D. H. Lin, et al. "Architecture of the cytoplasmic face of the nuclear pore." In: *Science* 376.6598 (2022), eabm9129. DOI: doi:10.1126/science.abm9129 (cit. on p. 53).

[204] M. Azimi and M. R. K. Mofrad. "Higher Nucleoporin-Importin beta Affinity at the Nuclear Basket Increases Nucleocytoplasmic Import." In: *PLOS ONE* 8.11 (2013), e81741. DOI: 10.1371/journal.pone.0081741 (cit. on p. 54).

[205] S. R. Wente and M. P. Rout. "The nuclear pore complex and nuclear transport." In: *Cold Spring Harb Perspect Biol* 2.10 (2010), a000562. ISSN: 1943-0264. DOI: 10.1101/cshperspect.a000562 (cit. on p. 53).

[206] A. Hoelz, E. W. Debler, and G. Blobel. "The Structure of the Nuclear Pore Complex." In: *Annual Review of Biochemistry* 80.1 (2011), pp. 613–643. ISSN: 0066-4154. DOI: 10.1146/annurev-biochem-060109-151030 (cit. on p. 53).

[207] T. Jovanovic-Talisman and A. Zilman. "Protein Transport by the Nuclear Pore Complex: Simple Biophysics of a Complex Biomachine." In: *Biophysical Journal* 113.1 (2017), pp. 6–14. ISSN: 0006-3495. DOI: https://doi.org/10.1016/j.bpj.2017.05.024 (cit. on p. 53).

[208] G. Kabachinski and T. U. Schwartz. "The nuclear pore complex - structure and function at a glance." In: *Journal of Cell Science* 128.3 (2015), pp. 423–429. DOI: 10.1242/jcs.083246 (cit. on p. 53).

[209] D. Deamer, M. Akeson, and D. Branton. "Three decades of nanopore sequencing." In: *Nature Biotechnology* 34.5 (2016), pp. 518–524. ISSN: 1546-1696. DOI: 10.1038/nbt.3423 (cit. on p. 54).

[210] Z.-L. Hu, M.-Z. Huo, Y.-L. Ying, and Y.-T. Long. "Biological Nanopore Approach for Single-Molecule Protein Sequencing." In: *Angewandte Chemie* 133.27 (2021), pp. 14862–14873. ISSN: 0044-8249. DOI: https://doi.org/10.1002/ange.202013462 (cit. on p. 54).

[211] A. Fragasso, S. Schmid, and C. Dekker. "Comparing Current Noise in Biological and Solid-State Nanopores." In: *ACS Nano* 14.2 (2020), pp. 1338–1349. ISSN: 1936-0851. DOI: 10.1021/acsnano.9b09353 (cit. on p. 54).

[212] S. Schmid, P. Stömmer, H. Dietz, and C. Dekker. "Nanopore electro-osmotic trap for the label-free study of single proteins and their conformations." In: *Nature Nanotechnology* 16.11 (2021), pp. 1244–1250. ISSN: 1748-3395. DOI: 10.1038/s41565-021-00958-5 (cit. on p. 54).

[213] S. Schmid and C. Dekker. "Nanopores: a versatile tool to study protein dynamics." In: *Essays in biochemistry* 65.1 (2021), pp. 93–107. ISSN: 0071-1365. DOI: 10.1042/ebc20200020 (cit. on p. 54).

[214] D. Branton, D. W. Deamer, A. Marziali, H. Bayley, S. A. Benner, T. Butler, M. Di Ventra, S. Garaj, A. Hibbs, X. Huang, et al. "The potential and challenges of nanopore sequencing." In: *Nature Biotechnology* 26.10 (2008), pp. 1146–1153. ISSN: 1546-1696. DOI: 10.1038/nbt.1495 (cit. on p. 54).

[215] D. Roy, W. L. A. Brooks, and B. S. Sumerlin. "New directions in thermoresponsive polymers." In: *Chemical Society Reviews* 42.17 (2013), pp. 7214–7243. ISSN: 0306-0012. DOI: 10.1039/C3CS35499G (cit. on p. 55).

[216] P. J. Kolbeck, D. Benaoudia, L. Chazot-Franguiadakis, G. Delecourt, J. Mathé, S. Li, R. Bonnet, P. Martin, J. Lipfert, A. Salvetti, et al. "Thermally Switchable Nanogate Based on Polymer Phase Transition." In: *Nano Letters* 23.11 (2023), pp. 4862–4869. ISSN: 1530-6984. DOI: 10.1021/acs.nanolett.3c00438 (cit. on p. 57).

[217] Y. Caspi, D. Zbaida, H. Cohen, and M. Elbaum. "Synthetic Mimic of Selective Transport Through the Nuclear Pore Complex." In: *Nano Letters* 8.11 (2008), pp. 3728–3734. ISSN: 1530-6984. DOI: 10.1021/nl801975q (cit. on p. 59).

[218] C. Dekker. "Solid-state nanopores." In: *Nature Nanotechnology* 2.4 (2007), pp. 209–215. ISSN: 1748-3395. DOI: 10.1038/nnano.2007.27 (cit. on p. 59).

[219] G. Emilsson, K. Xiong, Y. Sakiyama, B. Malekian, V. Ahlberg Gagnér, R. L. Schoch, R. Y. H. Lim, and A. B. Dahlin. "Polymer brushes in solid-state nanopores form an impenetrable entropic barrier for proteins." In: *Nanoscale* 10.10 (2018), pp. 4663–4669. ISSN: 2040-3364. DOI: 10.1039/C7NR09432A (cit. on p. 59).

[220] A Hriciga and J. M. Lehn. "pH regulation of divalent/monovalent Ca/K cation transport selectivity by a macrocyclic carrier molecule." In: *Proceedings of the National Academy of Sciences* 80.20 (1983), pp. 6426–6428. DOI: 10.1073/pnas.80.20.6426 (cit. on p. 59).

[221] B. Yameen, M. Ali, R. Neumann, W. Ensinger, W. Knoll, and O. Azzaroni. "Ionic Transport Through Single Solid-State Nanopores Controlled with Thermally Nanoactuated Macromolecular Gates." In: *Small* 5.11 (2009), pp. 1287–1291. ISSN: 1613-6810. DOI: 10.1002/smll.200801318 (cit. on p. 59).

[222] U. F. Keyser, B. N. Koeleman, S. van Dorp, D. Krapf, R. M. M. Smeets, S. G. Lemay, N. H. Dekker, and C. Dekker. "Direct force measurements on DNA in a solid-state nanopore." In: *Nature Physics* 2.7 (2006), pp. 473–477. ISSN: 1745-2481. DOI: 10.1038/nphys344 (cit. on p. 59).

[223] J. Roman, O. Français, N. Jarroux, G. Patriarche, J. Pelta, L. Bacri, and B. Le Pioufle. "Solid-State Nanopore Easy Chip Integration in a Cheap and Reusable Microfluidic Device for Ion Transport and Polymer Conformation Sensing." In: *ACS Sensors* 3.10 (2018), pp. 2129–2137. DOI: 10.1021/acssensors.8b00700 (cit. on p. 59).

[224] H. Alem, A.-S. Duwez, P. Lussis, P. Lipnik, A. M. Jonas, and S. Demoustier-Champagne. "Microstructure and thermo-responsive behavior of poly(N-isopropylacrylamide) brushes grafted in nanopores of track-etched membranes." In: *Journal of Membrane Science* 308.1 (2008), pp. 75–86. ISSN: 0376-7388. DOI: https://doi.org/10.1016/j.memsci.2007.09.036 (cit. on p. 59).

[225] M. Lepoitevin, T. Ma, M. Bechelany, J.-M. Janot, and S. Balme. "Functionalization of single solid state nanopores to mimic biological ion channels: A review." In: *Advances in Colloid and Interface Science* 250 (2017), pp. 195–213. ISSN: 0001-8686. DOI: https://doi.org/10.1016/j.cis.2017.09.001 (cit. on p. 59).

[226] I. Lokuge, X. Wang, and P. W. Bohn. "Temperature-Controlled Flow Switching in Nanocapillary Array Membranes Mediated by Poly(N-isopropylacrylamide) Polymer Brushes Grafted by Atom Transfer Radical Polymerization." In: *Langmuir* 23.1 (2007), pp. 305–311. ISSN: 0743-7463. DOI: 10.1021/la060813m (cit. on p. 59).

[227] N. Reber, A. Küchel, R. Spohr, A. Wolf, and M. Yoshida. "Transport properties of thermo-responsive ion track membranes." In: *Journal of Membrane Science* 193.1 (2001), pp. 49–58. ISSN: 0376-7388. DOI: https://doi.org/10.1016/S0376-7388(01)00460-4 (cit. on p. 59).

[228] N. Reber, H. Omichi, R. Spohr, M. Tamada, A. Wolf, and M. Yoshida. "Thermal switching of grafted single ion tracks." In: *Nuclear Instruments and Methods in Physics Research Section B: Beam Interactions with Materials and Atoms* 105.1 (1995), pp. 275–277. ISSN: 0168-583X. DOI: https://doi.org/10.1016/0168-583X(95)00578-1 (cit. on p. 59).

[229] R. Spohr, N. Reber, A. Wolf, G. M. Alder, V. Ang, C. L. Bashford, C. A. Pasternak, O. Hideki, and M. Yoshida. "Thermal control of drug release by a responsive ion track membrane observed by radio tracer flow dialysis." In: *Journal of Controlled Release* 50.1 (1998), pp. 1–11. ISSN: 0168-3659. DOI: https://doi.org/10.1016/S0168-3659(97)00076-X (cit. on p. 59).

[230] B. M. Venkatesan, B. Dorvel, S. Yemenicioglu, N. Watkins, I. Petrov, and R. Bashir. "Highly Sensitive, Mechanically Stable Nanopore Sensors for DNA Analysis." In: *Advanced Materials* 21.27 (2009), pp. 2771–2776. ISSN: 0935-9648. DOI: 10.1002/adma.200803786 (cit. on p. 59).

[231] N. Arroyo, S. Balme, and F. Picaud. "Impact of surface state on polyethylene glycol conformation confined inside a nanopore." In: *The Journal of Chemical Physics* 154.10 (2021), p. 104901. ISSN: 0021-9606. DOI: 10.1063/5.0040170 (cit. on p. 59).

[232] G. Chen and E. Dormidontova. "PEO-Grafted Gold Nanopore: Grafting Density, Chain Length, and Curvature Effects." In: *Macromolecules* 55.12 (2022), pp. 5222–5232. ISSN: 0024-9297. DOI: 10.1021/acs.macromol.2c00323 (cit. on p. 59).

[233] T. Ma, N. Arroyo, J. Marc Janot, F. Picaud, and S. Balme. "Conformation of Polyethylene Glycol inside Confined Space: Simulation and Experimental Approaches." In: *Nanomaterials* 11.1 (2021), p. 244. ISSN: 2079-4991 (cit. on p. 59).

[234] G. Emilsson, Y. Sakiyama, B. Malekian, K. Xiong, Z. Adali-Kaya, R. Y. H. Lim, and A. B. Dahlin. "Gating Protein Transport in Solid State Nanopores by Single Molecule Recognition." In: *ACS central science* 4.8 (2018), pp. 1007–1014. ISSN: 2374-7943 2374-7951. DOI: 10.1021/acscentsci.8b00268 (cit. on p. 59).

[235] R. Y. H. Lim and J. Deng. "Interaction Forces and Reversible Collapse of a Polymer Brush-Gated Nanopore." In: *ACS Nano* 3.10 (2009), pp. 2911–2918. ISSN: 1936-0851. DOI: 10.1021/nn900152m (cit. on p. 59).

[236] Y. Caspi, D. Zbaida, H. Cohen, and M. Elbaum. "Anomalous Diffusion of High Molecular Weight Polyisopropylacrylamide in Nanopores." In: *Macromolecules* 42.3 (2009), pp. 760–767. ISSN: 0024-9297. DOI: 10.1021/ma801248a (cit. on p. 59).

[237] R. Hoogenboom, H. M. L. Thijs, M. J. H. C. Jochems, B. M. van Lankvelt, M. W. M. Fijten, and U. S. Schubert. "Tuning the LCST of poly(2-oxazoline)s by varying composition and molecular weight: alternatives to poly(N-isopropylacrylamide)?" In: *Chemical Communications* 44 (2008), pp. 5758–5760. ISSN: 1359-7345. DOI: 10.1039/B813140F (cit. on pp. 62, 63).

[238] D. G. Lessard, M Ousalem, and X. X. Zhu. "Effect of the molecular weight on the lower critical solution temperature of poly(N,N-diethylacrylamide) in aqueous solutions." In: *Canadian Journal of Chemistry* 79.12 (2001), pp. 1870–1874. DOI: 10.1139/v01-180 (cit. on p. 62).

[239] J. Shan, Y. Zhao, N. Granqvist, and H. Tenhu. "Thermoresponsive Properties of N-Isopropylacrylamide Oligomer Brushes Grafted to Gold Nanoparticles: Effects of Molar Mass and Gold Core Size." In: *Macromolecules* 42.7 (2009), pp. 2696–2701. ISSN: 0024-9297. DOI: 10.1021/ma802482e (cit. on p. 62).

[240] Y. W. Tong and M. S. Shoichet. "Defining the Surface Chemistry of Ammonia-Modified Poly(tetrafluoroethylene-co-hexafluoropropylene) Films." In: *Macromolecules* 32.10 (1999), pp. 3464–3468. ISSN: 0024-9297. DOI: 10.1021/ma982028p (cit. on p. 62).

[241] C. Gay, P. G. de Gennes, E. Raphael, and F. Brochard-Wyart. "Injection Threshold for a Statistically Branched Polymer inside a Nanopore." In: *Macromolecules* 29.26 (1996), pp. 8379–8382. ISSN: 0024-9297. DOI: 10.1021/ma960941p (cit. on pp. 64, 66, 81).

[242] A. Halperin. “Collapse of grafted chains in poor solvents.” In: *J. Phys. France* 49.3 (1988), pp. 547–550 (cit. on pp. 64, 79).

[243] M. Mietzsch, C. Barnes, J. A. Hull, P. Chipman, J. Xie, N. Bhattacharya, D. Sousa, R. McKenna, G. Gao, and M. Agbandje-McKenna. “Comparative Analysis of the Capsid Structures of AAVrh.10, AAVrh.39, and AAV8.” In: *Journal of Virology* 94.6 (2020), e01769–19. DOI: doi:10.1128/JVI.01769-19 (cit. on p. 68).

[244] D. Belanger and J. Pinson. “Electrografting: a powerful method for surface modification.” In: *Chemical Society Reviews* 40.7 (2011), pp. 3995–4048. ISSN: 0306-0012. DOI: 10.1039/C0CS00149J (cit. on pp. 71, 76).

[245] V. Stockhausen, V. Q. Nguyen, P. Martin, and J. C. Lacroix. “Bottom-Up Electrochemical Fabrication of Conjugated Ultrathin Layers with Tailored Switchable Properties.” In: *ACS Applied Materials & Interfaces* 9.1 (2017), pp. 610–617. ISSN: 1944-8244. DOI: 10.1021/acsami.6b08754 (cit. on p. 71).

[246] A. Salvetti, S. Oreve, G. Chadeuf, Y. Favre D.; Cherel, P. Champion-Arnaud, J. David-Ameline, and P. Moullier. “Factors Influencing Recombinant Adeno-Associated Virus Production.” In: *Human Gene Therapy* 9.5 (1998), pp. 695–706. DOI: 10.1089/hum.1998.9.5-695 (cit. on p. 71).

[247] G. Delecourt, L. Plet, V. Bennevault, and P. Guégan. “Synthesis of Double Hydrophilic Block Copolymers Poly(2-oxazoline-b-ethylenimine) in a Two-Step Procedure.” In: *ACS Applied Polymer Materials* 2.7 (2020), pp. 2696–2705. DOI: 10.1021/acsapm.0c00308 (cit. on p. 74).

[248] L. Plet, G. Delecourt, M. Hanafi, N. Pantoustier, G. Pembouong, P. Midoux, V. Bennevault, and P. Guégan. “Controlled star poly(2-oxazoline)s: Synthesis, characterization.” In: *European Polymer Journal* 122 (2020), p. 109323. ISSN: 0014-3057. DOI: https://doi.org/10.1016/j.eurpolymj.2019.109323 (cit. on p. 74).

[249] H. Yamakawa. “Third Virial Coefficient of Polymer Solutions.” In: *The Journal of Chemical Physics* 42.5 (1965), pp. 1764–1771. ISSN: 0021-9606. DOI: 10.1063/1.1696188 (cit. on p. 82).

[250] K. L. Linegar, A. E. Adeniran, A. F. Kostko, and M. A. Anisimov. “Hydrodynamic radius of polyethylene glycol in solution obtained by dynamic light scattering.” In: *Colloid Journal* 72.2 (2010), pp. 279–281. ISSN: 1608-3067. DOI: 10.1134/S1061933X10020195 (cit. on p. 82).

[251] S. Biagi, L. Rovigatti, M. Abbasi, L. Bureau, F. Sciortino, and C. Misbah. “Hydrodynamic instability and flow reduction in polymer brush coated channels.” In: *Soft Matter* 17.40 (2021), pp. 9235–9245. ISSN: 1744-683X. DOI: 10.1039/D1SM00638J (cit. on p. 83).

[252] P. Reineck, C. J. Wienken, and D. Braun. “Thermophoresis of single stranded DNA.” In: *Electrophoresis* 31.2 (2010), pp. 279–286. ISSN: 0173-0835. DOI: https://doi.org/10.1002/elps.200900505 (cit. on p. 83).

[253] S. Duhr, S. Arduini, and D. Braun. "Thermophoresis of DNA determined by microfluidic fluorescence." In: *The European Physical Journal E* 15.3 (2004), pp. 277–286. ISSN: 1292-895X. DOI: 10.1140/epje/i2004-10073-5 (cit. on p. 83).

[254] I. Saaem and T. H. LaBean. "Overview of DNA origami for molecular self-assembly." In: *WIREs Nanomedicine and Nanobiotechnology* 5.2 (2013), pp. 150–162. ISSN: 1939-5116. DOI: https://doi.org/10.1002/wnan.1204 (cit. on p. 89).

[255] M. Scheckenbach, J. Bauer, J. Zähringer, F. Selbach, and P. Tinnefeld. "DNA origami nanorulers and emerging reference structures." In: *APL Materials* 8.11 (2020), p. 110902. DOI: 10.1063/5.0022885 (cit. on pp. 89, 90, 96, 105, 152).

[256] A. Kuzyk, R. Schreiber, Z. Fan, G. Pardatscher, E.-M. Roller, A. Högele, F. C. Simmel, A. O. Govorov, and T. Liedl. "DNA-based self-assembly of chiral plasmonic nanostructures with tailored optical response." In: *Nature* 483.7389 (2012), pp. 311–314. ISSN: 1476-4687. DOI: 10.1038/nature10889 (cit. on p. 90).

[257] Tanja Neumann, Jörg Barner, Dimitar Stamov (JPK BioAFM Business, Bruker Nano GmbH). *Application note: Correlative AFM and Super-Resolution STED Analysis of DNA Nanostructures*. 2019 (accessed March 09, 2023). URL: https://usa.jpk.com/app-technotes-img/AFM/pdf/bruker-jpk-app-afm-sted-nanoruler-origamis.19-1.pdf (cit. on p. 90).

[258] M. Heilemann, S. van — de — Linde, M. Schüttpelz, R. Kasper, B. Seefeldt, A. Mukherjee, P. Tinnefeld, and M. Sauer. "Fluoreszenzmikroskopie unterhalb der optischen Auflösungsgrenze mit konventionellen Fluoreszenzsonden." In: *Angewandte Chemie* 120.33 (2008), pp. 6266–6271. ISSN: 0044-8249. DOI: https://doi.org/10.1002/ange.200802376 (cit. on p. 89).

[259] A. Sharonov and R. M. Hochstrasser. "Wide-field subdiffraction imaging by accumulated binding of diffusing probes." In: *Proceedings of the National Academy of Sciences* 103.50 (2006), pp. 18911–18916. DOI: doi:10.1073/pnas.0609643104 (cit. on p. 89).

[260] R. Jungmann, C. Steinhauer, M. Scheible, A. Kuzyk, P. Tinnefeld, and F. C. Simmel. "Single-Molecule Kinetics and Super-Resolution Microscopy by Fluorescence Imaging of Transient Binding on DNA Origami." In: *Nano Letters* 10.11 (2010), pp. 4756–4761. ISSN: 1530-6984. DOI: 10.1021/nl103427w (cit. on pp. 89, 152).

[261] F. Balzarotti, Y. Eilers, K. C. Gwosch, A. H. Gynnå, V. Westphal, F. D. Stefani, J. Elf, and S. W. Hell. "Nanometer resolution imaging and tracking of fluorescent molecules with minimal photon fluxes." In: *Science* 355.6325 (2017), pp. 606–612. DOI: doi:10.1126/science.aak9913 (cit. on p. 89).

[262] K. C. Gwosch, J. K. Pape, F. Balzarotti, P. Hoess, J. Ellenberg, J. Ries, and S. W. Hell. "MINFLUX nanoscopy delivers 3D multicolor nanometer resolution in cells." In: *Nature Methods* 17.2 (2020), pp. 217–224. ISSN: 1548-7105. DOI: 10.1038/s41592-019-0688-0 (cit. on p. 89).

[263] M. G. L. Gustafsson. "Surpassing the lateral resolution limit by a factor of two using structured illumination microscopy." In: *Journal of Microscopy* 198.2 (2000), pp. 82–87. ISSN: 0022-2720. DOI: https://doi.org/10.1046/j.1365-2818.2000.00710.x (cit. on p. 89).

[264] M. G. L. Gustafsson. "Nonlinear structured-illumination microscopy: Wide-field fluorescence imaging with theoretically unlimited resolution." In: *Proceedings of the National Academy of Sciences* 102.37 (2005), pp. 13081–13086. DOI: doi:10.1073/pnas.0406877102 (cit. on p. 89).

[265] S. C. M. Reinhardt, L. A. Masullo, I. Baudrexel, P. R. Steen, R. Kowalewski, A. S. Eklund, S. Strauss, E. M. Unterauer, T. Schlichthaerle, M. T. Strauss, et al. "Ångström-resolution fluorescence microscopy." In: *Nature* 617.7962 (2023), pp. 711–716. ISSN: 0028-0836 (Print) 0028-0836. DOI: 10.1038/s41586-023-05925-9 (cit. on pp. 89, 152).

[266] J. S. Villarrubia. "Algorithms for Scanned Probe Microscope Image Simulation, Surface Reconstruction, and Tip Estimation." In: *Journal of research of the National Institute of Standards and Technology* 102.4 (1997), pp. 425–454. ISSN: 1044-677X 2165-7254. DOI: 10.6028/jres.102.030 (cit. on pp. 90, 91, 95, 99, 107, 160, 161).

[267] P. J. Kolbeck, M. Dass, I. V. Martynenko, R. J. A. van Dijk-Moes, K. J. H. Brouwer, A. van Blaaderen, W. Vanderlinden, T. Liedl, and J. Lipfert. "DNA Origami Fiducial for Accurate 3D Atomic Force Microscopy Imaging." In: *Nano Letters* 23.4 (2023). PMID: 36745573, pp. 1236–1243. DOI: 10.1021/acs.nanolett.2c04299 (cit. on p. 93).

[268] H. G. Hansma and J. H. Hoh. "Biomolecular Imaging with the Atomic Force Microscope." In: *Annual Review of Biophysics and Biomolecular Structure* 23.1 (1994), pp. 115–140. ISSN: 1056-8700. DOI: 10.1146/annurev.bb.23.060194.000555 (cit. on p. 95).

[269] R. García and R. Pérez. "Dynamic atomic force microscopy methods." In: *Surface Science Reports* 47.6 (2002), pp. 197–301. ISSN: 0167-5729. DOI: https://doi.org/10.1016/S0167-5729(02)00077-8 (cit. on p. 95).

[270] F. J. Giessibl. "Advances in atomic force microscopy." In: *Reviews of Modern Physics* 75.3 (2003), pp. 949–983. DOI: 10.1103/RevModPhys.75.949 (cit. on p. 95).

[271] T. Ando, T. Uchihashi, and N. Kodera. "High-Speed AFM and Applications to Biomolecular Systems." In: *Annual Review of Biophysics* 42.1 (2013), pp. 393–414. ISSN: 1936-122X. DOI: 10.1146/annurev-biophys-083012-130324 (cit. on p. 95).

[272] M. E. Fuentes-Perez, M. S. Dillingham, and F. Moreno-Herrero. "AFM volumetric methods for the characterization of proteins and nucleic acids." In: *Methods* 60.2 (2013), pp. 113–121. ISSN: 1046-2023. DOI: https://doi.org/10.1016/j.ymeth.2013.02.005 (cit. on pp. 95, 143).

[273] G. R. Heath, E. Kots, J. L. Robertson, S. Lansky, G. Khelashvili, H. Weinstein, and S. Scheuring. "Localization atomic force microscopy." In: *Nature* 594.7863 (2021), pp. 385–390. ISSN: 1476-4687. DOI: 10.1038/s41586-021-03551-x (cit. on pp. 95, 152).

[274] A. L. B. Pyne, A. Noy, K. H. S. Main, V. Velasco-Berrelleza, M. M. Piperakis, L. A. Mitchenall, F. M. Cugliandolo, J. G. Beton, C. E. M. Stevenson, B. W. Hoogenboom, et al. "Base-pair resolution analysis of the effect of supercoiling on DNA flexibility and major groove recognition by triplex-forming oligonucleotides." In: *Nature Communications* 12.1 (2021), p. 1053. ISSN: 2041-1723. DOI: 10.1038/s41467-021-21243-y (cit. on p. 95).

[275] M. Radmacher, R. W. Tillmann, M. Fritz, and H. E. Gaub. "From Molecules to Cells: Imaging Soft Samples with the Atomic Force Microscope." In: *Science* 257.5078 (1992), pp. 1900–1905. DOI: doi:10.1126/science.1411505 (cit. on p. 95).

[276] Y. Lyubchenko, L. Shlyakhtenko, R. Harrington, P. Oden, and S. Lindsay. "Atomic force microscopy of long DNA: imaging in air and under water." In: *Proceedings of the National Academy of Sciences* 90.6 (1993), pp. 2137–2140. ISSN: 0027-8424 (cit. on p. 95).

[277] F. Moreno-Herrero, M. de Jager, N. H. Dekker, R. Kanaar, C. Wyman, and C. Dekker. "Mesoscale conformational changes in the DNA-repair complex Rad50/Mre11/Nbs1 upon binding DNA." In: *Nature* 437.7057 (2005), pp. 440–443. ISSN: 1476-4687. DOI: 10.1038/nature03927 (cit. on p. 95).

[278] D. J. Müller and Y. F. Dufrêne. "Atomic force microscopy as a multifunctional molecular toolbox in nanobiotechnology." In: *Nature Nanotechnology* 3.5 (2008), pp. 261–269. ISSN: 1748-3395. DOI: 10.1038/nnano.2008.100 (cit. on p. 95).

[279] W. Vanderlinden, J. Lipfert, J. Demeulemeester, Z. Debyser, and S. De Feyter. "Structure, mechanics, and binding mode heterogeneity of LEDGF/p75-DNA nucleoprotein complexes revealed by scanning force microscopy." In: *Nanoscale* 6.9 (2014), pp. 4611–4619. ISSN: 2040-3364. DOI: 10.1039/C4NR00022F (cit. on pp. 95, 97).

[280] T. Brouns, H. De Keersmaecker, S. F. Konrad, N. Kodera, T. Ando, J. Lipfert, S. De Feyter, and W. Vanderlinden. "Free Energy Landscape and Dynamics of Supercoiled DNA by High-Speed Atomic Force Microscopy." In: *ACS Nano* 12.12 (2018), pp. 11907–11916. ISSN: 1936-0851. DOI: 10.1021/acsnano.8b06994 (cit. on p. 95).

[281] S. F. Konrad, W. Vanderlinden, W. Frederickx, T. Brouns, B. H. Menze, S. De Feyter, and J. Lipfert. "High-throughput AFM analysis reveals unwrapping pathways of H3 and CENP-A nucleosomes." In: *Nanoscale* 13.10 (2021), pp. 5435–5447. ISSN: 2040-3364. DOI: 10.1039/D0NR08564B (cit. on pp. 95, 107).

[282] S. F. Konrad, W. Vanderlinden, and J. Lipfert. "Quantifying epigenetic modulation of nucleosome breathing by high-throughput AFM imaging." In: *Biophysical Journal* 121.5 (2022), pp. 841–851. ISSN: 0006-3495. DOI: https://doi.org/10.1016/j.bpj.2022.01.014 (cit. on pp. 95–97).

[283] A. Pyne, R. Thompson, C. Leung, D. Roy, and B. W. Hoogenboom. "Single-Molecule Reconstruction of Oligonucleotide Secondary Structure by Atomic Force Microscopy." In: *Small* 10.16 (2014), pp. 3257–3261. ISSN: 1613-6810. DOI: https://doi.org/10.1002/smll.201400265 (cit. on pp. 95, 98).

[284] D. Vorselen, E. S. Kooreman, G. J. L. Wuite, and W. H. Roos. "Controlled tip wear on high roughness surfaces yields gradual broadening and rounding of cantilever tips." In: *Scientific Reports* 6.1 (2016), p. 36972. ISSN: 2045-2322. DOI: 10.1038/srep36972 (cit. on pp. 95, 96).

[285] Y. Matsunaga, S. Fuchigami, T. Ogane, and S. Takada. "End-to-End Differentiable Blind Tip Reconstruction for Noisy Atomic Force Microscopy Images." In: *bioRxiv* (2022), p. 2022.09.24.509314. DOI: 10.1101/2022.09.24.509314 (cit. on p. 95).

[286] H. U. Danzebrink, L. Koenders, G. Wilkening, A. Yacoot, and H. Kunzmann. "Advances in Scanning Force Microscopy for Dimensional Metrology." In: *CIRP Annals* 55.2 (2006), pp. 841–878. ISSN: 0007-8506. DOI: https://doi.org/10.1016/j.cirp.2006.10.010 (cit. on p. 95).

[287] M. Xu, D. Fujita, and K. Onishi. "Reconstruction of atomic force microscopy image by using nanofabricated tip characterizer toward the actual sample surface topography." In: *Review of Scientific Instruments* 80.4 (2009), p. 043703. DOI: 10.1063/1.3115182 (cit. on p. 95).

[288] M. E. Fuentes-Perez, E. J. Gwynn, M. S. Dillingham, and F. Moreno-Herrero. "Using DNA as a fiducial marker to study SMC complex interactions with the atomic force microscope." In: *Biophysical journal* 102.4 (2012), pp. 839–848. ISSN: 1542-0086 0006-3495. DOI: 10.1016/j.bpj.2012.01.022 (cit. on p. 96).

[289] A. T. Winzer, C. Kraft, S. Bhushan, V. Stepanenko, and I. Tessmer. "Correcting for AFM tip induced topography convolutions in protein-DNA samples." In: *Ultramicroscopy* 121 (2012), pp. 8–15. ISSN: 0304-3991. DOI: 10.1016/j.ultramic.2012.07.002 (cit. on p. 96).

[290] M.-H. Trinh, M. Odorico, L. Bellanger, M. Jacquemond, P. Parot, and J.-L. Pellequer. "Tobacco mosaic virus as an AFM tip calibrator." In: *Journal of Molecular Recognition* 24.3 (2011), pp. 503–510. ISSN: 0952-3499. DOI: https://doi.org/10.1002/jmr.1118 (cit. on p. 96).

[291] M. Chen, J. Parot, V. A. Hackley, S. Zou, and L. J. Johnston. "AFM characterization of cellulose nanocrystal height and width using internal calibration standards." In: *Cellulose* 28.4 (2021), pp. 1933–1946. ISSN: 1572-882X. DOI: 10.1007/s10570-021-03678-0 (cit. on p. 96).

[292] R. Bellotti, G. B. Picotto, and L. Ribotta. "AFM Measurements and Tip Characterization of Nanoparticles with Different Shapes." In: *Nanomanufacturing and Metrology* 5.2 (2022), pp. 127–138. ISSN: 2520-8128. DOI: 10.1007/s41871-022-00125-x (cit. on p. 96).

[293] R. Jungmann, T. Liedl, T. L. Sobey, W. Shih, and F. C. Simmel. "Isothermal Assembly of DNA Origami Structures Using Denaturing Agents." In: *Journal of the American Chemical Society* 130.31 (2008), pp. 10062–10063. ISSN: 0002-7863. DOI: 10.1021/ja8030196 (cit. on pp. 96, 97).

[294] S. M. Douglas, H. Dietz, T. Liedl, B. Högberg, F. Graf, and W. M. Shih. "Self-assembly of DNA into nanoscale three-dimensional shapes." In: *Nature* 459.7245 (2009), pp. 414–418. ISSN: 1476-4687. DOI: 10.1038/nature08016 (cit. on pp. 96, 105, 111).

[295] E. S. Andersen, M. Dong, M. M. Nielsen, K. Jahn, A. Lind-Thomsen, W. Mamdouh, K. V. Gothelf, F. Besenbacher, and J. Kjems. "DNA Origami Design of Dolphin-Shaped Structures with Flexible Tails." In: *ACS Nano* 2.6 (2008), pp. 1213–1218. ISSN: 1936-0851. DOI: 10.1021/nn800215j (cit. on p. 96).

[296] A. Kuzuya, Y. Sakai, T. Yamazaki, Y. Xu, and M. Komiyama. "Nanomechanical DNA origami 'single-molecule beacons' directly imaged by atomic force microscopy." In: *Nature Communications* 2.1 (2011), p. 449. ISSN: 2041-1723. DOI: 10.1038/ncomms1452 (cit. on p. 96).

[297] A. Rajendran, M. Endo, and H. Sugiyama. "Single-Molecule Analysis Using DNA Origami." In: *Angewandte Chemie International Edition* 51.4 (2012), pp. 874–890. ISSN: 1433-7851. DOI: https://doi.org/10.1002/anie.201102113 (cit. on p. 96).

[298] P. D. E. Fisher, Q. Shen, B. Akpinar, L. K. Davis, K. K. H. Chung, D. Baddeley, A. Sarić, T. J. Melia, B. W. Hoogenboom, C. Lin, et al. "A Programmable DNA Origami Platform for Organizing Intrinsically Disordered Nucleoporins within Nanopore Confinement." In: *ACS Nano* 12.2 (2018), pp. 1508–1518. ISSN: 1936-0851. DOI: 10.1021/acsnano.7b08044 (cit. on p. 96).

[299] S. Thamm, N. Slesiona, A. Dathe, A. Csáki, and W. Fritzsche. "AFM-Based Probing of the Flexibility and Surface Attachment of Immobilized DNA Origami." In: *Langmuir* 34.49 (2018), pp. 15093–15098. ISSN: 0743-7463. DOI: 10.1021/acs.langmuir.8b02362 (cit. on p. 96).

[300] S. Niekamp, N. Stuurman, and R. D. Vale. "A 6-nm ultra-photostable DNA FluoroCube for fluorescence imaging." In: *Nat Methods* 17.4 (2020), pp. 437–441. ISSN: 1548-7091 (Print) 1548-7091. DOI: 10.1038/s41592-020-0782-3 (cit. on p. 96).

[301] M. Scheckenbach, T. Schubert, C. Forthmann, V. Glembockyte, and P. Tinnefeld. "Self-Regeneration and Self-Healing in DNA Origami Nanostructures." In: *Angewandte Chemie International Edition* 60.9 (2021), pp. 4931–4938. ISSN: 1433-7851. DOI: https://doi.org/10.1002/anie.202012986 (cit. on p. 96).

[302] A. T. Blanchard, Z. Li, E. C. Duran, C. E. Scull, J. D. Hoff, K. R. Wright, V. Pan, and N. G. Walter. "Ultra-photostable DNA FluoroCubes: Mechanism of Photostability and Compatibility with FRET and Dark Quenching." In: *Nano Letters* 22.15 (2022), pp. 6235–6244. ISSN: 1530-6984. DOI: 10.1021/acs.nanolett.2c01757 (cit. on p. 96).

[303] M. Raab, J. J. Schmied, I. Jusuk, C. Forthmann, and P. Tinnefeld. "Fluorescence Microscopy with 6 nm Resolution on DNA Origami." In: *ChemPhysChem* 15.12 (2014), pp. 2431–2435. ISSN: 1439-4235. DOI: https://doi.org/10.1002/cphc.201402179 (cit. on pp. 96, 105, 152).

[304] J. J. Schmied, M. Raab, C. Forthmann, E. Pibiri, B. Wünsch, T. Dammeyer, and P. Tinnefeld. "DNA origami-based standards for quantitative fluorescence microscopy." In: *Nature Protocols* 9.6 (2014), pp. 1367–1391. ISSN: 1750-2799. DOI: 10.1038/nprot.2014.079 (cit. on pp. 96, 105, 152).

[305] C. Steinhauer, R. Jungmann, T. L. Sobey, F. C. Simmel, and P. Tinnefeld. "DNA origami as a nanoscopic ruler for super-resolution microscopy." In: *Angew Chem Int Ed Engl* 48.47 (2009), pp. 8870–3. ISSN: 1433-7851. DOI: 10.1002/anie.200903308 (cit. on pp. 96, 105, 152).

[306] W. M. Shih and C. Lin. "Knitting complex weaves with DNA origami." In: *Current Opinion in Structural Biology* 20.3 (2010), pp. 276–282. ISSN: 0959-440X. DOI: https://doi.org/10.1016/j.sbi.2010.03.009 (cit. on p. 96).

[307] W. Engelen and H. Dietz. "Advancing Biophysics Using DNA Origami." In: *Annual Review of Biophysics* 50.1 (2021), pp. 469–492. DOI: 10.1146/annurev-biophys-110520-125739 (cit. on p. 96).

[308] Y. Ke, S. M. Douglas, M. Liu, J. Sharma, A. Cheng, A. Leung, Y. Liu, W. M. Shih, and H. Yan. "Multilayer DNA Origami Packed on a Square Lattice." In: *Journal of the American Chemical Society* 131.43 (2009), pp. 15903–15908. ISSN: 0002-7863. DOI: 10.1021/ja906381y (cit. on p. 97).

[309] P. C. Nickels, B. Wünsch, P. Holzmeister, W. Bae, L. M. Kneer, D. Grohmann, P. Tinnefeld, and T. Liedl. "Molecular force spectroscopy with a DNA origami based nanoscopic force clamp." In: *Science* 354.6310 (2016), pp. 305–307. DOI: doi:10.1126/science.aah5974 (cit. on p. 97).

[310] A. Ray, K. Liosi, S. N. Ramakrishna, N. D. Spencer, A. Kuzuya, and Y. Yamakoshi. "Single-Molecule AFM Study of DNA Damage by 1O2 Generated from Photoexcited C60." In: *The Journal of Physical Chemistry Letters* 11.18 (2020), pp. 7819–7826. DOI: 10.1021/acs.jpclett.0c02257 (cit. on p. 97).

[311] H. Zhao, Y. Zhang, S. B. Zhang, C. Jiang, Q. Y. He, M. Q. Li, and R. L. Qian. "The structure of the nucleosome core particle of chromatin in chicken erythrocytes visualized by using atomic force microscopy." In: *Cell Research* 9.4 (1999), pp. 255–260. ISSN: 1001-0602. DOI: 10.1038/sj.cr.7290024 (cit. on p. 97).

[312] J. Pietkiewicz, K. Dzierzba, A. Bronowicka-Szydelko, M. Staniszewska, A. Bartys, and A. Gamian. "Preparation of bovine serum albumin monomee. for conjugation experiments by using different types of chromatography media." In: *Journal of Liquid Chromatography and Related Technologies* 36.5 (2013), pp. 658–670. ISSN: 1082-6076. DOI: 10.1080/10826076.2012.673205 (cit. on p. 97).

[313] W. Vanderlinden, T. Brouns, P. U. Walker, P. J. Kolbeck, L. F. Milles, W. Ott, P. C. Nickels, Z. Debyser, and J. Lipfert. "The free energy landscape of retroviral integration." In: *Nature Communications* 10.1 (2019), p. 4738. ISSN: 2041-1723. DOI: 10.1038/s41467-019-12649-w (cit. on pp. 97, 120, 125).

[314] L. K. Bruetzel, T. Gerling, S. M. Sedlak, P. U. Walker, W. Zheng, H. Dietz, and J. Lipfert. "Conformational Changes and Flexibility of DNA Devices Observed by Small-Angle X-ray Scattering." In: *Nano Letters* 16.8 (2016), pp. 4871–4879. ISSN: 1530-6984. DOI: 10.1021/acs.nanolett.6b01338 (cit. on pp. 98–100).

[315] S. Fischer, C. Hartl, K. Frank, J. O. Rädler, T. Liedl, and B. Nickel. "Shape and Interhelical Spacing of DNA Origami Nanostructures Studied by Small-Angle X-ray Scattering." In: *Nano Letters* 16.7 (2016), pp. 4282–4287. ISSN: 1530-6984. DOI: 10.1021/acs.nanolett.6b01335 (cit. on pp. 98–100, 106).

[316] V. Korpelainen, V. Linko, J. Seppä, A. Lassila, and M. A. Kostiainen. "DNA origami structures as calibration standards for nanometrology." In: *Measurement Science and Technology* 28.3 (2017), p. 034001. ISSN: 0957-0233 1361-6501. DOI: 10.1088/1361-6501/28/3/034001 (cit. on pp. 98, 106).

[317] X.-c. Bai, T. G. Martin, S. H. W. Scheres, and H. Dietz. "Cryo-EM structure of a 3D DNA-origami object." In: *Proceedings of the National Academy of Sciences* 109.49 (2012), pp. 20012–20017. DOI: doi:10.1073/pnas.1215713109 (cit. on p. 98).

[318] F. Moreno-Herrero, J. Colchero, and A. M. Baró. "DNA height in scanning force microscopy." In: *Ultramicroscopy* 96.2 (2003), pp. 167–174. ISSN: 0304-3991. DOI: https://doi.org/10.1016/S0304-3991(03)00004-4 (cit. on p. 98).

[319] F. Moreno-Herrero and J. Gomez-Herrero. "AFM: Basic Concepts." In: *Atomic Force Microscopy in Liquid*. 2012, pp. 1–34. DOI: https://doi.org/10.1002/9783527649808.ch1 (cit. on p. 99).

[320] T. Schlichthaerle, M. T. Strauss, F. Schueder, J. B. Woehrstein, and R. Jungmann. "DNA nanotechnology and fluorescence applications." In: *Current Opinion in Biotechnology* 39 (2016), pp. 41–47. ISSN: 0958-1669. DOI: https://doi.org/10.1016/j.copbio.2015.12.014 (cit. on pp. 105, 152).

[321] W. Frederickx, S. Rocha, Y. Fujita, K. Kennes, H. De Keersmaecker, S. De Feyter, H. Uji-i, and W. Vanderlinden. "Orthogonal Probing of Single-Molecule Heterogeneity by Correlative Fluorescence and Force Microscopy." In: *ACS Nano* 12.1 (2018), pp. 168–177. ISSN: 1936-0851. DOI: 10.1021/acsnano.7b05405 (cit. on pp. 105, 152).

[322] D. J. Müller, A. C. Dumitru, C. Lo Giudice, H. E. Gaub, P. Hinterdorfer, G. Hummer, J. J. De Yoreo, Y. F. Dufrêne, and D. Alsteens. "Atomic Force Microscopy-Based Force Spectroscopy and Multiparametric Imaging of Biomolecular and Cellular Systems." In: *Chemical Reviews* 121.19 (2021), pp. 11701–11725. ISSN: 0009-2665. DOI: 10.1021/acs.chemrev.0c00617 (cit. on pp. 105, 120, 152).

[323] L. Nguyen, M. Döblinger, T. Liedl, and A. Heuer-Jungemann. "DNA-Origami-Templated Silica Growth by Sol-Gel Chemistry." In: *Angewandte Chemie International Edition* 58.3 (2019), pp. 912–916. ISSN: 1433-7851. DOI: https://doi.org/10.1002/anie.201811323 (cit. on pp. 105, 152).

[324] M. F. Ober, A. Baptist, L. Wassermann, A. Heuer-Jungemann, and B. Nickel. "In situ small-angle X-ray scattering reveals strong condensation of DNA origami during silicification." In: *Nature Communications* 13.1 (2022), p. 5668. ISSN: 2041-1723. DOI: 10.1038/s41467-022-33083-5 (cit. on pp. 105, 152).

[325] H. Dietz, S. M. Douglas, and W. M. Shih. "Folding DNA into Twisted and Curved Nanoscale Shapes." In: *Science* 325.5941 (2009), pp. 725–730. DOI: doi:10.1126/science.1174251 (cit. on p. 106).

[326] K. F. Wagenbauer, F. A. S. Engelhardt, E. Stahl, V. K. Hechtl, P. Stömmer, F. Seebacher, L. Meregalli, P. Ketterer, T. Gerling, and H. Dietz. "How We Make DNA Origami." In: *ChemBioChem* 18.19 (2017), pp. 1873–1885. ISSN: 1439-4227. DOI: https://doi.org/10.1002/cbic.201700377 (cit. on p. 106).

[327] S. Shahabi, L. Treccani, and K. Rezwan. "Amino acid-catalyzed seed regrowth synthesis of photostable high fluorescent silica nanoparticles with tunable sizes for intracellular studies." In: *Journal of Nanoparticle Research* 17.6 (2015), p. 270. ISSN: 1572-896X. DOI: 10.1007/s11051-015-3072-8 (cit. on p. 106).

[328] F. Y. de Boer, R. J. A. van Dijk-Moes, A. Imhof, and K. P. Velikov. "Characterization of the Scattering and Absorption of Colored Zein Colloids in Optically Dense Dispersions." In: *Langmuir* 35.37 (2019), pp. 12091–12099. ISSN: 0743-7463. DOI: 10.1021/acs.langmuir.9b01357 (cit. on p. 106).

[329] L. S. Shlyakhtenko, A. A. Gall, and Y. L. Lyubchenko. "Mica functionalization for imaging of DNA and protein-DNA complexes with atomic force microscopy." In: *Methods in molecular biology (Clifton, N.J.)* 931 (2013), pp. 295–312. ISSN: 1940-6029 1064-3745. DOI: 10.1007/978-1-62703-056-4_14 (cit. on p. 107).

[330] P. Cherepanov, D. Surratt, J. Toelen, W. Pluymers, J. Griffith, E. De Clercq, and Z. Debyser. "Activity of recombinant HIV-1 integrase on mini-HIV DNA." In: *Nucleic acids research* 27.10 (1999), pp. 2202–2210. ISSN: 0305-1048 1362-4962. DOI: 10.1093/nar/27.10.2202 (cit. on pp. 107, 120, 125, 128, 139, 171).

[331] C. Weydert, B. van Heertum, L. Dirix, S. De Houwer, F. De Wit, J. Mast, S. J. Husson, K. Busschots, R. König, R. Gijsbers, et al. "Y-box-binding protein 1 supports the early and late steps of HIV replication." In: *PLOS ONE* 13.7 (2018), e0200080. DOI: 10.1371/journal.pone.0200080 (cit. on p. 119).

[332] H. Gien, M. Morse, M. J. McCauley, J. P. Kitzrow, K. Musier-Forsyth, R. J. Gorelick, I. Rouzina, and M. C. Williams. "HIV-1 Nucleocapsid Protein Binds Double-Stranded DNA in Multiple Modes to Regulate Compaction and Capsid Uncoating." In: *Viruses* 14.2 (2022). ISSN: 1999-4915. DOI: 10.3390/v14020235 (cit. on pp. 119, 120, 136, 137).

[333] In: *Retroviruses*. Ed. by J. M. Coffin, S. H. Hughes, and H. E. Varmus. Cold Spring Harbor (NY): Cold Spring Harbor Laboratory Press Copyright 1997, Cold Spring Harbor Laboratory Press., 1997 (cit. on p. 119).

[334] D. E. Christensen, B. K. Ganser-Pornillos, J. S. Johnson, O. Pornillos, and W. I. Sundquist. "Reconstitution and visualization of HIV-1 capsid-dependent replication and integration in vitro." In: *Science (New York, N.Y.)* 370.6513 (2020), eabc8420. ISSN: 1095-9203 0036-8075. DOI: 10.1126/science.abc8420 (cit. on p. 120).

[335] S. Rankovic, A. Deshpande, S. Harel, C. Aiken, I. Rousso, and F. Kirchhoff. "HIV-1 Uncoating Occurs via a Series of Rapid Biomechanical Changes in the Core Related to Individual Stages of Reverse Transcription." In: *Journal of Virology* 95.10 (2021), e00166–21. DOI: doi:10.1128/JVI.00166-21 (cit. on p. 120).

[336] D. Taganov Konstantin, I. Cuesta, R. Daniel, A. Cirillo Lisa, A. Katz Richard, S. Zaret Kenneth, and M. Skalka Anna. "Integrase-Specific Enhancement and Suppression of Retroviral DNA Integration by Compacted Chromatin Structure In Vitro." In: *Journal of Virology* 78.11 (2004), pp. 5848–5855. DOI: 10.1128/JVI.78.11.5848-5855.2004 (cit. on p. 120).

[337] G. Krishnamoorthy, B. Roques, J.-L. Darlix, and Y. Mély. "DNA condensation by the nucleocapsid protein of HIV-1: a mechanism ensuring DNA protection." In: *Nucleic Acids Research* 31.18 (2003), pp. 5425–5432. ISSN: 0305-1048. DOI: 10.1093/nar/gkg738 (cit. on p. 120).

[338] K. Jiang, N. Humbert, S. Kk, T. Lequeu, Y.-L. Lin, Y. Mely, and F. Westerlund. "Annealing of ssDNA and compaction of dsDNA by the HIV-1 nucleocapsid and Gag proteins visualized using nanofluidic channels." In: *Quarterly Reviews of Biophysics* 52 (2019), e2. ISSN: 0033-5835. DOI: 10.1017/S0033583518000124 (cit. on p. 120).

[339] K. Jiang, N. Humbert, S. K.K, I. Rouzina, Y. Mély, and F. Westerlund. "The HIV-1 nucleocapsid chaperone protein forms locally compacted globules on long double-stranded DNA." In: *Nucleic Acids Research* 49.8 (2021), pp. 4550–4563. ISSN: 0305-1048. DOI: 10.1093/nar/gkab236 (cit. on pp. 120, 137).

[340] S. G. Sarafianos, B. Marchand, K. Das, D. M. Himmel, M. A. Parniak, S. H. Hughes, and E. Arnold. "Structure and function of HIV-1 reverse transcriptase: molecular mechanisms of polymerization and inhibition." In: *J Mol Biol* 385.3 (2009), pp. 693–713. ISSN: 0022-2836 (Print) 0022-2836. DOI: 10.1016/j.jmb.2008.10.071 (cit. on pp. 120, 125).

[341] E. A. Abbondanzieri, G. Bokinsky, J. W. Rausch, J. X. Zhang, S. F. Le Grice, and X. Zhuang. "Dynamic binding orientations direct activity of HIV reverse transcriptase." In: *Nature* 453.7192 (2008), pp. 184–9. ISSN: 1476-4687 (Electronic) 0028-0836 (Linking). DOI: 10.1038/nature06941 (cit. on pp. 120, 125).

[342] R. Craigie. "Nucleoprotein Intermediates in HIV-1 DNA Integration: Structure and Function of HIV-1 Intasomes." In: *Subcell Biochem* 88 (2018), pp. 189–210. ISSN: 0306-0225 (Print) 0306-0225. DOI: 10.1007/978-981-10-8456-0_9 (cit. on pp. 120, 125).

[343] D. O. Passos, M. Li, R. Yang, S. V. Rebensburg, R. Ghirlando, Y. Jeon, N. Shkriabai, M. Kvaratskhelia, R. Craigie, and D. Lyumkis. "Cryo-EM structures and atomic model of the HIV-1 strand transfer complex intasome." In: *Science* 355.6320 (2017), pp. 89–92. ISSN: 0036-8075 (Print) 0036-8075. DOI: 10.1126/science.aah5163 (cit. on pp. 120, 125).

[344] B. Van Maele and Z. Debyser. "HIV-1 integration: an interplay between HIV-1 integrase, cellular and viral proteins." In: *AIDS Rev* 7.1 (2005), pp. 26–43. ISSN: 1139-6121 (Print) 1139-6121 (cit. on pp. 120, 125).

[345] J. A. Briggs, M. N. Simon, I. Gross, H. G. Kräusslich, S. D. Fuller, V. M. Vogt, and M. C. Johnson. "The stoichiometry of Gag protein in HIV-1." In: *Nat Struct Mol Biol* 11.7 (2004), pp. 672–5. ISSN: 1545-9993 (Print) 1545-9985. DOI: 10.1038/nsmb785 (cit. on pp. 120, 125).

[346] A. Ballandras-Colas, D. P. Maskell, E. Serrao, J. Locke, P. Swuec, S. R. Jónsson, A. Kotecha, N. J. Cook, V. E. Pye, I. A. Taylor, et al. "A supramolecular assembly mediates lentiviral DNA integration." In: *Science* 355.6320 (2017), pp. 93–95. ISSN: 0036-8075 (Print) 0036-8075. DOI: 10.1126/science.aah7002 (cit. on pp. 120, 125).

[347] M. Lelek, F. Di Nunzio, R. Henriques, P. Charneau, N. Arhel, and C. Zimmer. "Superresolution imaging of HIV in infected cells with FlAsH-PALM." In: *Proc Natl Acad Sci U S A* 109.22 (2012), pp. 8564–9. ISSN: 0027-8424 (Print) 0027-8424. DOI: 10.1073/pnas.1013267109 (cit. on pp. 120, 126, 129, 137).

[348] M. S. Briones, C. W. Dobard, and S. A. Chow. "Role of Human Immunodeficiency Virus Type 1 Integrase in Uncoating of the Viral Core." In: *Journal of Virology* 84.10 (2010), pp. 5181–5190. DOI: doi:10.1128/jvi.02382-09 (cit. on pp. 125, 137).

[349] S. De Houwer, J. Demeulemeester, W. Thys, S. Rocha, L. Dirix, R. Gijsbers, F. Christ, and Z. Debyser. "The HIV-1 Integrase Mutant R263A/K264A Is 2-fold Defective for TRN-SR2 Binding and Viral Nuclear Import." In: *Journal of Biological Chemistry* 289.36 (2014), pp. 25351–25361. ISSN: 0021-9258. DOI: 10.1074/jbc.M113.533281 (cit. on pp. 125, 137, 153).

[350] X. Li, Y. Koh, and A. Engelman. "Correlation of Recombinant Integrase Activity and Functional Preintegration Complex Formation during Acute Infection by Replication-Defective Integrase Mutant Human Immunodeficiency Virus." In: *Journal of Virology* 86.7 (2012), pp. 3861–3879. DOI: 10.1128/jvi.06386-11 (cit. on p. 126).

[351] J. H. Gibcus, K. Samejima, A. Goloborodko, I. Samejima, N. Naumova, J. Nuebler, M. T. Kanemaki, L. Xie, J. R. Paulson, W. C. Earnshaw, et al. "A pathway for mitotic chromosome formation." In: *Science* 359.6376 (2018), eaao6135. DOI: doi:10.1126/science.aao6135 (cit. on p. 126).

[352] Y. Yang, L. E. Sass, C. Du, P. Hsieh, and D. A. Erie. "Determination of protein–DNA binding constants and specificities from statistical analyses of single molecules: MutS–DNA interactions." In: *Nucleic Acids Research* 33.13 (2005), pp. 4322–4334. ISSN: 0305-1048. DOI: 10.1093/nar/gki708 (cit. on p. 126).

[353] S. Sankararaman and J. F. Marko. "Formation of loops in DNA under tension." In: *Physical Review E* 71.2 (2005), p. 021911. DOI: 10.1103/PhysRevE.71.021911 (cit. on p. 127).

[354] J. J. Kessl, M. Li, M. Ignatov, N. Shkriabai, J. O. Eidahl, L. Feng, K. Musier-Forsyth, R. Craigie, and M. Kvaratskhelia. "FRET analysis reveals distinct conformations of IN tetramers in the presence of viral DNA or LEDGF/p75." In: *Nucleic acids research* 39.20 (2011), pp. 9009–9022. ISSN: 1362-4962 0305-1048. DOI: 10.1093/nar/gkr581 (cit. on pp. 128, 143).

[355] J.-K. Ryu, C. Bouchoux, H. W. Liu, E. Kim, M. Minamino, R. de Groot, A. J. Katan, A. Bonato, D. Marenduzzo, D. Michieletto, et al. "Bridging-induced phase separation induced by cohesin SMC protein complexes." In: *Science Advances* 7.7 (2022), eabe5905. DOI: 10.1126/sciadv.abe5905 (cit. on p. 129).

[356] D. Alsteens, D. J. Müller, and Y. F. Dufrene. "Multiparametric Atomic Force Microscopy Imaging of Biomolecular and Cellular Systems." In: *Accounts of Chemical Research* 50.4 (2017), pp. 924–931. ISSN: 0001-4842. DOI: 10.1021/acs.accounts.6b00638 (cit. on p. 131).

[357] R. Garcia. "Nanomechanical mapping of soft materials with the atomic force microscope: methods, theory and applications." In: *Chemical Society Reviews* 49.16 (2020), pp. 5850–5884. ISSN: 0306-0012. DOI: 10.1039/D0CS00318B (cit. on p. 131).

[358] S. Wegmann, I. D. Medalsy, E. Mandelkow, and D. J. Müller. "The fuzzy coat of pathological human Tau fibrils is a two-layered polyelectrolyte brush." In: *Proceedings of the National Academy of Sciences* 110.4 (2013), E313–E321. DOI: doi:10.1073/pnas.1212100110 (cit. on p. 133).

[359] S. Boeynaems, A. S. Holehouse, V. Weinhardt, D. Kovacs, J. Van Lindt, C. Larabell, L. Van Den Bosch, R. Das, P. S. Tompa, R. V. Pappu, et al. "Spontaneous driving forces give rise to protein—RNA condensates with coexisting phases and complex material properties." In: *Proceedings of the National Academy of Sciences* 116.16 (2019), pp. 7889–7898. DOI: 10.1073/pnas.1821038116 (cit. on p. 133).

[360] D. A. Koster, V. Croquette, C. Dekker, S. Shuman, and N. H. Dekker. "Friction and torque govern the relaxation of DNA supercoils by eukaryotic topoisomerase IB." In: *Nature* 434.7033 (2005), pp. 671–674. ISSN: 1476-4687. DOI: 10.1038/nature03395 (cit. on p. 134).

[361] H. Bai, J. E. Kath, F. M. Zörgiebel, M. Sun, P. Ghosh, G. F. Hatfull, N. D. F. Grindley, and J. F. Marko. "Remote control of DNA-acting enzymes by varying the Brownian dynamics of a distant DNA end." In: *Proceedings of the National Academy of Sciences* 109.41 (2012), pp. 16546–16551. DOI: 10.1073/pnas.1203118109 (cit. on pp. 134, 135).

[362] P. C. Koneru, A. C. Francis, N. Deng, S. V. Rebensburg, A. C. Hoyte, J. Lindenberger, D. Adu-Ampratwum, R. C. Larue, M. F. Wempe, A. N. Engelman, et al. "HIV-1 integrase tetramers are the antiviral target of pyridine-based allosteric integrase inhibitors." In: *eLife* 8 (2019), e46344. ISSN: 2050-084X. DOI: 10.7554/eLife.46344 (cit. on p. 135).

[363] N. Li, C. Zuo, and Q. Cao. "Nanopores with Solvent-Sensitive Polymer Brushes: A Dissipative Particle Dynamics Simulation." In: *Journal of Macromolecular Science, Part B* 51.2 (2012), pp. 275–287. ISSN: 0022-2348. DOI: 10.1080/00222348.2011.596776 (cit. on p. 137).

[364] S. Lyonnais, R. J. Gorelick, F. Heniche-Boukhalfa, S. Bouaziz, V. Parissi, J.-F. Mouscadet, T. Restle, J. M. Gatell, E. Le Cam, and G. Mirambeau. "A protein ballet around the viral genome orchestrated by HIV-1 reverse transcriptase leads to an architectural switch: From nucleocapsid-condensed RNA to Vpr-bridged DNA." In: *Virus Research* 171.2 (2013), pp. 287–303. ISSN: 0168-1702. DOI: https://doi.org/10.1016/j.virusres.2012.09.008 (cit. on p. 137).

[365] J. Demeulemeester, C. Tintori, M. Botta, Z. Debyser, and F. Christ. "Development of an AlphaScreen-Based HIV-1 Integrase Dimerization Assay for Discovery of Novel Allosteric Inhibitors." In: *Journal of Biomolecular Screening* 17.5 (2012), pp. 618–628. ISSN: 1087-0571. DOI: 10.1177/1087057111436343 (cit. on p. 138).

[366] F. Christ, A. Voet, A. Marchand, S. Nicolet, B. A. Desimmie, D. Marchand, D. Bardiot, N. J. Van der Veken, B. Van Remoortel, S. V. Strelkov, et al. "Rational design of small-molecule inhibitors of the LEDGF/p75-integrase interaction and HIV replication." In: *Nature Chemical Biology* 6.6 (2010), pp. 442–448. ISSN: 1552-4469. DOI: 10.1038/nchembio.370 (cit. on p. 138).

[367] K. Bartholomeeusen, J. De Rijck, K. Busschots, L. Desender, R. Gijsbers, S. Emiliani, R. Benarous, Z. Debyser, and F. Christ. "Differential Interaction of HIV-1 Integrase and JPO2 with the C Terminus of LEDGF/p75." In: *Journal of Molecular Biology* 372.2 (2007), pp. 407–421. ISSN: 0022-2836. DOI: https://doi.org/10.1016/j.jmb.2007.06.090 (cit. on p. 138).

[368] K. Busschots, J. Vercammen, S. Emiliani, R. Benarous, Y. Engelborghs, F. Christ, and Z. Debyser. "The Interaction of LEDGF/p75 with Integrase Is Lentivirus-specific and Promotes DNA Binding*." In: *Journal of Biological Chemistry* 280.18 (2005), pp. 17841–17847. ISSN: 0021-9258. DOI: https://doi.org/10.1074/jbc.M411681200 (cit. on p. 138).

[369] G. Maertens, P. Cherepanov, W. Pluymers, K. Busschots, E. De Clercq, Z. Debyser, and Y. Engelborghs. "LEDGF/p75 Is Essential for Nuclear and Chromosomal Targeting of HIV-1 Integrase in Human Cells." In: *Journal of Biological Chemistry* 278.35 (2003), pp. 33528–33539. ISSN: 0021-9258. DOI: 10.1074/jbc.M303594200 (cit. on p. 138).

[370] F. Christ, S. Shaw, J. Demeulemeester, A. Desimmie Belete, A. Marchand, S. Butler, W. Smets, P. Chaltin, M. Westby, Z. Debyser, et al. "Small-Molecule Inhibitors of the LEDGF/p75 Binding Site of Integrase Block HIV Replication and Modulate Integrase Multimerization." In: *Antimicrobial Agents and Chemotherapy* 56.8 (2012), pp. 4365–4374. DOI: 10.1128/aac.00717-12 (cit. on p. 138).

[371] J. Lipfert, D. A. Koster, I. D. Vilfan, S. Hage, and N. H. Dekker. "Single-molecule magnetic tweezers studies of type IB topoisomerases." In: *Methods Mol Biol* 582 (2009), pp. 71–89. ISSN: 1064-3745. DOI: 10.1007/978-1-60761-340-4_7 (cit. on pp. 140, 163).

[372] M. Tsiang, G. S. Jones, M. Hung, S. Mukund, B. Han, X. Liu, K. Babaoglu, E. Lansdon, X. Chen, J. Todd, et al. "Affinities between the binding partners of the HIV-1 integrase dimer-lens epithelium-derived growth factor (IN dimer-LEDGF) complex." In: *J Biol Chem* 284.48 (2009), pp. 33580–99. ISSN: 0021-9258 (Print) 0021-9258. DOI: 10.1074/jbc.M109.040121 (cit. on p. 143).

[373] M. Tsiang, G. S. Jones, M. Hung, D. Samuel, N. Novikov, S. Mukund, K. M. Brendza, A. Niedziela-Majka, D. Jin, X. Liu, et al. "Dithiothreitol causes HIV-1 integrase dimer dissociation while agents interacting with the integrase dimer interface promote dimer formation." In: *Biochemistry* 50.10 (2011), pp. 1567–81. ISSN: 0006-2960. DOI: 10.1021/bi101504w (cit. on p. 143).

[374] R. S. Bojja, M. D. Andrake, G. Merkel, S. Weigand, J. Dunbrack R. L., and A. M. Skalka. "Architecture and assembly of HIV integrase multimers in the absence of DNA substrates." In: *J Biol Chem* 288.10 (2013), pp. 7373–86. ISSN: 0021-9258 (Print) 0021-9258. DOI: 10.1074/jbc.M112.434431 (cit. on p. 143).

[375] K. Gao, S. L. Butler, and F. Bushman. "Human immunodeficiency virus type 1 integrase: arrangement of protein domains in active cDNA complexes." In: *The EMBO Journal* 20.13 (2001), pp. 3565–3576. ISSN: 0261-4189. DOI: https://doi.org/10.1093/emboj/20.13.3565 (cit. on p. 143).

[376] A. Alian, S. L. Griner, V. Chiang, M. Tsiang, G. Jones, G. Birkus, R. Geleziunas, A. D. Leavitt, and R. M. Stroud. "Catalytically-active complex of HIV-1 integrase with a viral DNA substrate binds anti-integrase drugs." In: *Proceedings of the National Academy of Sciences* 106.20 (2009), pp. 8192–8197. DOI: doi:10.1073/pnas.0811919106 (cit. on p. 143).

[377] R. Iinuma, Y. Ke, R. Jungmann, T. Schlichthaerle, J. B. Woehrstein, and P. Yin. "Polyhedra Self-Assembled from DNA Tripods and Characterized with 3D DNA-PAINT." In: *Science* 344.6179 (2014), pp. 65–69. DOI: doi:10.1126/science.1250944 (cit. on p. 152).

[378] R. Jungmann, M. S. Avendano, J. B. Woehrstein, M. Dai, W. M. Shih, and P. Yin. "Multiplexed 3D cellular super-resolution imaging with DNA-PAINT and Exchange-PAINT." In: *Nature Methods* 11.3 (2014), pp. 313–318. ISSN: 1548-7105. DOI: 10.1038/nmeth.2835 (cit. on p. 152).

[379] L. M. Wassermann, M. Scheckenbach, A. V. Baptist, V. Glembockyte, and A. Heuer-Jungemann. "Full Site-Specific Addressability in DNA Origami-Templated Silica Nanostructures." In: *Advanced Materials* n/a.n/a (), p. 2212024. ISSN: 0935-9648. DOI: https://doi.org/10.1002/adma.202212024 (cit. on p. 152).

[380] R. A. Puras Lutzke, C. Vink, and R. H. Plasterk. "Characterization of the minimal DNA-binding domain of the HIV integrase protein." In: *Nucleic Acids Research* 22.20 (1994), pp. 4125–4131. ISSN: 0305-1048. DOI: 10.1093/nar/22.20.4125 (cit. on p. 153).

[381] F. Ceccherini-Silberstein, I. Malet, R. D'Arrigo, A. Antinori, A.-G. Marcelin, and C.-F. Perno. "Characterization and structural analysis of HIV-1 integrase conservation." In: *Aids Rev* 11.1 (2009), pp. 17–29. ISSN: 1139-6121 (cit. on p. 153).

[382] S. F. Konrad, W. Vanderlinden, and J. Lipfert. "A High-throughput Pipeline to Determine DNA and Nucleosome Conformations by AFM Imaging." In: *Bio-protocol* 11.19 (2021), e4180. ISSN: 2331-8325. DOI: 10.21769/BioProtoc.4180 (cit. on p. 157).

[383] P. J. Kolbeck. "DNA in the spotlight: visualization, quantification, and manipulation of DNA with small molecule intercalators." 2023. PhD thesis (cit. on pp. 162, 171).

[384] J. Lipfert, J. W. Kerssemakers, T. Jager, and N. H. Dekker. "Magnetic torque tweezers: measuring torsional stiffness in DNA and RecA-DNA filaments." In: *Nat Methods* 7.12 (2010), pp. 977–80. ISSN: 1548-7105 (Electronic) 1548-7091 (Linking). DOI: 10.1038/nmeth.1520 (cit. on p. 163).